Investigating the coronal X-ray characteristics – From Sun as a star to imaging spectroscopy

A thesis submitted in partial fulfillment of
the requirements for the degree of

Doctor of Philosophy

by

Biswajit Mondal

(Roll No. 17330010)

Under the supervision of

Dr. Santosh Vadawale
Professor
Astronomy and Astrophysics
Physical Research Laboratory, Ahmedabad, India.

DEPARTMENT OF PHYSICS

INDIAN INSTITUTE OF TECHNOLOGY GANDHINAGAR

2022

to

my family

DECLARATION

I declare that this written submission represents my ideas in my own words and where others' ideas or words have been included, I have adequately cited and referenced the original sources. I also declare that I have adhered to all principles of academic honesty and integrity and have not misrepresented or fabricated or falsified any idea/data/fact/source in my submission. I understand that any violation of the above will be cause for disciplinary action by the Institute and can also evoke penal action from the sources which have thus not been properly cited or from whom proper permission has not been taken when needed.

(Name: Biswajit Mondal)

(Roll No: 17330010)

CERTIFICATE

It is certified that the work contained in the thesis titled **"Investigating the coronal X-ray characteristics – From Sun as a star to imaging spectroscopy"** by **Biswajit Mondal** (Roll no: 17330010), has been carried out under my supervision and that this work has not been submitted elsewhere for degree.

I have read this dissertation and in my opinion, it is fully adequate in scope and quality as a dissertation for the degree of Doctor of Philosophy.

Prof. Santosh Vadawale
(Thesis Supervisor)
Professor
Astronomy & Astrophysics Division
Physical Research Laboratory
Navarangpura, Ahmedabad, India

Acknowledgements

First and foremost, I want to sincerely thank Prof. Santosh Vadawale, my adviser, for his unwavering support during my Ph.D. study and related research. He provided me with direction as I completed my Ph.D. and wrote this thesis.

Along with my adviser, I would like to express my gratitude to Dr. Aveek Sarkar for his continuous support and encouragement throughout my Ph.D. study. He is a member of my doctorate studies committee (DSC). I would like to thank my other DSC members, Dr. Shashikan Ganesh and Dr. Kinsuk Acharyya, for their useful suggestions during biannual meetings.

My sincere thank to Prof. Santosh Vadawale for providing me an opportunity to join the Chandrayaan-2/XSM team. I would like to thank other team members of XSM; Mr. N. P. S. Mithun, Dr. Aveek Sarkar, Dr. P. Janardhan, Dr. Bhuwan Joshi, Dr. Anil Bhardwaj, Dr. M. Shanmugam, Mr. Arpit R. Patel, Mr. Hitesh Kumar L. Adalja, Mr. Shiv Kumar Goyal, Mr. Tinkal Ladiya, Mr. Neeraj Kumar Tiwari, Mr. Nishant Singh, and Mr. Sushil Kumar. I thank Chandrayaan-2 project, mission operations, and ground segment teams for their support.

I am grateful to my collaborators – Dr. Giulio Del Zanna, Dr. Helen E Mason, Dr. James A Klimchuk, Dr. P.S. Athiray, Dr. S.S. Panini, and others for our stimulating conversations and innovative ideas that have advanced my knowledge.

I thank my fellow labmates in PRL – Mr. Mithun Neelkandan PS, Mr. Neeraj Tiwari, Mr. Hiteshkumar Adalja, and Mr. Cherukuri Sree Vaishnava for the useful discussions and for helping me in the research work.

I also thank all of my batchmates and friends for their support and all the fun we have had in the last few years. I am thankful to Ashish and Lakshitha for proofreading this thesis.

I am thankful to all of my teachers, especially Mr. Srikanta Mukherjee (Jhulan da) and Dr. Asim Kumar Mukherjee (AKM sir), for teaching me about physics and how to appreciate its beauty in everyday life. They taught me not only academic subjects but also important lessons in life.

Last but not least, I want to express my gratitude to my family, especially my parents, sister, and brother-in-law, for all of their support and care throughout the years.

(Biswajit Mondal)

Abstract

The specific physical mechanism underpinning the coronal heating mechanism, which causes the solar corona to be significantly hotter than the solar photosphere, remains a mystery. According to our current understanding of the problem, it is believed that the corona is heated by the continual deposition of small-scale energy, and the frequency of energy deposition can help us to comprehend the heating mechanism. In addition to the coronal heating problem, the spectroscopic observation revealed that the abundance of low FIP elements (whose First Ionization Potential is less than 10 eV) in the closed-loop active corona is 3–4 times higher (FIP bias) than their photospheric abundances. This phenomenon is known as the "FIP Effect", and its true origin is yet to be known. However, with the recent understanding, the FIP effect is believed to be a bi-product of the coronal heating mechanism.

To comprehend the FIP effect in various coronal structures, we have used the disk-integrated spectroscopic observations acquired by the Solar X-ray Monitor (XSM) onboard India's Chandrayaan-2 satellite. The XSM is a broadband spectrometer with a good energy resolution of better than 180 eV at 5.9 keV. It operates in the soft X-ray energy range of 1 to 15 keV with a cadence of 1 s. We have determined the temperature, emission measure, and elemental abundances for X-ray Bright Points (XBP), Active Regions (AR), and tiny solar flares by analyzing the XSM spectra taken during the minimum of Solar Cycle 24. We found that the derived parameters of AR and XBPs remain nearly constant over time with a temperature around ∼3 MK and ∼2 MK, respectively. The obtained abundances of Mg, Al, and Si show the FIP bias ∼2 for XBPs, which is lower than the values obtained in active regions (∼3). This is the first time we have provided a prolonged study of the abundances of XBPs, and show a lower FIP bias compared with the ARs. With our present understanding of the FIP effect, having the lower magnetic activity of the XBPs, it is expected to have a low FIP bias compared with the ARs. On the other hand, performing the time-resolved spectroscopic analysis of the XSM spectrum during the small B-class flares, for the first time, we examined the evolution of FIP bias during the small flares. Our results suggest a variation of FIP bias during the flares, and we proposed two scenarios to explain the results. The first scenario is based on the evaporation velocity of the flaring plasma from the lower to the upper atmosphere, and the second one relies on the flare-driven Alfvén waves.

By combining the unique X-ray data of XSM with the EUV observations of AIA/SDO, we have computed the plasma emissions of the XBPs at various temperatures, as determined by the Differential Emission Measure (DEM). We compared the observed DEM with the modeled DEM obtained from the hydrodynamic simulation of XBP loops. Our results suggest that the frequent heat deposition by impulsive events can mention the heating of XBPs plasma.

During the minimum of solar cycle 24, when solar activity was at its lowest, it was possible to study the spatially integrated plasma parameters from XBPs, ARs, and tiny solar flares using XSM's sun-as-star observations. However, to examine the spatiotemporal evolution of the individual features on the solar disc (e.g., XBPs, ARs, etc.), an imaging spectroscopic observation in the X-ray energy range is required. We are stressing the need for a future X-ray imaging spectroscopic instrument for the Sun. An imaging spectroscopic instrument needs X-ray optics that rely on X-ray mirrors. A single or several thin (10–100 Å) layers of materials make up an X-ray mirror. We have initiated the development of X-ray mirrors by setting up a thin-layer coating facility. Additionally, we developed a piece of software called "DarpanX" to design and characterize the X-ray mirrors. We also proposed a conceptual design for the Solar Imaging X-ray Spectrometer (SIXS), which operates in the 0.5–15.0 keV energy range. The instrument offers an energy resolution of more than 150 eV at 5.9 keV and a spatial resolution of $4''$. It will be able to advance our understanding of the FIP effect and coronal heating problems. We have stated the primary scientific aims of the proposed SIXS instrument and evaluated its ability to accomplish those objectives.

Keywords: X-ray spectroscopy, X-ray imaging, Solar corona, Quiet Sun, Solar flares, X-ray Bright Points, Coronal heating, Coronal abundances, FIP effect, FIP bias, X-ray reflection, X-ray optics, X-ray mirrors, Multilayer mirrors.

List of Publications

Publications attached with thesis:

1. S. V. Vadawale, **B. Mondal**, N. P. S. Mithun, A. Sarkar, P. Janardhan, B. Joshi, A. Bhardwaj, M. Shanmugam , A. R. Patel, H. K. L. Adalja, S. K. Goyal, T. Ladiya, N. K. Tiwari, N. Singh , and S. Kumar, "Observations of the Quiet Sun during the Deepest Solar Minimum of the Past Century with Chandrayaan-2 XSM: Elemental Abundances in the Quiescent Corona", The Astrophysical Journal Letters, doi: https://doi.org/10.3847/2041-8213/abf35d

2. **B. Mondal**, Aveek Sarkar, Santosh V. Vadawale, N. P. S. Mithun, P. Janardhan, Giulio Del Zanna, Helen E. Mason, Urmila Mitra-Kraev, and S. Narendranath, "Evolution of Elemental Abundances during B-Class Solar Flares: Soft X-Ray Spectral Measurements with Chandrayaan-2 XSM", The Astrophysical Journal, doi: https://doi.org/10.3847/1538-4357/ac14c1

3. G. Del Zanna, **B. Mondal**, Y. K. Rao, S. V. Vadawale, N. Mithun, K. Reeeves, H. E.Mason, A. Sarkar, P. Janardhan, and A. Bhardwaj. Multi-wavelength observations by XSM, Hinode and SDO of an active region. Chemical abundances and temperatures. Accepted for publication in The Astrophysical Journal.

4. **B. Mondal**, S. V. Vadawale, N.P.S. Mithun, C.S. Vaishnava, N.K. Tiwari, S.K. Goyal, S.S. Panini, V. Navalkar, C. Karmakar, M.R. Patel, R.B. Upadhyay, "DarpanX: A python package for modeling X-ray reflectivity of multilayer mirrors", Astronomy and Computing, doi: https://doi.org/10.1016/j.ascom.2020.100446

5. **B. Mondal**, J. A. Klimchuk, S. V. Vadawale, A. Sarkar, N. P. S. Mithun, et. al, "Role of small-scale impulsive events in heating the X-ray bright points of the quiet Sun", To be Submitted.

6. **B. Mondal**, S. V. Vadawale, and et al. “Evolution of active regions abundances”, (Under preparation).

Other publications:

1. S. V. Vadawale, N. P. S. Mithun, **B. Mondal**, A. Sarkar, P. Janardhan, B. Joshi, A. Bhardwaj, M. Shanmugam, A. R. Patel, H. K. L. Adalja, S. K. Goyal, T. Ladiya, N. K. Tiwari, N. Singh, and S. Kumar. Observations of the Quiet Sun during the Deepest Solar Minimum of the Past Century with Chandrayaan-2 XSM: Sub-A-class Microflares outside Active Regions., 912(1):L13, May 2021a. doi: 10.3847/2041-8213/abf0b0

2. N. P. S. Mithun, S. V. Vadawale, M. Shanmugam, A. R. Patel, N. K. Tiwari, H. L. Adalja, S. K. Goyal, T. Ladiya, N. Singh, S. Kumar, M. K. Tiwari, M. H. Modi, **B. Mondal**, A. Sarkar, B. Joshi, P. Janardhan, and A. Bhardwaj. Ground calibration of Solar X-ray Monitor on board the Chandrayaan-2 orbiter. Experimental Astronomy, 51(1):33–60, Feb. 2021. doi: 10.1007/s10686-020-09686-5

3. N. P. S. Mithun, S. V. Vadawale, A. Sarkar, M. Shanmugam, A. R. Patel, **B. Mondal**, B. Joshi, P. Janardhan, H. L. Adalja, S. K. Goyal, T. Ladiya, N. K. Tiwari, N. Singh, S. Kumar, M. K. Tiwari, M. H. Modi, and A. Bhardwaj. Solar X-Ray Monitor on Board the Chandrayaan-2 Orbiter: In-Flight Performance and Science Prospects., 295(10):139, Oct. 2020a. doi: 10.1007/s11207-020-01712-1

4. N. Lakshitha, **B. Mondal**, S. Narendranath, et al., Elemental abundances during A-class solar flares: Soft X-ray spectroscopy from Chandrayaan-2 XSM. (Under preparation)

List of Figures

List of Tables

Contents

Chapter 1

Introduction

Our nearest star, the Sun, is the primary source of energy for the entire solar system. Various observational evidence suggests that it was formed approximately 4.5 billion years ago. Because of its proximity and glow, it has generated enormous curiosity in the human mind. Earlier civilizations delineated the Sun as a God. Through the efforts of multiple scholars, including Anaxagoras, Giordano Bruno, Galileo, Kepler, Huygens, Newton, and Bessel, to name a few, we understood that it is a star at the center of the solar system. In terms of physical parameters, the Sun is an average star compared to other stars of the universe. It is also going through its half-life. Among all celestial objects, the Sun has been studied the most. With the latest technology available, it is regularly being observed in all bands of the electromagnetic spectrum. These observations help astronomers comprehend the physical processes that determine the growth and structure of stars.

The solar photosphere is primarily responsible for the optical radiation that we receive from the Sun. Optical emission from a much more tenuous and complex upper atmosphere, known as the corona, is less intense by many orders. This is why the solar corona is only visible when the solar disk is occulted, either artificially or by the moon. Ancient eclipse observations by Indians, Babylonians, and Chinese reported the viewing of the corona (Aschwanden, 2004). However, the true mystery of solar corona was not explored until the beginning of the twentieth century. The advances in atomic physics and spectroscopic eclipse observation revealed that the temperature of the solar corona exceeds million-degree, which is several orders of magnitude higher than the surface temperature ($\sim$5777 K). The main source of energy of the Sun gets generated at the core through the nuclear fusion process. The temperature keeps on falling until the surface, the photosphere. However, there onward, it keeps on increasing until the corona. How a hot atmosphere can reside on a much cooler photosphere is still a mystery, and in astrophysics, this is known as the "coronal heating problem". There have been several proposals capable of explaining the energy transport mechanism from the photosphere to the corona. However, none of them can be satisfactorily explained by the existing observations. Because of its high temperature and optically thin nature, the corona is bright in the energetic part of the electromagnetic spectrum, e.g., ultraviolet/X-rays (see Section 2.2), while the photosphere is almost invisible in this energy range.

Since the plasmas of the solar atmosphere have a common origin, it is expected that the elemental composition would be the same throughout. However, at the dawn of the UV and X-ray spectroscopic observation of the Sun, Pottasch (1963) first identified that elements which are having their first ionization potential (FIP) less than 10 eV (e.g., Mg, Si, and Fe) are more abundant in the corona compared to the photosphere. Later, it was reverified by several authors. The phenomenon is termed as the "FIP effect". It is to be mentioned here that the abundance of the elements with FIP more than 10 eV, known as high FIP elements (e.g., O, Ne, Ar, He, etc.), are either same or depleted in the corona. Like coronal heating, the true origin of the FIP effect is yet to be understood. However, with the current understanding, the FIP effect is believed to be a bi-product of the coronal heating mechanism (Dahlburg et al., 2016).

In this thesis, we address the question of coronal heating, along with the FIP effect in the solar atmosphere. We use the latest X-ray spectroscopic observations of the Sun and hydrodynamic simulations for in-depth understanding. We figure out the limitations of the present X-ray observations and propose a design for the X-ray imaging spectroscopic instrument that can resolve many unsolved mysteries of solar physics. This chapter provides a brief overview of the astrophysics of the Sun and its complex structures. Towards the end, a brief overview of the observation techniques of the solar corona is also provided.

1.1 Structure of the Sun and its atmosphere

The Sun is a typical star of $G2 - V$ spectral type in the main-sequence with a radius of $R_\odot \approx 7{\times}10^5$ Km, an age of $t_\odot \approx 4.6{\times}10^9$ years, and a mass of $M_\odot \approx 2{\times}10^{33}$ g (Weissman et al., 1999). In the optical, infrared, and shorter radio wavelength range, the solar surface is primarily radiated as a blackbody of effective temperature $T_\odot \approx 5777$ k (Carroll & Ostlie, 1996). However, the temperature structure of the solar atmosphere is more complicated. The atmosphere of the Sun is primarily divided into four layers; Photosphere, Chromosphere, Transition region, and Corona. Each of these layers prominently radiates at different wavebands of the electromagnetic spectrum, which allows us to probe and diagnose them. The following sections briefly describe the solar interior (Section 1.1.1) and its atmospheric layers (Section 1.1.2). At the end of this section, a brief description of the solar magnetic field (Section 1.1.3) is provided.

1.1.1 Interior of the Sun

Direct observation of the solar interior is not possible, as it is opaque to radiation. Thus, the model of the solar interior is based on the detailed theoretical calculation of stellar evolution and helioseismology, which is a study of the propagation of waves in the Sun's body that causes small observable oscillations of the surface (Carroll & Ostlie, 1996). Primarily the solar interior consists of three layers – Core, Radiative zone, and Convection zone, as depicted in Figure 1.1a.

The Core of the Sun comprises about 30% of the interior radius ($R_\odot$), i.e., it is extended up to a radius of $<0.3R_\odot$. It is very hot with a temperature of $\sim 1.57{\times}10^7$ K, and it is highly dense ($9{\times}10^{25}$ cm^{-3}). This high density and pressure aid in the continuous nuclear fusion reaction known as "proton-proton" (pp) chains, where two hydrogen atoms fuse to generate a helium atom. The pp-chains reaction also produces the weakly interacting electron-neutrinos (ν_e), positrons (e^+), and photons (γ). Most of the energy produced in the reaction is

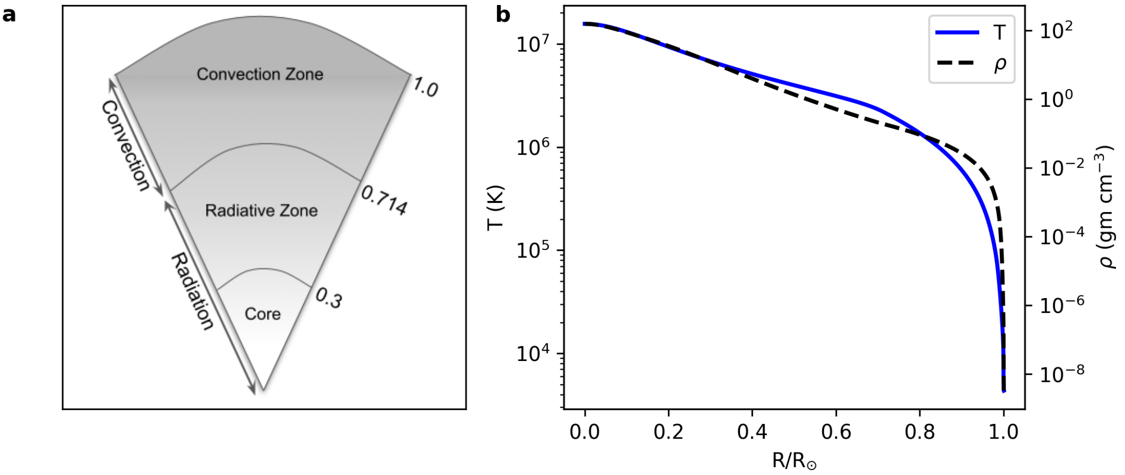

Figure 1.1: (a) A schematic diagram representing the different layers of the solar interior. (b) Temperature and density profile in the solar interior. (Temperature and density data of the solar model described by Christensen-Dalsgaard et al. (1996) is used).

carried outward from the core by photons.

Going further out from the solar core ($> 0.3R_\odot$), the density and temperature fall off (Figure 1.1b), and hence the pp-chain reaction stops. A decrease in temperature causes the radiation pressure to decrease with radius, and hence photons generated by the pp reaction at the core start diffusing at a larger radius. The region in the radius of 0.3R$_\odot$-0.714R$_\odot$ is called the radiative zone, where (as in the core) the energy is primarily transported through radiation.

Moving further out from the radiative zone ($> 0.714R_\odot$), the medium becomes optically thick and hence opaque to radiation due to a significant drop in temperature (Figure 1.1.1b). This region up to the surface of the Sun (1R$_\odot$) is known as the convection zone. In this region, thermal conduction plays an important role in transporting energy. The hot, buoyant material goes up and carries the excess energy outward, while the cold material falls inward. This cycle repeats, providing a continuous transport of the energy to the surface (Carroll & Ostlie, 1996).

1.1.2 The atmosphere of the Sun

The visible surface of the Sun is defined as the photosphere located above the Convection zone. This is the lowermost layer of the solar atmosphere and optically thin ($\tau \leq 1$) for the visible wavelength, which allows for the visible light to escape from this layer without absorption and reemitting. The base of the photosphere is usually defined as 100 Km below the level where the optical depth (τ_{5000}) at a wavelength of 5000 Å is unity (Carroll & Ostlie, 1996). At this depth, the temperature is approximately 9400 K, and moving outwards through the photosphere, the temperature of the gas decreases from its base value to a minimum value of 4400 K (Figure 1.3) at the height of around 500 Km above $\tau_{5000} = 1$. In the visible and infrared wavelengths, the photosphere is primarily emitting as a black body (Carroll & Ostlie, 1996). The high-resolution observation of the photosphere shows a granulation pattern caused by the convection below the photosphere, where the hot plasma rises (appears to be bright) and cooler plasma falls down, resulting in dark intergranular patterns. Figure 1.2a shows the image of the solar photosphere as observed by the 6173 Å waveband of Helioseismic and Magnetic Imager (HMI: Scherrer et al. (2012)) onboard Solar Dynamics Observatory(SDO: Pesnell et al. (2012)). The small dark spots in the show sunspots (see Section 1.1.3), are the region of concentrated magnetic fields on the solar surface, and it appears black due to the less temperature compared with the surrounding. At the center of the sunspot, the temperature may be as low as 3900 K, compared with the Sun's effective temperature of 5777 K (Carroll & Ostlie, 1996).

Above the solar photosphere, the atmospheric layer of the Sun is known as the chromosphere, which extends up to approximately 2100 Km (Carroll & Ostlie, 1996) as shown in Figure 1.3. Moving upwards through the chromosphere, the temperature rises from the bottom and reaches a value of more the 10^4 K at the top, whereas the density reduces significantly with height. Because of the tenuous plasma of this layer, it is approximately 10^{-4} times fainter than the photosphere in visible wavelength (Carroll & Ostlie, 1996). Due to the low temperature and high density, some emission lines that are not formed in the

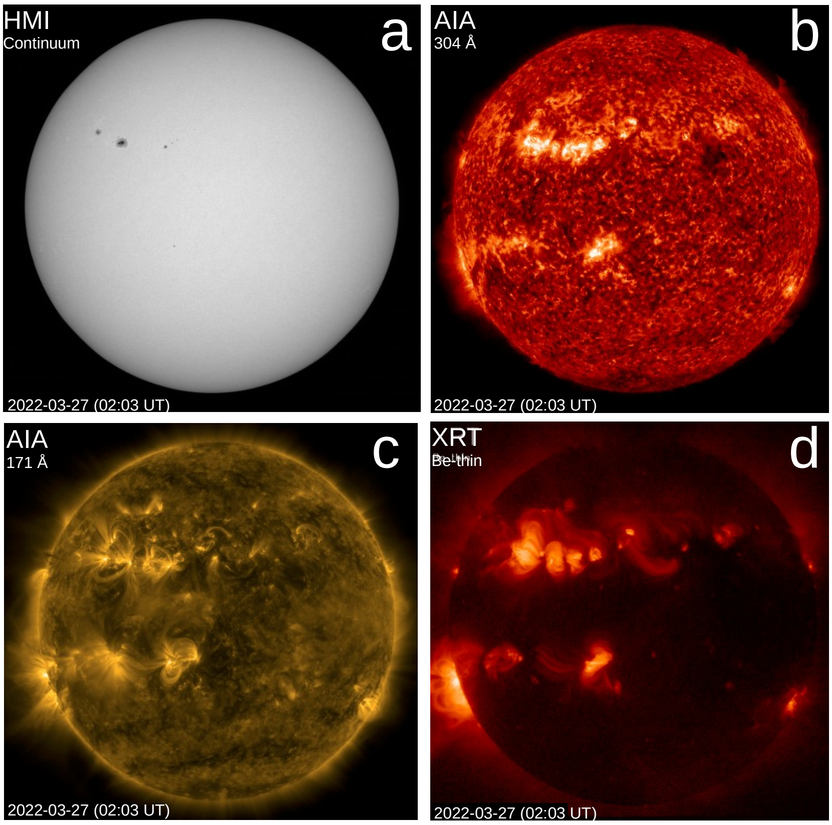

Figure 1.2: The layers of the solar atmosphere were observed by multiple wavelengths at ∼02:03 UTC on 27 March 2022. Panels **a** and **b** are represent the photosphere and chromosphere respectively. Panels **c** and **d** are represent are the EUV and X-ray images of the corona.

photosphere can be observed in the environment of the lower chromosphere. These include the Balmer-α line (Hα at 6563Å, and singly ionized calcium (Ca II) H and K lines at 3968 Å, and 3933 Å respectively (Phillips et al., 2008). However, the higher temperature upper chromosphere is very bright in UV wavelength. Figure 1.2b shows the full disk image of the solar chromosphere taken by the 304 Å waveband of Atmospheric Imaging Assembly (AIA: Lemen et al. (2012)) onboard SDO.

The temperature from the top of the chromosphere starts to increase rapidly and reaches a value of more than 10^5 K within a very thin layer of a few hundred Km. This thin layer, known as the transition region, is shown in Figure 1.3. Along with the temperature, the density of the medium also decreases rapidly. The upper portion of the transition region is very bright in the EUV wavelength of the electromagnetic spectrum.

The outermost atmospheric layer of the Sun is known as the corona.

The temperature of the solar corona exceeds 10^6 K, whereas the particle density is very low ($< 10^9$ cm^{-3}), as shown in Figure 1.3. Corona is very bright in the EUV, X-rays wavelength of the electromagnetic spectrum. It is very dynamic and consists of complex loop-like structures. Figure 1.2c and Figure 1.2d show the EUV and X-ray images of the solar corona at the same time as observed by 193 Å passband of AIA onboard SDO and Be-thin filter of X-ray Telescope (XRT: Golub et al. (2007)) onboard Hinode observatory. The loop-like structures in the images are the magnetically closed loops (see Section 1.1.3), whose footpoints are located beneath the chromosphere.

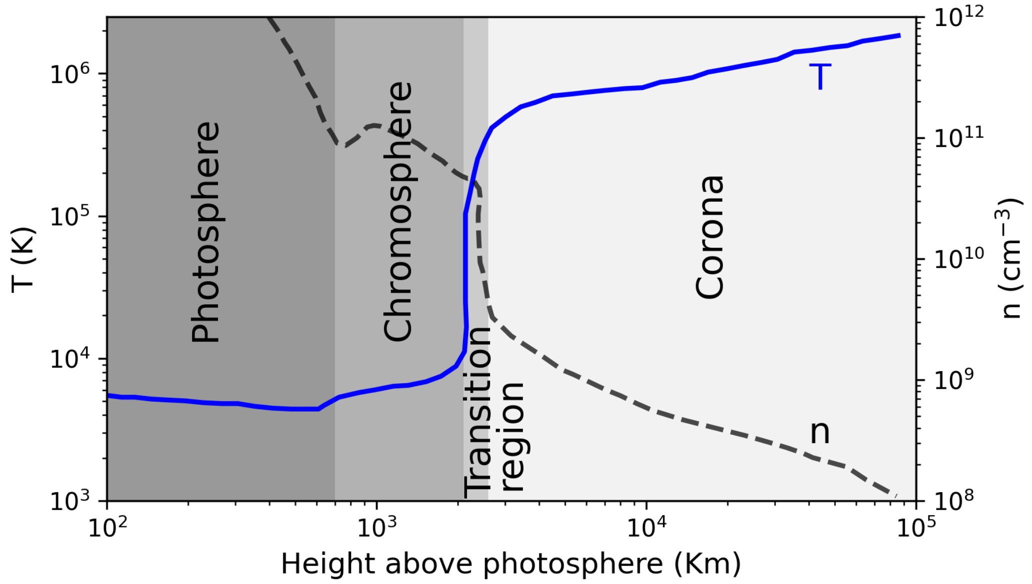

Figure 1.3: Temperature (blue curve, left axis) and density (black dashed curve, right axis) profile of the solar atmosphere above the surface. Different layers of the atmosphere are marked by the background shaded color. The density and temperature model of the chromosphere (Fontenla et al. (1990); Model FAL-C) and lower corona (Gabriel, 1976) are adopted from Figure-1.19 of Aschwanden (2004).

1.1.3 Solar magnetic cycle and its correlation with the coronal phenomenon: ARs, XBPs, and Flares

Like our Earth's magnetic field, Sun has its own magnetic field, which is nearly dipolar at the poles of the Sun. However, the magnetic field near the equator is more complex and highly non-uniform. The polarity of the field between the poles of the Sun reverses around every 11-year time period, known as the magnetic cycle (or simply, solar cycle) of the Sun. A full cycle of 22 years, after which the polarity restored its original configuration, is known as Hale cycle (Aschwanden, 2004). The reversal of the global solar magnetic fields evolved from a poloidal field towards a toroidal field under the influence of differential rotation (Babcock, 1961), where the rotation rate of the Sun is dependent on longitudinally as well as radially. The outer layers of the Sun near the equator rotate faster compared with the interior, whereas at higher latitude, the scenario is the opposite (Thompson et al., 1996). Near the base of the convection zone (Figure 1.1), the rotation rate at every latitude converges, such that the radiative zone rotates rigidly compared with the outer layers. This region at the base of the convection zone is referred to as tachocline (Aschwanden, 2004). The internal magnetic field in the tachocline (in order of 10^5G) is periodically strengthened and weekend, from where the buoyant magnetic flux tubes arise and occasionally emerge at the photosphere as a cool and dark bipolar structure, termed a sunspot. High above the photosphere, at the corona, the highly concentrated magnetic fields emerge from sunspots creating active regions (AR), which appear as bright loop-like structures in the EUV and X-ray wavelength.

Active Regions (AR)

The number of sunspots and ARs is highly variable during the solar cycle, reaching a maximum value during the middle of a cycle (called as solar cycle maximum) and dropping to a low level at the end of the cycle (known as solar cycle minimum). Thus the EUV/X-ray intensity of the Sun dynamically varies throughout the solar cycle. Figure 1.4 (blue color) shows the number of sunspots as a function of time for the last hundred years, covering the solar cycle number 16 to 24. The top row (orange shaded region) shows the full-disk X-ray images of the Sun taken by the Al-mesh filter of X-ray telescope (XRT: Golub et al. (2007)) onboard Hinode (Kosugi et al., 2007) observatory during the recent solar cycle-24. The appearance of the ARs is very common in the solar cycle maximum (in the years 2012 to 2016), visible as bright regions. Whereas during the solar cycle minimum (e.g., 2019 or 2020), the activity is very less with the appearance of very few sunspots/ARs or even without the presence of them.

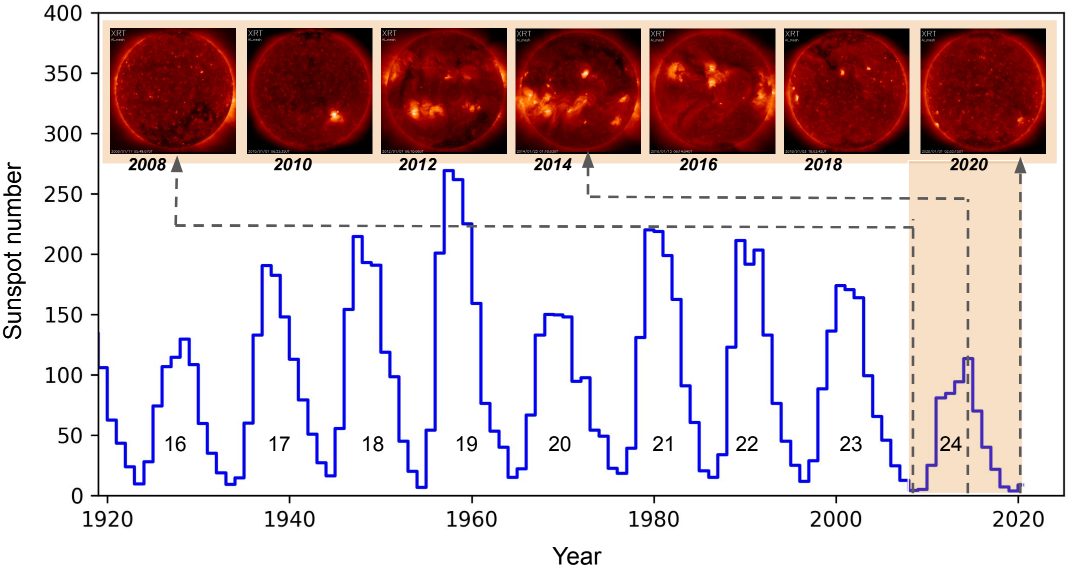

Figure 1.4: A number of sunspots as a function of time (blue) for the last hundred years. The sunspot data available by the Royal Observatory of Belgium is used in this plot. The top row shows the representative synoptic X-ray images of the Sun taken by the Al-mesh filter of XRT/Hinode during the period of solar cycle-24.

X-ray bright points (XBP)

X-ray photograph of the Sun taken by the early rocket flight in the 1970s for the first time showed the point like bright sources on the solar disk. These point-like structures, having a typical diameter of 30” with a bright core of 5”-10”, are known as X-ray bright points (XBP), and they are found to be located all over the solar disk (Vaiana et al., 1973b,a; Krieger et al., 1971; Golub et al., 1974a). The magnetic field strength of XBPs is much smaller than the ARs. Unlike the ARs, the XBPs are observed to appear almost uniformly throughout the solar cycle, which suggests their formation mechanism is different than the ARs (Hara & Nakakubo-Morimoto, 2003). The emission of XBPs is hidden behind the bright ARs during the solar cycle maximum, whereas during the minimum phase of the solar cycle, they are prominently visible in the X-ray images. Figure 1.5 shows the full disk X-ray image taken by the Be-thin filter (which is more sensitive to higher temperature) of XRT/Hinode during the quiet phase of the Sun, where the XBPs are clearly visible as small brightening in the absence of AR.

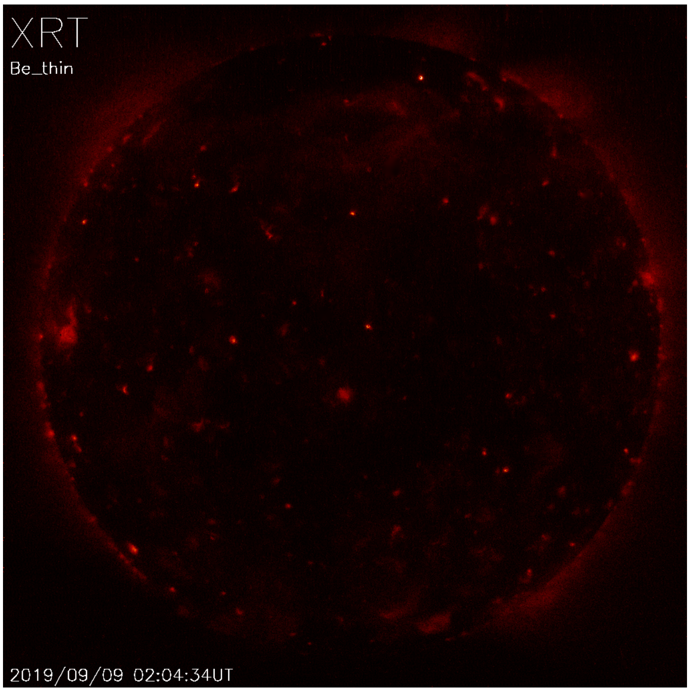

Figure 1.5: X-ray image of the Sun taken by Be-Thin filter of XRT/Hinode during the minimum of solar cycle 24. Most of the bright points are the XBPs.

Solar flares

Transient brightenings are often observed from ARs with a burst of energy, generally known as solar flares. The maximum energy released by a solar flare can be in the order of 10^{32}-10^{33} erg. Though solar flares are very commonly seen within the AR, they are also found to occur outside the AR with a release of a small amount of energy (in the order of $< 10^{27}$ erg, e.g., Kuhar et al. (2018); Sylwester et al. (2019); Vadawale et al. (2021b)). The modern classification system for solar flares uses the letters A, B, C, M, or X, according to the peak flux in watts per square meter (W/m^2) in soft X-rays of wavelengths of 1 to 8Å, measured at the Earth. Figure 1.6 shows the solar flares of different classifications as observed by the geosynchronous equatorial satellites (GOES). X-class flares are the biggest flares seen in the solar atmosphere with a peak flux of $> 10^{-4}$ W/m^2, whereas the peak flux reduces by order of magnitude for each class as we move towards M, C, B, and A-class flares.

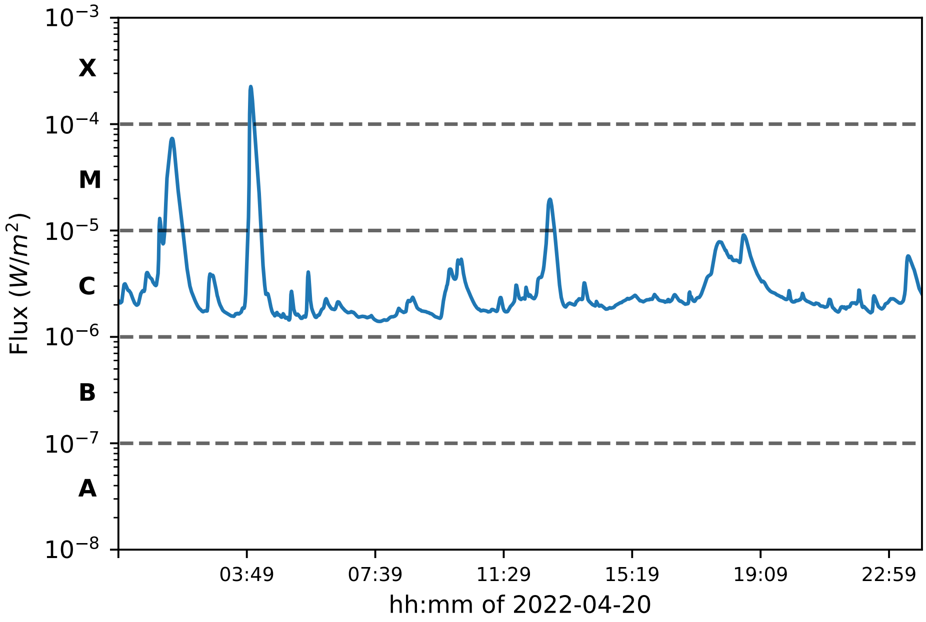

Figure 1.6: Solar X-ray flux was observed by GOES 1-8 Å waveband on 20 April 2022. The enhanced fluxes in the plot represent different classes of solar flares, defined by their peak flux.

1.2 Heating of solar corona

Since the discovery of the multi-million degree kelvin temperature of the solar corona, which is several times hotter than the solar surface, the true physical mechanism behind it remains a mystery. It has been found that the total energy loss through radiation and conduction from the corona has an energy flux of roughly 10^7 erg cm^{-2} s^{-1} in active regions and $3{\times}10^5$ erg cm^{-2} s^{-1} in quiet Sun (Withbroe & Noyes, 1977). Thus the required power for the coronal energy loss is a small fraction of the total flux irradiated from the solar photosphere (order of 10^9 erg cm^{-2} s^{-1}). The basic requirement of any coronal heating mechanism is how and exactly from where the energy is supplied to the corona. Several theories have been proposed to explain the sources of coronal heating. At present, it has been widely accepted that the mechanical motions of the plasma within or below the photosphere are primarily responsible for coronal heating (Klimchuk, 2006). These motions displace the base of the coronal magnetic field lines, and depending on the displacement's timescale, it either generates waves or stretches the field line. The waves produced due to the perturbation of the field lines can dissipate into the atmosphere and heat the medium. On the other hand, the energy stored within the stretched field lines can release their energy and heat the medium. Dissipation of the waves is referred to as an AC heating mechanism, whereas the dissipation of the stressed magnetic energy is known as DC heating. Both of these two mechanisms are described briefly in Section 1.2.1 and Section 1.2.2 respectively.

1.2.1 AC heating

The footpoints of the magnetic fields beneath the photosphere are frequently subjected to the turbulent velocity field of the underlying convection zone and thus move randomly across the photosphere. These turbulent motion of the magnetic footpoints induces a large flux of upward propagating waves of various modes, such as acoustic waves, slow/fast mode MHD waves, and Alfvén waves (Aschwanden, 2004). Considering these waves as a viable source to heat the corona, required to carry a sufficient amount of energy to the corona and dissipate that energy efficiently there. However, only a small fraction of the flux of some of the wave modes can penetrate the stiff temperature and density gradient of the chromosphere and transition region (Klimchuk, 2006). The magneto-acoustic waves (fast mode) are totally internally reflected somewhere in the chromosphere and can not reach the corona (Aschwanden, 2004), whereas the Alfvén waves of a specific frequency are not restricted by these constraints, and thus, a substantial fraction of Alfvén waves easily propagate to the corona. It has been found that the energy flux carried by the Alfvén waves is sufficient to heat the corona, but it is very difficult to dissipate their energy into the coronal environment (Aschwanden, 2004). Thus the energy supply to the corona through the AC mechanism is less certain. However, In recent years, efforts have been made to characterize wave energy content in the corona through observation and simulate wave heating numerically, with an emphasis on energy input, energy propagation, and energy dissipation (e.g., see Van Doorsselaere et al. (2020) and the references therein).

1.2.2 DC heating

The work done by the random motion of the magnetic foot-points produces continuous stress in the field lines and increases the free energy at a rate of upward Poynting flux (F_P in erg cm^{-2} s^{-1}) through the base (Klimchuk, 2006).

$$F_P = -\frac{1}{4\pi} B_v B_h V_h \tag{1.1}$$

Here B_v, B_h are the vertical and horizontal components of the magnetic field and V_h is the horizontal velocity of the foot-point. This process is demonstrated with a simple cartoon in Figure 1.7. Initially, the field lines are rooted between the top and bottom surfaces (Figure 1.7a). As time progresses, the foot-points move randomly and make an angle $\theta(t)$ at time t, with respect to the horizontal plane. In this way, when the field lines are sufficiently twisted and come close to the opposite polarity (shown by asterisks in panel b), they release the stored energy and change their topology (shown in panel c) to an equilibrium state (force-free) by a process referred to as magnetic reconnection. When two magnetic field lines having opposite polarity and are nearly anti-parallel orientation come very close to each other, a high magnetic gradient from positive to negative polarity arises, and somewhere in-between them, the field strength will be very less or zero. In general, the coronal plasma has a low β (the ratio between magnetic pressure and gas pressure) value, which prevents the magnetic field from diffusing along the field lines. But during the magnetic reconnection between the two field lines, nearly zero magnetic field regions produce a high β region, known as the diffusion region. The condition of the diffusion region allows the field to reorient itself and produce a new topology. High pressure is produced during the reconnection of the magnetic fields, which pushes the plasma and fields away from the diffusion region, and thus the magnetic energy is converted to kinetic energy.

Parker (1988) first envisaged that the bright X-ray AR corona is produced by the swarm of small-scale reconnection events from the braided and twisted magnetic field lines. These small-scale events have an energy of around 10^{24} erg, nine orders of magnitude lesser than the big solar flares ($\sim 10^{33}$ erg), and they are termed “nanoflares”. Though nanoflares are yet to be observed

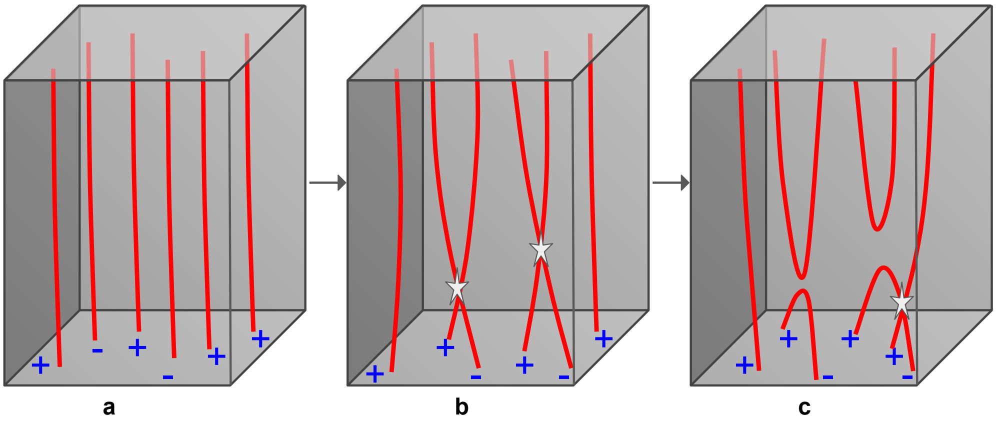

Figure 1.7: Evolution of the magnetic field lines due to the random motions of the footpoints.

directly with the present instrument capabilities, much progress has been made in understanding the role of them to heat the corona. Earlier modeling efforts (e.g.Cargill (1994); Cargill & Klimchuk (2004)) showed that nanoflares could heat the plasma of typical coronal temperature (1-2 Mk) to more than a few million-kelvin temperatures, the "so-called "smoking gun" of nanoflare heating. Thus nanoflare heated plasma will have a distribution of temperature, which is observed within the core of ARs (e.g., Tripathi et al. (2011); Winebarger et al. (2011); Del Zanna et al. (2015); Brosius et al. (2014); Caspi et al. (2015); Ishikawa et al. (2017)).

Although the original concept of nanoflare by Parker (1988) was concentrated only on the reconnection mechanism, the modern understanding of nanoflare is much more general. Klimchuk (2015) defined the nanoflare as any impulsive events irrespective of the underlying physical mechanism, i.e., they can be produced by the dissipation of waves or by reconnection. In a single magnetic flux tube, nanoflare events may occur very frequently or infrequently and determine their contribution to heating the plasma at different temperatures (Klimchuk, 2006, 2015). In this thesis, we have adopted the general concept of nanoflare Klimchuk (2015) and studied their properties to heat the solar corona during the quiet phase of the minimum of solar cycle-24.

1.3 Solar abundances: FIP effect

The study of the elemental abundances in different atmospheric layers of the Sun is of great interest in the entire solar physics community. It can furnish information on the energy and mass flow between the different layers. Within the core of active regions, it has been observed that the abundances of the elements whose First Ionization Potential (FIP) is less than 10 eV (e.g., Na, Fe, Ni, etc.) are 2-4 times higher (known as FIP bias) compared to their photospheric values (Pottasch, 1963; Feldman, 1992; Feldman & Laming, 2000; Feldman & Widing, 2003; Saba, 1995). This phenomenon is known as the FIP effect. Figure 1.8 shows a pictorial view of the FIP effect, where the abundance ratio (FIP bias) of the elements at the corona and photosphere is plotted as a function of the element's FIP. All the elements (e.g., Na, Fe, Ni, etc.) with FIP less than 10 eV have FIP-bias of 2-4, representing they are 2-4 times more in the amount present in the corona than in the photosphere. The FIP bias for the elements having FIP more than 10 eV (e.g., Ar, Ne, etc.) are close to one representing their composition in both photosphere and corona remain the same.

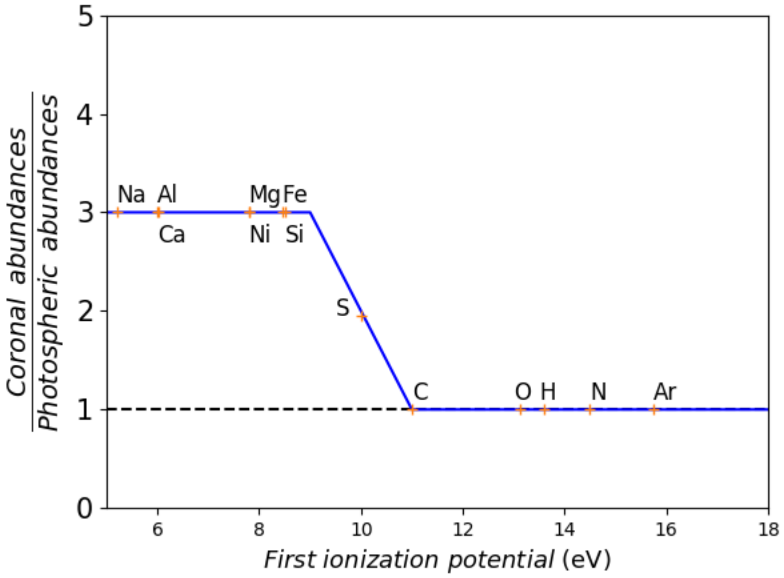

Figure 1.8: Diagram repressing the FIP effect. This figure is adopted from Feldman (1992).

Since the discovery of the FIP effect, several theories have been proposed to explain its origin (e.g., Hénoux (1998); Laming (2004) and references therein). The present understanding of the FIP effect is based on the upward reflection of the magnetic waves (Alfvén wave) from the top of the chromospheric layer, as explained by the cartoon shown in Figure 1.9. A magnetic-field loop is rooted in the lower atmosphere and expanded to the corona. The orange arrow at the left represents the increase of temperature with a height from the lower atmosphere. Alfvén waves can travel throughout the loop (as shown by the black arrows inside the loop), and the waves traveling from upward to downward can experience a high-density gradient causing a reflection of them. It is believed that the upward reflection of the waves happens near the top of the chromosphere, where the density gradient is very stiff (shaded layer near the top of the chromosphere). Due to the reflection of the waves, an upward force known as the 'Ponderomotive force' is experienced by ions (indicated by the magenta arrow) present in that layer (Laming, 2004, 2009, 2012, 2015, 2021). The ions influenced by the Ponderomotive force travel upward and increase their concentration in the corona. The temperature and pressure at the top of the chromosphere are such that only the elements having FIP less than 10 eV can ionize, whereas the high FIP elements remain neutral. Thus, only the ions of low FIP elements are influenced by the Ponderomotive force, causing an increment of their concentration in the corona, whereas the concentration of the high FIP elements remains the same.

The solar FIP effect has been extensively reviewed by various authors (e.g., Feldman (1992); Feldman & Laming (2000); Feldman & Widing (2003); Saba (1995)) in the last two decades, revels the composition primarily of the "closed-loop" ARs corona. Later on, it was found that different structures of the solar atmosphere have different FIP biases, e.g., Sylwester et al. (2014); Warren (2014a) found less FIP bias during the peak of large solar flares. FIP effect is also been observed in the solar wind plasma (e.g., Wenzel et al. (1992)) and a variation of the FIP bias with solar wind speed is found (Feldman et al., 1998; Bochsler, 2007; Laming, 2015). Using the new generation X-ray spectroscopic observations, in this thesis, we have extensively studied the abundance evolution during the small solar flares, XBPs, and ARs.

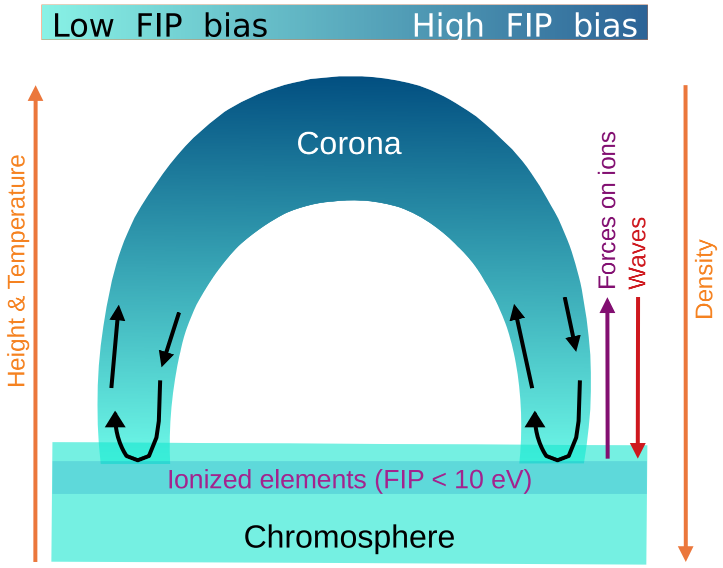

Figure 1.9: Diagram representing the Ponderomotive force model within a closed coronal loop. The black arrows represent the reflection of the downwards magnetic waves from a high-density gradient region believed to be in the upper chromosphere.

1.4 Observation of the solar corona

The solar corona consists of hot and optically thin tenuous plasma. The light elements (e.g., H, He) are completely ionized, whereas the heavier elements (Fe, O, C etc.) are ionized at their different ionization state, depending on the temperature. Thus, radiation from the solar corona mostly comes from the highly ionized elements, primarily in the EUV and X-ray energy bands of the electromagnetic spectrum. Since the radiation in these energy bands is absorbed by the earth's atmosphere, most of the observations and spectral diagnoses have been obtained from space-based remote-sensing instruments. Solar corona has been extensively observed in EUV and soft X-ray energy bands since the early 1960s by several rocket flights, and some of them have provided a very good energy-resolved spectrum. After the early observations, several spacecraft have been flown for spectroscopic observation. A brief overview of these observations can be found in Del Zanna & Mason (2018) and the references therein. These spectroscopic observations make it possible to understand the properties of the coronal plasma (e.g., temperature, density, elemental abundances, etc.).

In addition to the spectroscopic observations, imaging observation of the solar corona in the EUV and X-ray energy band helps us to determine the structure of the solar corona. Different structures on the solar disk show different intensity, e.g., ARs are much more intense than the XBPs in the X-ray/EUV energy range, which indicates that their density and temperature must be different. However, a details parametric property can only be achieved by spectroscopic measurements.

In this thesis, we have studied the solar corona through X-ray spectroscopic observation using a new generation X-ray spectrometer named Solar X-ray Monitor (XSM) that was launched in mid of 2019 onboard India's Chandrayaan-2 orbiter. XSM has a good energy resolution, cadence, and signal-to-noise ratio. However, it does not have any imaging capability and provides the disk-integrated spectrum (see Section 2.3.2). In the absence of an imaging capability of the XSM, we have used the operational imaging instruments (AIA onboard SDO and XRT onboard Hinode) along with the XSM observations to see the emission location on the solar disk (see Chapter 2).

Considering the structural dynamics of the solar corona, it is essential to observe the Sun through simultaneous imaging spectroscopic instruments of better spatial and energy resolution. In the near future, a simultaneous imaging spectroscopic instrument in the X-ray energy range is essential (see Section 2.2). Such instruments primarily consist of a detector module (see Section 2.3) along with an imaging component (see Section 2.4). Due to the energetic nature of the X-rays, they are challenging to image. It is possible using the grazing incidence reflection from the X-ray mirrors. We have studied the design, characterization, and development of X-ray mirrors. In the end, we have provided a conceptual design of the simultaneous imaging spectroscopic instrument in the X-ray energy range for future missions.

1.5 Thesis outline

Chapter 2: Coronal plasma diagnosis: Soft X-ray spectroscopy.

This chapter gives an overview of the X-ray emission processes from hot coronal plasma and the spectroscopic technique to diagnose the plasma parameters. We have used a new generation X-ray spectrometer, ‘Solar X-ray Monitor’ (XSM) for the plasma diagnosis. A brief overview of the XSM along with the other instruments and techniques used in the present thesis is described.

Chapter 3: FIP effect of quiet Sun XBPs, and ARs.

Here, the spectroscopic studies of the sun during the minimum of solar cycle 24 are carried out and the FIP bias of the XBPs and ARs is estimated.

Chapter 4: Evolution of plasma parameters during small flares.

This chapter gives a detailed analysis of the time-resolved X-ray spectroscopic study during the small B-class solar flares and derived the evolution of the plasma parameters throughout the flares.

Chapter 5: Insight into heating of XBPs.

This chapter is focused on the role of small-scale impulsive events to maintain the heating of the quiet Sun XBPs.

Chapter 6: Exploring imaging X-ray spectroscopy of the Sun - development of X-ray mirrors.

This chapter provides the details of the reflection technique of the X-rays using the X-ray mirrors, which is the primary requirement for future X-ray optics. It also describes the fabrication and characterization of these mirrors in our lab.

Chapter 7: Conceptual design of Solar Imaging X-ray Spectrometer (SIXS).

This chapter provides a conceptual design of an solar imaging spectroscopic instrument for the future mission.

Chapter 9: Summary and Future Work.

Here, we summarize the thesis work and discuss the future scopes.

Chapter 2

Coronal plasma diagnosis: Instrumentation and techniques

2.1 Introduction

Diagnosing the coronal plasma properties to get insights into the underlying properties of the solar corona is nontrivial as most of the measurements are restricted by remote sensing observations. Thus inferring the coronal plasma properties are based on the various diagnostics of the coronal emission at EUV to X-ray energy bands. This chapter is provided how the coronal emission produces in the EUV and X-ray energy range (Section 2.2). In Sections 2.3 and 2.4, we discuss the detection techniques of the X-ray (or EUV) emissions from remote sensing instruments through spectroscopy and imaging. We also discuss how to diagnose the plasma parameters by modeling the observed spectrum. In Section 2.5, we discuss how to combine imaging and spectroscopic observations to derive the temperature structure of the emitting plasma, characterized by Differential Emission Measure (DEM). At the end (Section 2.6) we discuss how to probe the nature of the heating from the observed DEM with the help of hydrodynamic simulation.

2.2 Soft X-ray and EUV emission mechanisms

Solar corona emits strongly in both soft X-ray and EUV regimes of the electromagnetic spectrum through continuum and line emission of ionized elements. The primary processes involved in the ionization of the atoms are collisional ionization (Figure 2.1a) and excitation autoionization (Figure 2.1b), whereas the atoms recombine in the process of dielectric recombination (Figure 2.1c) and radiative recombination (Figure 2.1d). In equilibrium, the ionization and recombination processes are balanced together for a particular element and determine the number density of the ion relative to the number density of the element, generally known as ionization fraction; e.g., Figure 2.2 shows the ionization fraction of the Fe calculated from the available ionization fraction within CHIANTI atomic database (Del Zanna et al., 2021).

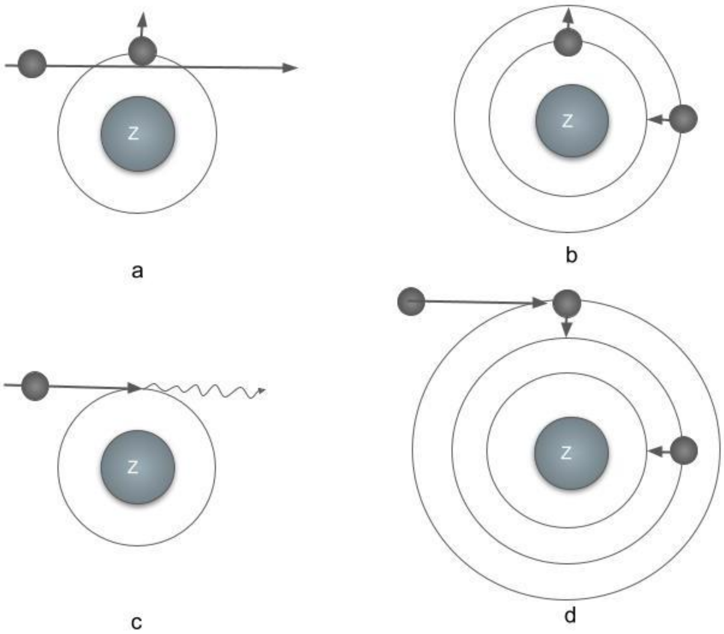

Figure 2.1: Diagram showing ionization and recombination processes: Collisional ionization in panel a, and Auto-ionization in panel b. Recombination processes: Radiative recombination in panel c, and Dielectric recombination in panel d. This figure is adopted from Aschwanden (2004).

The line emissions are primarily produced due to the atomic transitions of the ionized elements at their different ionization states. In contrast, the continuum emission mainly originates due to free-free, free-bound, and two-photons processes. We will briefly describe each of these processes below.

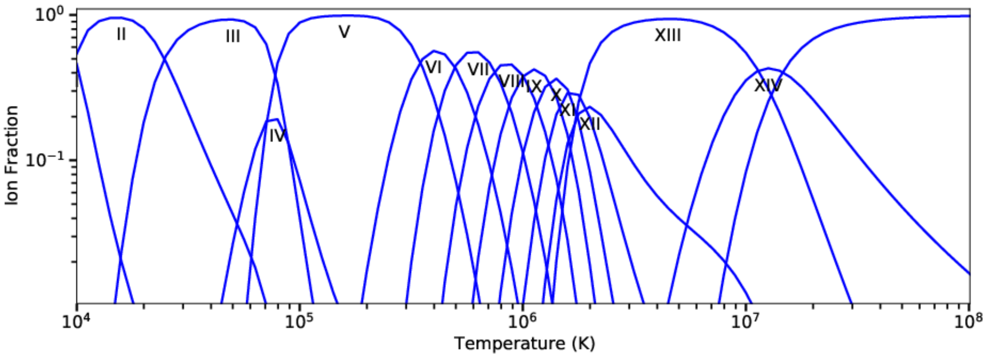

Figure 2.2: Ionization fraction of Fe, estimated using the CHIANTI atomic database.

2.2.1 Line emission

Consider an element, X is in the ionization state of m, then the transition of an electron from the higher state (j) to lower state (i) will release a photon of energy $\delta E = E_j - E_i = h\nu_{ij}$ (Figure 2.3). The flux ($F(\nu_{ij})$) of the observed

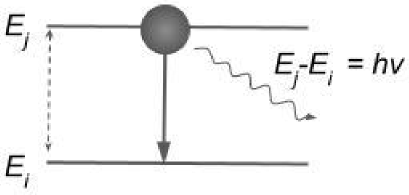

Figure 2.3: A Schematic two-label diagram shows an electron's transition from a higher energy state to a lower energy state and produces a photon of energy $h\nu$ in the process.

optically thin line of frequency, ν_{ij} will be (Aschwanden, 2004),

$$F(\nu_{ij}) = \frac{h\nu_{ij}}{4\pi R^2} \int_V n_j A_{ji} dV \;\; (erg\, cm^{-2}\, s^{-1}) \tag{2.1}$$

Here, V is the volume of the emitting plasma, and A_{ji} is the Einstein coefficient of the spontaneous transition probability from the upper to the lower state. The number density of the excited state, n_j, must be populated by balancing the excitation and de-excitation processes. An electron can be excited to a higher energy state by following different procedures, e.g., a collision of the free electron, collision with a proton, or stimulated by radiation. On the other hand, electrons can decay to a lower energy state by several processes, such as electron and proton collision, spontaneous radiative decay, and stimulation by a photon. All of these excitation and de-excitation processes can be found in a textbook (e.g., Aschwanden (2004)) or review article (e.g., Del Zanna & Mason (2018)). In Equation 2.1, n_j can be written as:

$$n_j = \frac{n_j}{n_{ion}} \frac{n_{ion}}{n_{el}} \frac{n_{el}}{n_H} \frac{n_H}{n_e} n_e \tag{2.2}$$

where n_j/n_{ion} is the number density of the upper level relative to the total number density of the ion, which can be estimated using CHIANTI by solving the statistical equilibrium for a number of low levels of the ion including all excitation and de-excitation mechanisms. n_{ion}/n_{el} is the ionization ratio of the ion relative to the number density of the element, known as ionization fraction (e.g., see Figure 2.2 for Si). $n_{el}/n_H = A_X$ is the absolute elemental abundance relative to Hydrogen, and $n_H/n_e \approx 0.83$ is the ratio of Hydrogen to the electron number density, based on the abundance ratio of $10 : 1$ of $H : He$ with complete ionization (Aschwanden, 2004). Generally, all of the atomic physics variables are combined into a single function known as contribution function $G(T, \nu_{ij}, A_X, n_e)$, as follows:

$$G(T, \nu_{ij}, A_X, n_e) = A_X \frac{h\nu_{ij}}{4\pi} \frac{A_{ji}}{n_e} \frac{n_j}{n_{ion}} \frac{n_{ion}}{n_{el}} \tag{2.3}$$

Now the flux of the observed line represented in Equation 2.1 reduces to,

$$F(\nu_{ij}) = G(T, \nu_{ij}, A_X, n_e) \int_V n_e n_H dV \tag{2.4}$$

The integral on the right-hand side, $\int_V n_e n_H dV$, is known as the volume Emission Measure (EM), which is an efficient tool to diagnose the coronal plasma and is used extensively in this thesis, as discussed in Section 2.5.

2.2.2 Free-free emission

The corona consists of fully ionized gas or plasma, and hence the electrons and ions move freely by interacting with each other through their electrostatic charges. In solar corona, the electrons are separated out from the atomic nuclei and can undergo manyfold interactions. The most common interaction between electrons and atomic nuclei is the free-free interaction, where a free electron (e(E)) of energy E is elastically scattered from an ion (Z) and escapes as a free electron of energy E' along with a photon ($h\nu$) (see Figure 2.4a), i.e., $Z + e(E) \longrightarrow Z + e(E') + h\nu$. The energy of the emitted photon corresponds to the kinetic energy difference between the incoming and outgoing electrons (i.e., $h\nu$ = E' - E). In this free-free process, the incoming electron loses its energy and is also known as "bremsstrahlung", which means 'breaking radiation' as introduced by Bohr, Bethe, and Heitler (Aschwanden, 2004).

2.2.3 Free-bound emission

Unlike the free-free emission, where a free electron interacts with the Coulomb interaction of an ion and becomes free at the end, the incoming free electron may capture a bound state of the target ion in the process of recombination. A free incoming electron of energy E captured by an ion, Z^{n+1} (see Figure 2.4b) into a bound state of Z^n with a release of a photon, i.e., $e + Z^{n+1} \longrightarrow Z^n + h\nu$. Here, the photon energy ($h\nu$) should be equal to the kinetic energy of the incoming electron in addition to the ionization energy (I) of the bound state n, i.e., $h\nu = E + I$. As the ionization energy (I) of different states is discrete, for a Maxwellian electron distribution, the free-bound continuum emission is characterized by discontinuities at the ionization thresholds.

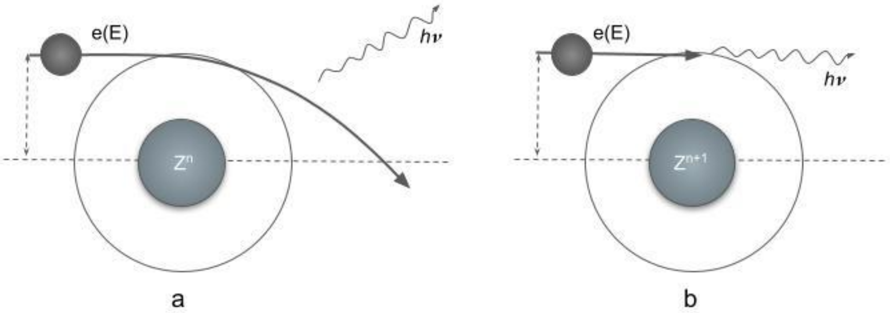

Figure 2.4: Diagram showing the free-free (a), and free-bound (b) emission mechanisms.

2.2.4 Two-photon emission

Along with the free-free and free-bound processes, another procedure that produces continuum radiation is the two-photon continuum, which is almost negligible except at very low temperatures, $\mathrm{T} < 3 \times 10^4$ K (Del Zanna & Mason, 2018). The lifetime of an excited state of an isolated atom depends on the rate at which it decays to the lower energy state with the emission of a single photon. However, in certain circumstances, such single-photon transition is strictly forbidden, e.g., $2s_{1/2}$ state of H (or H-like ions), and $1s\ 2s\ {}^1S_0$ state of He-like ions. In such cases, the radiative decay mechanism is the simultaneous emission of two photons; i.e., for H-like ions: $2s_{1/2} \longrightarrow 1s_{1/2} + h\nu_1 + h\nu_2$, and for He-like ions: $1s\ 2s\ {}^1S_0 \longrightarrow 1s^2\ {}^1S_0 + h\nu_1 + h\nu_2$. Following the energy conservation, the two photons must be emitting energy continuously (Drake, 1986).

Calculating the emission lines (Section 2.2.1) and estimating the continuum (Sections 2.2.2-2.2.4) requires detailed knowledge of the energy levels of the species, atomic transition states, transition probabilities, excitation rate, etc. In CHIANTI atomic database, all of these information has been collected from various laboratory measurements and theoretical calculations. In addition, it also provides the functionality to estimate the line and continuum emissions. Figure 2.5 shows the simulated spectrum (including continuum and line emissions) using CHIANTI V10 (Del Zanna et al., 2021) for the isothermal emissions from 2 MK (red solid line) and 20 MK (blue solid line) plasma. The component of the continuum free-free (dotted line), free-bound (dashed-dot line), and two-photon (dashed line) emissions corresponding to 20 MK is shown separately. The green shaded region shows the energy band of 0.5-15 KeV, where a large number of emission lines along with continuum are present in the spectrum at both low and high temperatures. Thus spectroscopic measurement in this energy band, known as soft X-ray, is crucial to study the properties of the emitting plasma.

2.3 Detection of X-ray emissions: Spectroscopy

In order to measure the X-ray (or EUV) photons, they must interact with the detector medium. The detector medium can be a solid material (e.g., Si, Al, etc.) or gaseous (inert gases are preferred) medium. The X-ray (or EUV) photons primarily interact with matter in three processes – (1) Photoelectric absorption,

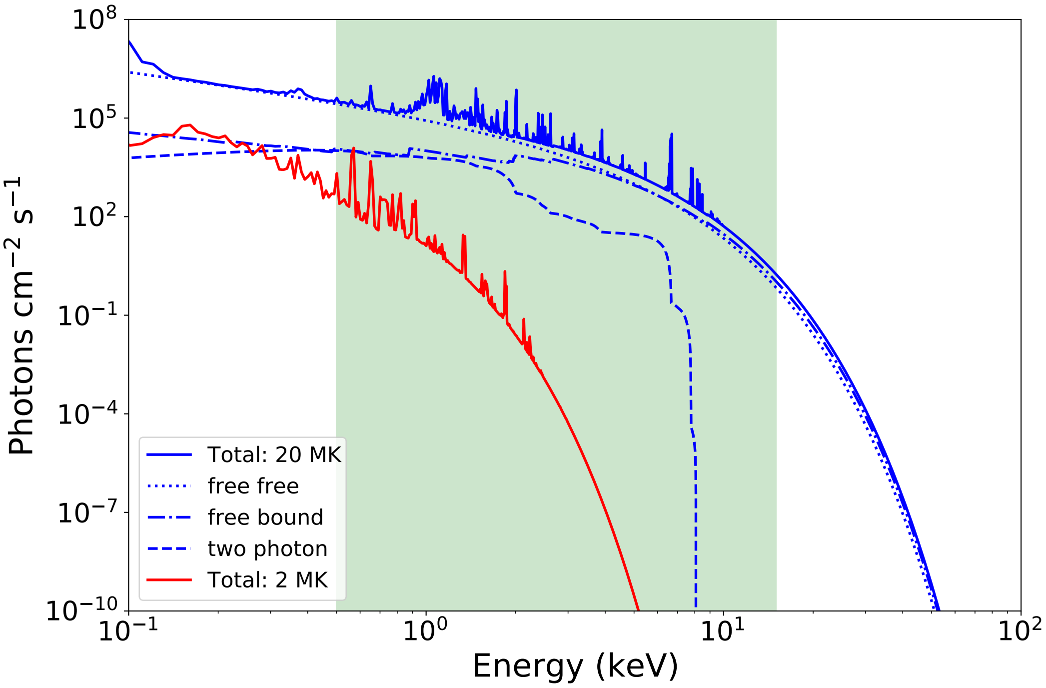

Figure 2.5: Synthetic isothermal spectrum for a plasma of temperature 20 MK (blue solid line) and 2 MK (red solid line) for a volume emission measure of 10^{49} cm^{-3} and 10^{46} cm^{-3}, respectively. The free-free, free-bound, and two-photon continuum for temperature 20 MK is shown as labeled in the plot. The green shaded region shows the 0.5-15 keV energy band. The coronal abundances suggested by Feldman (1992) along with CHIANTI V10 are used to generate this plot. The spectra are binned with an energy resolution of 1 eV.

where a photon interacts with the detector medium and produces photoelectrons (2) Compton scattering, where the incident photon scatters off from the free-electron within the detector medium. (3) Rayleigh scattering. In the soft X-ray (or EUV) energy band ($<$ 10 keV), the Photoelectric absorption dominates over the others, whereas at hard X-rays, above few tens of keV (e.g., 30 keV) and below 1 MeV, Compton scattering dominates. Figure 2.6 shows the interaction probability of the EUV and X-ray photons by a Silicon medium thickness $300 \mu m$. The interaction probabilities are estimated by using the GEometry ANd Tracking-4 (GEANT-4: Agostinelli et al. (2003); Allison et al. (2006, 2016)) simulation toolkit. Here we have considered that 10^{5} number of photons are incident on the detector medium at each energy and then have counted the number of interactions of different processes, that is normalized with the total incident photon numbers. Knoll (1979) provides a comprehensive reference of the interaction of photons with matters.

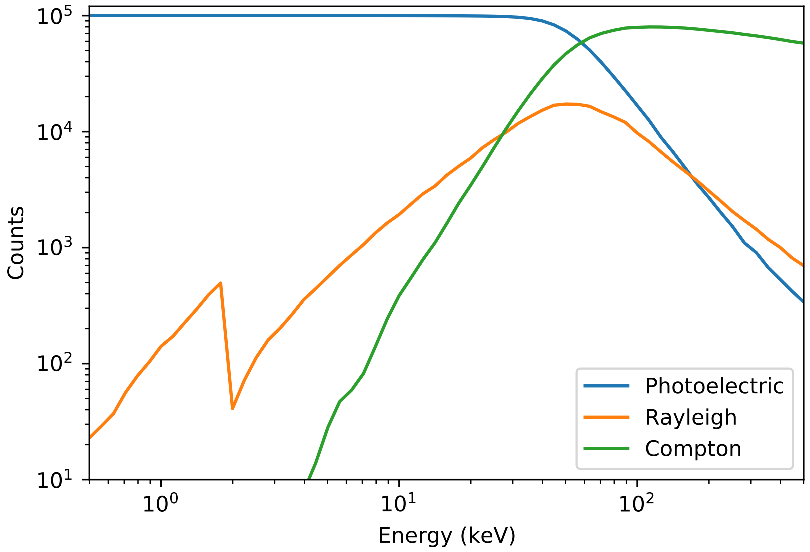

Figure 2.6: Probability of interaction of the photons through a 300 μm Si medium for Photoelectric absorption, Compton scattering, and Rayleigh scattering.

2.3.1 X-ray detector: spectroscopic measurements

A detector provides a measurement of the interaction of photons in the medium. The very first kind of X-ray detector made for the detection of X-ray flux from solar flares is the Geiger-Müller counter. Another type of detector, called the Ionization chamber, measures the integrated energy deposited by the photons. Both the Geiger-Müller counter and the Ionization chamber measure the X-ray photons without their energy information. Measurement of the photon energy was made possible with the development of Proportional counters. In a gas proportional counter, an inert gas (e.g., Ar) is used as a detector medium, and a voltage is applied across the detector medium. When incident photons interact with the detector medium, it produces photoelectrons and ions. These photoelectrons and ions further ionize the medium as they get accelerated before reaching the electrode. In this way, the original small charge is multiplied by a measurable charge pulse. One of the drawbacks of the proportional counter is that the gaseous medium becomes transparent for higher and higher energies and requires a larger volume of the detector medium. In this case, the scintillation counter is used, where the incident photons interact with an inorganic crystal (e.g., Sodium iodide, Caesium iodide, etc.) and produce flashes of optical light (fluorescence photons). These optical flashes are then recorded by a photodetector. In both the gas proportional counter and scintillation counter, the number of the secondary particles (ion-electron pairs or fluorescence photons) or the measured charge pulses are directly proportional to the incident photon's energy. The gas proportional counters are inefficient for detecting very high energy photons but offer an energy resolution in the order of $\sim$ 1 KeV at lower energies, whereas the scintillation counter offers a good response up to gamma-ray energies having a poor energy resolution due to the inefficiencies to create and measure the fluorescence photons.

Another kind of instrument is often used, known as a dispersive spectrometer, where a dispersive element (e.g., X-ray grating, crystal, or multilayer mirror) is used to disperse the incident X-ray photons of different energies in different directions and finally detected by the detector. The dispersion directions of the X-ray photons determine their energies. This type of instrument is flown in several missions and provides very high energy resolution spectroscopic measurements in this energy range. For example, the Bragg Crystal Spectrometer (BCS), where the Bragg crystal is used as a dispersive element, has been flown several times (e.g., Acton et al. (1980); Culhane et al. (1991); Sylwester et al. (2005)). The dispersive spectrometer has a very high energy resolution in the order of a few eV but operates at a very narrow energy band and thus is primarily suited for detailed observation of line emissions rather than of continuum.

In the present day, with the advent of technology, Solid-State-Device (SSD) is used as an X-ray detector. The working principle of SSD is similar to that of proportional counters, except that the detector medium is considered a solid, usually semiconductors (e.g., Silicon, Germanium, etc.) to absorb the incident photons and produce photoelectrons. SSD converts the incident photons to charges, which can be directly measured to determine the photon energy. The advantage of the SSD is that it can be operated with a much smaller power than the proportional counters. The material and geometry of SSD are chosen to optimize the energy response from a broad energy range and to provide an energy resolution of ∼100 eV to a few keV or better across the whole energy range. The most commonly used SSD in astronomical applications is known as Charge Coupled Devices (CCD). CCD usually consists of multiple small pixels arranged in a compact volume, which makes it a very efficient position-sensitive detector.

The highest resolution of a few eV (e.g., 2-3 eV (Bandler et al., 2019; Doriese et al., 2017)) in the broad-band X-ray spectroscopic measurements can be possible using the microcalorimeter detectors. These detectors are the recent development in X-ray detector technology. In microcalorimeter detectors, the temperature of the absorbing medium is maintained at absolute zero (< 0.1 K) temperature. Absorbing an X-ray photon with the detector medium generates heat, and measuring this small change of heat with a thermometer, estimates the incident photon energy. These detectors are challenging to make and are yet to be considered for the solar spectroscopic measurements.

Figure 2.7 shows the simulated solar spectrum (see Section 2.3.3) corresponding to 10 MK isothermal emission in the energy range of 0.5 KeV to 15 KeV for different instruments of different energy resolutions. The blue dashed line shows the spectrum of an instrument with an energy resolution of 1 KeV (e.g., proportional counters). The solid lines of different colors represent the simulated spectrum of the RESIK instrument (Sylwester et al., 2005) onboard the CORONAS-F mission. RESIK uses a Bragg crystal to achieve a very high-resolution spectrum. Because of the diffracting nature of the instrument, it uses four different detector channels (3.26 KeV-3.65 KeV, 2.90 KeV-3.24 KeV, 2.55 KeV-2.85 KeV, and 2.05 KeV-2.45 KeV) (Sylwester et al., 2005), whose spectra are marked by background shaded regions. A zoom-in view of the same is shown in the top right corner of Figure 2.7. Finally, the black dashed line shows the broad-band solar spectrum observed by an instrument of energy resolution 0.15 keV (e.g., using an SSD detector). Comparing the spectrum of all the instruments, we can conclude that a broad-band spectrometer with a good energy resolution is required for simultaneous measurements for the line emission along with the continuum emission, which is essential to study the plasma parameters, e.g., absolute (with respect to Hydrogen) abundances of elements.

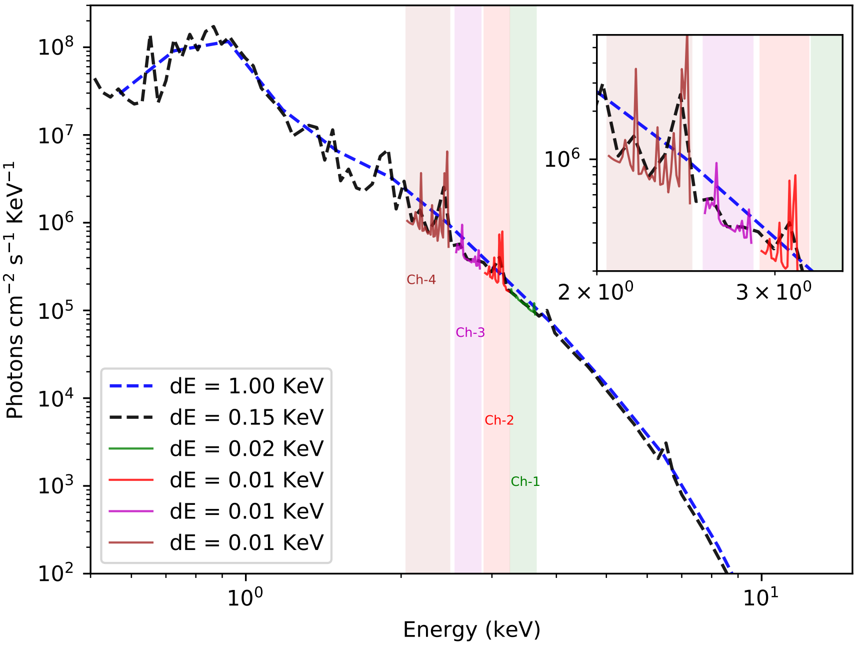

Figure 2.7: The simulated isothermal emission spectrum of 10 MK coronal plasma is seen by instruments of different energy resolutions. Details are mentioned in the text.

2.3.2 XSM: A new generation X-ray spectrometer

The Solar X-ray Monitor (XSM) is a new generation spectrometer for the Sun as a star observation in a soft X-ray energy band. The unique design of XSM makes it possible to record a good energy-resolved broad-band spectrum every second, covering a large dynamic range of X-ray intensity. It uses a state-of-art Silicon Drift Detector (SDD), which is a solid-state silicon device to measure the solar X-ray emission in the energy range of 1 KeV to 15 KeV with an energy resolution better than 180 eV at 5.9 KeV. It uses a filter wheel mechanism and onboard logic for auto-detection of large flares' activity to extend its dynamic range from lower than A class to X class. Details of technical specifications of XSM can be found in Shanmugam et al. (2020).

XSM was launched on 22 July 2019 onboard India's Chandrayaan 2 mission (Vanitha et al., 2020a), which is India's second mission to the Moon. It reached a nominal circular orbit around the Moon in early September, and XSM began its nominal solar observation on 12 September. The in-flight performance of the XSM is found to be identical to what was observed on the ground. Details of XSM ground calibration and in-flight performance are provided by Mithun et al. (2020a) and (Mithun et al., 2020b). Primarily XSM is designed and developed at Physical Research Laboratory (PRL), Ahmedabad, India. The recorded onboard data of XSM is downloaded and pre-processed at regular intervals to the ground station at Indian Space Science Data Center (ISSDC), Bangalore. The pre-processed data is downloaded to XSM Payload Operation Centre (POC) at PRL. For further processing of the raw data to be used in scientific analysis, XSM Data Analysis Software (XSMDAS: Mithun et al. (2021)) is available. Details of the generation of the solar light curve and spectra for the scientific analysis are given in Chapter 3. In the next section, we briefly describe the XSM instrument.

Unique design of XSM and its performance

The XSM is optimized to measure the solar X-ray spectrum with stable spectral performance over a broad range of solar X-ray activity. The objective of XSM is to measure the disk-integrated solar spectrum without any imaging. It uses an SDD detector along with a detector cap or collimator (see Figure 2.8a) of an aperture of radius $\sim$0.34 mm to restrict its field-of-view (FOV) within $\pm 40^0$. The cap's material has been chosen to block the background emission from all directions; hence, the XSM has a very low non-solar background. As the XSM is fixed mounted on a Moon orbiting spacecraft, the angle subtended by the Sun varies with time according to the spacecraft's attitude configuration. Hence, the large FOV of XSM maximizes the visibility of the Sun within its FOV. The spectral performance of the solid-state detectors is highly dependent on their temperature. Thus to maintain the stable spectral performance of the instrument, XSM uses a closed-loop cooling system to cool the detector to a stable temperature. The unique characteristic of the detector and readout electronics makes it possible to maintain a stable spectral performance without significant photon pileup up to an X-ray flux of 80000 counts/s, which corresponds to the M5 class of solar flare. To extend the XSM performance for the higher class

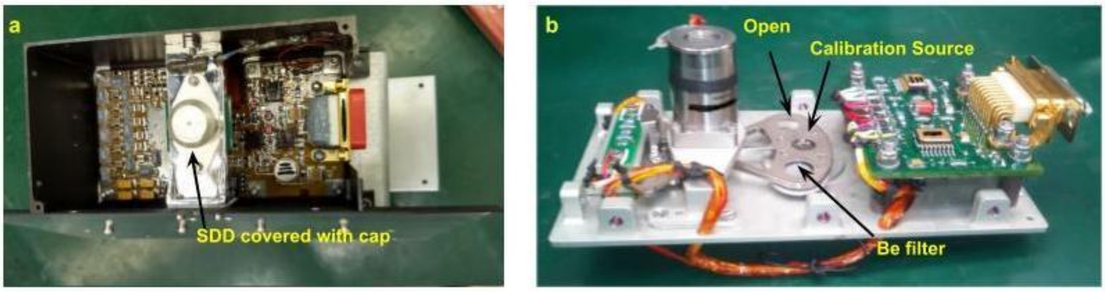

Figure 2.8: Left: XSM detector covered by the detector cap. Right: The filter wheel mechanism.

of solar flares, it uses a 250 μm Beryllium (Be) filter in front of the detector. This Be-filter is mounted on a filter wheel mechanism (see Figure 2.8b) along with onboard logic by which the Be-filter automatically comes in front of the detector once the threshold X-ray flux is reached. The filter wheel mechanism also contains a calibration Fe-55 radioactive source for the onboard calibration of the instrument. Figure 2.12a shows the on-axis energy response of the XSM without Be filter (blue line) and with Be filter (orange line).

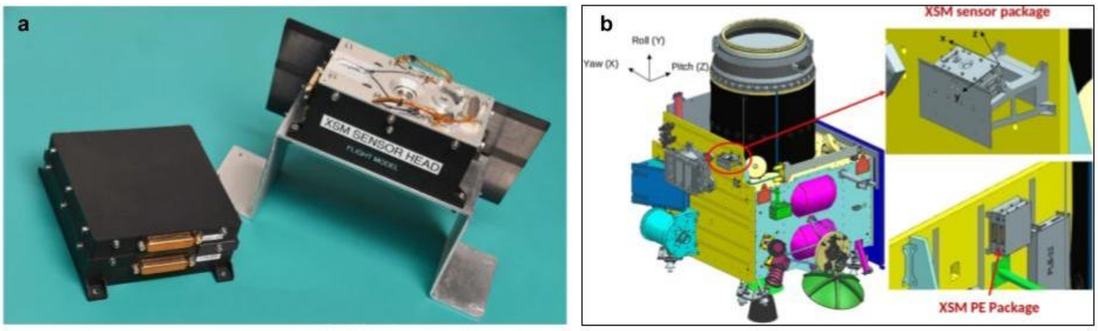

Figure 2.9: Integrated view of XSM; (a) Processing electronics are shown on the left side, whereas the sensor package, including the XSM detector along with front-end electronics and filter wheel mechanism, is shown on the right. (b) Schematic diagram of Chandrayaan 2 orbiter showing the mounting location of XSM detector package and processing electronics.

Figure 2.9a shows a photograph of the integrated XSM package in our laboratory before being integrated into the Chandrayaan 2 spacecraft. Figure 2.9b shows a schematic of the Chandrayaan 2 spacecraft along with the mounting of the XSM sensor package and processing electronics (PE). Since the launch of the XSM, it has been observing the Sun whenever visible within its FOV. Its spectral performance remains unchanged without any degradation, and it has observed different levels of solar activity; more details are given in Chapter 3. The representative spectrum of XSM for the different levels of solar activity is shown in Figure 2.10. For the higher activity (e.g., X1 class), the lower energy counts are reduces due to the observation with Be-filter.

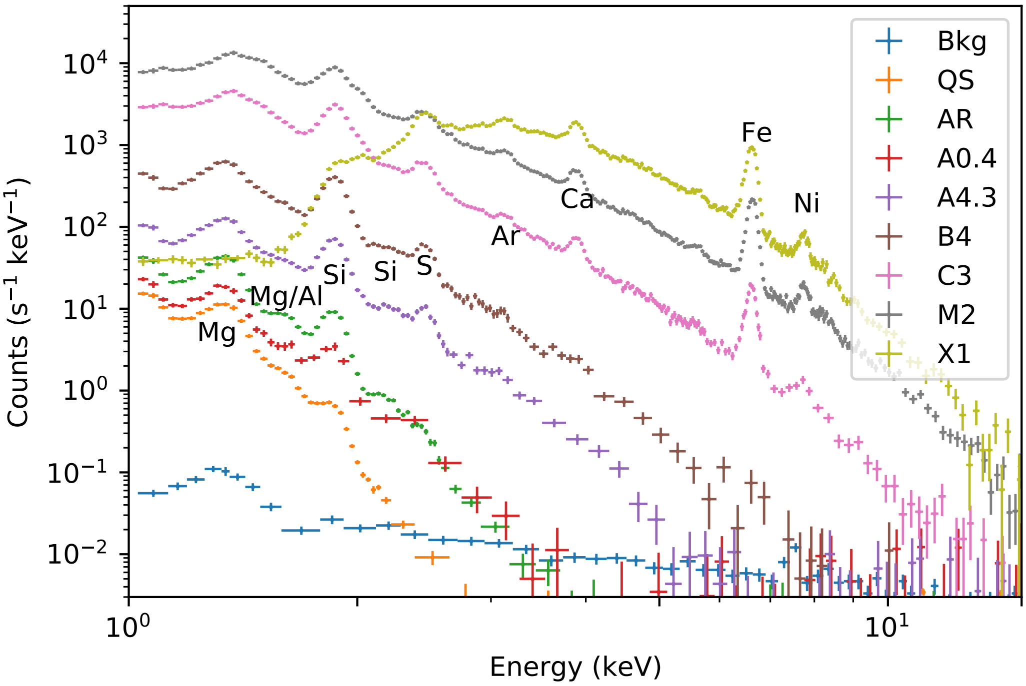

Figure 2.10: XSM observed spectrum of the Sun at the different levels of activity from Quiet Sun (QS) to X1-class flares. Because of the Be filter came in-front of the detector, the lower energy count reduced for the X1-class of activity. The blue color represent the non-solar background (Bkg) spectrum. All the spectrum from QS to X1 are subtracted by the BKg spectrum.

2.3.3 Extracting plasma parameters from broad-band X-ray spectrum:

Modeling the broad-band X-ray spectrum of emitting plasma containing lines and continuum emission tells us about emitting plasma properties, e.g., temperature, elemental abundances, emission measure, etc. The observed spectrum from a spectrometer contains photon counts ($O(J)$) at different instrument channels (J), corresponding to different energies. The photon counts, $O(J)$ (e.g., shown in Figure 2.10) is related to the actual theoretical model spectrum, $f(E)$ (e.g., shown in Figure 2.5) as follows:

$$O(J) = \int f(E) R(J,E) dE \tag{2.5}$$

Here, $R(I,E)$ is known as the instrument response function, which includes all the characteristics of the instrument and relates the instrument channel with the photon energies. Knowing $O(J)$ and $R(J,E)$, we would like to determine the actual spectrum ($f(E)$). Determining $f(E)$ requires an inversion of Equation 2.5, which is not possible in general, as such inversions tend to be non-unique and unstable to small changes in O(J)(xsp, 2020). The usual alternative is forward fit a model spectrum, $f(E)$ that is dependent on emitting plasma temperature (T), emission measure (EM), and the elemental abundances (A_x) (i.e., $f(E) = f(E, T, EM, A_x)$). Forward fit provides the best fit values of T, EM, A_x for which $f(E, T, EM, A_x)$ can reproduce the actual spectrum ($O(J)$).

In this thesis work, we model the observed soft X-ray broad-band spectrum of the Sun containing the line and continuum emission characterized by a temperature, emission measure, and abundances of various elements. This model spectrum is computed using the CHIANTI atomic database (Section 2.2), and for the spectral fitting, we have used X-ray spectral fitting package XSPEC (Arnaud et al., 1999). As the emission model computed from the CHIANTI database is not readily available in XSPEC, we have incorporated it as a local model named $CHISOTH$.

While it is possible to include this as a model in PyXspec, the Python version of XSPEC, by using the functions available in CHIANTIPy (the python version of CHIANTI), the execution time for each model calculation is prohibitively large. Another possibility is to use the option of the table model in XSPEC, where the model spectra over a multidimensional grid of parameters are stored in a file, and a spectrum for any required set of parameters is obtained by interpolation. However, this is also not a viable option due to the requirement of abundances of elements being independent parameters, resulting in very large file sizes. Thus, we adopt a different approach as discussed in Section 2.3.3

CHISOTH: An isothermal model

$CHISOTH$ is a local model in XSPEC for the spectral fitting of isothermal plasma emission estimated from the CHIANTI database. Detailed calculation of the emission spectrum from CHIANTI by including all the lines' transition states is a time-consuming process. Thus in CHISOTH, we adopt a different approach and store a library of spectra only over a grid of temperatures, but for each individual element. Then, the total model spectrum for a required temperature and abundances is obtained by the weighted addition of interpolated spectra of each element, as detailed below. The pre-computed element-wise spectra are recorded in a FITS file, and the model is implemented in C++, which can be compiled and loaded into XSPEC following the standard procedure *. In order to generate the spectral library, line and continuum spectra for each element (Z = 1 to 30) at unity abundance were computed over a logarithmic grid (δlog(T) = 0.004 K) of temperatures from 0.3 to 50 MK using CHIANTI routines. Line and continuum spectra were obtained separately, and all were added together to obtain the total spectra for each element at different temperatures, which are recorded in a FITS file. Within the XSPEC model, the spectrum for each element at any temperature T within the range is obtained by linear interpolation between the spectra at the nearest two grid points available in the spectral library. Then the total spectrum $f(E,T)$ is obtained by the weighted addition of spectra of individual elements as:

$$f(E,T) = EM * [f_H(E,T) + f_{He}(E,T) * N_{He} + ... + f_{Zn}(E,T) * N_{Zn}] \quad (2.6)$$

where EM is the volume emission measure, $f_X(E,T)$ is the spectrum for element X at unity abundance and emission measure and N_X is the abundance of an element X relative to that of H, which is related to the usually used logarithmic value A_X as:

$$A_X = 12 + log_{N_x} \quad (2.7)$$

---

*https://heasarc.gsfc.nasa.gov/xanadu/xspec/manual/XSappendixLocal.html

The model takes the logarithm of temperature (log T), abundances (A_X) of the elements with Z = 2 to Z = 30, and volume emission measure as input parameters. It may be noted that the volume emission measure is implemented as an overall normalization factor, which is in units of 10^{46} cm^{-3}. Using the features in XSPEC, it is possible to freeze specific parameters such as abundances of certain elements to fixed values while keeping others free during spectral fitting. It is also possible to fit the spectrum with a sum of multiple isothermal emission models, as used in this work. In order to verify the adequacy of the grid of temperatures used in the model, we carried out a comparison of the spectra obtained from the XSPEC model at non-grid temperature values with those obtained directly from CHIANTI. Figure 2.11 shows such a comparison at four representative temperatures. The upper panel shows the spectra obtained from the XSPEC model and CHIANTI, convolved with the XSM response, and the lower panel shows the ratio between the two. It can be seen from the figure that the differences are less than 0.1%, demonstrating the adequacy of the XSPEC model for analysis of broadband soft X-ray spectra of the Sun.

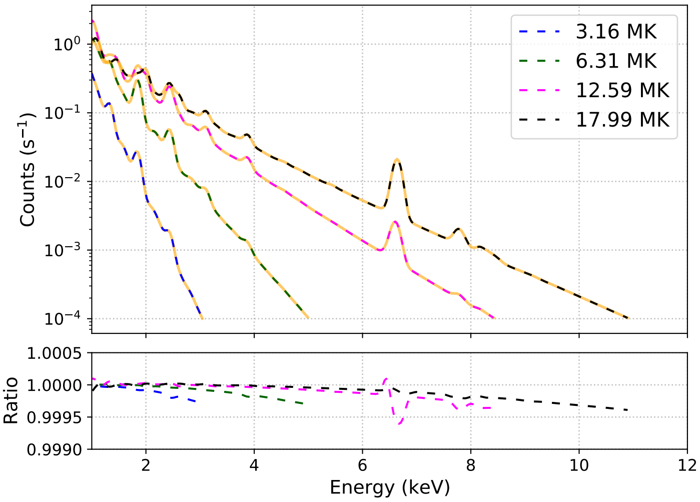

Figure 2.11: Comparison of the interpolated spectrum from the XSPEC model with that from direct calculations with CHIANTI. The upper panel shows the generated spectra for four different temperatures using CHIANTI (orange dashed line), overplotted with the spectrum obtained from XSPEC (dashed lines of blue, green, magenta, and black colors), and the lower panel shows the ratio between the two.

2.3.4 The temperature response function of XSM

A temperature response represents the sensitivity of an instrument channel to detect the plasma emission at different temperatures. As XSM provides the spectrum, we can divide the full spectrum with a few energy channels and estimate the temperature response corresponding to each channel. Here we show a representative set of XSM temperature response functions in the energy range of 1-15 keV divided into multiple bins in a logarithmic scale with $\Delta logE = 0.1$.

The XSM temperature responses are constructed from individual isothermal emission models over a logarithmic grid (δ(LogT) = 0.03) of temperatures (T) from 0.5 MK to 50 MK. We use the XSPEC (Arnaud et al., 1999) local model, "CHISOTH" (Section 2.3.3; Mondal et al. (2021b)), for the estimation of the isothermal emission spectrum at each temperature grid. The model takes the logarithm of the temperature (LogT), volume emission measure, and the abundances (Ax) of the elements with Z=2 to Z=30 as input parameters. The volume emission measure is implemented as a normalization factor, which is in the units of 10^{46} cm^{-3}. For the generation of the XSM temperature response, we keep the normalization (or emission measure) of the model as unity at different temperature grids. At the time of model calculation within XSPEC, we have used the on-axis energy response (RMF) function of the XSM. However, as the XSM effective area varies with time, the time-varying effective area file (ARF) is used for a typical observation on 20th September 2019. These RMF and ARF functions will be folded with the synthetic photon spectrum and produce the synthetic count spectrum of XSM in the units of $Counts\ s^{-1}\ keV^{-1}$ for an emission measure of $10^{46}\ cm^{-3}$. We have multiplied the output spectrum by a factor "$10^{-46} \times energy - bin$". to convert it into the units of $Counts\ cm^{3}\ s^{-1}$ for a unit emission measure. Now, to get the temperature response from these synthetic spectra at different temperature grids, we have integrated the average counts over the dynamic energy bins of XSM energy response. Here we have binned the energies from 1 keV to 15 keV in an interval of 2 keV. Thus we have a matrix of plasma temperatures and the XSM re-binned energy band for which we have the predicted count rates per unit emission measure as plotted in Figure 2.12b. XSM temperature responses indicate that the XSM is more sensitive

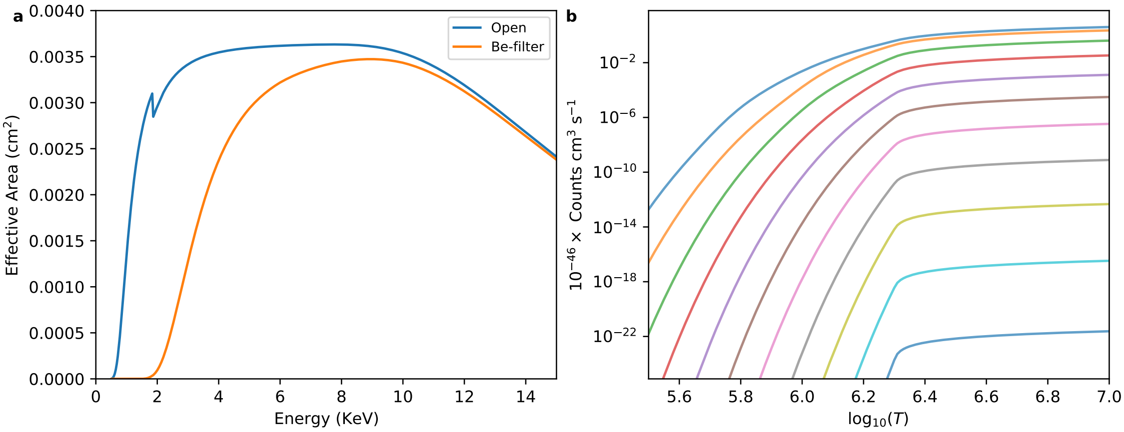

Figure 2.12: (a) XSM energy response curve. (b) XSM temperature response functions in the enegry range of 1-15 keV in an interval of 2 keV.

to the higher temperatures emission than the lower temperatures.

2.4 Imaging X-rays

Coronal plasma is highly nonuniform (e.g., see Figure 1.5 and top row of Figure 1.4), which demands imaging spectroscopic measurements to study the dynamics of the different structures (e.g., AR are very bright compared with XBP) on the solar disk. However, due to the lack of a detailed imaging spectroscopic instrument currently, to complement the spectroscopic observations from XSM, we have used existing X-ray (and EUV) imaging instruments, which provides an image of the sun for an integrated energy band. In this section, we will briefly discuss the imaging instruments used in this thesis after describing the imaging technique in X-ray (or EUV) energy ranges.

2.4.1 X-ray imaging techniques

The high energetic nature of X-rays (or EUV) makes it challenging to image the X-ray photons. An indirect method is often used for imaging X-rays using a collimator in front of the detector. Collimators are used to restrict the field-of-view (FOV) of the instrument such that only the bright X-ray photons from a spatially localized source reach the detector (e.g., a pin-hole camera, where the size of the pin-hole determines the FOV of the instrument) Another type of collimator includes the Scanning Modulation Collimator (SMC: Oda (1965)), where the incident X-ray flux is modulated by the shadow of the wire grids when the detector is scanning the source. From the modulated flux, the information about the source location is reconstructed.

A Coded mask is also used for indirect imaging of X-rays. The working principle of the coded mask is similar to that of SMC, with the exception of spatially distributed modulation of the incident flux instead of temporally. A coded mask consists of a one-dimensional or two-dimensional transparent and solid pattern of a specific design on a metallic plate. The incident photons parallelly passing through the transparent patterns of the mask can reach the detector, and others produce a shadow. The location of the shadow on the detector plane is directly related to the source location, and thus from this shadow pattern, the spatial information of the source is extracted.

Most of the astronomical X-ray sources are point sources, where we are only concerned about their location in the sky. Thus several astronomical missions have been flown with a collimator or a coded mask which efficiently tells us the location of the sources in the sky. However, for an extended X-ray source (like Sun) or a very faint X-ray source, these indirect imaging techniques are not sufficient to study the source in detail. In this case, front-end X-ray optics are required, which converge the X-ray photons from a larger area to a smaller area on the detector plane. But normal incident optics like an optical telescope does not work for X-ray energy band as most of the material is transparent in X-ray due to a near-unity refractive index (see Figure 6.2). However, X-rays can totally externally reflect from a highly polished surface of a metal substrate (known as X-ray mirrors) for a very shallow incident angle (known as grazing angle) from the surface (see Chapter 6). This technique is similar to the total internal reflection of the optical light from a surface. Based on this principle Wolter (1975) proposed, three configurations for the X-ray optics, known as Wolter-I, Wolter-II, and Wolter-III design. Among them, the Wolter-I design is very efficient for astronomical applications, where the X-rays are reflected in grazing angles from a truncated parabolic surface followed by a hyperbolic surface (see Chapter 7).

Wolter-I design has been flown in a few solar missions to image the Sun. Among them, the operating instruments which provide the images of the Sun in X-ray and EUV energy bands are the X-ray telescope (XRT: Golub et al. (2007)) onboard Hinode (Kosugi et al., 2007) observatory and Atmospheric Imaging Assembly (AIA: Lemen et al. (2012)) onboard Solar Dynamic Observatory (SDO: Pesnell et al. (2012)) respectively. Each of these instruments is briefly described in the below Sections 2.4.2-2.4.3.

2.4.2 XRT

The X-ray telescope (XRT) onboard the Hinode satellite provides high resolution (2") X-ray images of the Sun in different filters covering the energy of ∼0.2 KeV to ∼2 KeV. It uses Wolter-I optics of focal length ∼2.7 m along with an X-ray CCD (Golub et al., 2007). Instead of detailed spectroscopic measurements, it records the X-ray images of the Sun at different filter bands. The energy responses of its different filters are shown in Figure 2.13a, and the corresponding temperature responses of the filters are shown in Figure 2.13b. Each XRT filter provides the integrated intensity within its energy range without any detailed spectroscopic information.

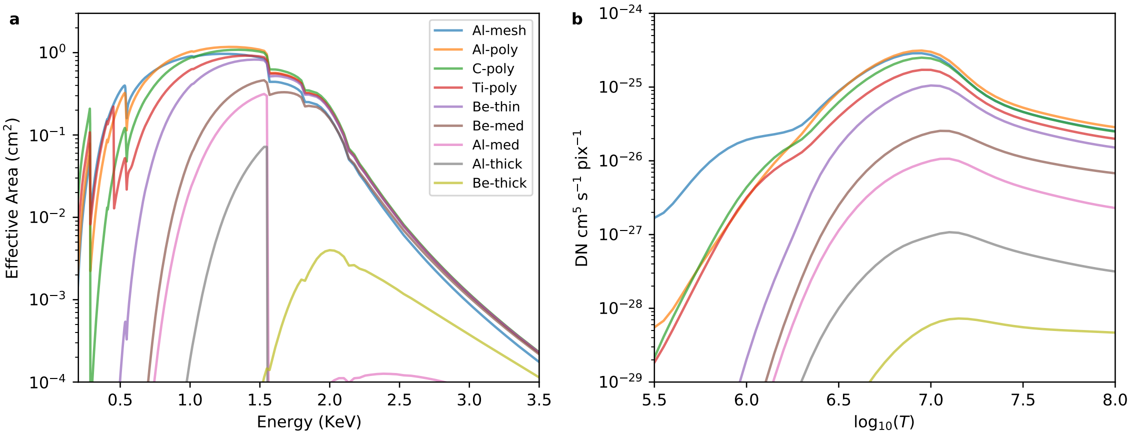

Figure 2.13: Left: The energy response functions for the XRT channels, and Right: the temperature response function corresponding to each channel.

2.4.3 AIA

AIA onboard SDO provides very high resolution (0.6”) images of the Sun in EUV energy bands. It uses six Wolter-I telescopes for simultaneous imaging of the full disk at different EUV energy bands. The energy response of these channels is shown in Figure 2.14a, and the temperature responses are shown in Figure 2.14b. Like XRT (Figure 2.13a), AIA records the image of the Sun for the integrated energy bands but at lower energies. Comparing the temperature response functions, AIA is more sensitive at lower temperatures, whereas the XRT is more sensitive at higher temperatures (Figure 2.13b and Figure 2.14b).

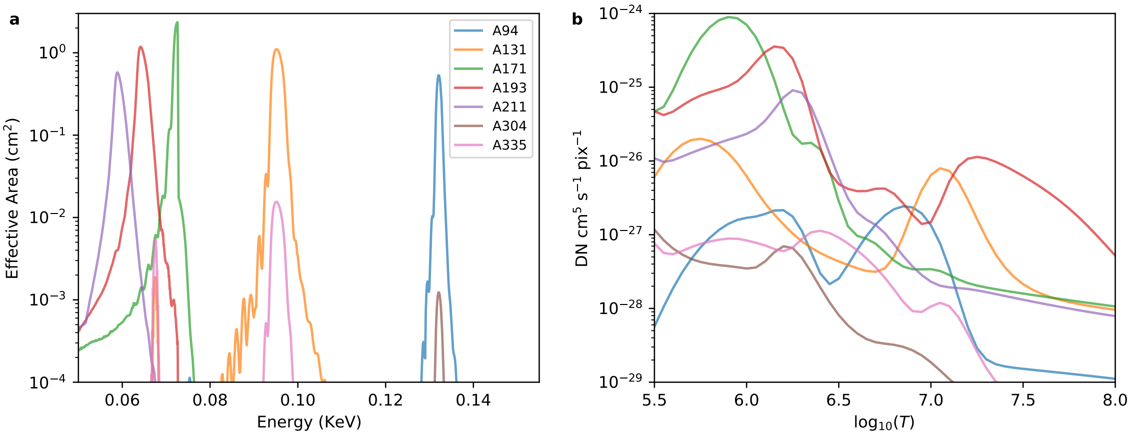

Figure 2.14: Left: The energy response functions for the AIA channels, and Right: the temperature response function corresponding to each channel.

2.5 Differential Emission Measure (DEM)

The observed intensity of an emitting plasma is proportional to $\int N_e N_H dV$ (cm^{-3}), defined as volume emission measure (EM) (e.g., Equation 2.4). If the emission is integrated along the line-of-sight height (dh) then it is called as column EM, i.e., EM $= \int_h N_e N_H dh$ (cm^{-5}). For a multithermal emission from plasma, we will get a distribution of EM as a function of temperature. In this case, the emission from the different temperature plasma is defined by Differential Emission Measure (DEM),

$$DEM(T) = \int_h N_e N_H (\frac{dT}{dh})^{-1} \ (cm^{-5} K^{-1}) \tag{2.8}$$

here, $(\frac{dT}{dh})^{-1}$ is the temperature gradient along the line of sight. The Differential Emission Measure gives an indication of the amount of plasma that is emitting the radiation observed and has a temperature between T and T+dT. The EM(T_i) for a particular temperature interval ΔT_i centered at temperature T_i, can be written as (Del Zanna & Mason, 2018),

$$EM(T_i) = \int_{(T_i - \frac{\Delta T_i}{2})}^{(T_i + \frac{\Delta T_i}{2})} DEM(T)dT \tag{2.9}$$

DEM can be estimated using the energy integrated observations of different energy channels (e.g., AIA/XRT filters). The observed intensity (O_J) of an energy channel (J) is related to the DEM as follows,

$$O_J = \int_T DEM(T)\, R_J(T)\, dT \; + \; \delta O_i \tag{2.10}$$

Here, $R_J(T)$ is the temperature response of the channel, and δO_J is the error associated with the observed intensity. Knowing the observed intensities (O_J) and temperature response functions for multiple energy channels, solving Equation 2.10 is an ill-posed inversion problem. The direct solution of this equation leads to amplification of the uncertainties and provides a spurious solution (Hannah & Kontar, 2012). Over the year, various methods have been developed to estimate the emission measure distribution. These methods include the forward fits by χ^2 minimization (e.g., Golub et al. (2004a)), Markov Chain Monte Carlo (MCMC: Kashyap & Drake (1998)), regularized inversion (Hannah & Kontar, 2012), and sparse basis pursuit (Cheung et al., 2015), sparse Bayesian inference (Warren et al., 2017). A few of them used in this thesis are described in the below Sections.

2.5.1 EM loci technique

Though the direct solution of Equation 2.10 is challenging, one easy way to know how the plasma is distributed at different temperatures is to plot the ratio of the observed intensity and temperature response function, i.e., $O_J/R_J(T)$ as a function of temperatures. These curves are known as emission measure loci curves. For an isothermal plasma, the loci curves of all the energy channels intersect at a single point, which represents the isothermal plasma temperature and EM. However, for a multi-thermal plasma, they will not intersect at a single point, but they provide the upper limits of the EM(T). This method was first provided by Strong (1979) and applied later on by Veck & Parkinson (1981a); Veck et al. (1984) and the following authors. For example, Figure 2.15 shows the EM loci curves for the simulated AIA counts in its energy channels corresponding to a nearly isothermal temperature of logT ≈ 6.0 and EM $\approx 2.3\times10^{21}$ cm^{-5}. In this case, the isothermal nature of the emitting plasma causes all the EM loci curves to meet at a single point.

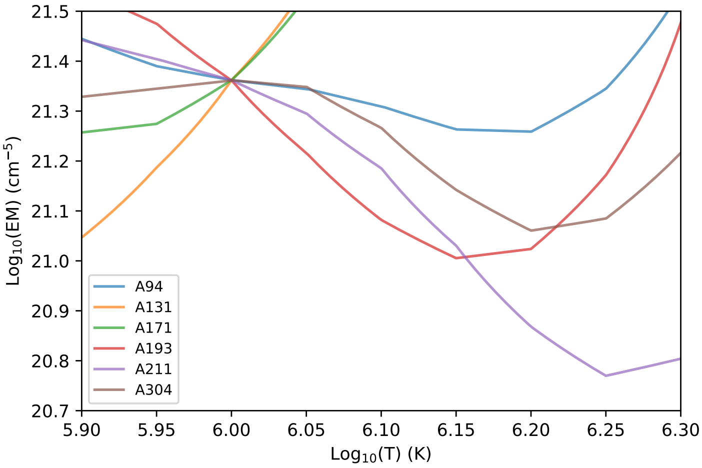

Figure 2.15: Emission measure loci curves corresponding to the different AIA channels for an isothermal emission.

2.5.2 Forward fitting

The forward fitting approach can be used to estimate the DEM from Equation 2.10. In this approach, a guess DEM profile (e.g., Gaussian, multiple Gaussian, spline, etc.) is considered to estimate the observed intensities (O_J) for all instrument channels. However, the primary difficulty here is to find out the optimal DEM solution which can reproduce the observed intensities.

This method has been employed by several authors; among them Golub et al. (2004a) has been employed this method for the estimation of the DEM from the observed intensities by the XRT filters. An IDL routine (*xrt_dem_iterative2.pro*[†]) for the same is available within the SSW package. It uses an initial spline DEM profile, and the optimal spline is obtained using IDL mpfit routines[‡], based on the non-linear least square method.

A general problem with forward modeling approach is estimating the relevance of the obtained best-fit solution. Due to the observed uncertainties, multiple DEM solutions could exist. This problem can be tackled using a Monte Carlo simulation, where the DEM is estimated by varying the observed intensities within their error bars and estimating the range of the DEM solution, which can reproduce the observed intensities within their uncertainties. This method is used in this thesis, as discussed in Chapter 5

2.5.3 Regularized Inversion

Hannah & Kontar (2012) provides a method to solve Equation 2.10 using "regularized inversion", which is demonstrated successfully to obtain an efficient DEM solution from the observed intensities. The work presented in this thesis used the Hannah & Kontar (2012) method (say *HC_dem*) to determine the combined DEM from AIA and XSM (see Chapter 5). We will briefly describe the *HC_dem* with an example.

Following Hannah & Kontar (2012), Equation 2.10 can be written in a matrix form,

$$\mathbf{g} = \mathbf{K}\zeta + \delta\mathbf{g} \tag{2.11}$$

here, $\mathbf{g}$ is the array of intensities for different instrument channels and $\delta\mathbf{g}$ is the associated errors. $\mathbf{K}$ is the matrix of temperature response functions associated with the instrument channels, and ζ is the DEM(T). Recovering ζ by simply inverting $\mathbf{K}$ is not possible due to the noise amplification from the observed uncertainties ($\delta\mathbf{g}$). In addition to that, the obtained DEM(T) may be under-determined if the number of detector channels is less than the number of temperature bins. An alternative approach to deal with these difficulties is to add linear constraints to ζ in the form of zeroth-order regularization. Then the

---

[†] https://hesperia.gsfc.nasa.gov/ssw/hinode/xrt/idl/util/xrt_dem_iterative2.pro

[‡] http://cow.physics.wisc.edu/ craigm/idl/fitting.html

regularization least-square problem of Equation 2.11 will be minimize,

$$||\bar{\mathbf{K}}\zeta - \bar{\mathbf{g}}||^2 + \lambda||\mathbf{L}(\zeta - \zeta_0)r||^2 \tag{2.12}$$

here $\bar{\mathbf{K}} = \mathbf{K}\ (\delta\mathbf{g})^{-1}$, $\bar{\mathbf{g}} = \mathbf{g}\ (\delta\mathbf{g})^{-1}$, λ is the regularization parameter, $\mathbf{L}$ is the constraint matrix, and ζ is the initial guess DEM. The solution of Equation 2.12 is unique. A more details description is given in Hannah & Kontar (2012). An IDL and python implementation of *HC_dem* has kindly been made publicly available by the authors[§].

The black dashed curve in Figure 2.16 shows a quiet Sun DEM available within the CHIANTI package, combined from Brooks et al. (2009). Considering this as a model DEM, we have simulated the AIA intensities. The EM loci curves (unit of cm^{-5} K^{-1}) associated with the simulated intensities of each AIA channel are shown by solid lines, which are above the actual DEM and represent the upper limits. Using the simulated intensities with a typical 20% uncertainties, we have recovered the DEM using the *HC_dem* method as shown by red error bars, which is close to the model DEM. The primary advantage of using the *HC_dem* method is that it provides both the x and y uncertainties associated with the predicted profile. The vertical errors are associated with the propagation of the uncertainties in the observed intensity by the regularized kernel matrix and are estimated by standard deviation of the several Monte-Carlo sampling of the regularized solution from $\mathbf{g}$ within the range of $\delta\mathbf{g}$. The horizontal errors represent the best possible temperature bias or the resolution of the method. In this particular example, the emission from the quiet Sun is faint, and hence the sensitivity of the AIA channels to detect this signal is less, which causes the error bars to be larger, specifically at higher temperatures, where the sensitivity of AIA channels drops (Figure 2.14b). This can be improved by combining the instrument channels which are more sensitive at higher temperatures, e.g., XSM (Figure 2.12). In this thesis, we have combined the observation of both the AIA and XSM to derive the DEM as discussed in Chapter 5.

[§] https://github.com/ianan/demreg

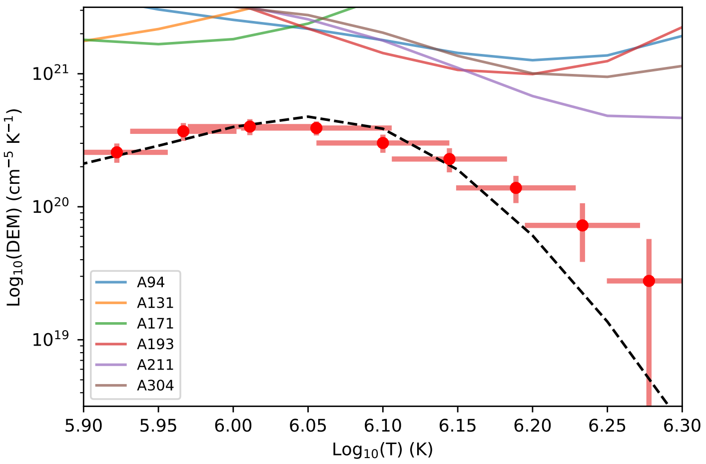

Figure 2.16: Recovered DEM (red error bars) for a model DEM (black dashed curve) using the *HC_dem* method. The solid color curves represent the EM loci curves corresponding to different AIA channels in the unit of $cm^{-5}K^{-1}$

2.6 Hydrodynamic simulation of coronal loops

Deriving DEM from the observed intensity is of great importance to know the temperature structure and hence the underlying thermodynamics of the emitting plasma. To understand the nature of the heating that maintained the observed temperature structure, a simulation of the emitting plasma is needed. With the present understanding, the solar corona consists of magnetically closed coronal loops, which are the primary building block of the coronal plasma. Field-aligned hydrodynamic models are often used to estimate the evolution of the plasma confined within the coronal loops (e.g., Nita et al. (2018)). One such model is the Enthalpy-bashed Thermal Evolution of Loops model (EBTEL; Klimchuk et al. (2008); Cargill et al. (2012); Cargill et al. (2012)). EBTEL is a zero-dimensional (0D) time-dependent hydrodynamic model that can accurately estimate the time evolution of the spatially averaged coronal temperature, density, and pressure of a single coronal loop heated by an assumed heating profile (time-dependent heating rate). The primary advantage of using EBTEL is its simulation timescale, which is an order of magnitude faster than the spatially resolved 1D models. Despite the simplicity of the EBTEL calculation, it can provide the plasma parameters very similar to the spatially average results of 1D models along with the loops. Along with the average coronal properties of the loop, EBTEL estimates the DEMs of the transition region and coronal portion of the loop separately at each time step. EBTEL is a very popular model to estimate the plasma evolution of the loops over a larger set of parameter space, and it is widely used by the solar physics community. This thesis uses the two-fluid version of EBTEL (EBTEL¶++: Barnes et al. (2016); Barnes et al. (2016)), where the ions and electrons are treated separately; a detailed implementation of it is given by Barnes et al. (2016).

Most of the coronal heating model is impulsive in nature (Klimchuk, 2015), i.e., the heat is deposited by means of impulsive events. The frequency of these heating events determines the shape of the overall DEM profile. Here, we demonstrate how the frequency of the heating event determined the shape of the observed DEM. Consider a coronal loop of length 10 Mm, which is heated with the series of impulsive events repeating at energy 200 s and each of which has a volumetric heating rate of $\sim 10^{-2}$ erg cm^{-3} s^{-1} following a triangular shape of time period 50 s. As these events are repeated very frequently, another event occurs before cooling an event to the background temperature; these are termed high-frequency (HF) events. The temperature evolution of these HF events is shown in blue color in Figure 2.17a. The composite DEM for all the events is shown in Figure 2.17b. The high-frequency nature of the heating makes a narrower DEM peaking at nearly the mean temperature of the heating ($\sim$ 1 MK). On the other hand, let us see what happens if the same loop is heated with the events of smaller frequency (e.g., repeating time between the events is now 2000s instead of 200s), but the individual event has one order of magnitude higher energy ($\sim 10^{-1}$ erg cm^{-3}). These events are known as low-frequency (LF) events. The time between the two events is large enough that each event can cool to a very low temperature before the start of the next event (orange color in Figure 2.17a). Due to the heating of the plasma in both high (events peak times) and low (e.g., events decay times) temperatures, emissions will come from both low and high-temperature plasma, which makes a broad distribution of the DEM, as shown in Figure 2.17b (orange curve). Thus the observed DEM represents the frequency of the impulsive events. This technique is used extensively to explain

---

¶https://rice-solar-physics.github.io/ebtelPlusPlus/

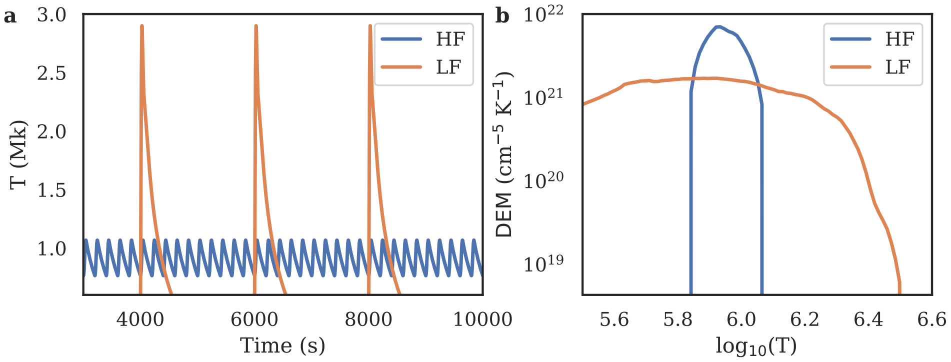

Figure 2.17: Left: Temperature evolution of a coronal loop, which is heated by high-frequency (HF) and low-frequency (LF) events. Right: The shape of the DEM corresponding to the HF and LF heating.

the observed DEM as discussed in Chapter 5

Chapter 3

FIP effect of quiet Sun XBPs, and ARs

Elements with low First Ionization Potential (FIP) are known to be three to four times more abundant in active region loops of the solar corona than in the photosphere (see Section 1.3). There have been observations suggesting that this observed "FIP bias" may be different in other parts of the solar corona, and such observations are thus important in understanding the underlying mechanism. The *Solar X-ray Monitor* (XSM) on board the Chandrayaan-2 mission (Section 2.3.2) carried out spectroscopic observations of the Sun in soft X-rays during the 2019-20 solar minimum. Looking into the number of sunspot-less days, this was the quietest solar minimum in the last hundred years. By modeling broadband X-ray spectra from XSM, we estimate the temperature and emission measure of the AR and quiet Sun XBPs. We also obtain the abundances of Mg, Al, and Si relative to H. We find that the derived parameters of AR and quiet Sun XBPs remain nearly constant over time with a temperature around $\sim$3 MK and $\sim$2 MK, respectively.We also obtain the abundances of Mg, Al, and Si relative to H, and find that the FIP bias is $\sim$2 for quiet Sun XBPs, which is lower than the values obtained in active regions ($\sim$3). The studies of quiet Sun XBPs are reported in our recent publication, Vadawale et al. (2021a) and the study of AR is under perpetration.

3.1 Introduction

Knowledge of elemental composition in the solar corona is crucial to understand various outstanding issues, such as energy / mass transfer between different atmospheric layers and the origin of the solar wind. However, it is challenging to measure the absolute elemental abundances (i.e., relative to hydrogen) which leads to a common practice of measuring coronal elemental abundances relative to other elements. One important problem related to the coronal elemental composition is the abundance enhancement of the low First Ionization Potential (FIP) elements (i.e., elements having FIP less than 10 eV) compared to their photospheric values, often termed as the FIP bias or FIP anomaly (see Chapter 1.3). Observations of the FIP anomaly started with the pioneering work of Pottasch (1963). Later, many researchers showed that the abundances of the low FIP elements in the corona can be as much as 3-4 times than that of the photosphere (Meyer, 1985; Feldman, 1992; Fludra & Schmelz, 1999; Schmelz et al., 2012). It was also observed that the FIP bias varies within different features of the corona (Feldman & Widing, 1993) and shows variation with both the solar cycle and magnetic activity of the Sun (Brooks et al., 2017; Pipin & Tomozov, 2018). A detailed review on the topic can be found in Del Zanna & Mason (2018).

While the origin of the FIP bias is not fully understood, recent reports based on the EUV imaging spectroscopy (e.g., Del Zanna, 2019, Doschek & Warren, 2019) show that the low-temperature ($\sim$1 MK) non-active corona has nearly photospheric abundances. In contrast, hot loops (2-4 MK) at the core of the active region with high magnetic field show stronger (3-4) FIP bias (Feldman, 1992; Feldman & Laming, 2000; Feldman & Widing, 2003; Saba, 1995; Del Zanna & Mason, 2014). Multiple theories have been proposed in literature to explain the FIP bias (see Laming, 2015 for a review); however, the widely accepted theory is that based on the Ponderomotive force model (Laming, 2004, 2009) (see Chapter 1.3). This model can successfully explain the higher FIP bias in hot, magnetically closed loops as well as photospheric abundances in the relatively cooler open field structures. It also predicts that higher magnetic activity may lead to higher FIP abundance in the solar corona.

Although early visible light solar eclipse observations (Mason, 1975) measured coronal abundances relative to hydrogen, most of the XUV spectroscopic observations determine abundances relative to some other elements, such as O or Si. On the other hand, broad-band soft X-ray spectroscopic observations are capable of measuring absolute abundances by considering the line to continuum ratio, as initially proposed by Walker (1972) and attempted by Walker et al. (1974a,b). Lately, there have been multiple studies presenting measurement of absolute abundances by self consistently modeling the continuum and characteristic lines in the observed soft X-ray spectra (e.g. Narendranath et al., 2014; Warren, 2014b; Dennis et al., 2015; Caspi et al., 2015; Moore et al., 2018; Narendranath et al., 2020a; Schwab et al., 2020). However, these reports are based on observations of solar flares or active regions, where the underlying continuum is easier to measure due to high X-ray flux.

Similar studies during quiet Sun periods have not been possible so far due to very low signal as well as difficulties in measuring the real continuum. Here we present the first such study of quiet corona using Chandrayaan-2/Solar X-ray Monitor (XSM: Chapter 2.3.2) which observes the Sun as a star in the soft X-ray band. These observations carried out during the 2019/20 solar minimum, believed to be the deepest minimum in the past hundred years (Janardhan et al., 2011, 2015), provided a unique opportunity for long duration solar X-ray observations in the absence of solar active regions (AR), thereby enabling one to infer the temperature, emission measure and elemental abundances in the quiescent solar corona. Along with that, Whenever a single AR is present on the solar disk, we measure the absolute abundances of that AR throughout its evolution. The rest of this article is organized as follows. Section 3.2 provides the details of observations and data analysis. Results of quiet periods and ARs are presented and discussed in Section 3.3 and Section 3.4 respectively. Finally the Chapter is summarized in Section 3.5.

3.2 Observations and Data Analysis

The visibility of the Sun varies with two pre-defined orbital seasons of the Chandrayaan-2 orbiter, namely 'dawn-dusk' (DD) and 'noon-midnight' (NM), arising because of the attitude configurations of the spacecraft in the lunar orbit and lasting for about three months each (Vanitha et al., 2020b). The primary observing periods for XSM are the DD seasons, typically lasting from mid-February to mid-May and mid-August to mid-November (Mithun et al., 2020a,b). In this work, we use the data from the first two DD seasons from September 12 to November 20, 2019 (DD1) and February 14 to May 19, 2020 (DD2).

The XSM processing electronics generates X-ray spectrum on-board at every second. The raw (level-1) XSM data thus consists of one second spectra as well as other auxiliary information such as house-keeping parameters and observation geometry, organized as day-wise FITS files. The standard level-2 calibrated data includes solar X-ray light curves in the full energy range of 1 – 15 keV at one second cadence and full spectra at a cadence of 60 s. The XSM specific Data Analysis Software (XSMDAS) (Mithun et al., 2021) is used for basic data reduction as well as for generating light curves and spectra with any user selected time bins greater than one second. The only other user input required for analysis is to select Good Time Intervals (GTI) for the generation of light curve and spectrum. The default GTI selection includes the conditions for nominal ranges of the instrument health parameters and excludes periods when the Sun angle is greater than 38° or when the Sun is occulted by the Moon. It should be noted that the default condition on the Sun angle considers the radius of the Sun to be $3R_\odot$ in order to avoid any partial exposure to the extended corona.

Since the XSM is fixed mounted on the Chandrayaan-2 spacecraft, the position of the Sun within it's FOV continuously changes throughout the orbit, resulting in a continuous change in the effective area of XSM. The XSMDAS provides two options to account for these variations: it can provide corrected count rate as if it were observed on-axis, typically used for light curves and time resolved spectra saved as type-II PHA file; or the spectra can be retained as observed counts and the variation of the effective area are accumulated in a corresponding ancillary response file (ARF), typically used for time integrated spectra saved in type-I PHA file.

For the present analysis, we use effective area corrected daily time-resolved spectra for obtaining flux light curves. The time bin size was chosen to be two minutes so as to have sufficient counts in each spectra, given the very low X-ray intensity of the Sun. The XSM flux light curve, $F(t)$ over any energy range E_1 to E_2 can then be generated from the type-II PHA files $S(E,t)$ using the equation:

$$F(t) = \sum_{E=E_1}^{E_2} \frac{S(E,t)\ E}{A(E)} \tag{3.1}$$

where $A(E)$ is the on-axis effective area of the XSM. It should be noted that this assumes a diagonal redistribution matrix which, though not strictly correct, is adequate to estimate flux over broad energy ranges. We then obtained the X-ray flux light curve in the energy range 1.55 – 12.4 keV (same as the conventional GOES XRS band covering the wavelength range of 1 – 8 Å) using time resolved spectra over the first two DD seasons, which is shown in Figure 3.1.

The flux light curve in Figure 3.1 clearly shows periods of elevated X-ray intensity due to the presence of active regions on the Sun. The orange background marks the periods when NOAA active regions were present on the solar disk. The pink background marks the periods when NOAA assigned active regions were not present, but the XSM light curve shows enhancement and corresponding EUV and X-ray images from SDO/AIA and Hinode/XRT, respectively, show bright regions. Representative full disk images of the Sun taken by AIA 94Å channel (left) and XRT Be-thin filter (right) during the blue, orange, and pink shaded regions are shown in Figure 3.2. Since one of the objective of the present analysis was to focus on the quiet periods, we concentrated on the periods marked by the blue background in Figure 3.1, covering the intervals September 12-30 and October 14-26 in 2019 and February 14 - March 7, March 21-29, April 13-23, and May 10-13 in 2020, spanning a total of 76 days. We find that even during these intervals, when there were no active regions present on the Sun, the XSM light curve shows a number of small flare-like episodes (microflares), which is discussed

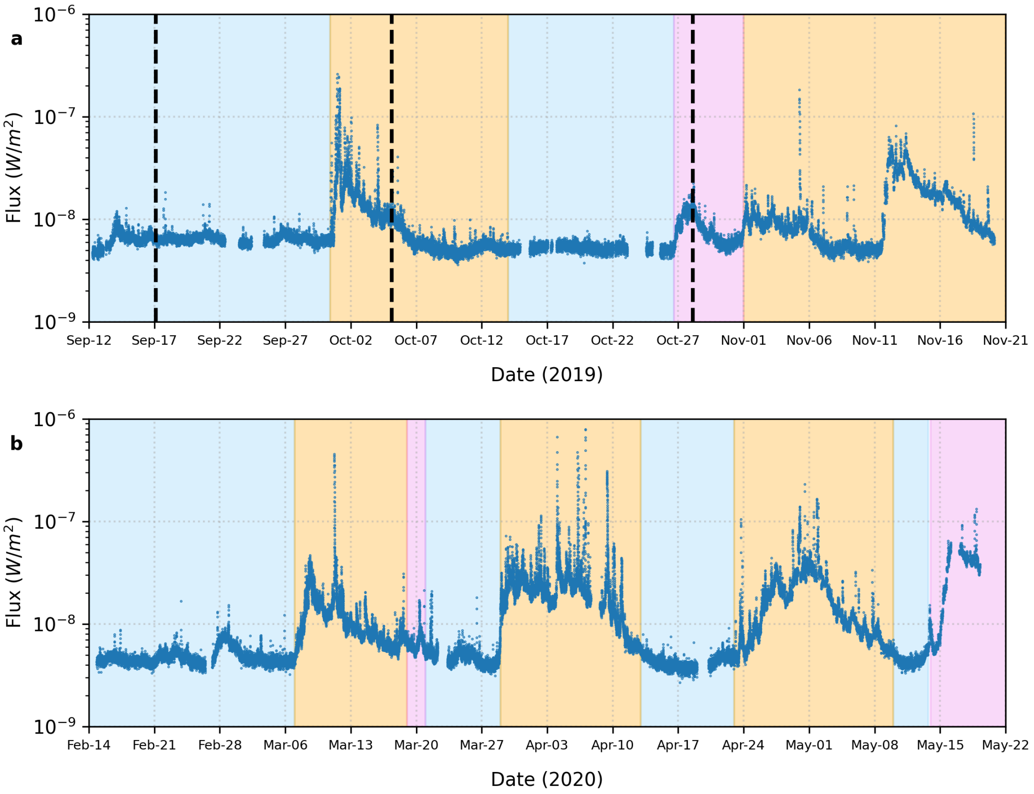

Figure 3.1: Solar X-ray flux in 1 – 8 Å (1.55 – 12.4 keV) from XSM observations for the two DD seasons. Background colors in the figure correspond to intervals with active regions (orange), enhanced X-ray activity (pink), and quiet Sun observations (blue).

in Vadawale et al. (2021b). For the purpose of the spectroscopic investigation of the X-ray emission from a purely quiescent corona, we conservatively ignore such microflares, along with sufficient pre and post flare buffer durations, obtained by visual inspection as shown in Figure 3.3. These identified time intervals were used as user GTI to generate quiet Sun spectra for carrying out a detailed spectral analysis.

To perform spectral fitting in XSPEC (Arnaud, 1996), we generated XSM spectra (type-I PHA) and ARF for quiet Sun observations on each of the selected days with the user GTIs corresponding to the non-flaring periods. Three days with very low exposures were ignored from further analysis. The non-solar background spectrum was obtained using XSM observations when the Sun was outside its FOV. Spectra below 1.3 keV were not used in fitting due to uncertainties in the response for the observations used in the present work (Mithun

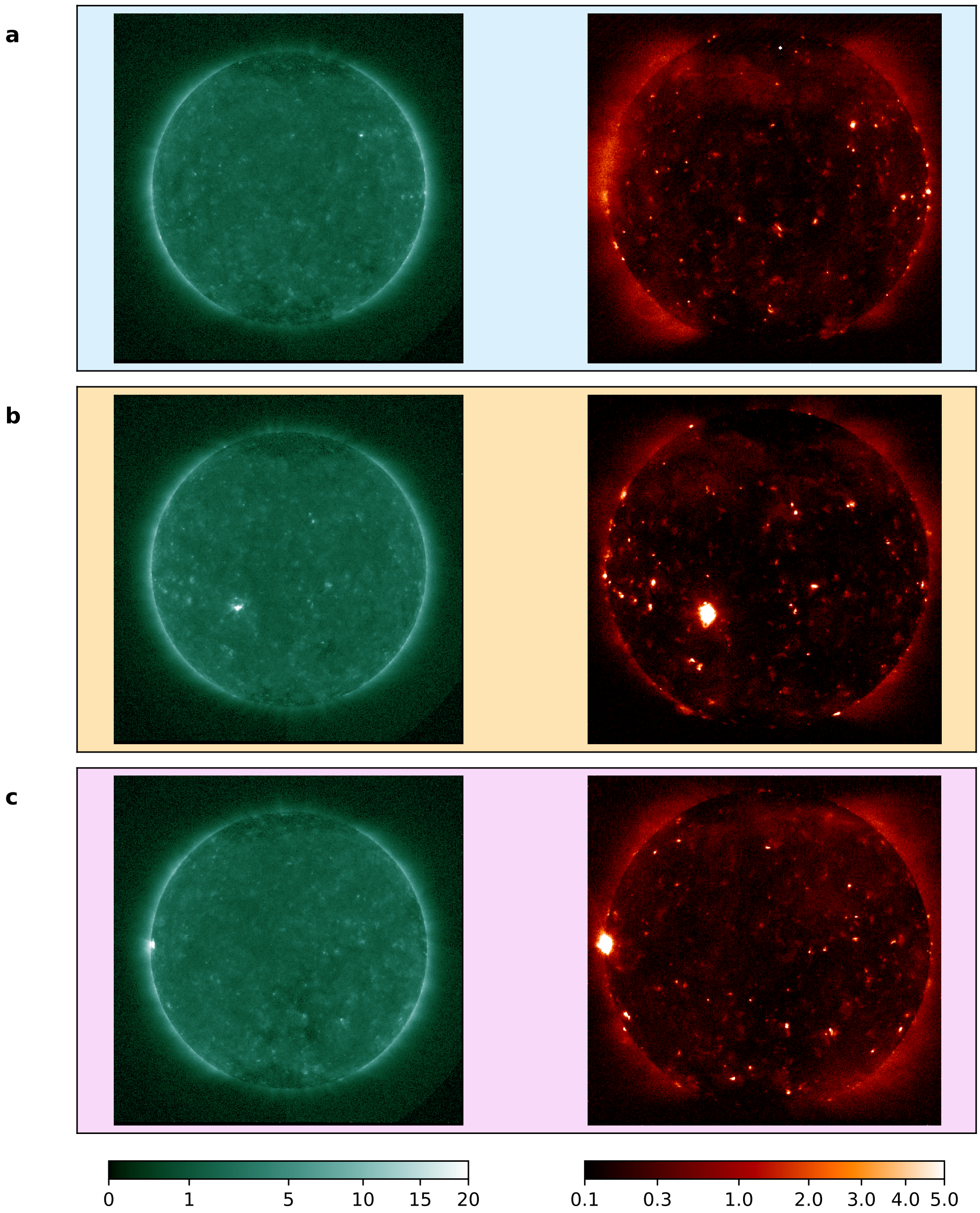

Figure 3.2: Representative full disk images of the Sun taken by AIA (left) and XRT (right) during the period of blue, orange, and pink shaded duration in Figure 3.1. The exact of these three images are shown by vertical black dashed lines in Figure 3.1.

et al., 2020b). For spectral fitting, we use the *chisoth* model as discussed in Section 2.3.3.

In addition to the quiet Sun periods, we also perform the spectral analysis during the period of quiescent ARs. For this purpose, we have chosen the AR12749 and AR12759. Top panels of Figure 3.4 and Figure 3.5 show the 1-15 keV lightcurves of XSM during the disk passage of these two ARs. Represen-

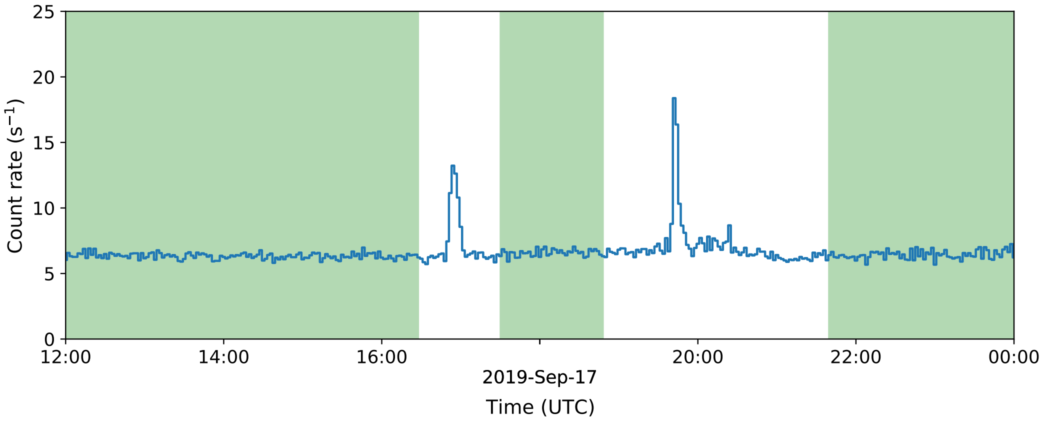

Figure 3.3: An example of selection of non-flaring quiescent period based on the XSM light curve is shown. Durations shaded green, which exclude the flare duration with additional margin before and after the flare, were selected as periods of observation of the quiescent corona and used for spectral analysis.

tative full disk X-ray images taken by the XRT Be-thin filter are shown in the bottom panels. AR12749 appeared from the east limb on Sept 29, 2019. While passing through the solar disk, AR12749 became fainter towards the west limb and went behind the limb on 14 Oct (Figure 3.4b). AR12759 (Figure 3.5) appeared from the east limb on 29 Mar 2020 and crossed through the solar disk till 14 Apr before being hidden behind the west limb. Full disk images show that during the passage of these two ARs, no other AR was present on the solar disk. Thus the enhanced X-ray emission observed by the XSM during the disk passage of these two ARs primarily originates from them. These ARs produced many small A/B-class flares as seen by multiple spikes in XSM lightcuves. For the purpose of the spectroscopic investigation of the X-ray emission from the quiescent ARs core, we have selected the time duration when the ARs is quiescent without occurring any flares. We ignore the duration of the repeated flaring activities along with sufficient pre and post flare buffer durations. These identified time intervals are used as a user defined GTI to generate the spectra for quiescent ARs for carrying out the detail spectral analysis.

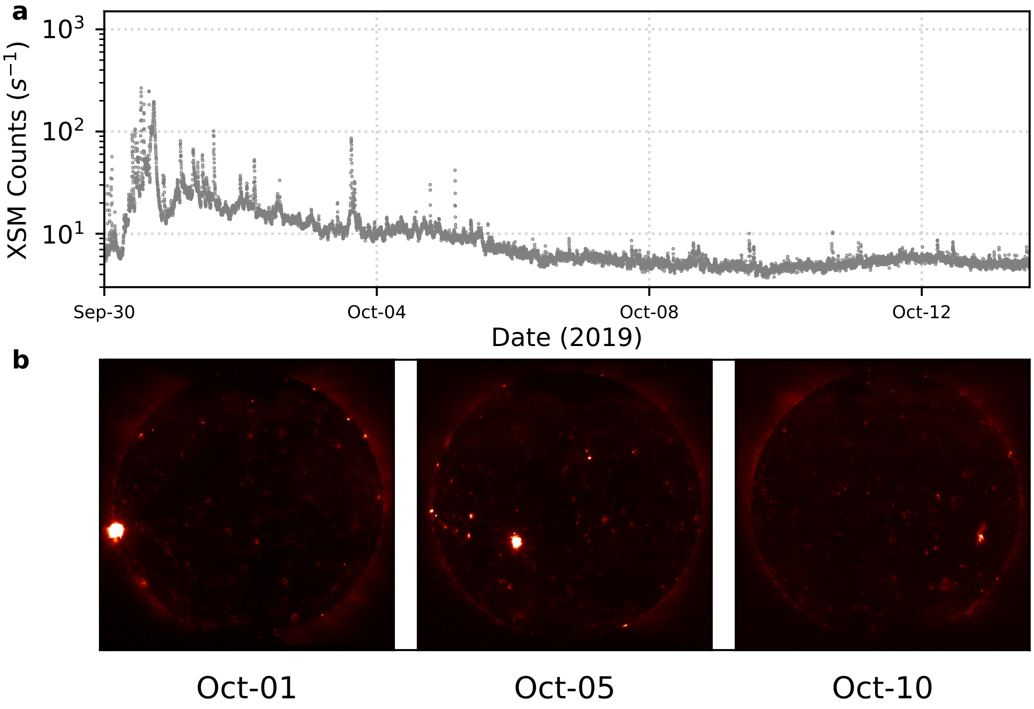

Figure 3.4: XSM 1-15 keV light curve (top) during the disk passage of AR12749. Bottom panel show the evolution of this AR in the full disk X-ray images taken by XRT Be-thin filter.

3.3 Results and Discussion on quiet periods

XSM observations during the first two DD seasons cover the period of possibly the lowest solar activity since the beginning of modern solar observations. The light curve shown in Figure 3.1 exhibits long periods when the solar X-ray intensity is very low but steady. It should be noted that the non-solar X-ray background measured by XSM over the entire energy range is at least 35 times lower as discussed in Mithun et al. (2020b). We find that the lowest solar X-ray flux measured by XSM in the GOES 1 – 8 Å band is about 6×10^{-10} $W\ m^{-2}$, corresponding to the A0.06 class of solar activity, which is well below the sensitivity of the GOES-16 XRS instrument. Considering the fact that no active regions were present for an extended period during these observations, it is reasonable to assume that the solar corona was the quietest during these observations and that the XSM has measured the absolute floor level of the solar X-ray intensity.

We find that the solar X-ray spectra integrated over any of the selected 73 days is dominant over the non-solar background spectrum up to 2.3 keV,

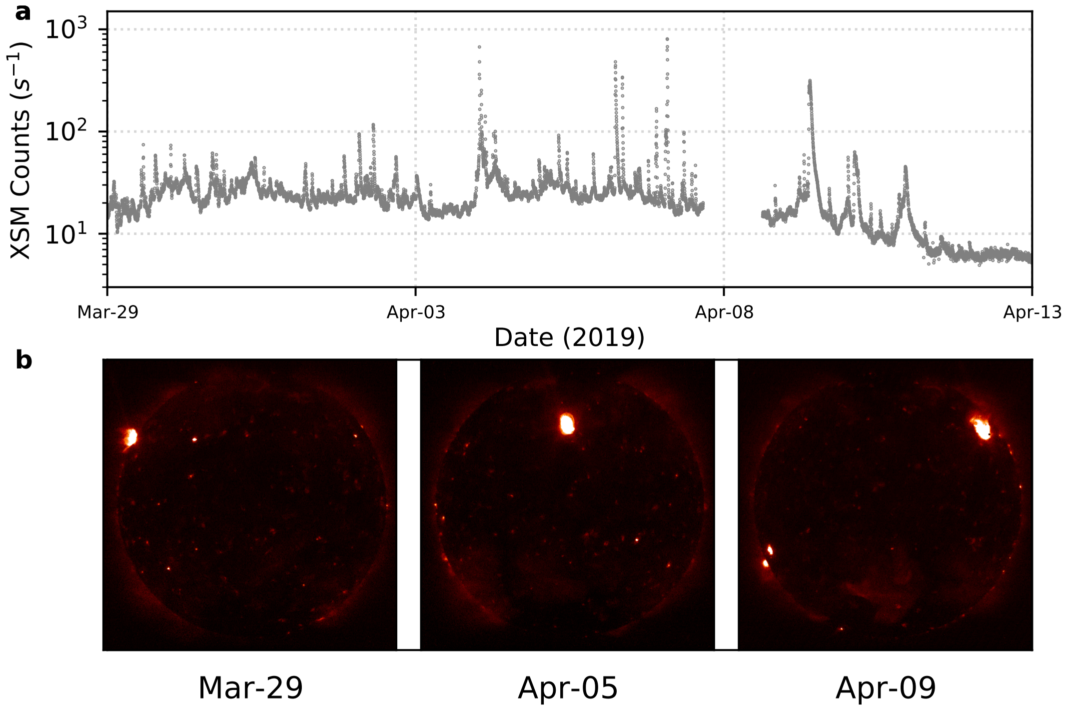

Figure 3.5: XSM 1-15 keV light curve (top) during the disk passage of AR12759. Bottom panel show the evolution of this AR in the full disk X-ray images taken by XRT Be-thin filter. Data data unavailability from the XSM causes the gap in the lightcurve of Apr 8.

as seen from Figure 3.6. The spectra show a clear signature of thermal X-ray emission with the line complexes of Mg, Al, and Si. Hence, we fit the spectra in the energy range of 1.3 to 2.3 keV with the CHIANTI based isothermal plasma emission model that allows us to constrain the temperature, emission measure and abundances of Mg, Al, and Si. Abundances of all other elements, which do not contribute to the line emission in the energy range considered for fitting, are fixed to their known coronal abundance values. We verified that small changes in the abundances of these elements, or fixing them to their photospheric values, do not have any impact on the inferred parameters. Figure 3.6 shows the spectral fit results for two days of observation. It can be seen that the observed spectrum is well fitted with the isothermal model and similar fits were obtained for all spectra. One sigma errors on all free parameters of the model were also estimated using the standard procedure in XSPEC.

By analysing integrated spectra for each day of the selected quiet Sun periods, we obtained temperature, EM, and abundances of Mg, Al, and Si as

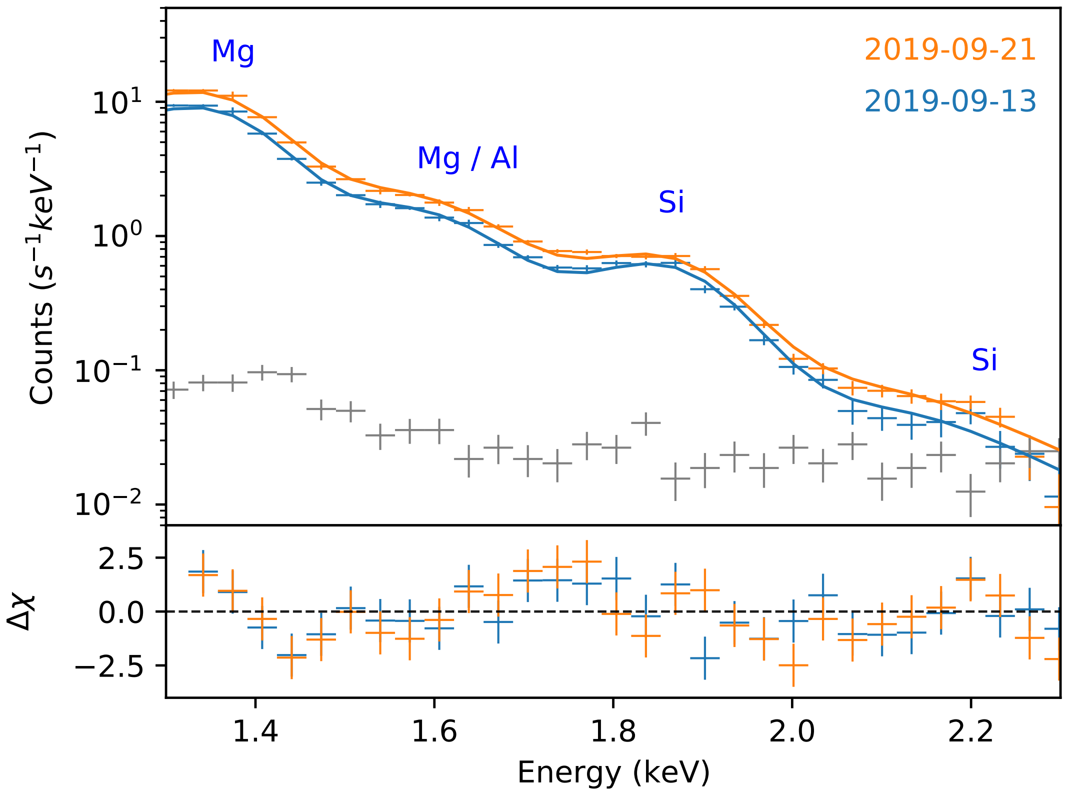

Figure 3.6: Soft X-ray spectra measured by the XSM for two representative days of quiet Sun observations are shown. Solid lines represent the best fit isothermal model and the residuals are shown in the bottom panel. Gray points correspond to non-solar background spectrum.

shown in Figure 3.7. We find that the isothermal temperature and EM of the quiet corona typically remain constant around ~2.05 MK and $\sim 1.5 \times 10^{47}\ cm^{-3}$, respectively. However, there are small variations in temperature and emission measure, which are correlated with the variations in X-ray flux. Sylwester et al. (2019) reported isothermal temperatures of ~1.69 MK for the quiescent corona using X-ray spectroscopic observations in a similar energy range using SphinX observations during the 2009 solar minimum, which is lower than the estimates from XSM. They also noted that the isothermal fit does not explain the observed spectra completely and had shown the presence of higher temperature components with DEM analysis, unlike in the present case where the XSM spectra in the range of 1.3 – 2.3 keV is consistent with isothermal models. One possible reason for the difference could be that the abundances were frozen to coronal

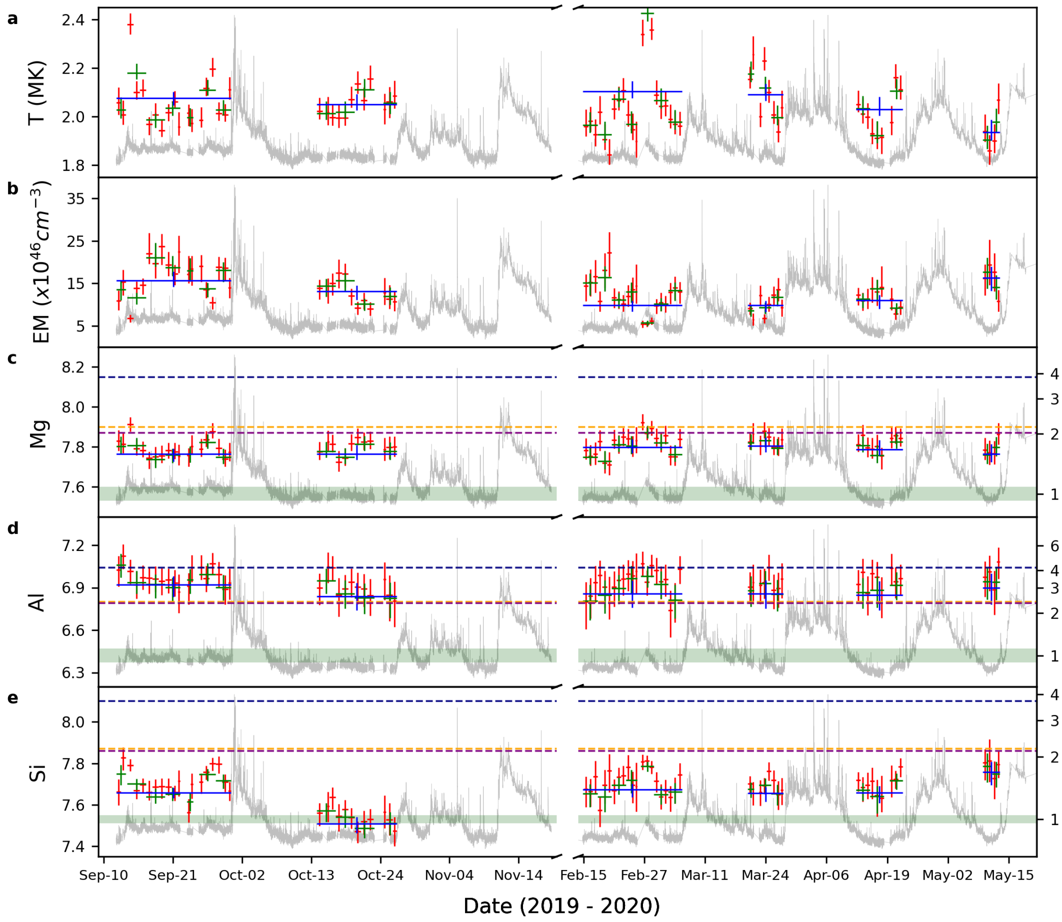

Figure 3.7: The five panels show the results of the spectral fitting, viz. Temperature (**a**), EM (**b**), as well as the absolute abundances of Mg (**c**), Al (**d**), and Si (**e**) in logarithmic scale with A(H)=12. The red, green and blue points represent the best fit parameters obtained from the spectra integrated over one day, multiple days (2–4 days), and each quiet period, respectively. The y-error bars represents 1σ uncertainty for each parameter, whereas the x-error bars represent the duration over which a given spectrum is integrated. XSM light curves for the entire duration are shown in gray in the background. For a quick comparison with the reported values of abundances for these elements, the corresponding panels (**c-e**) also show lines representing active region values reported by Feldman (1992) (*navy blue*), Fludra & Schmelz (1999) (*orange*), and Schmelz et al. (2012) (*purple*). The range of photospheric abundances from various authors compiled in the CHIANTI database are shown as green bands. The right y-axis in panels **c-e** show the FIP bias values for the respective elements with respect to average photospheric abundances.

values in the case of SphinX analysis as they could not be constrained due to relatively poorer energy resolution, whereas the abundances could be fitted in the case of XSM observations.

Observation Period	T (MK)	EM (10^{46} cm^{-3})	Mg	Al	Si
2019 Sep 12 - Sep 30	$2.07^{+0.02}_{-0.02}$	$15.6^{+2.08}_{-1.46}$	$7.76^{+0.02}_{-0.03}$	$6.92^{+0.06}_{-0.08}$	$7.65^{+0.02}_{-0.02}$
2019 Oct 14 - Oct 26	$2.05^{+0.04}_{-0.02}$	$13.1^{+1.36}_{-2.04}$	$7.76^{+0.04}_{-0.02}$	$6.83^{+0.09}_{-0.09}$	$7.50^{+0.03}_{-0.04}$
2020 Feb 14 - Mar 7	$2.10^{+0.04}_{-0.02}$	$9.86^{+1.07}_{-1.49}$	$7.79^{+0.04}_{-0.03}$	$6.85^{+0.09}_{-0.09}$	$7.67^{+0.02}_{-0.03}$
2020 Mar 21 - Mar 29	$2.09^{+0.04}_{-0.02}$	$9.81^{+1.09}_{-1.54}$	$7.80^{+0.04}_{-0.03}$	$6.85^{+0.09}_{-0.10}$	$7.65^{+0.02}_{-0.04}$
2020 Apr 13 - Apr 23	$2.02^{+0.05}_{-0.02}$	$10.9^{+1.24}_{-1.99}$	$7.78^{+0.04}_{-0.03}$	$6.84^{+0.09}_{-0.10}$	$7.65^{+0.03}_{-0.05}$
2020 May 10 - May 13	$1.93^{+0.05}_{-0.03}$	$16.3^{+2.64}_{-3.13}$	$7.76^{+0.04}_{-0.04}$	$6.89^{+0.09}_{-0.11}$	$7.75^{+0.04}_{-0.06}$

Table 3.1: Quiet Sun parameters obtained from XSM spectra integrated over each quiet period.

The estimated abundances for the low FIP elements Mg, Al, and Si are most of the time higher than the photospheric values. However, compared to various coronal abundance values reported in the literature for active regions (Feldman, 1992; Fludra & Schmelz, 1999; Schmelz et al., 2012), our average values are 20 – 60 % lower for Mg and Si. Whereas, for Al, the present derived values are ~30 % lower than the Feldman (1992) value, but comparable with the others. We note that the contribution of Al in the energy band comprising of Al lines is about 10%, resulting in a lower sensitivity to Al abundance as reflected in relatively larger error bars. In order to establish the robustness of the measurements of Al abundances as well as other parameters, we carried out Markov-Chain Monte-Carlo (MCMC) analysis and the results are shown in Figure 3.8. These results clearly show that all parameters including Al abundances are reasonably well constrained. To verify the consistency of our elemental abundance estimates over multiple days, we carried out analysis of the spectra integrated over 2-4 days. These results are also shown in the Figure 3.7. We also carried out similar analysis for the spectra integrated over the whole duration of the respective quiet period (represented by blue lines in Figure 3.7) and the results are given in Table 3.3. We note that the abundance of Si during the period of 14 to 26 October is anomalously low compared to other selected periods and further investigations are needed to identify the reason behind this.

In order to investigate the reason for the different FIP bias in the XSM observations, we checked the X-ray images from the X-ray Telescope (XRT) on board Hinode (Golub et al., 2007) taken with the Be-thin filter, which has

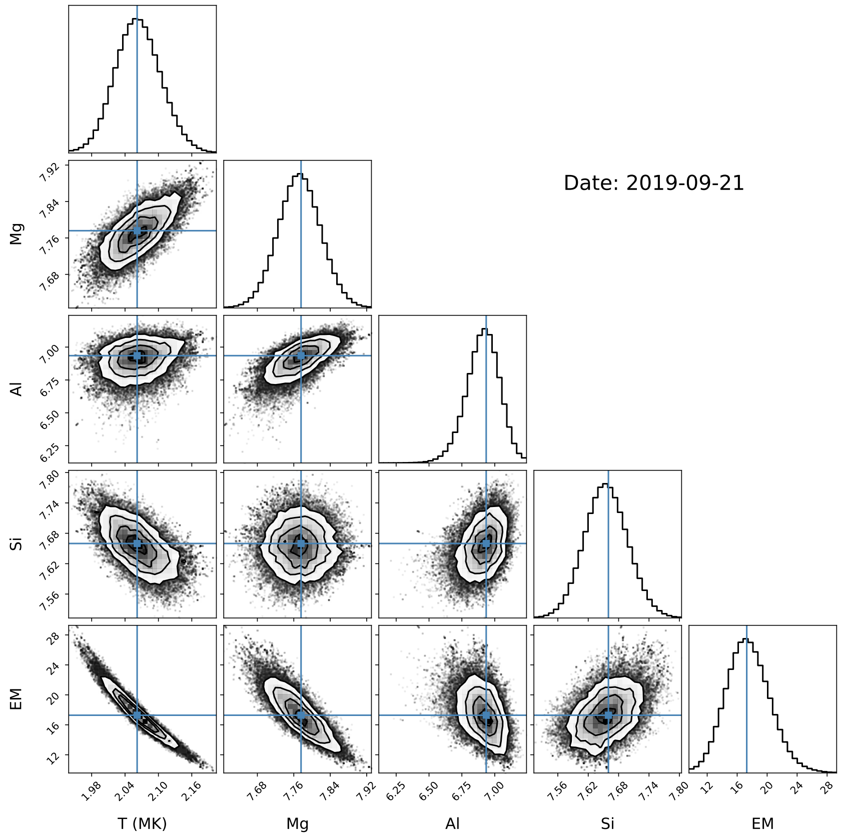

Figure 3.8: Corner plot showing results of MCMC analysis of representative quiet Sun spectrum on 21 September, 2019. The histograms represent marginalized distributions of each parameter. Correlations between all pairs of parameters are shown in the scatter plots overlaid by the contours corresponding to 1, 2, and 3 sigma levels. Best fit parameters are shown by the blue lines. Similar plots for all 73 days are available as a figure set in the online journal.

a similar efficiency as the XSM at lower energies. The X-ray images during the selected days show that most of the X-ray emission observed in the XSM energy range arises from a few hot spots, known as X-ray Bright Points (XBP), first reported by Golub et al. (1974b). To verify this further, we simulated the expected XSM count rate from the quiet coronal region excluding any XBPs using the Differential Emission Measure (DEM) from Brooks et al. (2009). We generated synthetic spectra with CHIANTI using this DEM and convolved it with the XSM detector response matrix to obtain the expected count rate. We find that the X-ray emission from the diffuse corona having peak temperature around 1 MK and photospheric elemental abundances can account for only 30 to 50 % of the observed count rate, suggesting that the majority of X-ray emission observed by XSM originates in XBPs. This is further confirmed by the fact that the overall temperature of around ∼2 MK, as observed by XSM, is much higher than that known for the quiet and diffuse corona. Observations with Hinode XRT have also reported temperatures ranging from 1.1 to 3.4 MK for XBPs (Kariyappa et al., 2011). Thus, we conclude that the intermediate FIP bias observed by XSM most likely corresponds to the XBPs. To the best of our knowledge, this is the first report of the elemental abundances for XBPs having a temperature of ∼ 2 MK. According to present theoretical understanding of FIP bias (Laming, 2009; Dahlburg et al., 2016), the XBPs having intermediate field strengths and temperatures are expected to have intermediate FIP bias; however, there has been no observational evidence so far supporting this conjecture. Our observations confirm this expectation for the first time with robust abundance measurements over an extended period.

3.4 Results and Discussion on quiescent ARs

During the first two DD seasons, XSM observed the Sun when single AR was present (define as an AR period) on the solar disk. We find that the presence of the AR (orange shaded regions in Figure 3.1), increases the base-line X-ray flux to more than a order of magnitude from the quiet period (blue shaded regions). Thus we conclude that the X-ray emission of AR period dominated by the emission from AR. This is further verified by comparing the X-ray spectrum during the quiet period and that of AR period (Figure 3.6 and Figure 3.9). The AR periods spectra show a thermal X-ray emission up to ∼3.0 keV as seen from Figure 3.9. Similar to the quiet period, the spectra show a clear signature of the thermal X-ray emission from the line complex of Mg, Al, Si, and S. Thus, we fit the spectra with the isothermal model, *chisoth*, by considering the plasma temperature, EM, and the abundances of Mg, Al, and Si as a free parameters. Though the S line complex is also visible in the spectra, because of its poor statistics, including it in the spectral fits as a free parameters causes a large uncertainty in the measurement of S abundance. Hence, we fixed the S abundances with the known coronal abundances. Along with that, the abundances of other elements whose line complexes are not visible in the energy range are kept fixed to their respective coronal values (Feldman et al., 1992) for spectral fitting. Figure 3.9 shows the spectral fit results for two representative days of observation from AR12749 and AR12759 respectively. The observed spectra are found to well fitted by the isothermal model (solid lines) and a similar fit were obtained for all the spectra of AR periods. The one sigma errors are also estimated associated with each of the free parameters using the standard procedure in the XSPEC.

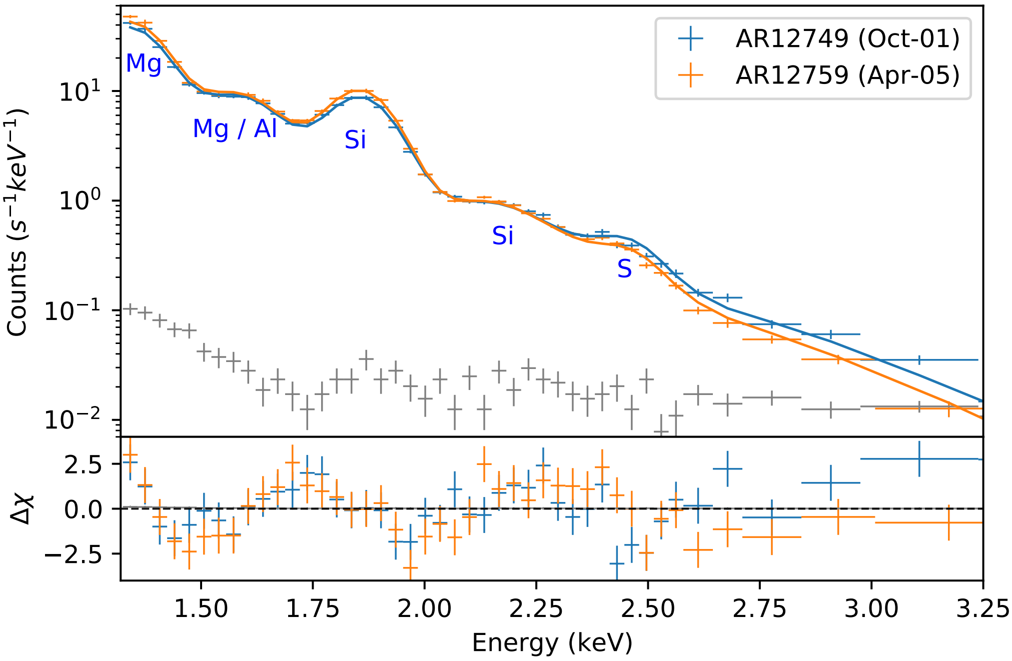

Figure 3.9: Soft X-ray spectra measured by the XSM for two representative days of AR period are shown. Solid lines represent the best fit isothermal model and the residuals are shown in the bottom panel. Gray points correspond to non-solar background spectrum.

Analysing the one day integrated spectra of the AR periods, we obtained the isothermal temperature, EM, and the absolute abundances of the elements Mg, Al, and Si as shown in the Figue 3.10. We find an average isothermal temperature of ∼3.04 MK, which is higher than the isothermal temperature obtained for the quiet periods (Table 3.1). This temperature is close to the temperature of the AR core reported in the earlier studies (e.g., Del Zanna (2013); Winebarger et al. (2012)). We find an isothermal EM of $\sim 4.02\times10^{46}$ cm^{-3}, which is much smaller than the EM of quiet periods (see Table 3.1). The ∼3 MK emission from the AR core produces from a very small volume on solar disk compared with the ∼2 MK emission from the quiet regions. As the EM is proportional to the volume of the emitting plasma, the smaller EM for the AR core is very reasonable. Similar to the temperature and EM of quiet period, we find a small variation of the isothermal temperature and EM of AR periods throughout the evolution of the ARs.

The obtained abundances of low FIP elements Mg, Al, and Si are alwayse higher than the photospheric values, indicating a consistent FIP bias throughout the AR period. Comparing with the various abundance values reported in the literature for ARs (e.g., Feldman et al. (1992); Fludra & Schmelz (1999); Del Zanna (2013)), our average abundances for Mg and Si are in between the values reported by (Feldman et al., 1992) and Fludra & Schmelz (1999), whereas the Al abundance is ∼30%-60% higher. Though, the repeating flaring activity is very common within the AR, the quiescent AR core FIP bias for a particular element remain almost constant throughout the evolution of the AR. Thus the process of the FIP effect of the quiescent AR does not affected by the flaring activity within the AR.

3.5 Summary

In the Sun-as-a-star mode observations, carrying out a prolonged study of the quiet solar corona and AR are often challenging because of the presence of multiple bright activities that typically persist throughout the solar cycle. The 2019-20 solar minimum offered such an opportunity for extended quiet corona observations when there were no active regions present on the visible solar disk. This also offered to study the ARs when most of the coronal emissions were dominated by the presence of a single AR. The XSM on board Chandrayaan-2 was the only X-ray spectrometer operational during a good part of this minimum and optimally utilized this opportunity. It measured the X-ray emission from the solar corona when a single AR was present on the solar disk and showed an enhancement in the X-ray flux. Spectroscopic analysis of these periods of XSM

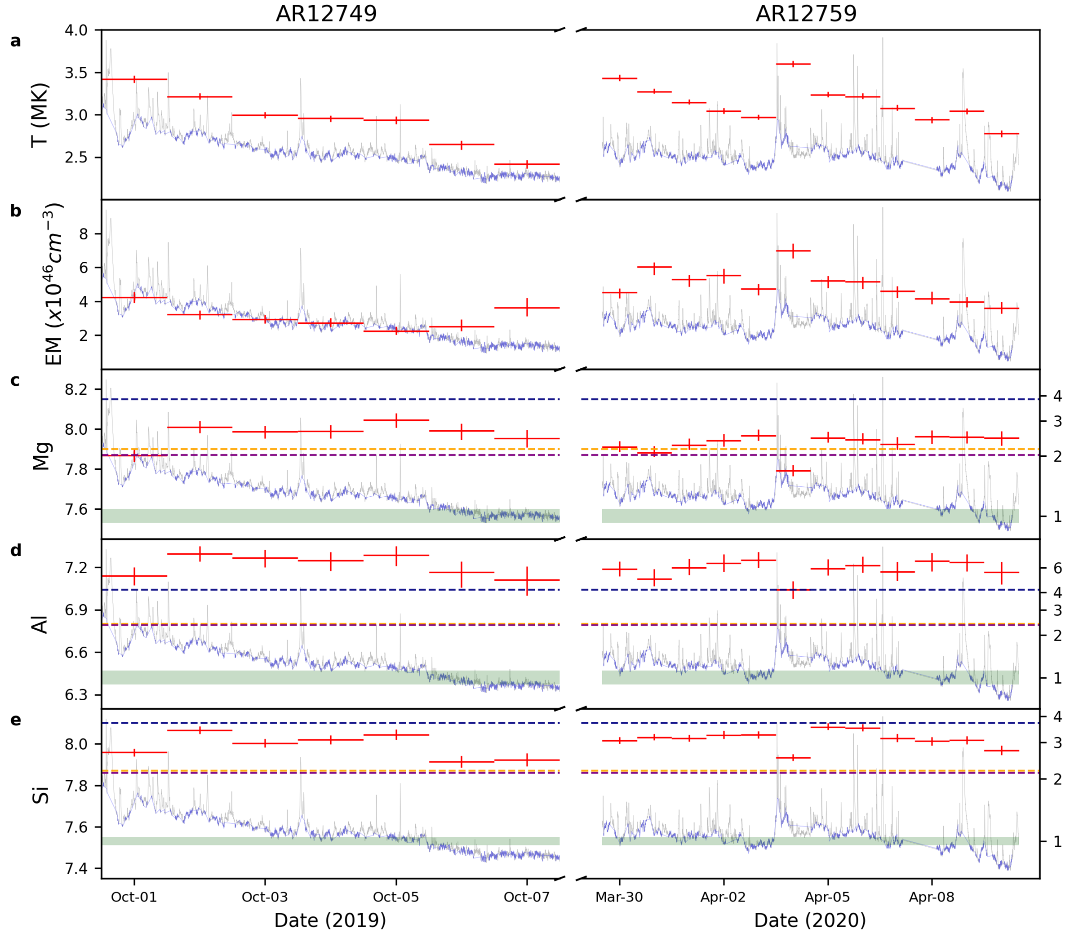

Figure 3.10: The five panels show the results of the spectral fitting, viz. Temperature (a), EM (b), as well as the absolute abundances of Mg (c), Al (d), and Si (e) in logarithmic scale with A(H)=12. Red error bars represent the evolution of the best fitted parameters, where the y-error bars represents 1σ uncertainty for each parameter and the x-error bars represent the duration over which a given spectrum is integrated. XSM light curves for the AR12749 and AR12759 are shown in gray in the background and the blue color on the XSM light curves represent the time duration excluding the flaring activities. For a quick comparison with the reported values of abundances for these elements, the corresponding panels (c—e) also show lines representing active region values reported by Feldman (1992) (navy blue), Fludra & Schmelz (1999) (orange), and Schmelz et al. (2012) (purple). The range of photospheric abundances from various authors compiled in the CHIANTI database are shown as green bands. The right y-axis in panels c—e show the FIP bias values for the respective elements with respect to average photospheric abundances.

observation shows that plasma temperature in the AR is around ∼3 MK and that the abundances of low FIP elements are close to the coronal abundances showing coronal FIP bias. These results are consistent with the earlier studies of AR cores.

During this minimum, XSM measured possibly the lowest intensity of the coronal X-rays with high significance and we find that the bulk of this X-ray emission likely originates in the XBPs when no AR was present. Detailed spectroscopic analysis of these observations shows that plasma temperature in the XBPs is around ~ 2 MK and that the abundances of the low FIP elements in the XBPs are at a level intermediate to their photospheric and coronal abundances. This is the first time XSM has provided a prolonged study of the abundances of XBPs and shows a lower FIP bias compared with the ARs. Our results are consistent with the ponderomotive force model, which is widely considered to be responsible for the coronal FIP bias. Having the lower magnetic activity of the XBPs, it is expected to have a low FIP bias compared with the ARs.

Such a rare opportunity to study the Sun during its quiet period is not likely to be available at least for a decade until the end of the solar cycle 25. Though the XSM may not be operational during the next solar minimum, it will observe the Sun at least during the rising phase of Solar Cycle 25. Thus, with its superior sensitivity, energy resolution, and time cadence, XSM is expected to provide rich observations having far reaching consequences for the study of highly dynamic Sun.

Chapter 4

Evolution of plasma parameters during small flares.

The previous Chapter provides the measurements of the absolute abundances of XBPs and ARs using the XSM observations during the period from September 2019 to May 2020, covering the minimum of Solar Cycle 24. During this period XSM also observed nine B-class flares ranging from B1.3 to B4.5. Using time-resolved spectroscopic analysis during these flares, we examined the evolution of temperature, emission measure, and absolute elemental abundances of four elements – Mg, Al, Si, and S. These are the first measurements of absolute abundances during such small flares and this study offers a unique insight into the evolution of absolute abundances as the flares evolve. Our results demonstrate that the abundances of these four elements decrease towards their photospheric values during the peak phase of the flares. During the decay phase, the abundances are observed to quickly return to their pre-flare coronal values. The depletion of elemental abundances during the flares is consistent with the standard flare model, suggesting the injection of fresh material into coronal loops as a result of chromospheric evaporation. To explain the quick recovery of the so-called coronal “First Ionization Potential (FIP) bias” we propose two scenarios based on the Ponderomotive force model. Most of this work is published in Mondal et al. (2021b) and a part is also published in Del Zanna et al. (2022).

4.1 Introduction

In the previous Chapter we have provided a detailed study of the FIP effect of XBPs and that of the ARs. We found that the FIP bias in XBPs (FIP bias ~ 2) are less than the ARs (FIP bias ~ 3). Now one can ask, what is the FIP bias during the solar flares? By analyzing EUV low-temperature (less than 1 MK) spectral lines of flares and surges observed by Skylab, Feldman & Widing (1990) & Feldman (1992) noted that the relative abundances of several elements (e.g., O and Mg) were close to their photospheric values, i.e., FIP bias is unity. These were interpreted as a consequences of chromospheric evaporation during the events, injecting photospheric plasma into the corona. Later, with the improved spectroscopic capability in the X-rays and EUV, nearly photospheric abundances have been found for several large flares (Del Zanna & Woods, 2013; Warren, 2014a; Sylwester et al., 2014, 2015; Dennis et al., 2015). In these cases, the observations were of hot (about 10 MK) flare plasma, and line to continuum measurements indicated that indeed the absolute values were close to photospheric. We note, however, that a large scatter of values has been reported, partly due to the uncertainty in the continuum evaluation, partly due to the use of different analysis techniques. One interesting aspect of such studies is that none reported variations during the events, which are generally long-lasting for several hours.

Detailed studies of larger flares were possible because of their strong signal to noise ratio. However, it is also important to investigate their smaller counterparts. Observations show that smaller flares occur much more frequently than the bigger ones (Hudson, 1991), so understanding their physics will be of great interest. As detailed observations have been lacking, it is not clear if the evolution of these smaller events follows the standard flare model. It is only recently, with the advent of better instrumentation, that in-depth studies of smaller flares are becoming feasible (Kuhar et al., 2018; Mitra-Kraev & Del Zanna, 2019; Athiray et al., 2020; Cooper et al., 2020; Glesener et al., 2020; Duncan et al., 2021; Vadawale et al., 2021b). Lately, using X-ray time resolved spectroscopy, Narendranath et al. (2020b) have carried out abundance studies of flares as small as GOES B9-class. Like the larger ones, these small flares have also shown a depletion of low FIP elements relative to H, during their evolution.

The high sensitivity of XSM and its capability of measuring elemental abundances on an absolute scale (i.e., with respect to H) enable us to perform a comprehensive study of smaller flares. In this chapter, we present the evolution of temperature, emission measure, and absolute abundances of Mg, Al, Si, and S during a set of nine GOES B1.3-B4.5 class flares. These flares were observed during the minimum of solar cycle 24. At the time of these observations the Sun was extremely quiet, less dynamic and had single isolated active regions on the disk. For the first time, we show a clear and consistent variation of elemental abundances over the entire duration of these flares.

The rest of the chapter is organized as follows: In Section 4.2 we present the observation, XSM data analysis, and identification of events. In Section 4.3 we describe the details of the spectroscopic analysis. After discussing the overall results in Section 4.4, we summarize the article in Section 4.5.

4.2 Observations and Data Analysis

In the present work, we focus on the largest observed flares, all of which are B-class as observed by XSM during the first two prime observing seasons from September 12 to November 20, 2019 (DD1) and February 14 to May 19, 2020 (DD2). See Chapter 3.2 for the details of XSM data reduction procedure. Figure 4.1 (panels **a** and **b**) shows the solar X-ray light curve observed by the XSM in the energy range of 1 to 15 keV during DD seasons (DD1 and DD2). Shaded regions of the light curve show enhanced X-ray emission due to the presence of active regions (AR). The different colors represent different NOAA ARs, with each of them showing a number of flaring episodes. Since the objective of the present analysis is to investigate the temporal evolution of the flares, we select all the large flares for which the XSM count rate increases by more than 200 cps from the pre-flare baseline. We find a total of ten events satisfying this criterion and these events have been marked by vertical red lines in the figure. However, the flare of November 5, 2019, peaking at 06:11 UT was only partially observed by the XSM. We therefore exclude this event from further analysis.

Figure 4.2 shows an enlarged view of the X-ray light curves observed by the XSM (blue) for these nine flares, which have been designated with appropriate identifiers corresponding to the flare peak time, following the standard convention (Leibacher et al., 2010). The figure also includes 1 – 8 Å GOES-16 X-Ray Sensors (XRS) light curves in grey color for comparison, showing that the nine selected flares are all small B-class events with the peak flux ranging from 1.34×10^{-7} W/m^2 to 4.50×10^{-7} W/m^2. It should be noted that some of the earlier studies (e.g. Christe et al., 2008; Hannah et al., 2008) have referred to such events as microflares; however, since the XSM has observed many weaker sub-A class events that have been referred to as microflares in an earlier paper (Vadawale et al., 2021b), we continue to refer to the selected events as B-class flares.

Since the XSM observes disk-integrated X-ray emission from the Sun, we use Solar Dynamics Observatory/Atmospheric Imaging Assembly (SDO/AIA) (Lemen et al., 2012) images in the 94 Å channel to examine the spatial distribution of the enhanced activity on the solar disk. AIA images at the time of the flares (examples in Figure 4.1c) show that only isolated ARs are present on the solar disk. For each flare we derive the AIA 94 Å light curve integrated over the regions around the respective AR (marked by small yellow boxes on the corresponding full disk AIA images in Figure 4.1c), they are shown with brown dashed curves in Figure 4.2. Their similarity with the XSM light curves confirm that the entire enhancement of X-ray intensity observed by the XSM during these flares originated within the respective AR. This confirms that the disk-integrated XSM observations can be used to study the temporal evolution and properties of the flaring plasma.

In order to investigate the temporal evolution during the selected flares, we divide each flare duration into multiple smaller time intervals corresponding to various phases of each flares. The intervals for each flare, shown as alternate background shades in Figure 4.2, are selected based on visual inspection of the XSM light curve in the energy range of 1 – 15 keV, such that all intervals have a sufficient number of counts to perform spectral analysis. These time intervals are then used as user GTI in XSMDAS (see Chapter 3.2) to generate a series of spectra for all nine flares. The modelling of these spectra is then carried out using two different approaches, as discussed in detail in the next section. The first approach assumes that the emission arises from plasma having two distinct components corresponding to the flaring plasma and the rest of the coronal plasma, respectively. The second approach assumes that the emission arises from a single component isothermal plasma. The first approach requires spectrum corresponding to a non-flaring plasma, which is generated for the non-flaring time intervals as shown in Figure 4.3a for two representative flares, viz. SOL2020-04-06T05:48 and SOL2020-04-06T08:32. The blue line shows the full day light curve while the green shaded regions show periods for which the non-flaring emission spectrum is generated. Such non-flaring time intervals are visually selected from the corresponding daily light curves for all flares, with the exception of the two flares SOL2019-09-30T23:00 and SOL2019-10-01T01:44. For these two flares, it is difficult to select a reliable non-flaring duration because of the multiple small flaring episodes occurring within the same AR as shown in Figure 4.3b. Moreover, the AR starts appearing from the eastern limb of the sun during these two events. Hence, the spectral analysis of these flares is restricted to the isothermal plasma assumption (second approach).

4.3 Time resolved Spectral Analysis

Soft X-ray spectra of the solar corona provides information on the physical conditions and radiative processes in the emitting plasma. It typically consists of a continuum arising from free-free, free-bound, and two-photon radiative processes superimposed by emission lines corresponding to different ionization states of various elements. The expected spectrum for a given set of physical parameters such as temperature (T), density (usually represented as emission measure, EM) as well as the abundances of various elements, can be analytically calculated (Del Zanna & Mason, 2018). This analytical or synthetic spectrum, when fitted to the observed spectrum, can constrain the physical parameters of the observed plasma. We use the CHIANTI database version 10 (Del Zanna et al.,

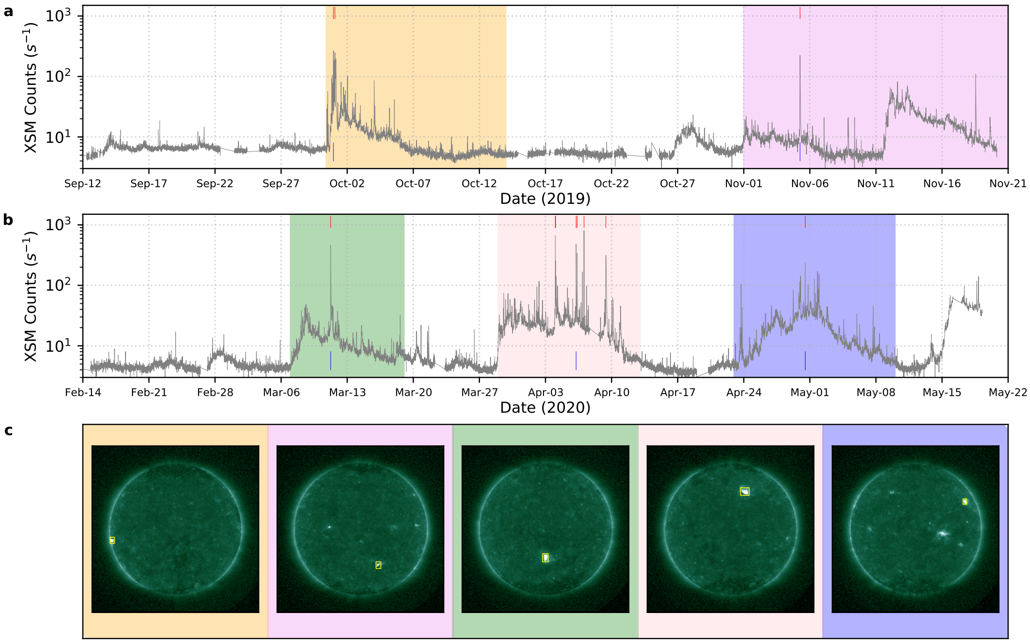

Figure 4.1: Panels **a** and **b** show the X-ray light curve in the 1-15 keV energy range with a time cadence of 120 s, as measured by XSM during the two 'Dawn-Dusk' seasons (DD1 and DD2), respectively. Different color background shades represent periods when AR, recognized by National Oceanic and Atmospheric Administration (NOAA), are present on the solar-disk. Panel **c** shows representative full disk EUV images by AIA/SDO (94 Å channel) for the duration marked by the blue vertical line of the corresponding shaded regions of panel **a** and **b**. Vertical red lines represent the peak time of the selected flares.

2021) to generate the synthetic spectra and XSPEC (an X-ray spectral fitting package (Arnaud et al., 1999)) to fit the spectrum. Since the synthetic spectrum calculated by CHIANTI can not be directly used in XSPEC for spectral fitting, we have developed a local XSPEC model, *chisoth*, from a wide range of pre-calculated spectra, as described in Chapter 2.3.3.

The main objective of our analysis is to study the evolution of plasma properties during the course of the nine selected B-class flares. Since these are relatively small flares, it is likely that during different flare phases there are considerable contributions from non-flaring plasma. Usually, such contributions are subtracted from the flare spectrum by considering a pre-flare spectrum as background. However, this is not preferable in the case of XSM because the sun angle, and thus the effective area of the instrument, changes continuously. Hence, we model the spectrum of the non-flaring plasma independently and include it as a fixed component while fitting the flare spectrum. An additional

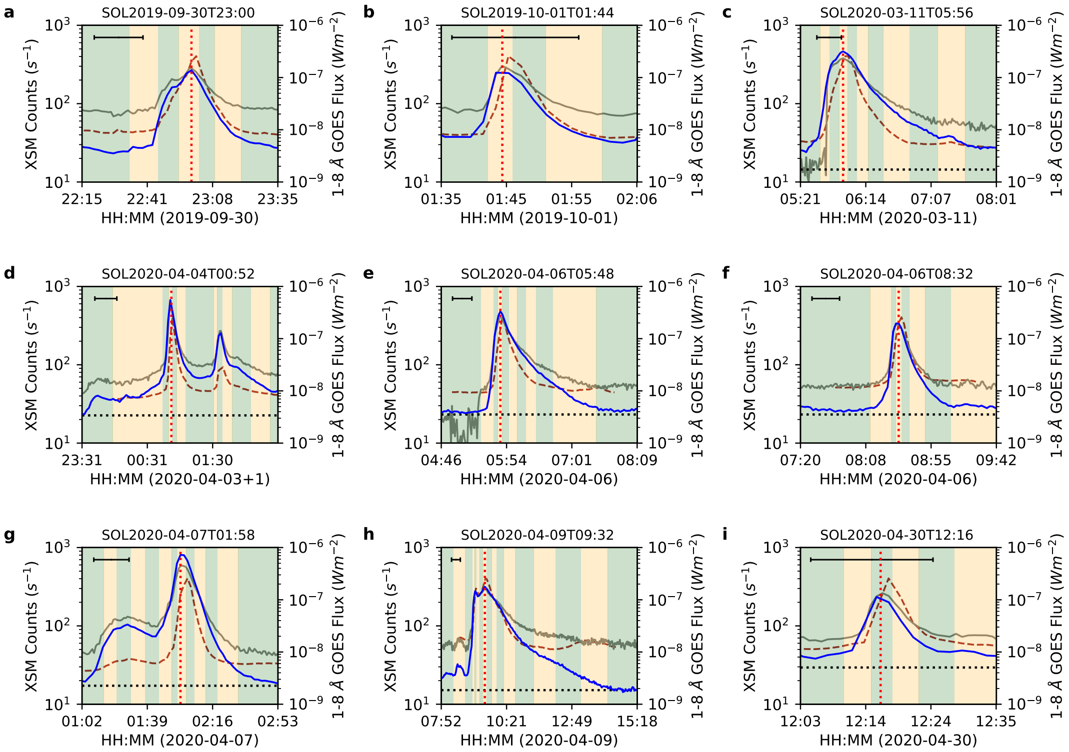

Figure 4.2: The 1-15 keV XSM X-ray light curves (blue) for the selected flares. The observed GOES-16 XRS fluxes of these flares are shown by grey lines while the brown dashed lines show the normalized (with XSM count rates) AIA 94 Å fluxes, spatially integrated over the associated AR as marked by the yellow boxes in Figure 4.1c. Background green and orange shaded regions represent durations for which the integrated XSM spectra have been generated for time-resolved spectroscopy as described in Section 4.2. The vertical red dotted lines represent the flare peak time. Black horizontal dotted lines in panels **c-i** are the average count rates for the non-flaring plasma as discussed in Section 4.3. The black scale-bars at the top left of each panel represent a 20-minute time interval on the x-axis. A flare ID, for each flare corresponding to the flare peak time in the format SOLyyyy-mm-ddThh:mm, is given on the top of every panel.

advantage of this approach is that in most cases it is possible to co-add several epochs having the same intensity and spectra, as shown in Figure 4.3a, to increase the statistical significance of the non-flaring spectrum. We then fit this non-flaring X-ray spectrum with our isothermal model. Though the model allows one to vary the abundances of all elements in the range of Z=2 to 30, we retain the abundances of only Mg, Al, and Si, for which the line features are observable in the spectra, as free parameters. Abundances of the remaining

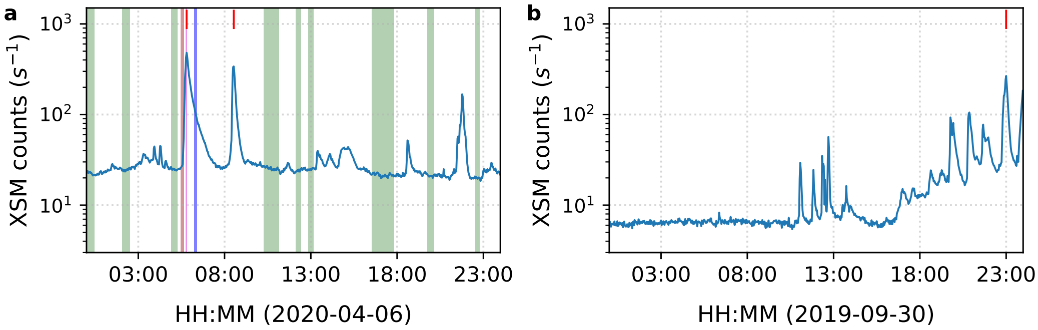

Figure 4.3: Full day XSM 1-15 keV solar X-ray light curve on 2020-04-06 (**a**) and 2019-09-30 (**b**). Selected flare peak times for the same day are shown by the red vertical lines. In panel **a** the green shaded regions demarcate the time durations used to generate the non-flaring emission spectrum required for the two-temperature spectral fitting for the flares SOL2020-04-06T05:48 and SOL2020-04-06T08:32. The brown, violet, and blue shaded regions show the time interval of the spectra shown in Figure 4.4. Panel **b** shows multiple small flaring episodes before and after the flare SOL2019-09-30T23:00. All of these flares occur within the same AR, which appeared at the eastern limb of the Sun. Because of this, a reliable non-flaring emission could not be established for this flare.

elements are fixed to their respective coronal values taken from the combined dataset "sun_coronal_1999_fludra_ext.abund" (hereafter A_F99) available within the CHIANTI package. These are so-called 'hybrid' abundances, where the abundances of low (high) FIP elements were increased (decreased) compared to their photospheric values, by about a factor of two. The other two free parameters of the model are temperature (T) and emission measure (EM). We carry out the spectral analysis to determine the T, EM and abundances of Mg, Al, and Si of non-flaring plasma for all the flares except SOL2019-09-30T23:00 and SOL2019-10-01T01:44 as discussed in Section 4.2. Table 5.1 shows the best fitted parameters for all the non-flaring spectra.

Next, we focus on the spectra generated for the different phases of the selected nine flares as shown in Figure 4.2. We fit each spectrum with a model consisting of two isothermal components. All parameters of the first component are fixed to their respective values obtained from non-flaring intervals, whereas for the second component, T, EM, Mg, Al, and Si are kept as free parameters and fitted for each spectrum. We also keep S abundance as a free parameter whenever fitting for S is statistically feasible. During the flare peak, occasionally Ar and Ca line complexes are also visible, however, because of their poor statistics, including them in the spectral fits and deriving their abundances leads to large error bars. Hence, we fix their abundances as a constant parameter during spectral fitting. We have verified that keeping abundances of these two elements either as free or fixed do not affect any other fit parameters. The one sigma uncertainties on all free parameters are obtained using the standard procedure in XSPEC. The representative spectral fits for the flare SOL2020-04-06T05:48, for the three time durations (marked by brown, violet, and blue shaded regions in Figure 4.3a) are shown in Figure 4.4a. The fit results for all phases of the same flare are shown in Figure 4.8.

For the two flares SOL2019-09-30T23:00 and SOL2019-10-01T01:44, it was not possible to carry out the spectral analysis with the two-component model due to the lack of reliable non-flaring spectra. Hence, for these two flares, we resorted to using only a model with a single temperature. However, in order to investigate any differences between the results obtained by the two spectral fitting approaches, we also carried out a time resolved spectral analysis, for all nine flares, under the isothermal assumption with a single component model.

The spectral fits with the single component model for the same spectra of the flare SOL2020-04-06T05:48 are shown in Figure 4.4b and the fit results for all phases of the flare are over-plotted in Figure 4.8. We find that, for all flares where both the two component and single component analysis is possible, the results obtained with both approaches are similar within error-bars. Table 5.1 shows the values for the time intervals containing the temperature and emission measure peaks. This suggests that even for these small B-class flares, the emission from the flaring plasma dominates over the emission from the non-flaring plasma and hence for the flares SOL2019-09-30T23:00 and SOL2019-10-01T01:44, the results of the single component analysis also represents variations associated to the flare loops.

For a further verification of the XSM analysis and cross-calibration of XSM with AIA/SDO, we forward model a representative XSM spectrum during the peak of a flare using the the multithermal plasma emission characterized by Emission Measure (EM : see Chapter 2.5) distribution obtained from the AIA pass-bands. Using the observations of AIA pass-bands and the measured abundances from the XSM observation, Del Zanna et al. (2022) derived the spatially resolved EM during the peak of the flare; SOL2020-04-09T09:32. The resulting column EM values for a range of temperatures are shown in Figure 4.5. Here, the EM values include the emissions of the AR core (within which SOL2020-04-09T09:32 occur) along with the emissions from SOL2020-04-09T09:32. It is to be noted that the high temperatures are not well constrained, as the only hot channel with enough signal was the AIA 94Å. For this reason, the maximum temperature for the inversion was set to log T [K]=6.9. From the column EM values we calculate a volume EM by averaging the emission measures over the core of the flare (higher EM at temerature bin log T = 6.7 to 6.9), in a region covering 100 × 50 pixels in the x and y direction, respectively. The resulting volume EM is shown in Figure 4.6. We then used this volume EM to predict the XSM spectrum, which is shown, together with the observed one, in Figure 4.7. There is excellent agreement between the two verify the reliability of the measured abundances from XSM spectral analysis.

4.4 Results and Discussion

In this study, we have performed a spectroscopic analysis of nine B-class flares. Using time-resolved spectroscopy of these flares, we have shown the evolution of elemental abundances, temperature, and emission measure over their lifetime. Results from a representative flare (SOL2020-04-06T05:48) are demonstrated in Figure 4.8. The different panels demonstrate the time evolution of temperature (a), emission measure (b), and abundances of four elements (c-f), namely, Mg, Al, Si & S. Temperature (Figure 4.9), emission measure (Figure 4.10), and abundance (Figure 4.11-4.13) evolution of all other flares are shown separately. In the background of each plot, the light curve of the respective flare is shown with a solid grey line.

Temperatures (Figures 4.8a, Figure 4.9) and emission measures (Figures 4.8b, Figure 4.10) of these flares rise with their soft X-ray activity, showing maxima near the time of the flare peaks. In most of the flares, the temper-

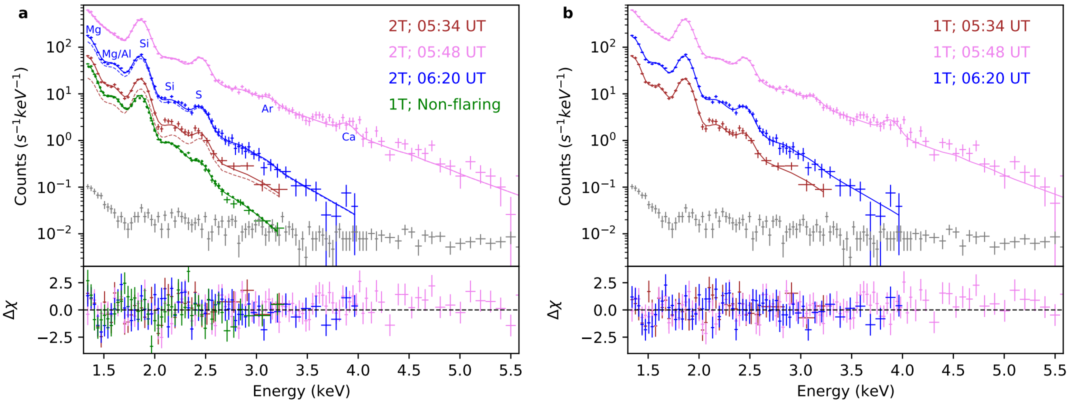

Figure 4.4: Fitted spectrum for the Flare SOL2020-04-06T05:48. The brown color represents the rising phase at 05:34 UT, violet is for the flare peak at 05:48 UT and blue is for the decay phase at 06:20 UT. Panel **a** shows the fitted spectra using a two temperature isothermal emission model (solid lines), while panel **b** shows the fitted spectra using a single temperature model (solid lines). The green color in panel **a** represents the fitted spectrum for the emission due to non-flaring plasma considered in the two component model. The dashed lines in panel **a** represent modeled spectra of the flaring emission component. The grey points show the non-solar background spectrum acquired for the times when the Sun was out of the XSM FOV. The energy ranges of the respective spectral fits were restricted to the energies where the solar X-ray spectrum dominates over the non-solar background.

ature peaks lie ahead of the emission measure peaks. These can be identified by comparing Figure 4.9 with Figure 4.10 (or Table 5.1). However, two flares, namely, SOL2019-09-30T23:00 and SOL2020-03-11T05:56 (panels a and c) do not follow the trend, possibly due to larger time bins at the flare peak compared to the small flare duration. During the impulsive phases, elemental abundances (Figure 4.8(c-f), Figures 4.11-4.13) are seen to reduce quickly from the coronal to near photospheric values, while the minima occurring almost simultaneously with the emission measure peaks. However, the abundances swiftly return to the coronal values during the decay phases of the flares.

Considering our 'Sun as a star' observation, one may think the quick recovery of the coronal abundances may not be physical but merely be an effect of emission swapping from the flaring loop to the rest of the corona. However, results derived using our two temperature models, where emission from flaring and non-flaring plasmas are treated separately, show a similar abundance recovery (red points in Figure 4.8(c-f), Figures 4.11-4.13). This confirms that this

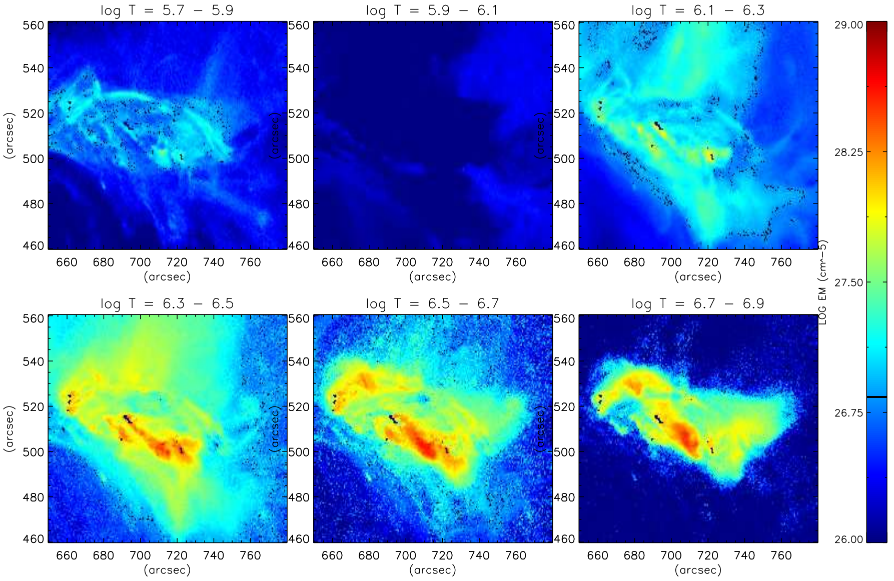

Figure 4.5: Emission Measure distribution during the peak of the flare SOL2020-04-06T05:48 in selected temperature bins. The EM distribution is shown for the AR core within which SOL2020-04-06T05:48 occur. (This figure is adapted from Del Zanna et al. (2022))

abundance recovery is not due to emission swapping. For a further verification that the measured abundances by XSM are not affected by the huge amount of lower temperature emission from the AR core, we have forward modeled the XSM spectrum using the multithermal plasma emission distribution during the peak of the flare SOL2020-04-06T05:48. This multithermal emission distribution is derived independently using the AIA pass-bands and the measured abundances by XSM. The forward modeled spectrum is well agreed with the observed spectrum (Figure 4.7) indicating that the measured abundances by XSM are not affected by the cool emission from the AR plasma.

Following the standard flare model (CSHKP: Carmichael (1964); Sturrock (1966); Hirayama (1974); Kopp & Pneuman (1976)), the evolution of temperature and emission measure can be explained by invoking chromospheric evaporation. After the flare onset, both temperature and emission measure start rising. When the coronal temperature achieves its peak, the heat energy from the

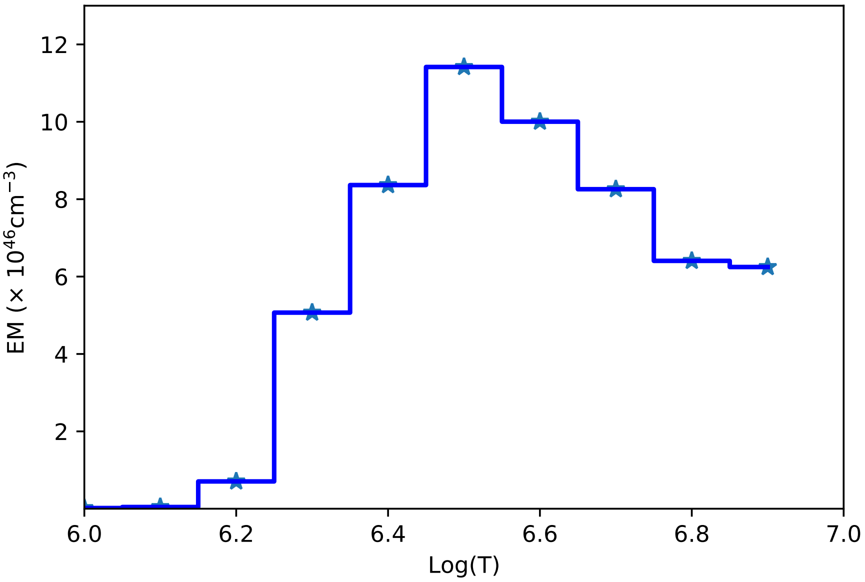

Figure 4.6: Averaged volume EM obtained from the AR core as shown in Figure 4.5.

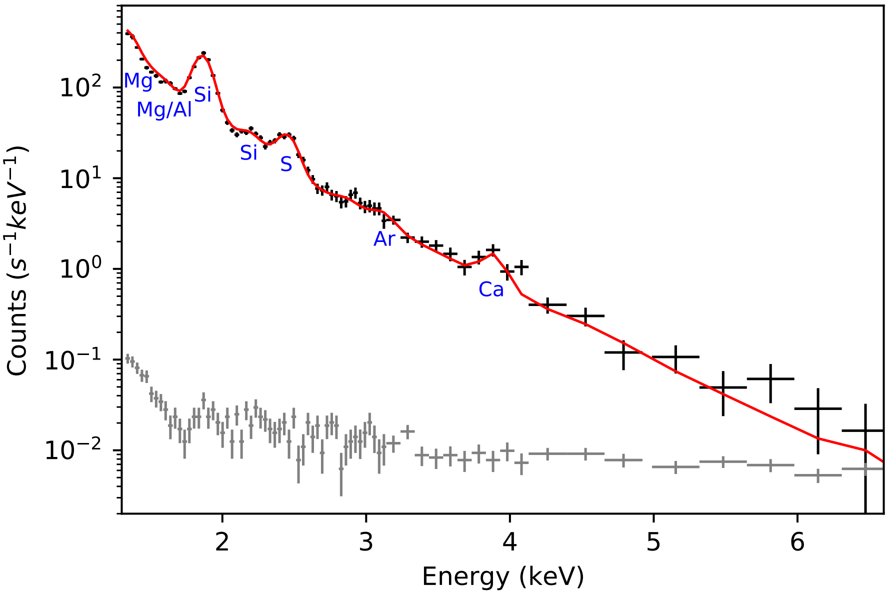

Figure 4.7: XSM averaged spectrum during the peak of SOL2020-04-06T05:48, with the predicted spectrum (red) derived from the average volume EM obtained from AIA pass-bands as shown in Figure 4.6. The grey color represent the non-solar back ground spectrum observed by XSM.

reconnection site travels down to the chromosphere and starts evaporating chromospheric plasma into the loop with high velocity (Antonucci et al., 1985). The peak of the emission measure is recorded once the loop gets filled with the high-density heated evaporated material (Ryan et al., 2012; Klimchuk, 2017). As the evaporative upflow can bring in fresh unfractionated chromospheric material into the corona, it can also explain the quick abundance depletion. However, explanation of the fast recovery (in minutes time scale) of the coronal FIP bias during the decay phases of the flares demands the support of additional mechanisms.

One of the most widely accepted theories to explain the FIP bias in the closed loop coronal plasma is based on the Ponderomotive force model. The said force originates at the chromospheric layers of the magnetic flux tubes due to multiple reflections of the coronal Alfvén waves (Laming, 2004). According to this theory, the FIP dependent elemental fractionation arises because the upwards Ponderomotive forces act only on the ions. Since the density and temperature of the chromospheric layer favor the ionization of low FIP elements, only these elements get fractionated there. Low FIP ions then experience the Ponderomotive force and drift upwards, enhancing their concentration in closed coronal loops. Observations suggest it takes several days for the FIP bias to get established in non-flaring active regions (Widing & Feldman, 2001), although we note that the Skylab measurements discussed by Widing & Feldman (2001) refer to cool transition region lines and the results are not directly related to the abundances of the hot core loops. In this context, two possibilities can be thought to be responsible for the quick transitions (order of minutes) of the coronal FIP bias during the impulsive and decay phases of all observed flares in this study. The schematic representations of these two possibilities are presented in Figure 4.14.

The first possibility envisages that the newly evaporated chromospheric material comes from a region beneath the fractionation layer, having almost non-fractionated photospheric plasma. It has been observed earlier that the injection of fresh material continues throughout the duration of the flare (Zarro & Lemen, 1988; Czaykowska et al., 1999). The injection velocity is highest during the impulsive phase of the flare and gradually reduces towards the decay phase (Fletcher et al., 2011). At the time of the initial phase, when the upflow velocity is high, plasma does not get enough time to spend in the fractionation layer to get fractionated and thus unfractionated photospheric plasma is injected into the coronal loop – exhibiting a depletion of the coronal FIP bias. Once the flow speed reduces below $\sim$ 1 km/sec (Laming, 2004, 2017) at the top of the chromosphere, it is plausible to assume that the evaporated material takes longer to cross the thin fractionation layer and gets fractionated while traveling through it. In this scenario, the quick enhancement of the FIP bias is not only due to the slow drift of the ions but also due to the bulk velocity of the already (partly) fractionated material filling the loop. As the velocity of the evaporated material decreases, the plasma gets fractionated to a higher degree, and thus the FIP bias is restored to the pre-flare level by the time the flare emission decays completely.

The second possibility relies on the flare driven high amplitude Alfvén waves. Immediately after the flare, heat energy carried by the suprathermal electrons (Benz, 2017) may travel faster towards the loop footpoints than the Alfvén waves to evaporate plasma from the chromosphere. The evaporated chromospheric non-fractionated plasma is responsible for the initial depletion of the FIP bias. However, once the newly generated Alfvén waves reach the fractionation layer, they start fractionating plasma through the generation of the Ponderomotive force. The high amplitude nature of these waves help to fractionate plasma in a faster time scale (Dahlburg et al., 2016). These Alfvén waves may also carry a significant fraction of the released magnetic energy from the flaring site to the chromosphere, which may also assist the evaporation (Fletcher & Hudson, 2008). The fractionated plasma then gets transported to the coronal loop, assisted by the evaporative upflow, which helps to recover the coronal FIP bias in a faster time scale.

Although all the observed flares show a similar variation of the abundance evolution, the abundance recovery time scale during the decay phase varies from flare to flare. In general, it ranges between $\sim$10 to $\sim$90 minutes. The second scenario, which explains the faster fractionation as well as transport, appears to be a more plausible mechanism to explain the faster recovery of the FIP bias. Whereas, if the recovery happens over a longer time scale ($\sim$ several hours) it can be explained through the former. Reconnection driven Alfvén waves are yet to be observed in flaring loops. However, the observations presented in this article imply their role in altering the coronal FIP bias. XSM observes the Sun as a star, therefore misses any spatial information. On the other hand, it is to be noted from SDO observations that the flaring reconnection and the post-flare loops have fairly complicated geometric structures. Though the schematics of Figure 4.14 consider a single magnetic structure, in reality it can be more complicated.

We also note a couple of other interesting points - Figure 4.8 shows that, unlike the other three elements, the abundance of Si does not quite reach the photospheric value during the episodic event. The same is true for other flares as well. The abundance values of Si near the flare peak (Table 5.1, except the flares SOL2019-09-30T23:00, SOL2019-10-01T01:44, and SOL2020-04-04T00:52) are in good agreement with earlier large flare observation (Veck & Parkinson, 1981b). It may be possible that at the chromospheric height where the evaporating plasma originates, the abundance of Si is already greater than that of the photosphere, indicating the fractionation of Si at lower chromospheric height. As a result, the evaporated plasma in the flaring loop exhibits Si abundance between photospheric and the coronal values, whereas the other elements exhibit photospheric abundance.

It has been seen that the abundance of Mg during flare peaks depletes down to sub-photospheric values (Figures 4.8c, 4.11) on many occasions. Such abundance depletion may be mistaken as evidence of the inverse FIP effect. However, we find that this could be due to the effect of input abundances of unresolved lines in the continuum spectra. When we change the input abundances from A_F99 (CHIANTI abundance dataset: “sun_coronal_fludra_1999_ext.abund”) to A_F92 (CHIANTI abundane dataset: “sun_coronal_feldman_1992_ext.abund”) the abundance of Mg remains within the photospheric range. For a similar reason, the measured abundances of flares SOL2019-09-30T23:00 (Panel a of Fgure 4.11,4.13), SOL2019-10-01T01:44 (Panel b of Fgure 4.11,4.13), and SOL2020-04-04T00:52 (Panel d of Fgure 4.11,4.13), record lower values than the other flares. To check further how input abundances affect our derived parameters, we compare our single component fit results (Figure 4.15) of a typical B-class flare SOL2020-04-06T05:48 for two sets of input abundances; namely, A_F92, and A_F99. The temperature values (Figure 4.15) for both the input abundances remain almost unaltered. However, the rest of the parameters maintain a nearly constant offset. This is due to elements having a higher presence in the solar atmosphere, like O, C, etc., besides H and He. They play a crucial role in determining the soft X-ray continuum. When changing the abundances, the overall continuum gets changed. Figure 4.16 shows the soft X-ray continuum at different temperatures. It also shows how the continuum shifts when the abundance list is changed from A_F92, and A_F99. Since the continuum gets changed, the derived parameters resulting from the continuum are also affected. Though the exact values of the absolute abundances depend on the chosen input abundance list, the abundance evolutionary trend during flares and the coronal abundance recovery time scale remain independent of the abundance list.

Having analyzed several B-class flares and identified their spectroscopic behaviour over time, we can conclude that these flares also follow the standard flare model. In a manner similar to their larger, more energetic counterparts, they also show near photospheric abundances during their evolution. During the post flare phases, the quick recovery of the coronal abundances on a time scale of minutes can be successfully explained through the Ponderomotive force model. To study this issue further, a careful analysis of multi-wavelength imaging and spectroscopic observations is necessary. We have carried out a campaign of multi-wavelength observations (with Hinode/EIS and XRT) and the results will be discussed in follow-up papers.

4.5 Summary

In this work, we presented the temporal evolution of elemental abundances during solar flares of GOES B1-B4 class, the weakest events for which such studies have been possible so far, using observations with XSM on board Chandrayaan-2. This study was possible due to the extremely quiet solar conditions currently prevailing along with the availability of appropriate instrumentation. By modelling the soft X-ray spectra obtained with the XSM during different phases of these flares, measurements of temperature, emission measure, and abundances

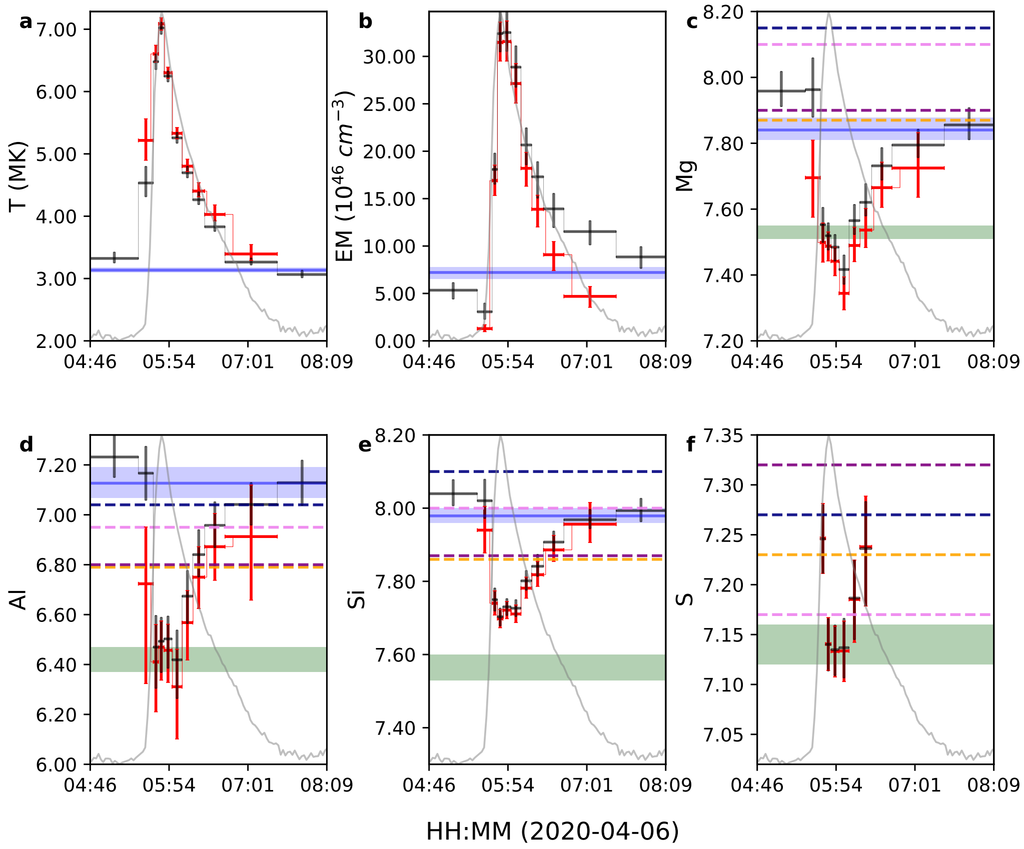

Figure 4.8: The six panels show the results of the time resolved X-ray spectroscopy for the flare SOL2020-04-06T05:48. Panels **a-b** show the variation of temperature and emission measure, respectively, during flare activity, while panels **c-f** show the variation of elemental abundances of Mg (**c**), Al (**d**), Si (**e**), S (**f**) in logarithmic scale. Spectra are fitted by both a single component isothermal model and a two component isothermal model, as discussed in the text. The black and red points represent the best fit parameters obtained from the fitted spectra using a one component model (black) and a two component model (red), respectively. The y-error bars represents 1σ uncertainties for each of the parameters, whereas the x-error bars represent the duration over which a spectrum is integrated. For a quick comparison with the reported abundance values for these elements, the corresponding panels (**c-f**) also show the coronal value of abundances compiled in the CHIANTI database of "sun_coronal_feldman_1992_ext.abund" (A_F92, navy blue), "sun_coronal_fludra_1999_ext.abund" (A_F99, Purple), and "sun_coronal_schmelz_2012.abund" (A_S12, orange) and also reported by Del Zanna (2013) (violet). The range of reported photospheric abundances from various sources compiled in the CHIANTI database are shown as green bands. The X-ray XSM light curve is over plotted in grey color in the background.

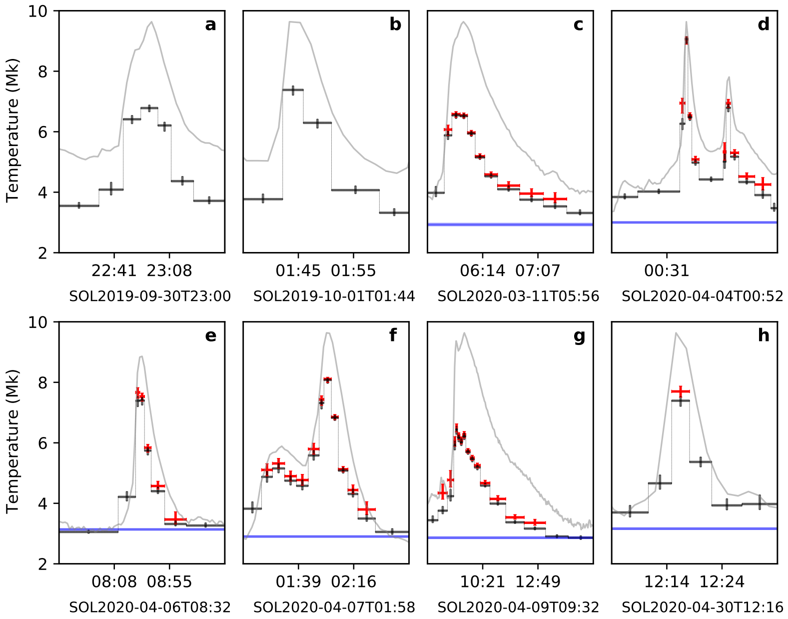

Figure 4.9: Temperature evolution similar to Figure 4.8a, but for different flares.

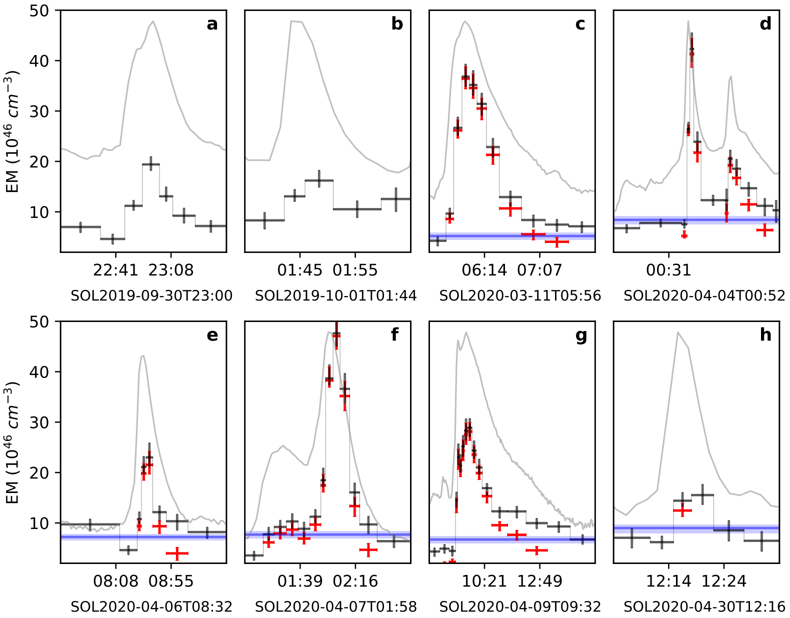

Figure 4.10: Evolution of the emission measure similar to Figure 4.8b, but for different flares.

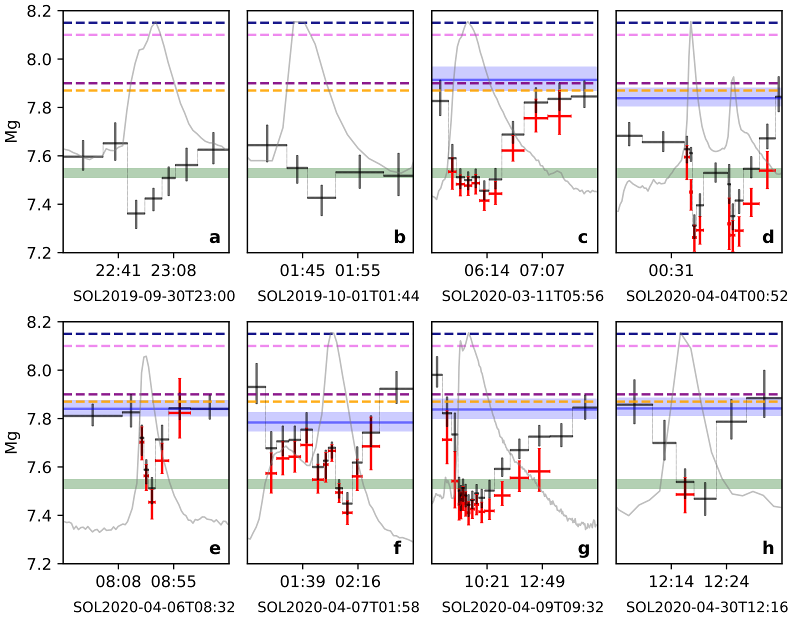

Figure 4.11: Evolution of the absolute Mg abundance similar to Figure 4.8c, but for different flares.

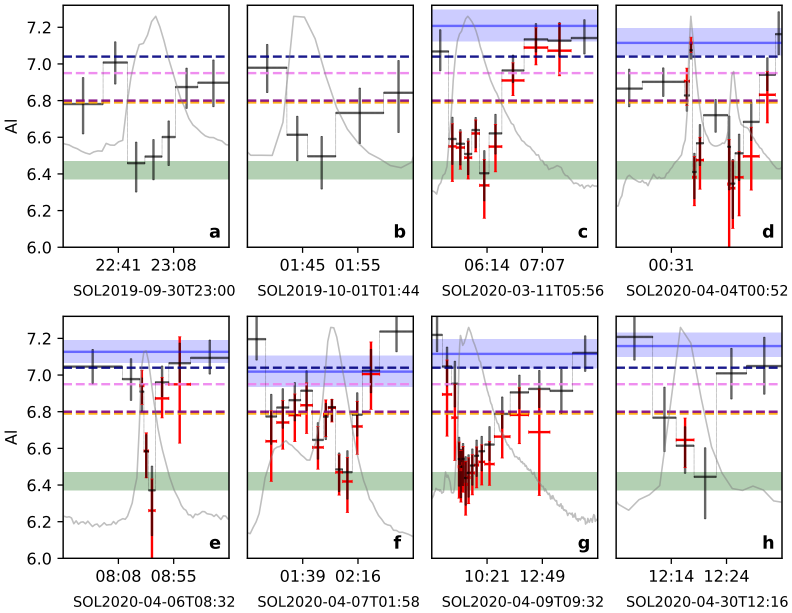

Figure 4.12: Evolution of the absolute Al abundance similar to Figure 4.8d, but for different flares.

Flare ID[a]	NOAA[b] AR	Model[c]	max.[d] T $\times 10^6$K (Time bin)	max.[e] EM $\times 10^{46}$cm^{-3} (Time bin)	Mg[f]	Al[f]	Si[f]	S[f]
SOL2019-09-30T23:00	12749	$1T$	$6.78^{+0.10}_{-0.12}$ (22 : 54-23 : 03)	$19.4^{+1.56}_{-1.22}$ (22 : 54-23 : 03)	$7.42^{+0.04}_{-0.05}$	$6.49^{+0.09}_{-0.12}$	$7.55^{+0.02}_{-0.02}$	$6.93^{+0.03}_{-0.03}$
		$2T$	–	–	–	–	–	–
		NF	–	–	–	–	–	–
SOL2019-10-01T01:44	12749	$1T$	$7.38^{+0.13}_{-0.17}$ (01 : 42-01 : 46)	$16.2^{+2.04}_{-1.32}$ (01 : 46-01 : 51)	$7.42^{+0.05}_{-0.07}$	$6.49^{+0.10}_{-0.17}$	$7.62^{+0.02}_{-0.03}$	$7.02^{+0.03}_{-0.04}$
		$2T$	–	–	–	–	–	–
		NF	–	–	–	–	–	–
SOL2020-03-11T05:56	12758	$1T$	$6.54^{+0.07}_{-0.10}$ (05 : 44-05 : 52)	$36.8^{+2.46}_{-1.97}$ (05 : 52-05 : 59)	$7.49^{+0.03}_{-0.04}$	$6.50^{+0.08}_{-0.11}$	$7.72^{+0.02}_{-0.02}$	$7.09^{+0.02}_{-0.02}$
		$2T$	$6.58^{+0.08}_{-0.10}$ (05 : 44-05 : 52)	$36.4^{+2.37}_{-2.04}$ (05 : 52-05 : 59)	$7.47^{+0.03}_{-0.04}$	$6.48^{+0.08}_{-0.11}$	$7.71^{+0.02}_{-0.02}$	$7.09^{+0.02}_{-0.02}$
		NF	$2.92^{+0.06}_{-0.04}$	$5.20^{+0.65}_{-0.77}$	$7.91^{+0.05}_{-0.04}$	$7.20^{+0.08}_{-0.08}$	$7.99^{+0.03}_{-0.03}$	–
SOL2020-04-04T00:52	12759	$1T$	$9.06^{+0.08}_{-0.14}$ (00 : 50-00 : 53)	$42.3^{+3.20}_{-2.54}$ (00 : 53-00 : 57)	$7.31^{+0.04}_{-0.05}$	$6.41^{+0.10}_{-0.14}$	$7.55^{+0.02}_{-0.02}$	$7.02^{+0.02}_{-0.02}$
		$2T$	$9.06^{+0.08}_{-0.16}$ (00 : 50-00 : 53)	$41.3^{+3.07}_{-2.65}$ (00 : 53-00 : 57)	$7.26^{+0.05}_{-0.05}$	$6.38^{+0.11}_{-0.15}$	$7.54^{+0.02}_{-0.02}$	$7.02^{+0.02}_{-0.02}$
		NF	$2.99^{+0.04}_{-0.03}$	$8.41^{+0.67}_{-0.94}$	$7.83^{+0.04}_{-0.03}$	$7.11^{+0.07}_{-0.06}$	$7.98^{+0.02}_{-0.02}$	–
SOL2020-04-06T05:48	12759	$1T$	$7.02^{+0.09}_{-0.10}$ (05 : 45-05 : 50)	$32.5^{+2.31}_{-1.98}$ (05 : 50-05 : 56)	$7.48^{+0.03}_{-0.04}$	$6.50^{+0.09}_{-0.11}$	$7.73^{+0.02}_{-0.02}$	$7.13^{+0.02}_{-0.02}$
		$2T$	$7.08^{+0.09}_{-0.10}$ (05 : 45-05 : 50)	$31.5^{+2.17}_{-2.05}$ (05 : 50-05 : 56)	$7.44^{+0.04}_{-0.04}$	$6.45^{+0.10}_{-0.12}$	$7.72^{+0.02}_{-0.02}$	$7.13^{+0.02}_{-0.02}$
		NF	$3.13^{+0.04}_{-0.03}$	$7.21^{+0.55}_{-0.66}$	$7.84^{+0.03}_{-0.03}$	$7.12^{+0.06}_{-0.05}$	$7.97^{+0.02}_{-0.01}$	–
SOL2020-04-06T08:32	12759	$1T$	$7.40^{+0.10}_{-0.15}$ (08 : 30-08 : 34)	$23.0^{+2.88}_{-1.80}$ (08 : 34-08 : 39)	$7.51^{+0.04}_{-0.06}$	$6.37^{+0.13}_{-0.24}$	$7.76^{+0.02}_{-0.03}$	$7.08^{+0.03}_{-0.04}$
		$2T$	$7.66^{+0.15}_{-0.18}$ (08 : 26-08 : 30)	$21.5^{+2.69}_{-1.83}$ (08 : 34-08 : 39)	$7.45^{+0.05}_{-0.06}$	$6.26^{+0.17}_{-0.35}$	$7.75^{+0.02}_{-0.03}$	$7.07^{+0.03}_{-0.04}$
		NF	$3.13^{+0.04}_{-0.03}$	$7.21^{+0.55}_{-0.66}$	$7.84^{+0.03}_{-0.03}$	$7.12^{+0.06}_{-0.05}$	$7.97^{+0.02}_{-0.01}$	–
SOL2020-04-07T01:58	12759	$1T$	$8.08^{+0.05}_{-0.11}$ (01 : 56-02 : 01)	$47.6^{+3.18}_{-2.57}$ (02 : 01-02 : 05)	$7.51^{+0.03}_{-0.04}$	$6.48^{+0.09}_{-0.12}$	$7.71^{+0.02}_{-0.02}$	$7.08^{+0.02}_{-0.02}$
		$2T$	$8.11^{+0.05}_{-0.11}$ (01 : 56-02 : 01)	$47.0^{+3.07}_{-2.64}$ (02 : 01-02 : 05)	$7.49^{+0.03}_{-0.04}$	$6.46^{+0.09}_{-0.12}$	$7.71^{+0.02}_{-0.02}$	$7.08^{+0.02}_{-0.02}$
		NF	$2.89^{+0.04}_{-0.03}$	$7.68^{+0.65}_{-0.80}$	$7.78^{+0.04}_{-0.03}$	$7.01^{+0.08}_{-0.08}$	$7.92^{+0.02}_{-0.02}$	–
SOL2020-04-09T09:32	12759	$1T$	$6.44^{+0.09}_{-0.16}$ (09 : 08-09 : 13)	$28.8^{+1.84}_{-1.78}$ (09 : 36-09 : 47)	$7.46^{+0.03}_{-0.03}$	$6.50^{+0.09}_{-0.10}$	$7.71^{+0.02}_{-0.02}$	$7.12^{+0.02}_{-0.02}$
		$2T$	$6.52^{+0.10}_{-0.16}$ (09 : 08-09 : 13)	$28.1^{+1.79}_{-1.76}$ (09 : 36-09 : 47)	$7.42^{+0.03}_{-0.03}$	$6.46^{+0.09}_{-0.11}$	$7.71^{+0.02}_{-0.02}$	$7.12^{+0.02}_{-0.02}$
		NF	$2.85^{+0.04}_{-0.03}$	$6.71^{+0.67}_{-0.76}$	$7.83^{+0.04}_{-0.03}$	$7.11^{+0.08}_{-0.07}$	$7.91^{+0.02}_{-0.02}$	–
SOL2020-04-30T12:16	12762	$1T$	$7.39^{+0.14}_{-0.18}$ (12 : 15-12 : 18)	$15.5^{+2.14}_{-1.88}$ (12 : 18-12 : 22)	$7.46^{+0.06}_{-0.06}$	$6.44^{+0.15}_{-0.22}$	$7.68^{+0.03}_{-0.03}$	$7.13^{+0.05}_{-0.05}$
		$2T$	$7.69^{+0.17}_{-0.18}$ (12 : 15-12 : 18)	$12.4^{+1.40}_{-1.19}$ (12 : 15-12 : 18)	$7.48^{+0.06}_{-0.07}$	$6.64^{+0.11}_{-0.15}$	$7.67^{+0.03}_{-0.03}$	$7.12^{+0.04}_{-0.04}$
		NF	$3.15^{+0.05}_{-0.03}$	$8.98^{+0.70}_{-1.01}$	$7.84^{+0.04}_{-0.03}$	$7.15^{+0.07}_{-0.05}$	$7.94^{+0.02}_{-0.02}$	–

Table 4.1: Plasma parameters obtained from the spectral analysis. [a]Flare ID correspond to the time at the peak of the flare in the format SOLyyyy-mm-ddThh:mm. [b]Active region number defined by NOAA for the associated flares. [c]Model used for the spectral fitting. $1T$ indicates the single component isothermal model. $2T$ indicates the two component model, where one component represent the flaring plasma emission and other component represent the non-flaring (NF) plasma emission, whose fitted parameters are given in the third row of each flare group. [d]Maximum temperature for the flares and the associated time bin in UT. [e]Maximum emission measure and the associated time bin in UT. [f]Elemental abundances when the emission measure is peaking. Errors represent the 1σ limits associated with the parameters.

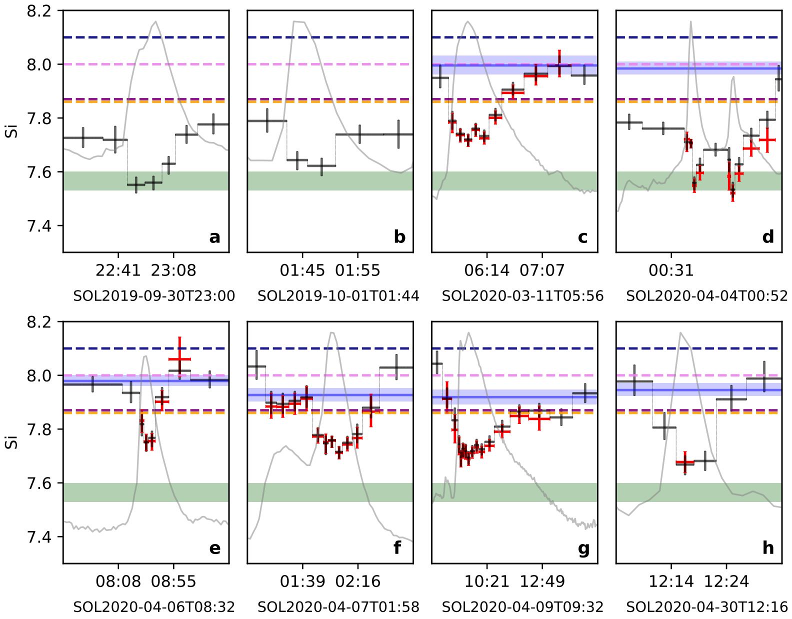

Figure 4.13: Evolution of the absolute Si abundance similar to Figure 4.8e, but for different flares.

of Mg, Al, Si, and S were obtained. We have shown that the abundances of these elements are nearly photospheric during the peak phase, compared to their 3-4 times higher pre-flare values. Beyond the flare peak, the abundances are seen to get enriched again and they recover back to the coronal values at the end of the flare. This suggests that during the flares, the coronal loops are quickly filled with plasma originating from the lower parts of the solar atmosphere without having sufficient time for the usually observed fractionation in non-flaring loops to take place. Our observation of quick recovery to the coronal values show that any process giving rise to such fraction must be occurring on a time scale of few tens of minutes.

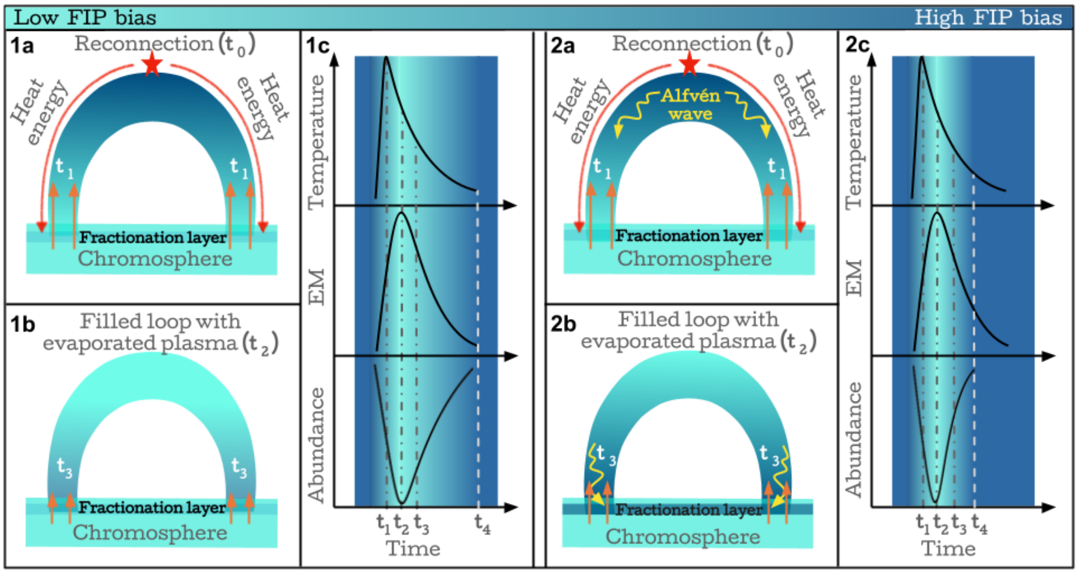

Figure 4.14: Schematic representation of flaring loop dynamics with lighter colors representing low FIP bias, and darker colors indicating high FIP bias. **Scenario 1:** (1a) Impulsive phase – After the flare onset (at time t_0), heat energy travels down to the chromosphere and evaporates the plasma there. The temperature peak is identified at the start (time t_1) of the chromospheric evaporation. During the initial phase, plasma evaporates with high velocity and quickly passes through the fractionation layer without getting fractionated, resulting in depletion of the coronal FIP bias. The Emission Measure (EM) peak is achieved (time t_2) once the loop gets filled with the chromospheric plasma. At around the same time, the abundances of the FIP elements also attain their minima. (1b) Decay phase – The speed of the evaporative upflow slows down significantly allowing plasma enough time in the fractionation layer to get fractionated. The fractionated plasma eventually fills the coronal part of the loop thereby demonstrating the recovery of the coronal FIP bias. (1c) Representative curves of temperature, Emission Measure (EM), and elemental abundance evolution. Time t_4 marks the time of complete recovery of the coronal FIP bias. **Scenario 2:** (2a) At the time of the flare onset (time t_0), high amplitude Alfvén waves are initiated. The released heat energy gets transported to the chromosphere by suprathermal electrons, at speeds faster than the Alfvén waves. Evaporation starts at time t_1, and reduces the coronal FIP bias. The temperature peak is observed around this time. (2b) The EM peak and abundance minima are achieved when the loop is filled with the evaporated plasma (t_2). Once the flare-driven Alfvén waves arrive at the chromosphere (time t_3), they rapidly fractionate the plasma. These Alfvén waves also carry significant heat from the flaring site to assist the evaporation. The fractionated plasma is then transported to the coronal part of the loop through evaporative upflows, which help in rapidly recovering the coronal FIP bias. (2c) Representative curves of Temperature, EM, and elemental abundances for the second scenario.

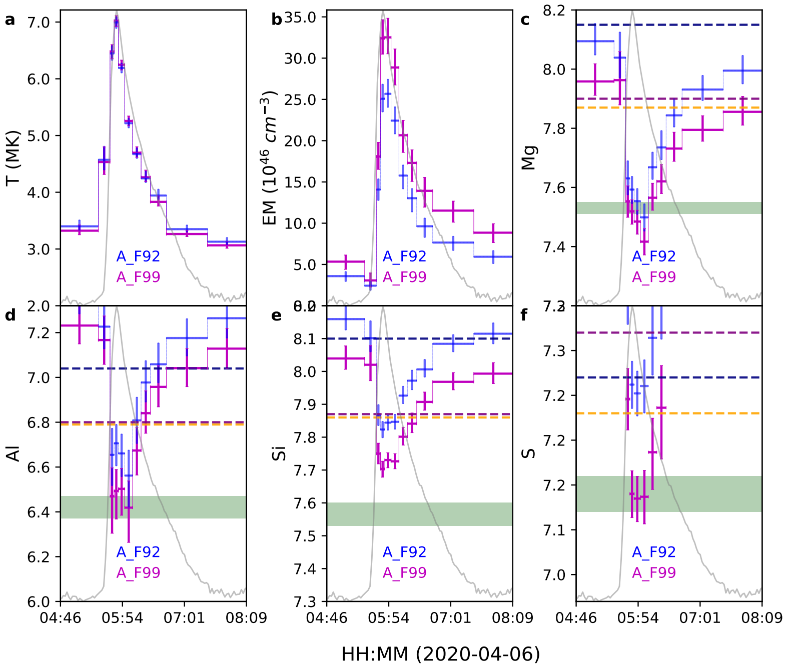

Figure 4.15: The six panels show the results of the time resolved X-ray spectral fitting using a single component model for the flare SOL2020-04-06T05:48. The blue points with error bars show the fitted parameters by taking a fixed abundance parameter from A_F92 and the magenta points with error bars show the same by using abundances values from A_F99.

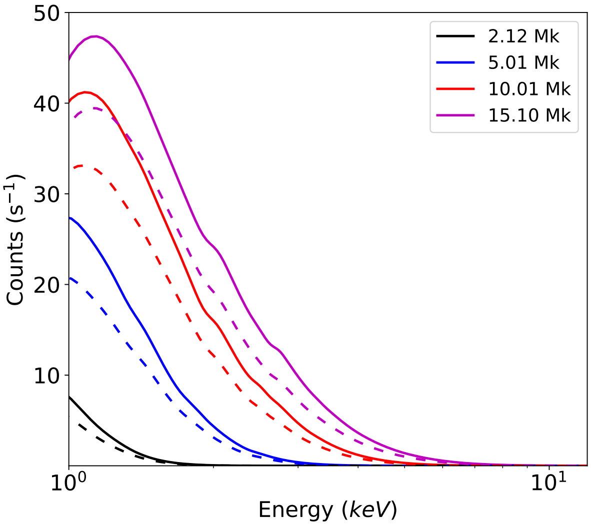

Figure 4.16: The continuum spectrum at different temperature with a fixed emission measure of 2.0e47 cm^{-3} by using the elemental abundances from A_F92 (solid lines) and A_F99 (dashed lines).

Chapter 5

Insight into heating of XBPs

The small-scale impulsive events, commonly referred to as nanoflares, are thought to be one of the prime candidates that can keep the solar corona hot at its multi-million Kelvin temperature. Individual nanoflares are difficult to be detected with the current generation instruments, however, their presence can be inferred through some indirect techniques such as Differential Emission Measure (DEM) analysis (see Chapter 2.5). Here we employ this technique to investigate the possibility of nanoflare heating of quiet corona during the minimum of solar cycle 24. This was the deepest minima in last hundred years and there were extended periods without presence of any active regions (AR). In the absence of conventional active regions, X-ray bright points (XBP) are the dominant contributor of the disk integrated X-rays. We estimate the DEM of the XBPs using observations from the XSM and AIA. We attempt to differentiate the X-ray emission from the XBPs from that of the total coronal X-ray emission, and compare it with the predicted DEM of XBPs assuming these are heated by nanoflares. The XBPs are found to be associated with bipolar magnetic fields and consist of small-scale loops. We simulate such XBP loops using the EBTEL++ hydrodynamic code (see Chapter 2.6). The lengths and magnetic field strengths of these loops are obtained through potential field extrapolation of the corresponding photospheric magnetogram. Each loop is assumed to be heated by random nanoflares having energy that depends on the loop properties. The composite frequency distribution for all the loops has a power-law slope close to 2.5. The simulation output is then used to obtain the integrated DEM. It agrees remarkably well with the observed DEM at temperatures above 1 MK, suggesting that the nanoflares distribution as predicted by our model can explain the XBPs heating.

5.1 Introduction

Understanding the mechanism/mechanisms that heats the solar corona to several orders of magnitude, higher than the surface temperature ($\approx$ 6000K) remains a long-standing problem in Astrophysics. It is well accepted that the magnetic field lines protruding out of the photosphere play a crucial role in heating the corona. The footpoints of the magnetic fields are randomly moved by the convective motions below the photosphere, causing either building up the magnetic stress within the fields quasi-statically or generating waves depending on the time sale of motion (Klimchuk, 2006). Dissipation of magnetic stress is known as DC heating whereas the dissipation of waves is known as AC heating (see Chapter 1.2). Most of the models explaining coronal heating suggest that the heating is impulsive in nature (Klimchuk, 2006). Klimchuk (2015) defines the small-scale impulsive events as nanoflares irrespective of underlying physical mechanism. The occurrence frequency of these nanoflares determines whether they can provide sufficient energy required for the total heating. Thus it is of great importance to investigate the likely frequency of nanoflares to validate the impulsive heating models.

Due to the line-of-sight averaging and other effects (e.g., the capability of the present generation instruments, the efficiency of thermal conduction, and the non-equilibrium ionization (Bradshaw & Cargill, 2006; Reale & Orlando, 2008)), the direct observations of the nanoflares are difficult. Instead of their direct observable signature several indirect method are used to infer their existence, e.g., 'Intensity Fluctuations' (Katsukawa & Tsuneta, 2001; Sakamoto et al., 2008), 'Time Lags' (Viall & Klimchuk, 2012, 2013, 2015; Bradshaw & Viall, 2016), 'differential emission measure' (DEM) or the 'emission measure distribution' (EMD). The DEM gives an estimation of the amount of plasma present at different temperatures and the integration of DEM over-temperature bins provides the EMD (see Chapter 2.5).

The DEM technique has been extensively used by many observational studies to interpret the heating of quiescent active region core in terms of heating frequencies (e.g., Tripathi et al. (2011); Winebarger et al. (2011); Del Zanna et al. (2015); Brosius et al. (2014); Caspi et al. (2015); Ishikawa et al. (2017)). However, the estimation of DEM to study the quiet Sun heating is very sparse in the literature. Earlier studies of the quiet Sun DEM (Lanzafame et al., 2005; Brooks et al., 2009; Del Zanna, 2019) show a peak at lower temperature of around 1 MK. Determining the quiet Sun DEM at higher temperatures (>2 MK) is difficult due to the faint emission at these temperatures (Del Zanna & Mason, 2018).

In the present study, we derive the quiet Sun DEM using the Sun as a star observation during the minimum of solar cycle 24. Here, the quiet Sun includes, the quiet diffuse regions (defined as QDR), so-called diffuse corona emitting in the temperature $\sim$ 1 MK; cool coronal holes which mostly emit at a lower temperature ($<$ 1 MK); the X-ray emitting regions (XER), which are the origin of most of the X-ray emission including the limb brightening and X-ray bright points (XBP). We use the combined observation in soft X-rays and Extreme Ultraviolet (EUV) energy bands by XSM (Chapter 2.3.2) and AIA (Chapter 2.4.3). The XSM observations during the minimum of solar cycle 24 are used earlier to study the quiet solar corona by assuming an isothermal assumption (see Chapter 3 or Vadawale et al. (2021a)). Comparing the X-ray images of the Sun by the XRT Be-thin filter, whose higher energy response is similar to the XSM lower energy response, Vadawale et al. (2021a) infer that a large fraction ($>$ 50%) of the quiet Sun X-ray emission arises from the X-ray Bright Points (XBP). They derived the isothermal temperature, emission measure, and elemental abundances for XBPs. In the present study, we have extracted the contribution of XER and then XBPs to the total quiet Sun emission to estimate their DEM separately. We quantify the emission from the XER and XBPs to the total X-ray emission.

XBPs consist of small-scale rapidly evolving coronal loops (Madjarska, 2019). Using the Enthalpy-bashed Thermal Evolution of Loop (EBTEL: Chapter 2.6) model, we simulate the XBP loops. Estimating the length-average evolution of the plasma temperature and density within the loops, we derive the composite DEM, which is compared with the observation.

The frequency distribution of the impulsive events, so-called nanoflares for which the simulated DEM of XBPs matches with the observation, is further compared with the frequency distribution of the microflares as observed by XSM, (Vadawale et al., 2021b) in the quiet Sun. These microflares have energies $\sim 3 \times 10^{26} - 6 \times 10^{27}$ erg, and most of them are found to associate with XBPs.

The rest of the chapter is organized as follows; In Section 5.2 the observation and the data analysis of the XSM and AIA are presented. In Section 5.3 the detailed method of the combined DEM analysis and results are described. Description of the XBPs simulation setup and results are given in Section 5.4. Finally, we discuss and summarize the primary findings of the work in Section 5.5.

5.2 Observations and Data Analysis

We use the X-ray observation of the Sun by XSM. During September 2019 to May 2020 period of XSM observations, there were 76 days when no active regions (AR) were present on the solar disk (Chapter 3.2), known as the quiet-Sun (QS) period. Comparing with the X-ray full disk images taken by XRT/Hinode, it was found that most of the X-rays observed by XSM during the QS periods come from the X-ray Bright Points (XBP) and the limb brightening. In the present study two representative intervals are selected from the QS duration on September 20, 2019 (00:07 UTC - 01:49 UTC, defined as QS-1) and September 16, 2019, (20:00 UTC - 22:00 UTC, defined as QS-2). Following the standard analysis procedure described in Chapter 3, we generate the XSM observed flux light curves in the energy range of 1-8Å for the full days of QS-1 and QS-2 as shown in Figure 5.1a,b. The orange shaded color marks the duration of QS-1 and QS-2.

Since the main objective of the present study is to estimate the DEM/EMD for the QS period, it is necessary to include EUV observations along with X-ray observations. Thus, we combine the EUV observation from AIA. AIA records the continuous full-disk images of the Sun in different EUV energy channels (94 Å, 131 Å, 171 Å, 193 Å, 211 Å, 304 Å, 355 Å) with a cadence of 12s. During the QS-1 and QS-2 periods, the level-1 AIA full-disk images in all of its pass-bands are downloaded from Joint Science Operations Center (JSOC) and processed to level-1.5 using the standard routines available in the SolarSoft (SSW; Freeland & Handy (1998)). A representative full-disk image frame of the AIA 94 Å channel during the QS-1 period is shown in Figure 5.1c.

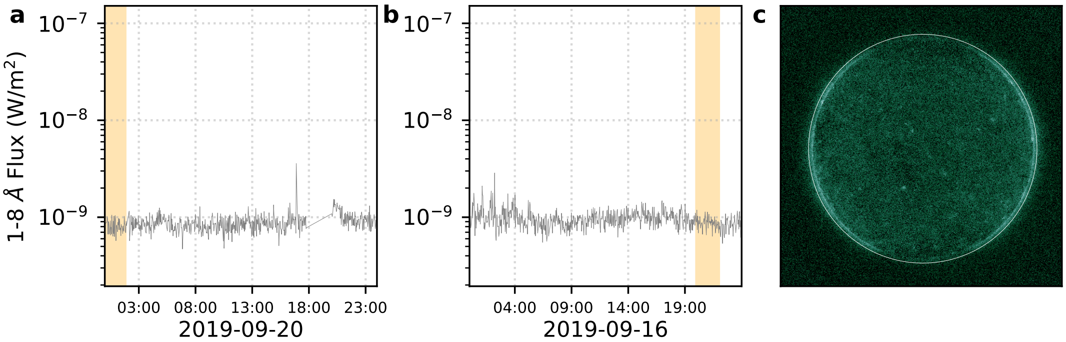

Figure 5.1: Panels **a** and **b** shows the 1-8 Å light curve of the Sun observed by XSM during Sep 20 and Sep 16 2019. The orange shaded region represents the duration of QS-1 and QS-2 as mentioned in the text. Panel **c** show a representative full disk image of the Sun during QS 1 taken by AIA 94 Å channel.

5.3 Combined DEM Analysis

The DEM or EMD gives an indication of the amount of plasma that is emitting the radiation observed, and has a temperature between T and T+dT (Del Zanna & Mason, 2018). To estimate the DEM we use the simultaneous observation at several EUV and X-ray energy bands, sensitive to different temperatures. We use the five EUV channels of AIA, 94 Å, 131 Å, 171 Å, 193 Å, and 211 Å that are sensitive to temperatures more that $logT = 5.6$. We exclude the channel 335 Å due to a long-term drop in sensitivity resulting from accumulated contamination (Boerner et al., 2014; Athiray et al., 2020). For each AIA channel, we consider the integrated intensity of all the positive finite pixels below a solar radius of 1.04 $R_{\odot}$ (white circle in Figure 5.1c), from where most of the emissions are coming in all the energies. We have verified that the final results remain unaffected even if we consider the pixels within a larger radius or even the full AIA Field-Of-View (FOV). For the X-ray observation, we divide the XSM spectrum into four energy channels of 1.29-1.45 keV, 1.45-1.75 keV, 1.72-1.95 keV, and 1.95-2.5 keV. Each bin is considered over an energy range, where the spectrum contains a line complex of particular element/elements ($Mg, Mg + Al, Si$, and $Si + S$) with good statistics. Thus we obtain the observed intensity in a total of nine instrument channels, five channels from AIA, and four channels from XSM.

The Observed intensity (O_i) at i'th instrument channels is related by the DEM as follows:

$$O_i = \int_T DEM(T)\, R_i(T)\, dT \; + \; \delta O_i \tag{5.1}$$

Here, δO_i is the uncertainty associated with O_i, and $R_i(T)$ is the temperature response function of the i'th channel. A temperature response represents the sensitivity of an instrument channel to detect the plasma emission at different temperatures. Details of the XSM and AIA temperature response functions for the present analysis is described in the next section.

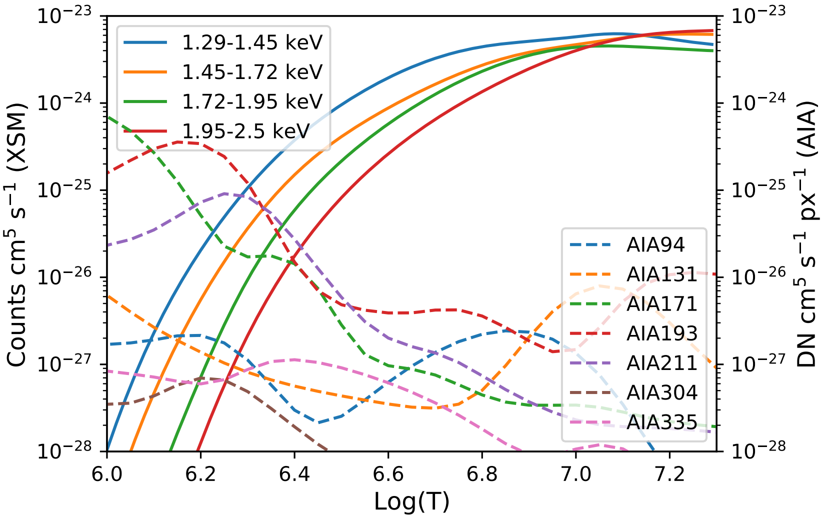

Figure 5.2: Temperature response functions for XSM (solid lines in unit Counts cm^5 s^{-1}), AIA (dashed lines in unit DN cm^5 s$^-1$ px$^-1$)

Figure 5.2 shows the temperature response functions for all AIA (dashed lines) channels along with the four XSM channels (solid lines). The detailed method to obtain the temperature response functions of XSM is described in Chapter 2.3.4. The temperature response functions for the AIA EUV channels are obtained using the standard routine *aia_get_response.pro* available within the SSW by adopting the latest calibrations, which incorporate the time-dependent corrections in the effective area. We use the same quiet Sun abundances, reported in Chapter 3 (or in Vadawale et al. (2021a)) with CHIANTI version 10, to derive both the XSM and AIA temperature response functions. From Figure 5.2, it is seen that the XSM temperature sensitivity starts to increase above 2 MK, whereas the AIA sensitivity starts dropping at those temperatures. Furthermore, XSM also shows a good overlap in the temperature sensitivity with the AIA. Thus, the combined DEM derived by XSM and AIA allows constraining both low and high-temperature emissions.

5.3.1 Full Sun DEM ($DEM_{FullSun}$)

We know the observed intensities (O_i) and temperature response functions for all the energy channels. Thus, deriving the DEM from Eq. 5.1 is a forward-fitting problem (see Chapter 2.5.2). We use the *xrt_dem_iterative2.pro* (Golub et al., 2004b) method (define *xrt_dem*) for the DEM recovery. Which is a forward-fitting routine to find the DEM solution from Eq. 5.1 by considering a spline function for the DEM curve. This routine is a standard tool-set for solar data analysis in the SolarSoftWare (SSW; Freeland & Handy (1998)) package. The best-fit DEM is identified iteratively using a nonlinear least-square method by comparing the predicted and observed fluxes. This method has been widely used in DEM fitting with SDO/AIA, Hinode/XRT, Hinode/EUV Imaging Spectrometer (EIS), and FOXI data (e.g., Golub et al. (2007); Winebarger et al. (2011); Ishikawa et al. (2017); Wright et al. (2017); Athiray et al. (2020)). Here, we consider a temperature range of $5.9 \leq \log T \leq 6.8$ with a bin size of $\delta \log T = 0.03$ for the DEM estimation. The uncertainties in the recovered DEM are estimated through the Monte-Carlo (MC) runs, which are performed by varying the observed intensities randomly within the observed errors. The errors with the AIA observed counts at each channel are estimated using the standard procedure, *aia_bp_estimate.pro* (Boerner et al., 2012). Uncertainties in the XSM observation primarily contain the Poisons error associated with the counting statistics and small systematic errors at each spectral channel provided by the XSM data processing software. To estimate the uncertainties in the recovered DEM solution, we perform a large set (500000) of MC runs over the observed counts. Among all the MC samples, we ignore the spurious DEM solutions, e,g., selecting the DEM solutions that can describe the observed flux at all channels with a reduced-chi square of less than equal to 2. The histogram of the DEMs at each temperature node is derived using the accepted DEM solutions. From the peak of the DEM histogram at each temperature node, we estimate the one-sigma uncertainties.

The full-Sun DEM (defined as $DEM_{FullSun}$) and the 1-sigma error bars are shown in Figure 5.3a for QS-1 (red) and QS-2 (blue). The solid line represents the peak of the DEM histogram at each temperature node. We derive the EMD (units of cm^{-3}) from DEM (units of cm^{-5}k^{-1}) by multiplying the DEM with $(area \times T\delta logT)$. Derived EMD for QS-1 and QS-2 are shown in Figure 5.3c. Dividing the observed counts with the temperature response function associated with each channel gives the Emission-measure loci curves, which indicate the upper limit of the EMD. The Emission-measure loci curves for the QS-1 (red curves) and QS-2 (blue curves) at the five AIA channels (left side) and four XSM channels (right side) are overplotted.

Note that, here we assume an integrated emission from the AIA images which includes the emission from the quiet region, XBPs, and the limb emission. However, from the full disk X-ray images (e.g., XRT/Hinode Be-thin filter images) one can see that the X-ray emission from the quiet region is very very faint compared with the XBPs and limb emissions. Thus, in the next step we identify the X-ray Emitting Regions (XER) from the AIA full-disk images as discussed in Section 5.3.2 and then combined the intensity of XER from AIA images with the XSM observation to estimate the combined DEM of XER, as discussed in Section 5.3.3.

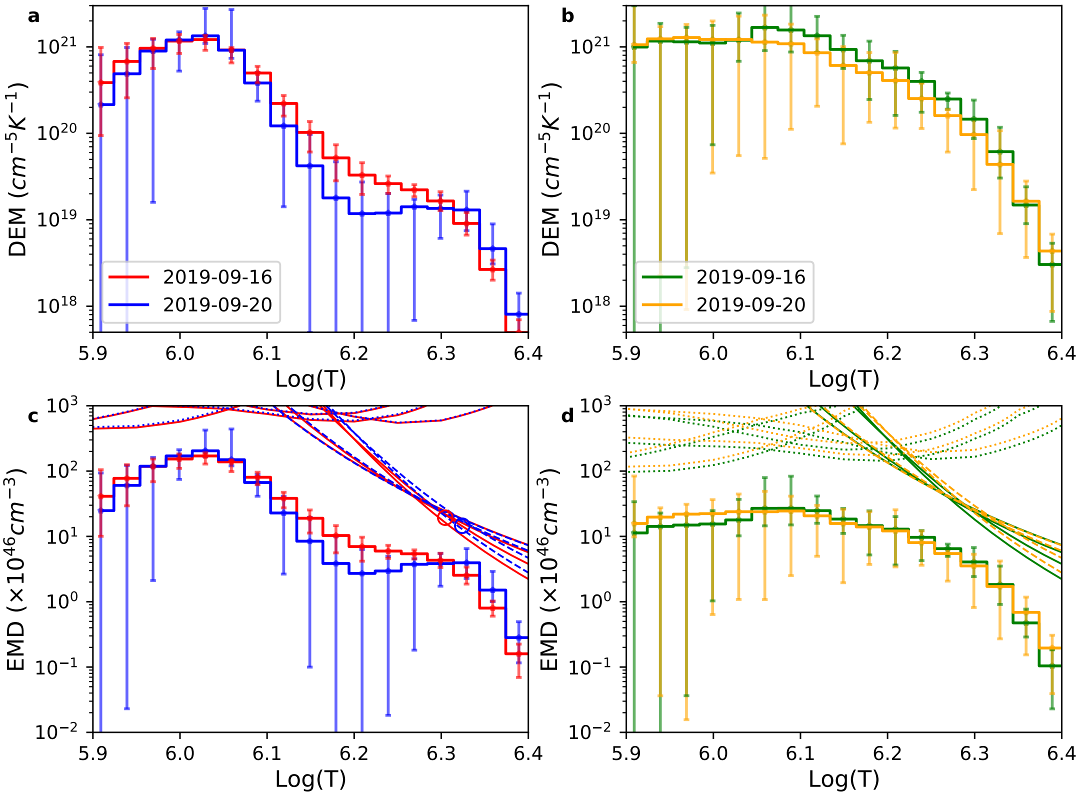

Figure 5.3: Panels **a** and **c** shows the full Sun DEM and EMD profile for QS-1 (red) and QS-2 (blue). Panels b and d shows the DEM and EMD for the XERs associated with QS-1 and QS-2. The EM loci curves for AIA (dashed lines) and XSM (solid lines) are overplotted in Panels **c** and **d**. The red and blue circular points in Panel **c** represent the isothermal temperature and EM for the XER as reported by Vadawale et al. (2021a)

5.3.2 Identification of XER in AIA EUV images

In the full-disk X-ray and EUV images of the Sun, the XER are found to be bright compared with the surrounding quiet Sun emission. Thus, the XER emission can be separated out using a source detection technique. In this study, we have used the astronomical source detection algorithm, "*Photutils*" (Bradley et al., 2021) over the full-disk image of AIA 193 Å channel to estimate the typical emitting regions of the XER. *Photutils* is a Python library that provides tools to detect astronomical sources using image segmentation. The detected sources must have a minimum number of adjacent pixels, each of them greater than a given threshold value in an image. Usually, the threshold value is determined by a multiplication factor of the background noise (sigma). In our case, we have estimated the background noise of the quiet Sun emission in AIA 193 Å images using the "*detect_threshold*" method of the Photutils and defined a threshold level of two times the background noise. We apply a 2D circular Gaussian kernel with a Full-Width-Half-Maximum (FWHM) of three pixels to smooth the image prior to applying the threshold. Using the "*detect_sources*" method of the Photutils we find out all the distinct sources that have a minimum of five connected pixels. A mask frame of the same dimension as the original image is prepared by considering all the detected source pixels values as one and the rest are set to zero. The convolution of the mask frame with the original image give us the mask image, which provides the typical contribution of the XER. The same mask frame is used in all the AIA channels to find out the XER contribution in the respective pass-band.

Figure 5.4a,d shows a representative full-disk solar image and a zoomed view of the same image on 20-09-2019, taken by the AIA 193 Å channel. The bright regions represent the emission from XER. Figure 5.4b,e shows the masked images of the original images (Figure 5.4a,d) produced by the convolution of the original image with the mask frame. The comparison of the masked images with the X-ray full disk images taken by the XRT Be-Thin filter, primarily gives the contribution of the XER, as shown in Figure 5.4c,f. We find that the masked images (e.g., Figure 5.4e) are well-matched with the observed X-ray images (Figure 5.4f), except for some negligible portions here and there.

5.3.3 DEM of XER (DEM_{XER})

Knowing the integrated emission from the XER in AIA images (Section 5.3.2) and along with the X-ray emission detected by XSM, we derive the DEM of X-ray emitting regions (say DEM_{XER}) in a similar method as the full-Sun DEM (Section 5.3.1). Figure 5.3b and Figure 5.3d show the DEM and EMD of the XER during QS-1 (green) and QS-2 (orange). The EM-loci curves for all AIA channels (left) and XSM channels (right) are also shown in Figure 5.3d. Comparing the EMD of full Sun (Figure 5.3c) and for XER (Figure 5.3d), we can say that the higher temperature ($>$ 1.5 MK) portion of both the EMD is very similar. At lower temperatures, where the EMD is primarily determined by the AIA the full

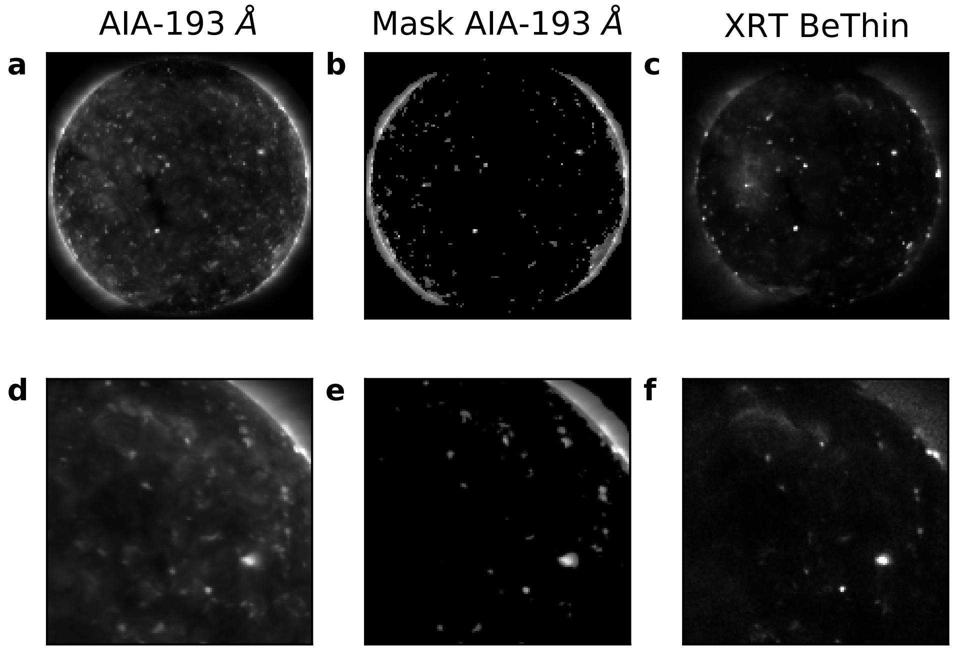

Figure 5.4: Full disk images of the Sun during QS-1 taken by AIA 193Å channel (Panel **a**) and XRT Be thin filter (Panel **c**). Panel **c** show the XERs extracted from the AIA 193Å image. Panels shown in the bottom row represent a portion of the solar disk shown in the above panels.

Sun EMD shows an excess emission.

5.3.4 Reliability of Recovered DEMs

To verify the reliability of the recovered DEM/EMD as discussed in Sections 5.3.1 and 5.3.3, we estimate the predicted counts in all channels and the XSM spectra by using the recovered DEM and then compare them with the observed intensities and XSM spectra. The top panel of Figure 5.5a shows the observed (points with error bars) and predicted (box points) intensities (same color as Figures 5.3) at all the instrument channels using the DEM shown in Figure 5.3. The bottom panel indicates the delta-chi ((Observed-Predicted) / Error) between the observed and predicted intensities. The predicted intensities for all the recovered DEM are matches with the observed intensities within their error bars.

Further, we forward-model the XSM spectra using the recovered EMD of both the full Sun (blue and red solid lines correspond to QS-1 and QS-2) and XER (orange and green solid lines correspond to QS-1 and QS-2), as shown by solid lines in Figure 5.5b. For comparison, the observed XSM spectra during QS-1 (green error bars) and QS-2 (orange error bars) are overplotted. The modeled spectra derive from the EMDs are well agreed with the observed one. As XSM is sensitive to the higher temperature, the excess emission at a lower temperature of full-Sun EMD (Figure 5.3c) is not contributing much to the modeled XSM spectra and thus the full-Sun EMD could explain the observed XSM spectra, similar to the X-ray emitting regions EMD. This verifies that most of the emission observed by XSM primarily originates from X-ray emitting regions.

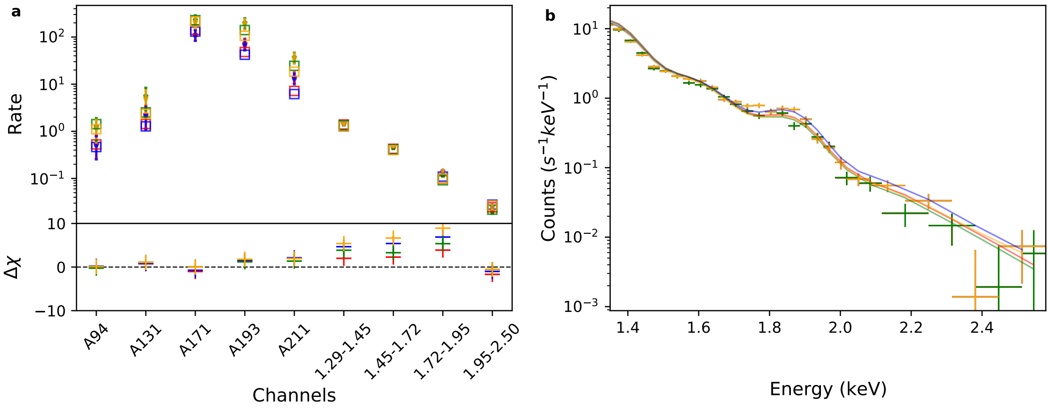

Figure 5.5: Panel **a** represent the observed intensities of QS-1 and QS-2 measured by the different channels of AIA and XSM and the square boxes represent the predicted intensities using the DEM shown in Figure 5.3. The below panel shows the delta-chi between the observed and predicted intensities. The error bars in Panel **b** shows the observed XSM spectra of QS-1 and QS-2. The solid lines represent the predicted XSM spectra using the DEM shown in Figure 5.3.

5.3.5 DEM of XBPs (DEM_{XBP})

The DEM of XER is contributed by the XBPs and the limb brightening. Though the limb seems to be very bright in the full-disk images (Figure 5.4; specifically in AIA energy bands), it is well known that the limb emission primarily comes from the cool plasma of a huge volume. Thus it is expected that the limb emissions contribute to the lower temperature of the DEM, whereas the high-temperature emission is primarily contributed by the XBPs. However, in our recovered DEM we found that at lower temperatures the error bars are very large and we could not predict DEM at very low temperatures, e.g., logT < 5.9. This is due to the fact that at those temperatures the emissions are very faint and hence noisy, which could not be recovered by the *xrt_dem* method. This uncertainty has been demonstrated nicely by Hannah & Kontar (2012) for a set of simulated data of AR, quiet Sun for different AIA channels.

Using a regularized inversion (see Chapter 2.5.3) to solve Equation 5.1, Hannah & Kontar (2012) gave a different approach to estimate the DEM from the observed intensity of different instrument channels. The major advantage of this method is that it determines the errors of estimated DEM along with the uncertainty in temperature intervals. In the next step, we apply Hannah & Kontar (2012) method* (define as *HC_dem*) to recover the DEM for our case.

Using the *HC_dem* method we have recovered the DEM_{XER} of QS-1 up to a lower temperature of log(T) = 5.6 as shown by black error bars in Figure 5.6a. Though, this method provides very similar results at higher temperatures (> 1MK) as we get from the *xrt_dem* method (shown by grey error bars), at lower temperatures it provides a very large error in the log(T) resolution, which could underestimate the lower temperature DEM in a similar way demonstrated by Hannah & Kontar (2012).

Our objective here is to extract the DEM of XBPs (define as DEM_{XBP}) located within an area of $1000'' \times 1000''$ (say F_v) at disk center. This could be very straightforward if we know the counts detected by the XSM only from the XBPs located inside the F_v. But, most of the emission detected by XSM is from both XBPs from the whole disk and from the limb. However, roughly, we can estimate the XSM detected intensity of the XBPs inside F_v by degrading the XSM counts by a factor f. In the first step, we estimate the factor f as the ratio of the number of XBPs inside F_v and that of the whole disk. In this way we are overestimating the XSM counts for the XBPs inside F_v, by ignoring the limb emission and hence we are getting a spurious solution of DEM_{XBPs}. In the next step, we have estimated the factor f as the ratio of the area of XBPs inside F_v and the area of total XER. In this case, we are getting a reasonable solution of the DEM_{XBP}. Blue error bars in Figure 5.6a show the estimated DEM_{XBP} and this DEM predicted the observed intensities very well (Figure 5.6b). The

---

*https://github.com/ianan/demreg/tree/master/python

DEM_{XBP} differs from the DEM of total XER only at lower temperatures (<1 MK), which is expected as at lower temperatures the limb emission contributes to the total DEM.

A more sophisticated verification of the limb emission is done by estimating the typical DEM of the limb (say DEM_{limb}) emission using the different channels of AIA along with the XRT filter images. We select a small portion of the limb and then estimated the counts in AIA EUV channels along with the XRT '$Al-mesh$', '$Al-poly$', '$Be-thin$' filters. Using a 20% uncertainty with the observed intensity along with a calibration factor of 2 (Athiray et al., 2020) for XRT, we estimated the DEM_{limb}. The recovered DEM for the limb is shown in orange color in Figure 5.6. This also indicates that the limb is only contributing at a lower temperature.

It should be noted that at temperatures below 1 MK, there may be some uncertainty in determination of f, and hence in DEM_XBPs, however, at temperature above 1 MK the estimated DEM_XBPs is quite robust, as the contribution of the limb emission at these temperature is negligible. Thus it can be safely assumed that the DEM_XBPs shown in Figure 5.6 represents the 'average' DEM for the XBPs.

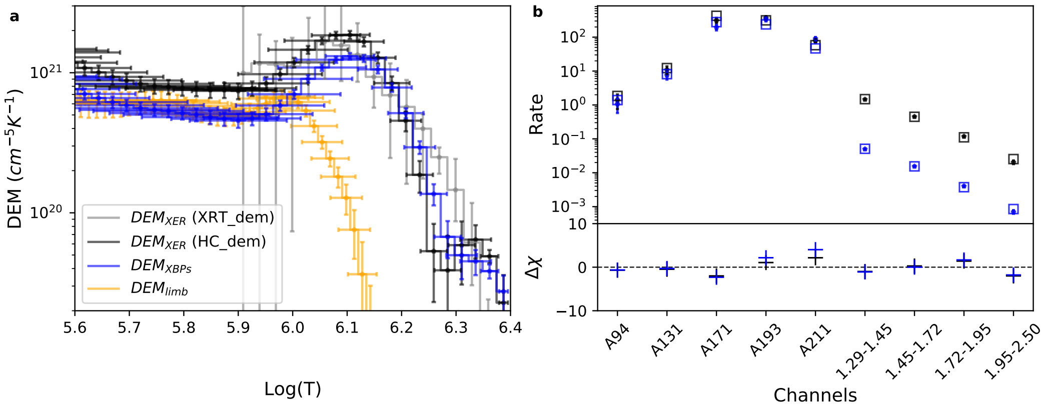

Figure 5.6: Panel **a** shows the observed DEM of XER (black), XBPs (blue), and limb (orange) derived by HC_dem method. The DEM of XER derived by XRT_dem method is overplotted by grey color. Panel **b** shows the observed (error bars) and predicted counts at different instrument channels.

5.4 Hydrodynamic Simulations of XBPs emission

To investigate the energy requirement for XBPs to maintain the observed DEM (DEM_{XBP}), we carry out hydrodynamic simulations. XBPs are found to be associated with bipolar magnetic field regions, similar to the active regions, and consist of independent, rapidly evolving small-scale loops (Madjarska, 2019). It is thus natural to assume that the hot emission of XBPs is associated with the confined plasma within the small-scale magnetic loop systems, termed a magnetic skeleton. Field-aligned hydrodynamic models are often used to estimate the evolution of the plasma confined within the coronal loops (e.g., Nita et al. (2018)). One such model is Enthalpy-bashed Thermal Evolution of Loops model (see Chapter 2.6). EBTEL is a zero-dimensional (0D) time-dependent hydrodynamic model that can accurately estimate the time evolution of the spatially averaged coronal temperature, density, and pressure of a single coronal loop heated by an assumed heating profile (time-dependent heating rate). Along with the average coronal properties of the loop, EBTEL estimates the DEMs of the transition region and coronal portion of the loop separately at each time step. In this work we have used the two-fluid version of EBTEL, called as EBTEL++, where the ions and electrons are treated separately (Chapter 2.6).

Using the high resolution full-disk photospheric magnetic field measurements from the Helioseismic and Magnetic Imager (HMI: Scherrer et al. (2012)) onboard the SDO, we have extrapolated the magnetic field lines and produced the magnetic “skeletons” associated with the XBPs as discussed in Section 5.4.1, which provides us the loop lengths and magnetic field strength of the loops. We have heated these magnetic skeletons by heating profiles, depending on the loop length and the magnetic field strength of the loops as discussed in Section 5.4.2 and provided them as an input to EBTEL.

5.4.1 Magnetic skeleton of XBPs

We are interested in modeling all the XBPs emissions near the disk center within an area of 1000″ × 1000″ (defined as F_v in Section 5.3.5). Using the location of all the XBPs within F_v (Section 5.3.2) we identified their counterpart on the full-disk line-of-sight (LOS) HMI magnetogram and finds that all of them are associated with magnetic bipolar regions. Considering these bipolar regions as a lower boundary, we extrapolate their field lines up to a height of 200 HMI pixels (72 Mm). For this purpose, we use the Linear Force-Free Extrapolation code, $j\_b\_lff.pro$ (Nakagawa & Raadu, 1972; Seehafer, 1978), available within the SSW by setting the force-free parameter $\alpha = 0$. Using the three-dimensional extrapolated magnetic fields data, we trace field lines through the volume surrounded by individual XBP following the streamline tracing method.

We assume that each traced field line corresponds to a coronal loop, and the loop has a constant radius (r) of 1 Mm throughout the height. The number of loops associated with an XBP, forming the magnetic skeleton is estimated by equating the total cross-sectional area of all the loops (considering both the foot-points) with the estimated area of the XBP from AIA images; e.g., if the area of i^{th} XBP is A_i, which consist with N_i number of loops then;

$$N_i = \frac{A_i}{2\pi r^2} \tag{5.2}$$

Using the coordinates (x_k, y_k, z_k) and magnetic field strength (B_{x_k}, B_{y_k}, B_{z_k}) of each of the loop along their length, we derive their length (L) and average magnetic field ($< B >$) strength along the loop, as follows:

$$L = \sum_k \sqrt{((x_{k+1} - x_k)^2 + (y_{k+1} - y_i)^2 + (z_{k+1} - z_k)^2)} \tag{5.3}$$

$$< B >= \frac{\sum_k \sqrt{B_{x_k}^2 + B_{y_k}^2 + B_{z_k}^2} \times dl_k}{\sum_k dl_k} \tag{5.4}$$

Figure 5.7a shows the AIA 193Å image of one of the XBP and the corresponding HMI magnetogram is shown in Figure 5.7b. A set of (plane of sky projection) extrapolated field lines (blue lines) are overplotted in the same figure and the 3D view of the field lines or magnetic skeleton is shown in panel c. A qualitative comparison between the extrapolated field lines and the brightening visible in the AIA image reveals that the field extrapolation and line tracing adequately capture the geometry of the XBP.

We find the existence of 25 XBPs inside the chosen area, F_v. For each of these XBP, we extrapolate the magnetic field lines and estimate the loop lengths and magnetic field strengths. Figure 5.7d shows the distribution of all the loop lengths associated with all the XBPs and Figure 5.7e shows the distribution of their average magnetic field strength ($< B >$) along the loop length. The loop length distribution is found to peaking at near 30 Mm. The average magnetic field is found to inversely vary with loop length. The $< B > \propto L^{-1}$ relation is overplotted by a black solid line as a reference.

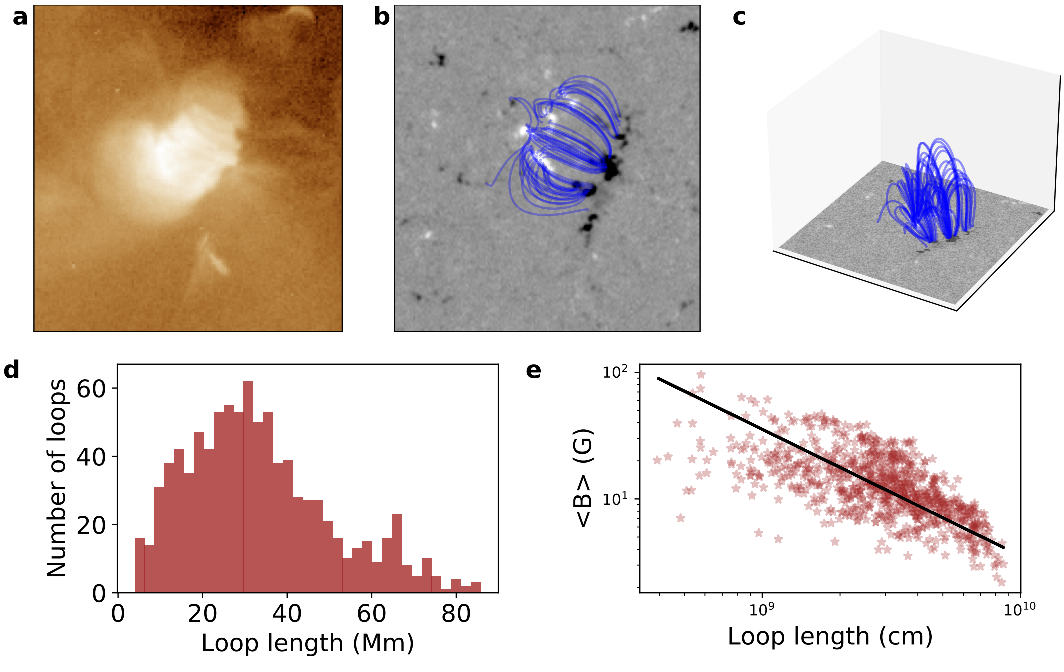

Figure 5.7: Panel **a** shows the representative image of an XBP as observed by AIA 193Å channel. Panel **b** shows the HMI magnetogram associated with the XBP and the blue curves are the plane-of-sky projected extrapolated field lines. A 3D view of the extrapolated field lines are shown in Panel **c**. Panel d and **e** shows the distribution of the loop lengths and magnetic field strength for all the loops associated with all the XBPs.

5.4.2 Heating function

Once we extrapolated the magnetic skeleton of the XBPs, the loops need to be filled with thermal plasma and to be deposited a volumetric heat (in a unit of erg cm^{-3} s^{-1}) with sufficient amount and frequency in the form of a heating function to maintained the coronal temperature. W assume that the heating function has two parts – the impulsive heating by the transient events and the other is steady background heating. The steady background heating is chosen such that, it can maintain a background temperature of nearly 5.0×10^5 K in all the loops. The required heating to maintain the background temperature is estimated by using the scaling law (Aschwanden, 2004),

$$H_{bkg}[ergcm^{-3}s^{-1}] \simeq \frac{2}{7}\left(\frac{10}{9}\right)^{\frac{7}{2}} k_0 \frac{\bar{T}^{\frac{7}{2}}}{L^2} \tag{5.5}$$

Here, k_0=8.12×10^{-7} in cgs, $\bar{T}$ is the average temperature (in our case 5.0×10^5 K) of the coronal part of the loop, which is related with the loop top temperature (T$_a$) as, $\bar{T} \approx 0.9T_a$ (Cargill et al., 2012).

Following Parker (1988) and Klimchuk (2015), an impulsive event can occur with the release of stored magnetic energy within the loop due to the magnetic stress produced by the photospheric driver. The total energy corresponding to an event should be in the range of minimum and maximum magnetic free energy that a loop can store in the process of the misalignment of the field from the vertical. If the misalignment angle is θ, then the free energy density associated with the loop will be,

$$H = \frac{(tan(\theta) < B >)^2}{8\pi}(erg\, cm^{-3}) \tag{5.6}$$

For the coronal energy loss the critical value of θ (known as Parker angle) for which the energy must release, lies within 10^0-20^0 (Parker, 1988; Klimchuk, 2015) and hence the critical value of $tan(\theta) = c$ should be in the range of $0.2 - 0.3$.

In this study, we define the impulsive heating function in terms of a series of symmetric triangular heating profiles having a duration (τ) of 100s (e.g., Klimchuk et al. (2008); Cargill et al. (2012); Barnes et al. (2016)). The heating rate (H_0) for each event is randomly chosen between the minimum (H_0^{min}) and maximum (H_0^{max}) value of the heating rate associated with a loop. H_0^{max} is estimated using Equation 5.6, e.g., for j^{th} loop of i^{th} XBP it will be,

$$H_{0_{ij}}^{max} = \frac{1}{\tau} \frac{(c < B >_{ij})^2}{8\pi} (erg\, cm^{-3}\, s^{-1}) \tag{5.7}$$

whereas H_0^{min} is considered to be $0.01 \times H_0^{max}$.

As the free energy associated with a stressed loop is being released during an impulsive event, naturally, releasing a larger amount of energy causes a larger delay in storing enough energy that can be released during the next impulsive event. Taking into account this important consequence, we assume that the delay time between the two consecutive events is proportional to the energy of 1st event, i.e., the delay time between $(l-1)^{th}$ and l^{th} event will be,

$$d_{ij}^{l} = q \times H_{ij}^{l-1} \tag{5.8}$$

The value of the proportionality constant, q is estimated by equating the average Poynting flux ($< F >$ in units of erg cm^{-2} s^{-1}) associated with a loop with the average energy released by the impulsive events. This makes the above equation in the form:

$$d_{ij}^{l} = \frac{\tau L}{< F >} \times H_{ij}^{l-1} \tag{5.9}$$

In the present study, we estimate $< F >$ by two different methods – In the first case, considering that all the loops associated with all the XBPs have the same average Poynting flux (called as $Constant - F$ model), which is calculated from the observed DEM_{XBP}, as discussed in Section 5.4.2.1. In the second case, we considered that each loop has different $< F >$, estimated from the Poynting flux going to the corona due to the foot-point motions of the loops (called as $Variable - F$ model) as discussed in Section 5.4.2.2.

5.4.2.1 Constant Poynting flux (Constant−F model)

The total radiation loss ($\mathcal{R}$) from the solar atmosphere can be estimated using the observed line-of-sight EMD (in the unit of cm^{-5}) and radiation loss function

($\Lambda(T)$) as follows:

$$\mathcal{R} = \sum_i EMD(T_i)\,\Lambda(T_i) \tag{5.10}$$

Using the radiation loss function adopted in the EBTEL (Klimchuk et al., 2008) and the observed EMD of the XBPs, we find the average radiation loss for XBPs is 1.95×10^5 erg cm^{-2} s^{-1}.

Since the corona is also cooled by thermal conduction, the actual Poynting flux is usually 2-3 times more than the total radiation losses. Thus, the average Poynting flux to each loop is,

$$< F >= g \times 1.95 \times 10^5 \; (erg\, cm^{-2}\, s^{-1}) \tag{5.11}$$

Here, g is a constant in the range of 2 to 3.

Deriving the heating profile by combining Equations 5.6, 5.9, and 5.11 (Constant−F model) has four variable parameters; L, $< B >$, $c = tan(\theta)$, and g. Figure 5.8a (blue line) shows the heating profile for a loop of L =30 Mm, $< B >$=10 G, $g = 2.0$, and $c = 0.25$. The L and B are derived from the magnetic modeling of the photospheric magnetogram (Section 5.4.1) while the exact values of c and g are unknown. However, we know their expected range for the coronal loops as summarized in the first row of Table 5.1. We have varied the values of c and g within their expected range to match the observation as discussed in Section 5.4.3. Figure 5.8b shows the distribution of the heating events associated with the loop distribution of XBPs (Figure 5.7d) for the combination of c =0.2, 0.3 and g =2.0, 3.0.

Model	$c = \tan(\theta)$	g	V_h(Km/s)
$Constant - F$	0.2-0.3	2-3	–
$Variable - F$	0.2-0.3	–	0.5-2.0

Table 5.1: Variable parameters and their expected range for the Constant−F and Variable−F models.

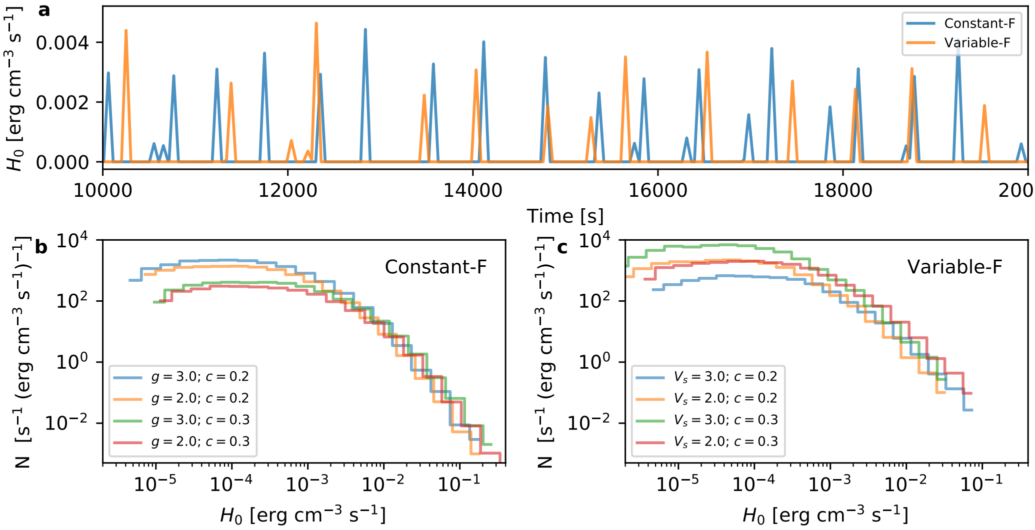

Figure 5.8: Panel **a** shows the representative heating function for a typical loop derived by using Constant−F and Variable−F models. Panel **b** and **c** shows the heating frequency distribution of the events for Constant−F and Variable−F models respectively.

5.4.2.2 Variable Poynting flux (Variable−F model)

Instead of considering the constant average Poynting flux in all the loops, typical average Poynting flux associated with an individual loop can be estimated as follows: Due to the work done by the photospheric driver, the upward average Poynting flux associated with the loop is (Klimchuk, 2015),

$$< F >= -\frac{1}{4\pi} V_h \tan(\theta) \; (< B >)^2 \tag{5.12}$$

Here V_h is the horizontal velocity of the photospheric driver. The less β (β is the ratio of the gas pressure to magnetic pressure) nature of the coronal plasma makes the coronal loops expand in the corona compared with their base. Including the effect of the loop expansion, the average Poynting flux in the coronal portion of the loop can be estimated by combining Equation 5.12 with the conservation of Poynting flux and magnetic flux throughout the loop. Then, the average Poynting flux through the coronal portion of the j^{th} loop of i^{th} XBP is;

$$< F >_{ij}= -\frac{1}{4\pi} V_h \tan(\theta) \; B_{ij}^{base} < B >_{ij} \tag{5.13}$$

Here, B_{base} is the magnetic field at the coronal base (or top of the transition region). We consider that the coronal base is located at around 2 Mm height from the photosphere and thus we estimate the field strength of all the XBP loops at around 2 Mm height. Hence, deriving the heating profile by combining Equations 5.6, 5.9, and 5.13 (Variable−F model) has five variable parameters; L, $< B >$, B^{base}, $c = tan(\theta)$ and V_h. Figure 5.8a (orange color) shows the derived heating profile for a loop of L =30 Mm, $< B >$=10 G, B^{base} =15 G, V_h = 1 Km/s, c =0.25. Values of L, $< B >$ and $< B^{base} >$ are estimated from the magnetic modeling of the loops, whereas the exact values of V_h and c are unknown. However, the expected range for these two variables is known and summarized in the second row of Table 5.1. For an example, Figure 5.8c shows the distribution of the heating events corresponding to the loop distribution of XBPs (Figure 5.7d) for a combination of V_s =0.5, 1.5 and c =0.2, 0.3. This distribution is found to vary slightly according to the values of V_h, and c and thus, we have varied the values of V_s and c within their expected range to match the observation as discussed in Section 5.4.3.

5.4.3 Simulated DEM

Once the loop lengths and heating profile for all the loops associated with all the XBPs are available, we run the EBTEL for individual loops in a parallel computing environment of a machine on 32 cores. Thus, in the simulation setup the EBTEL is called multiple times associated with the different loops. We simulate the evolution of the loops for the duration of 20000s. The estimated DEM of the transition region and coronal portion of the loops are stored for the last 7200s of simulation time, similar to the observed DEM exposure time. Combining the DEM of all the loops, we estimate the composite simulated DEM for all the XBPs.

The simulation setup is ran multiple times by varying the input parameters within their expected range (Table 5.1) for both Constant−F (Section 5.4.2.1) and Variable−F (Section 5.4.2.2) models. We estimate the composite simulated DEM for each run and compare it with the observed DEM

(DEM_{XBP}). The input parameters for which the simulated DEM well describes the observed DEM are summarized in Table 5.2 and plotted in Figure 5.9 (brown and blue colors). The transition region and coronal portion of the simulated DEM are shown by dotted and dashed lines, respectively, whereas solid lines show the total DEMs. Though both the model can predict the emission at a higher temperature (logT > 6.0) close to the observed emission, at lower temperature (logT < 6.0) both of them predict ∼2 to 5 times higher emission. This low-temperature emission primarily comes from the transition region of the loops, which is poorly constrained by the AIA channels, as indicated by the larger error bars in the observed DEM. Thus the recovered DEM at low temperature can underpredict the actual emission as demonstrated by Hannah et al. (2008). To verify this scenario, we have predicted the AIA and XSM intensities from the simulated DEMs of the transition region and corona and recovered their DEMs using the *HC_dem* method (Section 5.3.5) by considering a typical 20% uncertainty in the simulated intensities. We find that the recovered coronal emission from the simulated intensities (logT>6.0 in Figure 5.10) matches well with the observed DEM. However, the recovered transition region DEM (logT<6.0) still shows a 2 to 3 times higher emission than the observed DEM. Thus the deviation of the simulated and observed DEMs at a lower temperature is not only because of the observational uncertainty; rather, it indicates that the simulated transition region predicts a larger emission than the observed one – details possible explanations for this deviation are given in Section 5.5.

Model	$c = \tan(\theta)$	g	V_h(Km/s)
$Constant - F$	0.21	2.47	–
$Variable - F$	0.21	–	1.5

Table 5.2: Best Suited parameters for the Constant−F and Variable−F models.

5.4.4 Frequency distribution of impulsive events

Figure 5.11a shows the frequency distribution of the impulsive events heating rate for the model parameters (Table 5.2) for which the simulated DEM matches the observed one. This distribution at higher heating rates (H_0) is close to a

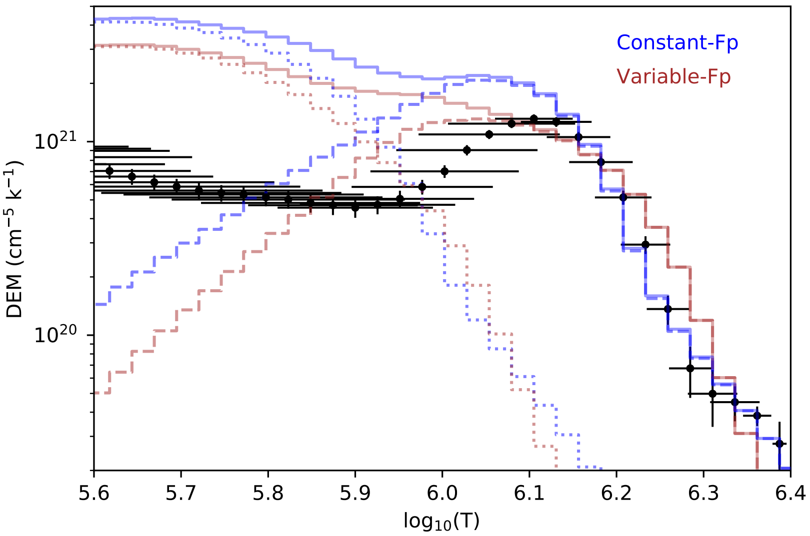

Figure 5.9: Observed DEM (black errorbars) and simulated DEMs using Constant−F (blue color) and Variable−F model (brown color). The contribution of the transition regions and coronal DEMs to the total simulated DEM (solid lines) are shown separately by dotted and dashed lines.

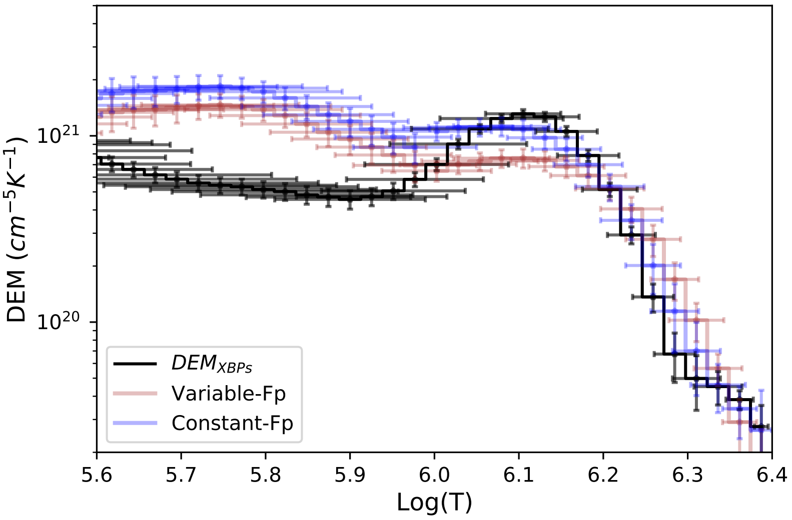

Figure 5.10: Observed DEM of XBPs (black) compared with the recovered DEM obtain from the simulated AIA and XSM intensities from the simulated DEM shown in Figure 5.9

power-law distribution of slope 2.5 indicated by a reference line in grey color. We convert the heating rate distribution (blue dashed line in Figure 5.11a) with their energy distribution by multiplying the event duration and volume of the loops. The energy distribution for the Constant−F model is shown by the blue dashed line in Figure 5.11b, which is compared with the frequency distribution of the quiet Sun microflares as observed by XSM (Vadawale et al., 2021b). During the minimum of solar cycle 24, these microflares are found to occur everywhere on the Sun outside the conventional AR and most of them are associated with the XBPs. A comprehensive discussion on this is given in Section 5.5.

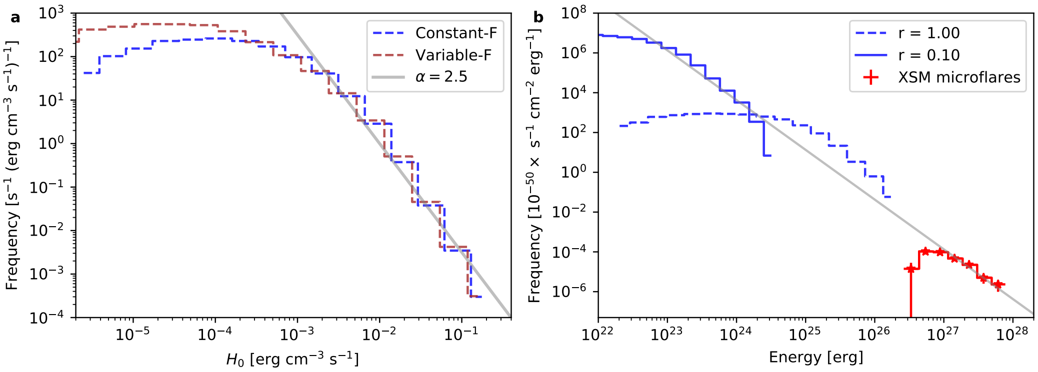

Figure 5.11: Panel **a**: Heating frequency distribution of Constant−F (blue) and Variable−F (brown) models. Grey line represent a comparison powerlaw with a slope of 2.5. Panel **b**: Energy distribution of the events for Constant−F model derived from the heating frequency shown in panel **a**. The dashed and solid blue lines represent the energy distribution estimated by considering the a a constant loop radius of 1 Mm and 0.1 Mm respectively. The grey solid line represent the power law function of slope 2.5, which intersects with the XSM observed microflare frequency distribution at higher energies.

5.5 Discussion and Summary

In the present work, we utilize the full disk observation of the Sun using the AIA and XSM to derive the DEM of the disk-integrated Sun ($DEM_{FullSun}$), X-ray emitting region (DEM_{XER}), and X-ray bright points (DEM_{XBP}) during the minimum of solar cycle 24. Our analysis suggests that in the absence of ARs, XBPs are the primary contributor to the overall X-ray emission of the global Sun. We model the observed DEM of XBPs by hydrodynamic loop simulations. The simulated DEM is then compared with the observed one. The primary findings of this paper are summarized below.

Emission from QuietSun, XER, and XBPs : The disk integrated DEM ($DEM_{FullSun}$; Figure 5.3a) shows a lower temperature (∼1 MK) peak along with an extended faint (approximately 2-3 order of magnitude less than the peak around 1 Mk) emission in the temperature range of 6.1<log(T)<6.4. The peak is likely to be dominated by the emission from the cool quiet regions (so-called diffuse corona) occupied in most of the solar disk. This peak emission is similar to the earlier observation of the quiet Sun DEM (e.g., Lanzafame et al. (2005); Brooks et al. (2009); Del Zanna (2019); Sylwester et al. (2019)). The emission measure loci curves above the EMD profile (Figure 5.3c) indicates that the high temperature (logT $>$ 6.1) emission is primarily constrained by the X-ray emitting regions (XER), observed by XSM. For further verification of it, we have derived the DEM of XER.

Extracting the X-ray emitting regions from the full-disk AIA images (Section 5.3.2) and combining them with the X-ray observation of XSM, we have derived the DEM of XER (DEM_{XER}; Figure 5.3b). The comparison of the EMD of the full Sun (Figure 5.3c) to that of the XER (Figure 5.3d) show that the higher temperature component of both the distribution is identical. This suggest that the higher temperature component in $DEM_{FullSun}$ is originated in the XER.

In the absence of any ARs, the XER are consists with X-ray bright points as well as the limb emission. Though the DEM_{XER} shows a broad distribution from below 1 MK to 2.5 Mk, it is well known that the limb brightening primarily comes from a huge volume of low-temperature plasma (typically $<$ 1 MK). To distinguish the XBPs emission we have derived the DEM for the XBPs (DEM_{XBP}) present at the center of the solar disk (Figure 5.6a, blue color) by estimating a typical XSM intensity from the chosen XBPs (Section 5.3.3). Both the DEM_{XER} (black color) and DEM_{XBP} (blue color) show a similar emission at a higher temperature above log(T) $>$ 6.1, where the XBPs are known to be primary sources of X-rays. At lower temperatures, the DEM_{XER} shows higher emission than DEM_{XBP}, which could be due to the contribution of the limb brightening in DEM_{XER}. To verify it further, a typical DEM of the limb is derived from the intensity of a small limb area selected from the full disk images taken by AIA and XRT (orange color). Limb DEM shows a significant emission at lower temperatures of log(T) $<$ 6.1.

To quantify the emission from the quiet regions, XER, and XBPs we have estimated the radiative flux from the estimated DEMs and radiative loss function (Klimchuk et al., 2008) as described in Equation 5.10. Radiative fluxes are estimated in two temperature ranges; one is in the low-temperature emission ($\mathcal{R}$(5.6≤ logT≤ 6.1)) and another is in the high temperature emission ($\mathcal{R}$(6.1≤ logT≤ 6.4)) as summarized in Table 5.3. The radiation flux of full Sun, dominated by the quiet regions is $\sim$0.9×10^5 erg cm^{-2} s^{-1}, which is close to the average radiation flux from quiet Sun (10^5 erg cm^{-2} s^{-1} Withbroe & Noyes (1977)). At higher temperatures (logT > 6.1) the full Sun radiation is almost an order of magnitude lesser. Radiation from the XBPs over the radiation from XER is found to be more than 63% for the lower temperature (logT<6.1) range and more than 85% at the higher temperature (log(T)>6.1) range. Thus at the higher temperature, most of the X-ray emissions observed by XSM originated from the XBPs.

DEM used	$\mathcal{R}(5.6 \leq logT \leq 6.1)$ (erg cm^{-2} s^{-1})	$\mathcal{R}(6.1 \leq logT \leq 6.4)$ (erg cm^{-2} s^{-1})
$DEM_{FullSun}$	0.78×10^5	0.09×10^5
DEM_{XER}	1.69×10^5	1.01×10^5
DEM_{XBP}	1.08×10^5	0.87×10^5

Table 5.3: Measured radiation flux from average quiet Sun ($DEM_{FullSun}$), XER (DEM_{XER}), and XBPs (DEM_{XBPs}).

The X-ray emission from the XERs during QS-1 and QS-2 was modeled using isothermal temperature and EM byVadawale et al. (2021a) The isothermal temperature (T) and emission measure (EM) reported by Vadawale et al. (2021a) are shown in Figure 5.3c by red and blue circular points. The isothermal T and EM are found to lie close to the intersection of the emission-measure loci curves of XSM, which indicated that the isothermal modeling provided the upper limit of the EM.

Simulation of XBPs loops : Like active regions, XBPs consist of small-scale coronal loops (Madjarska, 2019). XBPs are found to be associated with bipolar regions (e.g., Figure 5.7b) on the photospheric magnetogram. Potential field extrapolation of these magnetogram (Section 5.4.1) provides the loop structures (e.g., Figure 5.7a,b,c) along with their length and magnetic field strength. The composite distribution of loop lengths associated with all the XBPs (Figure 5.7d) shows a peak of around 30 Mm, which is much smaller than the typical loop length of the active region (order of 10^2 Mm). The average field strength (Figure 5.7e) of the loops is found to be inversely proportional to their length by a slope (δ) close to -1 (black solid line in Figure 5.7e), which is similar to the slope derived for the ARs loops (Mandrini et al., 2000).

In this study using the observational constraint on the loop parameters, we have simulated the XBPs loop by the hydrodynamic EBTEL model (Section 5.4). The loops are heated impulsively by a heating profile derived from the loop parameters and the average Poynting flux associated with the loop (Section 5.8). The average Poynting flux associated with each loop is derived in two ways; the Constant−F model (Section 5.4.2.1) and Variable−F (Section 5.4.2.2) model. Each of these models is associated with two unknown parameters (c, g or c, V_h) as summarized in Table 5.1. Varying these unknown parameters within their expected range obtained from earlier studies, we have predicted the composite DEM of XBPs from the simulation and compared it with the observed one. The input parameters, for which the predicted DEM matches with the observation are found to lie within their expected range, as summarized in Table 5.3. The Parker angle (θ) is found to $\sim 12^0$, which is close to the typical value of 10^0 for active region (Klimchuk, 2006). As the loops loose their energy by both conduction and radiation and the total loss is known to be $g = 2$ to $g = 3$ times the radiation flux, the obtained value of $g = 2.5$ is very reasonable. In addition, the horizontal motion of the footpoints is found to be ∼1.5 Km/s, which is close to the observable range.

Observed and Simulated DEM : Figure 5.9 shows the comparison between observed and simulated DEMs. The DEM obtained by the Constant−F model (blue line) is found to well explain the observed DEM (black error bars) at higher temperatures (log(T)>6.1), where most of the emission comees from the corona (dashed blue line). However, the DEM predicted by the Variable−F model (brown line) show a slight deviation from the observed DEM at a higher temperature range (log(T)>6.1), which could be due to the uncertainty of measuring the Poynting flux from Equation 5.13 (see Section 5.4.2.2 for details) by assuming the coronal base at a height of 2 Mm.

Simulated DEM shows a two to five times higher emission at lower temperatures. A possibility of its could be the observed DEM is underestimated due to the instrumental sensitivity. To verify it, we have derived the AIA and XSM intensity using the transition region and coronal DEM obtain from the model and derived the DEM if observed by AIA and XSM (Figure 5.10). The reconstructed model DEMs also show a two to three times higher emission for the transition region at a lower temperature (logT $<$ 6.0). Prediction of higher emission from the transition region is not a surprising result, it has been seen in earlier coronal loop models as well and its true origin of it is yet to be known. One of the possible explanations for it is the absorption of the transition region emission by the chromospheric jets (e.g., spicules) at similar heights having cold chromospheric plasma. This has been found to cause a decrease in the transition region emission by a factor of 2-3 (De Pontieu et al., 2009).

$Frequency\ distribution\ of\ impulsive\ events$: The composite frequency distribution of the impulsive heating (Figure 5.11a) rates (H_0) is very similar to a power-law at higher values of H_0 ($> 10^{-3}$ erg cm^{-3} s^{-1}), whereas at lower H_0 it became flat. The flattening at lower energy indicates the lack of very small loops with larger field strength. A comparison power-law of slope 2.5 is overplotted by grey color. A power-law slope of more than 2 indicates that the small scale impulsive events or nanoflares are the dominant source of the heating (Parker, 1988) over the larger flares, e.g., quiet Sun microflares which occurs occasionally with an average frequency of ∼1.8/days (Vadawale et al., 2021b).

Multiplying the volume of the loops, we estimate the energy distribution of the events as shown by the dashed blue line in Figure 5.11b. This distribution shows a higher normalization factor than the quiet Sun microflare frequency distribution (red points) as observed by XSM (Vadawale et al., 2021b). The normalization factor for the nanoflare distribution is dependent on the number of loops used in the simulation which is further dependent on the radius of the loops (Equation 5.2). In our study we have used a constant radius of 1 Mm for all the loops and it is found that the simulated DEM is independent of loops radius unless uses an extreme values comparable of the size of XBP. Instead of 1 Mm using a loop radius of 0.1 Mm, the nanoflare distribution (blue solid line) is found to match with the extrapolated regions of the observed microflare distribution.

Estimating the DEM and hence the radiation flux from quiet corona, X-ray emitting regions, and XBPs, we found most of the quiet or diffuse corona emits at lower temperatures (logT < 6.1). Whereas most of the emission above logT=6.1 originates from XBPs. Modeling the XBPs DEM indicates that the XBPs heating is maintained by the small-scale nanoflares originated by the release of stored magnetic energy within the stressed magnetic loops. To understand the details heating mechanism, further observational and modeling effort is required by considering the various other scenarios of the coronal heating (see Table 3 of Mandrini et al. (2000)). In addition, a spatially resolved spectroscopic observation with an instrument that can have both low and high-temperature diagnostic capability is very essential to understand the heating of individual XBP or the individual loops. In follow-up works, we will attempt to study some of these issues in detail.

Chapter 6

Exploring imaging X-ray spectroscopy of the Sun - development of X-ray mirrors

So far in this thesis, we have studied the coronal plasma using the Sun as a star observations during the minimum of solar cycle 24. However, the extended X-ray emission of the Sun, which is highly dynamic throughout space and time, demands an imaging spectroscopic observation to probe the spatial variation of the plasma parameters. An imaging spectroscopic instrument primarily consists of two components – A front-end X-ray optics and a detector module. Realizing the X-ray optics is challenging due to the energetic nature of the X-ray photons. It is feasible by reflecting the X-rays using X-ray mirrors of defined geometry and specifications. Recently, we have initiated the development of X-ray mirrors. Along with the development of the X-ray mirrors, appropriate software tools are required to design such mirrors and their characterization with X-ray reflectivity measurements. In this context, we have developed a program, DarpanX, to calculate X-ray reflectivity for different types of X-ray mirrors. In this chapter, along with the development of the X-ray mirror in our lab, we present details of DarpanX implementation and its validation for different types of X-ray mirror structures. A part of this Chapter is directly adopted from Mondal et al. (2021a).

6.1 Introduction

Using the disk-integrated X-ray spectroscopic observation of the solar corona, we have studied the coronal plasma in Chapter 3, 4, and 5. However, the extended and dynamic X-ray emissions of the corona demands an spatially resolved observation to study the variation of the plasma properties at different regions. For example, Figure 6.1 demonstrates the different activity of the Sun in X-rays as observed by the Be-thin filter of XRT/Hinode. Panel *a* represent the X-ray image during the minimum period of the solar cycle 24 when no ARs were present on the solar disk, and most of the X-rays are dominated by the small XBPs. During these periods, using the disk-integrated X-ray spectroscopic observation of XSM, we have studied the average plasma parameters of XBPs as discussed in Chapter 3.3. However, to study the regions outside the small XBPs (e.g., white box in panel *a*) or the variation of the plasma parameters in different XBP, a spatially resolved spectroscopic observation is needed. The disk-integrated observations of XSM has also been used to study the integrated plasma emission of an AR (see Chapter 3.4) located on the solar disk without any other major activity (e.g., Figure 3.4 or Figure 6.1b). But, it is well known that the X-ray emission is highly dynamic throughout the AR (e.g., the single AR present in Figure 6.1b is zoomed-in and shown at the bottom). Thus, to study the variation of the plasma parameters throughout a single AR requires a spatially resolved spectroscopic observation. Another complexity in disk-integrated observation comes when the Sun becomes more active, and more than one AR or activity is present simultaneously on the solar disk (e.g., Figure 6.1c). In this case, the X-ray emission is mixed up from the different AR/activity, which demands imaging spectroscopic measurements to study the individual source of X-ray emission.

An imaging spectroscopic instrument requires an X-ray optics that relies on the X-ray reflection from X-ray mirrors of defined geometry. At X-ray wavelengths, the refractive indices of all materials are close to unity, restricting the reflectivities to a very small grazing incidence angle. Hence, it is a common practice to employ small grazing incident angles to design X-ray reflecting systems. Several optical designs, such as K-B optics (Kirkpatrick & Baez, 1948),

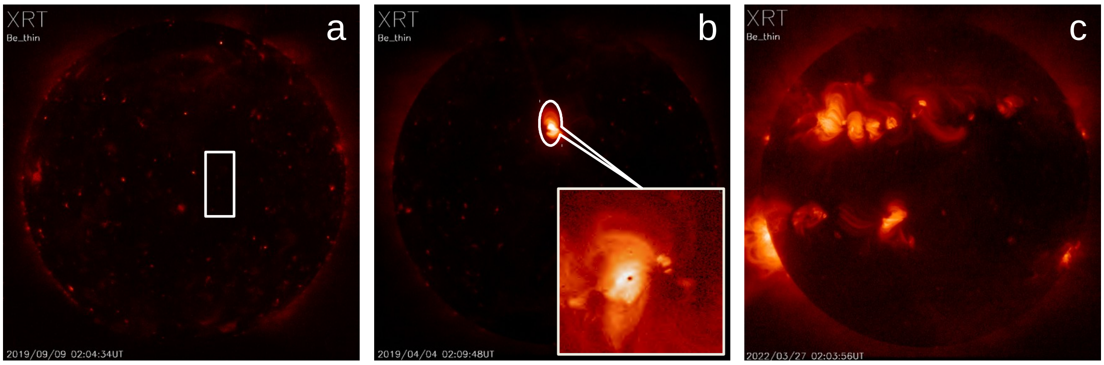

Figure 6.1: X-ray images of the Sun at its different activity. These images are observed by the Be-thin filter of XRT/Hinode.

Wolter type I, II, III (Wolter, 1975), etc. are developed for such grazing incidence applications. The critical angle for total X-ray reflection is inversely proportional to the energy of the incident X-rays (see Section 6.2 and Equation 6.6). The reflection of higher energy X-rays requires a shallower critical angle that increases the focal length of the optics.

Another approach to achieving reasonable X-ray reflectivity for incidence angles greater than the critical angle is to develop multilayer mirrors (see Section 6.2.2). A multilayer mirror consists of a large number of alternate thin film layers of high-Z and low-Z materials deposited on a highly polished substrate. The operational principle of multilayer mirrors is similar to Bragg's crystal. When X-rays are incident at an angle greater than the critical angle, a small fraction of the wave is reflected from the top layer, and the rest of the wave is transmitted. The transmitted wave gets divided into transmitting and reflecting components at each layer interface. The reflected components then get added up constructively, resulting in enhanced reflectivity. If the thickness of the alternative bilayers is constant, the enhancement in reflectivity is usually limited to a narrow energy band satisfying the Bragg condition. However, by varying the thickness of the alternate high-Z and low-Z material in a controlled manner (Joensen et al., 1993; Joensen et al., 1995; Seely et al., 1996; Tawara et al., 1998), it is possible to achieve broadband reflectivity for relatively larger incidence angles. With the advancement in thin-film fabrication technology, a variety of multilayer mirrors can be fabricated to reflect X-rays (Windt et al., 2003; Windt, 2015).

In India, we have initiated the development of X-ray optics for future X-ray astronomy mission and have established a multilayer mirror coating facility based on Magnetron Sputtering technique at Physical Research Laboratory (PRL), Ahmedabad. In this context, we have developed a program “DarpanX” (‘Darpan’ means mirror in Sanskrit) to aid the design of an X-ray mirrors as well as their characterization by using X-ray reflectivity (XRR) data.

While the process for X-ray reflection from a mirror is governed by Bragg’s law, the overall reflectivity of the mirror prominently depends on the surface micro-roughness, inter-layer roughness, interdiffusion at the interfaces, layer density, thickness, and uniformity of all layers. Precise knowledge of these parameters is essential for the accurate modeling of X-ray reflectivity. Traditional microscopic and optical interferometric techniques give information about the top surface roughness and uniformity. Hence, they cannot be used to model the mirror properties and performance completely. Transmission electron microscopy (TEM) gives information about the interlayer roughness and thickness, but it is not useful to probe the surface uniformity. TEM is also a destructive technique; hence it is not suitable to test the final product. XRR is a non-destructive technique that provides information about the thickness of all layers, interlayer roughness, and diffusion, the density of thin films, etc. This relatively inexpensive technique can also be performed at multiple energies to understand the energy-dependent physical properties of the X-ray mirrors.

In order to estimate the parameters of multilayer mirrors from XRR measurements, it is necessary to have an efficient algorithm that calculates the X-ray reflectivity as a function for a given set of parameters and geometry. There are a few software programs such as IMD (Windt, 1998), PPM (Pythonic Program for Multilayers) (Spiga et al., 2004, 2006), GenXBjörck & Andersson (2007), Motofit (Nelson, 2006), Reflex (Vignaud & Gibaud, 2019), etc. that are available to perform this task. Most of these are available as standalone programs with a graphical user interface. Particularly the IMD software is widely used in the design and characterization of X-ray mirrors for astronomical applications. Our main objective in developing DarpanX is to implement the X-ray reflectivity calculation as a model compatible with the standard X-ray astronomical fitting software such as XSPEC (Arnaud et al., 1999) and ISIS (Houck et al., 2013). Particularly, the XSPEC software is widely used and has advanced fitting methods such as genetic algorithms and Markov Chain Monte Carlo (MCMC) for finding global minima and thus can be efficiently used to measure various parameters of the multilayer mirrors with the DarpanX. Further, the time required for fitting can be reduced by exploiting the parallel processing capabilities of XSPEC or that of DarpanX. DarpanX can also be used as a stand-alone tool for the design of multilayer mirrors with the flexibility to design any type of multilayer structure.

This chapter is organized as follows: Section 6.2 describes the basics of the X-ray reflection technique using the X-ray mirrors. After discussion of the fabrication of the X-ray mirrors in Section 6.3, the testing of the fabricated mirrors using the X-ray reflectivity measurement is provided in Section 6.4. Section 6.5 provides a brief description of DarpanX algorithm, implementations, and the validation of algorithms by the comparison of the DarpanX results with IMD. Section 6.6 describes the experimental validation of DarpanX by using XRR measurements of single-layer (W and Si) and multilayer (W/B_4C) samples and Section 6.7 summarizes the chapter.

6.2 X-ray reflection

In electromagnetic theory, a plane wave (initial amplitude, $\mathbf{E_0}$ and wavelength λ_0) propagating through a medium in the x-direction can be represented as,

$$\mathbf{E} = \mathbf{E_0} exp[\frac{2\pi i}{\lambda_0}(nx - ct)] \tag{6.1}$$

Here, n is the refractive index of the medium. If ρ, r_e A, N_a, f are the ‘Mass density’, ‘classical electron radius’, ‘Atomic weight’, ‘Avogadro number’ and ‘scattering cross-section’ of the medium respectively, then from the Drude model for the metal one can calculate,

$$n = 1 - \frac{N_a r_e}{2\pi A}\lambda^2 \rho f \tag{6.2}$$

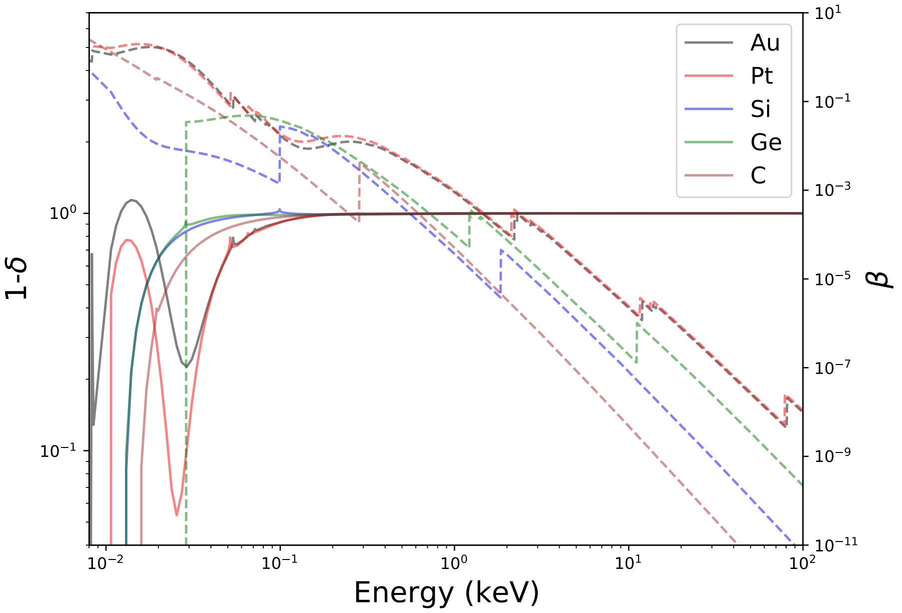

Figure 6.2: Real (solid lines) and imaginary (dashed lines) parts of refractive index as a function of energy for different materials as labeled. This plot is generated using the functionality available in DarpanX (Section 6.5).

Taking into account the photoelectric absorption by bound electrons, the scattering cross-section is a complex quantity, i.e., $f = f_1 + if_2$. f_2 is primarily responsible for absorption. The Equation 6.2 can be written as,

$$n = 1 - \delta + i\beta \tag{6.3}$$

Thus the refractive index, n has a real ($n_r = 1 - \delta$) and an imaginary ($n_i = \beta$) components. The β is is responsible for the absorption losses of the wave through the medium. In the X-ray energy range, n_r is close to unity for almost all the material. For example, using the form factor data available in NIST (National Institute of Standards and Technology), the real and imaginary parts of the n are plotted as a function of energy for various materials in Figure 6.2.

Consider an electromagnetic wave incident on the interface between two mediums whose refractive indices are n_1 and n_2 respectively. Let θ_1 and θ_2 be the incident and refracted angles (angles are measured from the interface). The

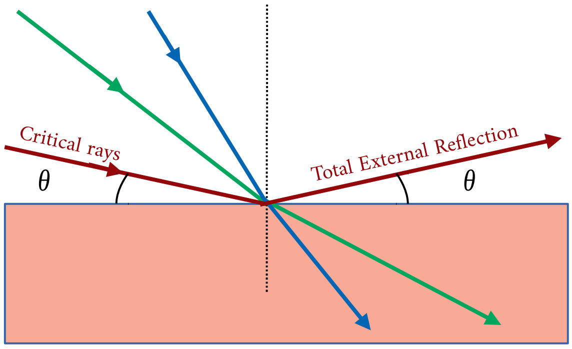

.

Figure 6.3: Schematic diagram showing the Total External Reflection for the incident rays at a shallow angle, θ

θ_1 and θ_2 are related by the Snells law,

$$n_1 Cos(\theta_1) = n_2 Cos(\theta_2) \tag{6.4}$$

For X-ray energies, $n_1 \approx 1$ and $n_2 \approx 1$ (neglecting photoelectric absorption). Hence the $\theta_1 \approx \theta_2$, that causes the X-rays to either passes through with a negligible deviation of their original path or it will be absorbed by the medium due to the photoelectric absorption. However, the X-ray reflection between the interface of the two mediums is possible due to the Total External Reflection (TER) from the interface for a very narrow angle, known as the critical angle (θ_c), described in Figure 6.3.

At $\theta_1 = \theta_c$ (Equation 6.4), $\theta_2 \sim 0^o$. Thus, $Cos^2(\theta_c) = n^2 = (1-\delta)^2 \approx (1-2\delta)$ (here, $n = n_2/n_1$, is the relative refractive index of the second medium and $\delta << 1$). As $\theta_c << 1$,

$$\theta_c \approx \sqrt{2\delta} = \sqrt{\frac{N_a r_e h^2 c^2}{\pi}} \frac{\rho^{\frac{1}{2}}}{E} \sqrt{\frac{Z}{A}} \tag{6.5}$$

At the interface of the two medium at $\theta_1 = \theta_c$, a 100% reflectivity can not be achieve due to the photoelectric absorption and the X-ray scattering by the finite surface microroughness. If we express ρ in g/cm^3, E in keV, θ_c in $mrad$ and considering light element approximation ($\frac{Z}{A} \approx \frac{1}{2}$),

$$\theta_c \approx 19.34 \frac{\rho^{\frac{1}{2}}}{E} \tag{6.6}$$

Thus, θ_c is inversely dependent on the incident energy and proportional to the square root of material density. The below sections describe the mathematical formalism to calculate optical functions (Reflectivity, Transmitivity, and Absorbance) of the incident rays on the interface of two mediums.

6.2.1 Theoretical calculation of optical functions

Laws of reflection/refraction at the boundary between two mediums for an electromagnetic wave are governed by Fresnel's equations. These equations relate the amplitudes of reflected and refracted waves with those of the incident wave.

Fresnel equations for an ideal interface

Consider an electromagnetic wave incident on the interface between two mediums whose refractive indices are n_1 and n_2 respectively. Let θ_1 and θ_2 be the incident and refracted angles (angles are measured from the interface). Then, Fresnel equations (eq:6.7-6.10), give the amplitudes of reflected (r) and transmitted (t) waves Born et al. (1999); Jackson (1999).

$$r_{\perp} = \frac{n_1 Sin(\theta_1) - n_2 Sin(\theta_2)}{n_1 Sin(\theta_1) + n_2 Sin(\theta_2)} \tag{6.7}$$

$$r_{\parallel} = \frac{n_2 Sin(\theta_1) - n_1 Sin(\theta_2)}{n_2 Sin(\theta_1) + n_1 Sin(\theta_2)} \tag{6.8}$$

$$t_{\perp} = \frac{2 n_1 Sin(\theta_1)}{n_1 Sin(\theta_1) + n_2 Sin(\theta_2)} \tag{6.9}$$

$$t_{\parallel} = \frac{2 n_1 Sin(\theta_1)}{n_2 Sin(\theta_1) + n_1 Sin(\theta_2)} \tag{6.10}$$

Here $\perp$ and $\parallel$ represent the perpendicular and parallel components of the electric field vectors with respect to the plane of the interface of the incident wave.

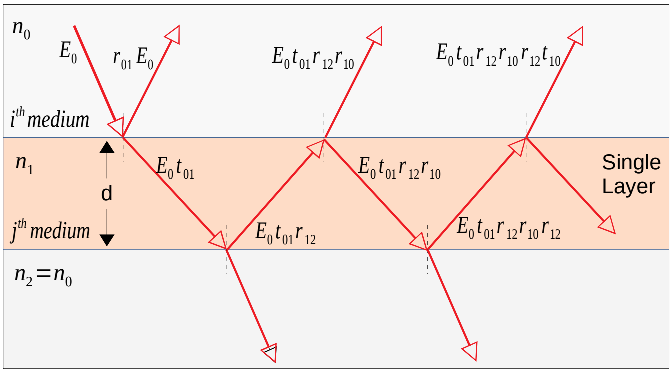

Figure 6.4: Ray diagram of a single layer with the ideal interface.

The square of amplitudes of reflected and transmitted waves given by Fresnel equations gives the optical functions, namely reflectivity, and transmitivity.

Optical functions for single/multi layer with ideal interface

Figure-6.4 shows a single layer of thickness d and refractive index n_1. Here t_{ij} and r_{ij} are the transmission and reflection coefficients of the rays traveling from i^{th} medium and incident on the interface between the i^{th} and j^{th} ($i = 0$ and $j = 1$ in case of single layer) mediums. There will be a phase difference between the two successive reflected rays at the 1^{st} interface, which can be calculated from geometry as,

$$\triangle\phi_{01} = \frac{4\pi}{\lambda} n_1 d.Sin(\theta_1) \tag{6.11}$$

The incident rays are repetitively transmitted and reflected at each interface and finally some fraction returns to the i^{th} medium. All of these components of rays produce an interference pattern. Taking into account the phase shift ($\triangle\phi$) between the repeated reflection of rays in each interface, and adding all the components after considering the energy conservation, the net amplitude of the rays reaching back to the i^{th} medium will be,

$$E_r = r_{01}E_0 + r_{12}(1-r_{01}^2)E_0e^{i\triangle\phi_{01}} - r_{01}r_{01}^2(1-r_{12}^2)E_0e^{2i\triangle\phi_{01}} + r_{01}^2(1-r_{12}^3)E_0e^{3i\triangle\phi_{01}}...inf \tag{6.12}$$

Thus, the amplitude of reflected wave will be:

$$\Re = \frac{E_r}{E_0} = r_{01} + \frac{r_{12}(1-r_{01}^2)e^{i\triangle\phi_{01}}}{1 + r_{01}r_{12}r^{i\triangle\phi_{01}}} \tag{6.13}$$

$$\Rightarrow \Re = \frac{r_{01} + r_{12}e^{i\triangle\phi_{01}}}{1 + r_{01}r_{12}e^{i\triangle\phi_{01}}} \tag{6.14}$$

Here the 1^{st} term of RHS of eq-6.13 gives the reflection due to single interface and the 2^{nd} term represents the interference effect, which modulate the single interface reflectivity. It may be noted that at an incidence angle, $\theta_0 < \theta_c$, $r_{01} \approx 1$ and $r_{12} \approx 0$. The physically measurable quantity is reflectivity, $R = |\Re|^2$. Similar to amplitude of reflection, we can calculate the transmission amplitude of the transmitted rays as:

$$\tau = \frac{E_t}{E_0} = \frac{t_{01}t_{12}e^{\frac{i\triangle\phi_{01}}{2}}}{1 + r_{01}r_{12}e^{i\triangle\phi_{01}}} \tag{6.15}$$

Hence, the transmitivity will be,

$$T = |\tau|^2 * \frac{n_1 Cos(\theta_1)}{n_0 Cos(\theta_0)} \tag{6.16}$$

Instead of using a single layer a more efficient reflectivity can be achieved using multiple layers of alternate high-Z (absorber) and low-Z (spacer) materials, known as Multilayer mirrors. Consider a plane wave incident on a multilayer, which is essentially a series of N layers located on a substrate. Then, the total number of interfaces will be $N + 1$. Let σ_i, d_i, and n_i be the interfacial roughness, thickness and refractive index of the i^{th} layer (where, i= 1,2,3....,N from the top layer) respectively and n_0, n_s are the refractive indices of the ambient and substrate below the bottom most layers. Then from eq-6.14, the bottom most layer has amplitude of reflectivity,

$$\Re_N = \frac{r_{(N-1)N} + r_{N(N+1)}e^{i\triangle\phi_{(N-1)N}}}{1 + r_{(N-1)N}r_{N(N+1)}e^{i\triangle\phi_{(N-1)N}}} \tag{6.17}$$

Here $(N + 1)$ corresponds to the substrate and $\triangle\phi_{(N-1)N} = \frac{4\pi}{\lambda} d_N Sin(\theta_N)$ is the phase difference between the successive reflected rays from N^{th} and $(N - 1)^{th}$ interface. Then the amplitude of reflection due to the combination of N^{th} and $(N - 1)^{th}$ layer will be,

$$\Re_{N-1} = \frac{r_{(N-2)(N-1)} + \Re_N e^{i\triangle\phi_{(N-2)(N-1)}}}{1 + r_{(N-2)(N-1)}\Re_N e^{i\triangle\phi_{(N-2)(N-1)}}} \tag{6.18}$$

By progressively calculating the formula over all the N layers of the multilayer structure, we get the final amplitude of reflection of the complete multilayer system as:

$$\Re_0 = \frac{r_{01} + \Re_1 e^{i\triangle\phi_{01}}}{1 + r_{01}\Re_1 e^{i\triangle\phi_{01}}} \tag{6.19}$$

Then the reflectivity of the multilayer system for all the layers will be, $R = |\Re_0|^2$. Similarly, we can calculate the transmission amplitude and the transmittance of the multilayer system. The absorbance is given by 1-(R + T), for specular reflection.

Interface Roughness Correction

Above calculation is based on the consideration of ideal interface (i.e, surface roughness (σ) = 0). In reality, the boundary surfaces are rough. In one dimension, the surface profile may be completely described by a function $z(x)$, which gives the height profile at every (x) points. For the best polished surface we can assume, $< z >= \frac{1}{L}\int_0^L z(x)dx = 0$ and $< z^2 >= \frac{1}{L}\int_0^L z^2(x)dx > 0$. Here $< z^2 >= \sigma^2$ is called the variance and σ is called the rms surface roughness and L is the length of the surface along the x-direction. For a smooth surface $z(x) = z_0 = constant$, which does not hold true for real surfaces. Thus the roughness of a surface can be characterized by its rms value σ.

Suppose $w(z)$ is the height distribution of $z(x)$, then the Fresnel coefficients can be modified by multiplying the Debye-Waller factor Spiga (2005), as:

$$r'[i] = r[i] * \bar{w}(q_z[i]) \tag{6.20}$$

Here $r[i]$ is the Fresnels coefficient for smooth surface and $\bar{w}(q_z[i]) = \int w(z)exp(izq_z[i])dz$ where, $q_z[i] = \frac{2\pi}{\lambda}sin\theta_i$ and θ_i is the propagation angle in the i^{th} layer.

For the low spatial frequencies of the roughness spectrum, the Fresnel reflection coefficient is usually multiplied by the Debye-Waller factor (equation 6.20), while for the high spatial frequencies, the correction coefficient is given by the Nevot-Croce correction factor Stoev & Sakurai (1999); Nevot et al. (1988); Windt (2013). This model is widely used for the calculation of the X-ray reflectivity of multilayers. Considering Nevot-Croce correction factor one can modify the Fresnel's coefficients by using the following equation:

$$r'[i] = r[i] * \bar{w}(2\sqrt{q_z[i].q_z[i+1]}) \tag{6.21}$$

Stearns (1989) provided the functional form of 'w' and corresponding '$\bar{w}$' for a different type (error function, exponential, linear, sinusoidal) of one-dimensional interface profiles. These functional forms can be used for different types of interface profiles.

6.2.2 The reflectivity of Single and Multilayer X-ray mirrors

Here we demonstrate how the reflectivity of the X-ray mirror depends on the mirror properties. Consider a single layer Platinum (Pt) mirror of different thickness (50 Å, 200 Å, and 500000 Å) with ideal surface (i.e., $\sigma = 0$). The X-ray reflectivity profile for this single layer is calculated as a function of grazing angles (solid curves in Figure 6.5a) of the incident X-rays of energy 8.0 keV. The X-ray reflectivity as a function of incident X-ray energies at a fixed grazing angle of 0.5^0 is also calculated and shown by solid curves in Figure 6.5b. The oscillation in the reflectivity with angles/energies is produced due to the interference effect provided by the last term in Equation 6.5, which is strongly dependent on the layer thickness. This oscillation is known as 'Kiessing fringes'. All of these reflectivities are for ideal surfaces (σ=0). Instead of an ideal surface, if we consider finite surface roughness (σ) values then the reflectivity drops significantly. The dashed curves are the reflectivity profile for the single layer of thickness 200 Å for different σ values.

The reflectivity from a single layer mirror drops exponentially after the critical angle (Figure 6.5a) or critical energy (Figure 6.5b). Beyond the critical angle or energy, the reflectivity can be improved by using a multilayer mirror consisting of several layers of high-Z and low-Z materials. Depending on the variation of the layer thickness, their arrangements, etc, throughout the multilayer system, they are classified in different ways. Here we describe two of

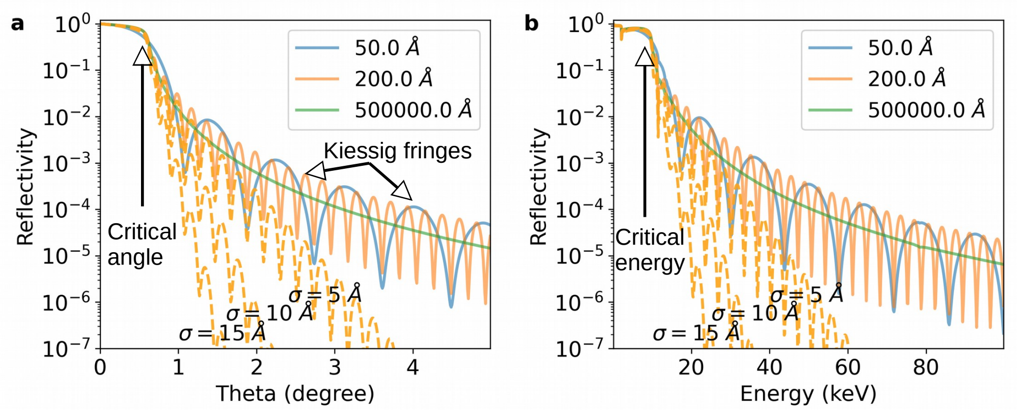

Figure 6.5: Demonstrating the X-ray reflectivity as a function of grazing angle (panel a) and as a function of incident photon energies (panel b) from a single Pt layer of thicknesses 50 Å (blue), 200 Å (orange), and 500000 Å (green) respectively. The solid curves are for an ideal surface with surface roughness, σ=0 Å. The orange dashed curves represent the reflectivity for the 200 Å Pt layer of different surface roughness values as annotated in the plots. The calculation of reflectivity is done using the software, DarpanX as discussed in Section 6.5

them – *Bilayer* system and *the Dept-graded* system. The structure of a *Bilayer* system is demonstrated in Figure 6.6a. It consists of alternative layers of high-Z (blue color) and low-Z (grey color) material, where thickness of all high-Z and all low-Z layers are constant throughout the system. The total thickness of a single bilayer pair is called *Period* of the system and the ratio of the thickness of the high-Z layer to that of the *Period* is called *Gamma* (Γ). Thus a *Bilayer* system consists of multiple bi-layers of constant *Period* and Γ values. Whereas a *Depts-graded* system also consists of several bi-layers but the *Period* and Γ values of the bi-layers vary throughout the system (Figure 6.6b).

Figure 6.7 (blue curve) shows the reflectivity profile as a function of energy for a *Bilayer* mirror consisting of 150 bi-layers of *Pt* (high-Z) and *SiC* (low-Z). Whereas the orange curve represents the reflectivity profile for a *Dept-graded* mirror consisting of the same bilayer pairs but their *Period* and Γ are varying throughout the system. The *Bilayer* mirror provides the reflectivity peaks at discrete energy ranges, whereas the *Depth-graded* mirror provides an almost constant reflectivity profile for a broad energy range.

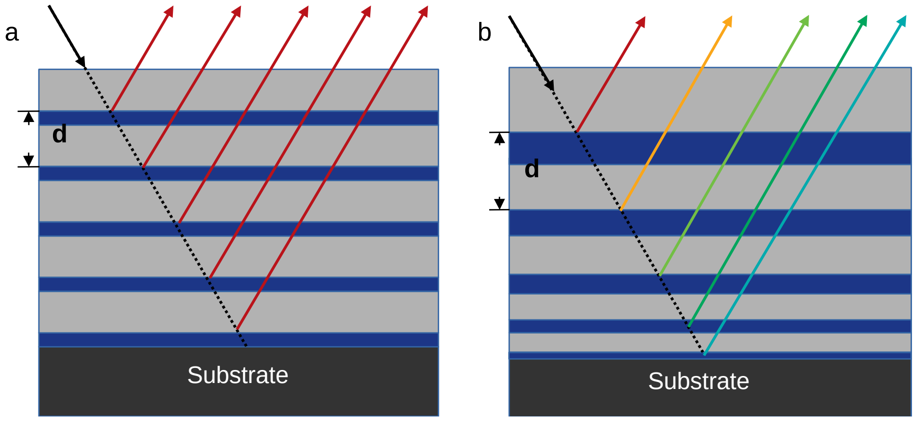

Figure 6.6: Demonstrate the structure of a *Bilayer* (panel a) and *Depth-graded* (panel b) multilayer mirrors.

6.3 Fabrication of the X-ray mirrors

Development of the X-ray mirrors requires a thin layer coating of the material on the top of a substrate. The multilayer mirrors require a coating of high-Z and low-Z materials with thicknesses ranging from a few tens to a few hundred angstroms. Recently we have initiated the development of X-ray mirrors by setting up an coating facility at Physical Research Laboratory (PRL), a brief description of it is given in the below Sections.

6.3.1 Formation of a thin layer

In the present days, various techniques are available for depositing a thin layer of material on top of a substrate to form a thin film (more details can be found in Spiga (2005); Singam (2019)). Among them, we have used the plasma spattering technique for the realization of X-ray mirrors. In the sputtering process, the fast energetic ions bombard a solid material, known as the target, and evaporate the target material. The evaporated target atoms then travel towards the substrate and condensate on the top of the substrate surface. The cartoon shown in Figure 6.8 demonstrates the sputtering process. Here, the target and the substrate are kept at the high negative and positive potential within a vacuum chamber, which is filled with an inert gas (e.g., Ar). Due to the applied voltage between the target and substrate, Ar gas becomes ionized and produces plasma

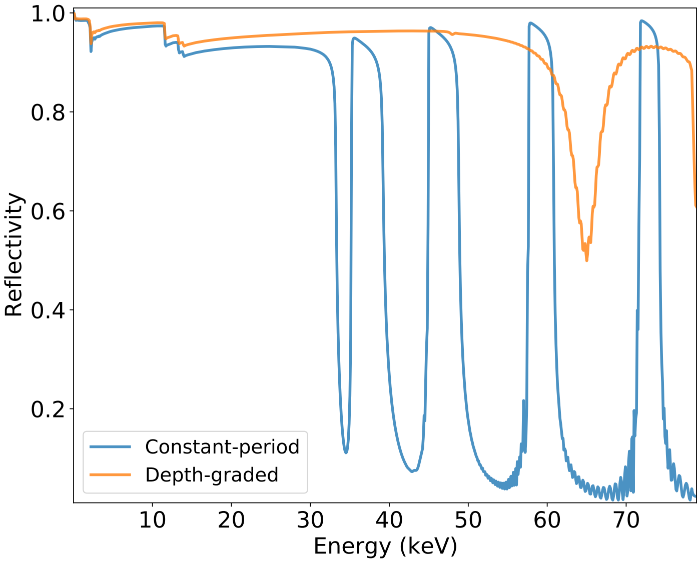

Figure 6.7: Reflectivity profile for a *Bilayer* (blue curve) and *Depth-graded* (Orange curve) multilayer mirror.

of Ar ions (Ar^+) and electrons (e^-). The Ar^+ ions travel towards the target and bombard with the target material causing the sputtering of the target atoms. Sputtered atoms then travel some distance and deposit on the top of the substrate. As more and more atoms deposit on the substrate, they are binding with each other in the molecular level to form a tightly bound atomic layer. The efficiency of the sputtering and hence the thickness of the deposited layer depends on various factors; the time of sputtering, target material, the pressure of the inside chamber, power between the target and substrate, etc. Though the basic mechanism of the sputtering mechanism is simple, there are complexities;

(1) The electrons produced during the time of ionization of Ar can travel towards the substrate and disturb the coating. This problem can be resolved using a small magnetic field near the target, which tracks the electrons surrounding the target. These electrons also can increase the efficiency of the ionization of the Ar atoms by colliding with the Ar atoms. This type of target is called a magnetron target and sputtering is known as magnetron sputtering.

(2) The sputtered atoms from the target travel toward the substrate and have kinetic energy. If this kinetic energy is strong enough to break the bonding

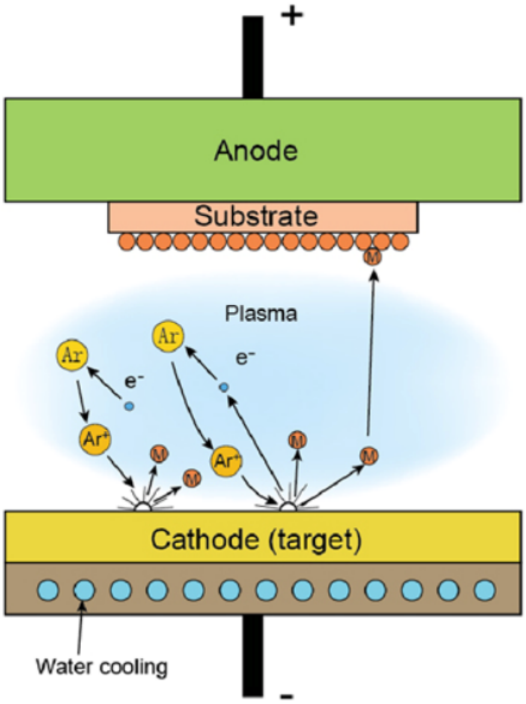

Figure 6.8: Schematic diagram showing the sputtering process of the target material to form a thin layer on the substrate. This figure is directly adopted from http://www.micromagnetics.com/

of the deposited layer on the substrate, then their collision with the substrate can be re-sputtered from the already deposited layer, causing an inefficient process. This process will be less effective in the case of magnetron sputtering.

(3) If the target material is an insulator or semiconductor (e.g., Si) instead of the metal, then initially the sputtering process starts but after some times the surface of the target becomes positively charged. These positive charges stop sputtering by repelling the Ar^+ ions. Whereas, in the case of a metal target the positive charge of the target surface is discharged by the negative potential of the target, which is not the case for insulators or semiconductors. This problem can be resolved using a Radio-Frequency AC power supply instead of the DC power in between the target and substrate. The AC power supply alters their polarity with a certain frequency helps to discharge the positive charge on the insulator surface and continues the sputtering process. This type of sputtering is called RF sputtering.

In our lab, we used an RF magnetron sputtering system, where a small magnetic field is used within the target along with an RF AC power supply. The below section describe the details of the system.

6.3.2 Coating Facility at PRL

The sputtering system at PRL consists of a vacuum chamber of diameter ∼65 cm and height ∼35 cm (Figure 6.9) and it is operated using a control system connected to a computer. Two stationary targets are placed at the center of a vacuum chamber, each having size of 4×30 cm^2 (width × length) (Figure 6.10). One target contains a high-Z material (e.g., W) and another contains a low-Z material (e.g., Si) for the requirement of multilayer coating. Substrates are placed on a rotating platform so that they can be moved in front of one target to another to deposit successive layers of high-Z and low-Z material to form a multilayer mirror. All the components (e.g., targets, turbo pumps, etc) of the system are cooled by circulating cooled water (some of the blue pipes in Figure 6.9).

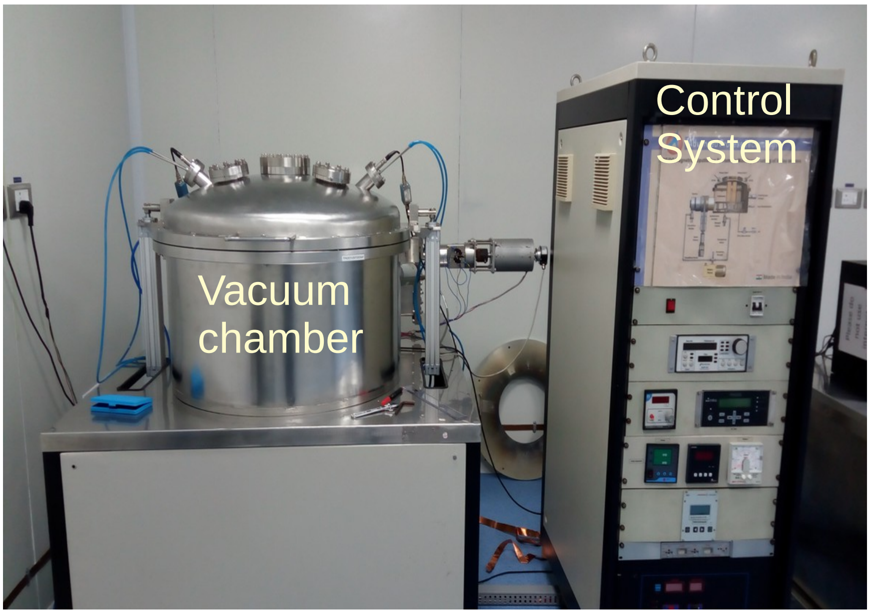

Figure 6.9: RF Magnetron Sputtering system installed at PRL.

The coating thickness on the substrate can be controlled by the sputtering Ar gas pressure, sputtering power, or by changing the rotation speed of the substrate table during the coating. Thus before the production of the multilayer X-ray mirror, we have to characterize the system for all of these parameters so that for a given set of parameters, the required thickness can be achieved. For

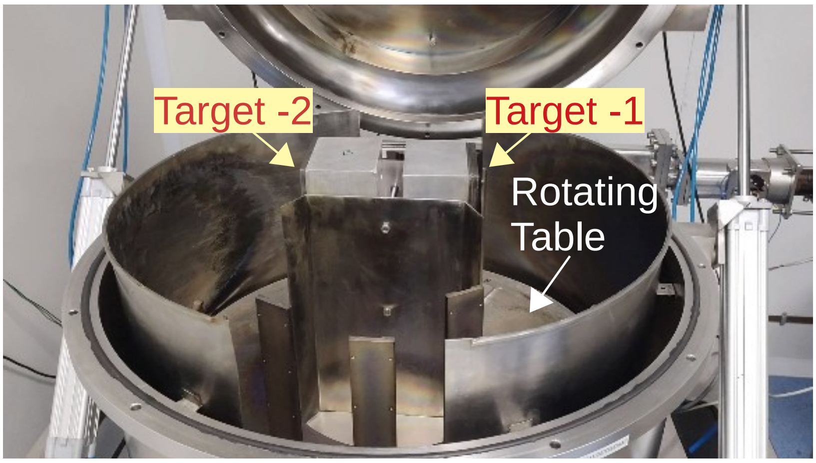

Figure 6.10: Inside of the sputtering system chamber shown in Figure 6.9.

the purpose of characterization of the sputtering system, single layers of each target material are deposited on a $20 \times 20 \times 0.3$ mm^3 (width × length × height) polished borosilicate SCHOTT glass substrate, with various operating parameters of the sputtering system. These glass substrates are chopped from a sheet of dimension 350 × 450 mm^2. Chopping this thin glass foil is another challenging task and various methods can be used (Zhang, 2009). For this purpose, we have used a diamond wheel imported from MDI Advanced Processing GmbH Mainz, Germany. Which is integrated within a custom-made mechanism as shown in Figure 6.11.

Figure 6.12a and Figure 6.12b show the image of a substrate before and after coating respectively. Figure 6.12b shows a few of the single-layer characterize samples of different thickness stored in a storage box and Figure 6.12c show the representative single-layer mirror with a coating of W (top two) and Si (bottom one) of different thickness.

6.4 Testing the mirror reflectivity

After forming the X-ray mirrors as discussed in Section 6.3.2, to know their efficiency of reflecting the X-rays required to measure their reflectivity profile. The overall reflectivity of the mirror prominently depends on the surface micro-roughness, inter-layer roughness, interdiffusion at the interfaces, layer density,

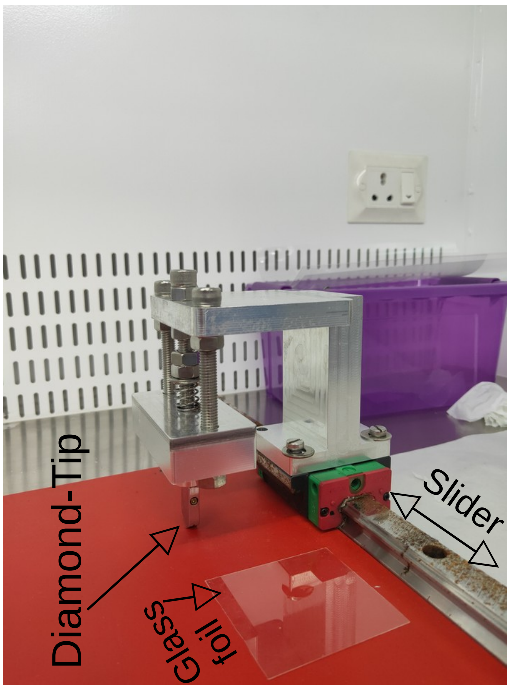

Figure 6.11: Substrate copper mechanism

thickness, and uniformity. We use the X-ray reflectivity (XRR) technique to measure the reflectivity profile of an X-ray mirror. XRR technique is a non-destructive technique that provides information about the thickness of all layers, interlayer roughness, and diffusion, the density of thin films, etc. This relatively inexpensive technique can also be performed at multiple energies to understand the energy-dependent physical properties of the X-ray mirrors. Figure 6.13 describes the working principle of XRR measurement. The test mirror foil is kept in the middle, on which an X-ray beam is being incident from a source and the reflected X-rays from the mirror are detected by a detector. In this way, the reflected X-rays are measured for different incident angles.

For all of the fabricated mirror foils as described in Section 6.3.2, the X-ray reflectivity measurements are carried out using High-Resolution X-ray Diffraction (HRXRD) system by Bruker (Bruker D8 DISCOVER) at Space Applications Center (SAC), Ahmedabad, India. XRR measurements were carried out at incident X-ray energy of 8.047 keV with the incident beam slit and detector slit of each 0.2 mm. XRR scan measurements for each sample were obtained after carrying out the alignment of the system. Figure 6.14 shows a represen-

Figure 6.12: Panels **a** and **b** show the image of a substrate before coating and after coating respectively. Panel **c**: a set of single-layer mirrors coated with different thicknesses of Si or W. Panel **d**: Zoom view of three mirror foils. At the backside of each foil, a unique id is given corresponding to the sputtering parameters.

tative XRR profile for a single layer Si mirror. The Kiessing fringes and the critical angle (θ_c) of total external reflection are annoyed in the figure. To obtain the layer parameters (e.g., thickness, density, surface roughness etc) of the mirror we have to model the measured XRR profile. For that purpose, we have used a software package, named as DarpanX, which is developed in this thesis work. DarpanX has the capability to fit the measured XRR profile with the model reflectivity profile by varying the different layer parameters. In the end, it returns the best fitted model parameters, which describe the measured XRR profile well. After discussing the DarpanX implementation and its validation in Section 6.5, representative modelings of the measured XRR profiles are described in Section 6.6.

6.5 DarpanX: Algorithm, Implementation

DarpanX is a program designed to compute the reflectivity of single/multilayer mirrors as a function of energy and incidence angle. Calculation of reflectivity and transmitivity in DarpanX is based on the Fresnel equations, modified for the finite surface roughness. A short description of theoretical calculation used in DarpanX is given in Section-6.2.1. A flowchart of the algorithm employed in

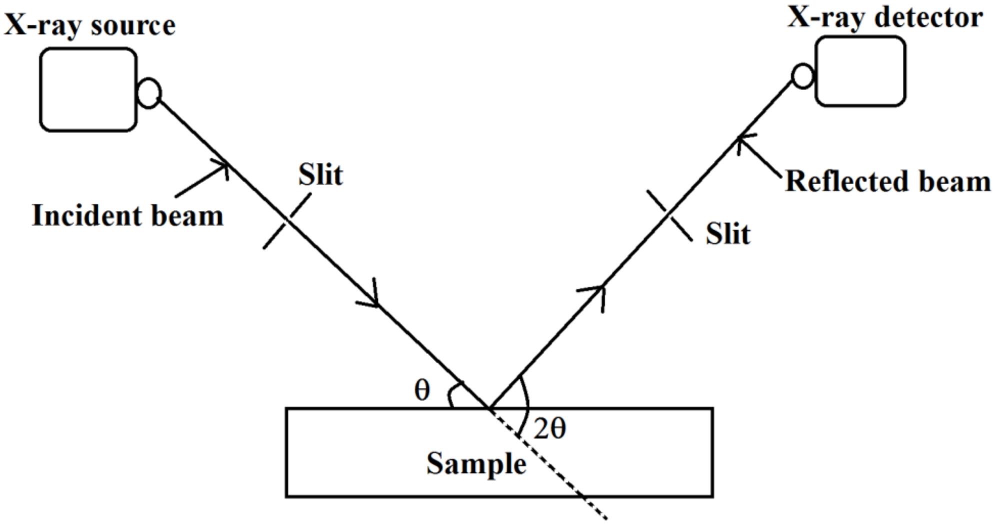

Figure 6.13: Schematic of XRR measurement.

DarpanX is given in Figure 6.15. Two sub-blocks in the flowchart correspond to the theoretical computation of reflectivity and fitting of experimentally measured reflectivity data with the theoretical model.

DarpanX takes parameters like the number of layers (N), materials, thickness (d), density (ρ), and surface roughness (σ) of layers as input to construct the single/multilayer structure. For the computation of refractive indices (from Equation 6.2) of the materials, DarpanX uses the X-ray form factors (f_1 and f_2) in the energy range 0.001 keV to 433 keV provided by the NIST (National Institute of Standards and Technology) database ref (2020) for 92 elements from Z=1 to Z=92. Accordingly, the refractive index profile for the multilayer structure is obtained. Then, Fresnel's coefficient for each interface is computed and corrected for surface imperfections. Using these modified Fresnel coefficients, the optical function for the complete system is calculated in a recursive manner.

In order to compare the theoretical model of reflectivity with the XRR measurements further corrections for projection effect and instrument angular resolution are required. At very low angles of the incidence onto a small mirror sample, only a fraction of the incident beam is covered by the reflecting surface of the sample and reflectivity needs to be modified for this projection effect by

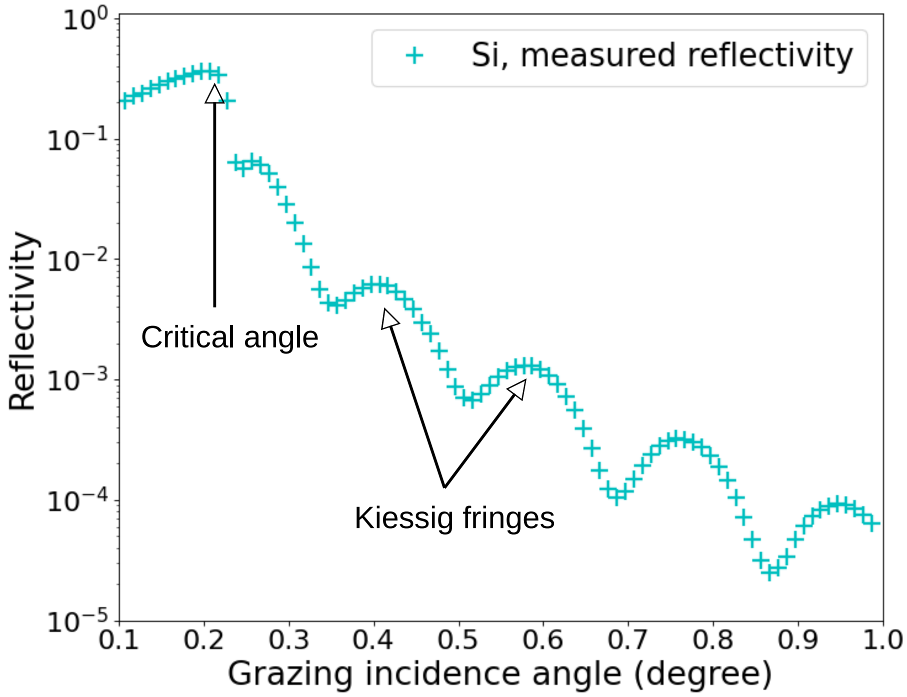

Figure 6.14: XRR profile for a single layer Si mirror foil

multiplying it with a factor f defined as:

$$f = \frac{A_{\rm r}}{A_{\rm i}} \tag{6.22}$$

where A_r is the sample area along the incident beam direction and $A_i = L/sin(\theta)$ is the projected area of the incident beam on the sample, with L being the beam diameter and θ the incidence angle. It is to be noted that this correction is required only when $A_r \leq A_i$. This is included in the DarpanX model calculation. In order to take into account the finite angular resolution of the XRR instrument, the reflectivity computed from the model is then convolved with a Gaussian profile, whose FWHM represents the instrumental resolution.

DarpanX implements these algorithms to compute X-ray reflectivity in Python 3. It is written as an object-oriented program and is packaged as a module that can be imported into the user program. The theoretical calculations in the upper block of the flowchart shown in the Figure 6.15 are implemented by the various methods of a class called '*ML_Structure*'. To use the DarpanX as

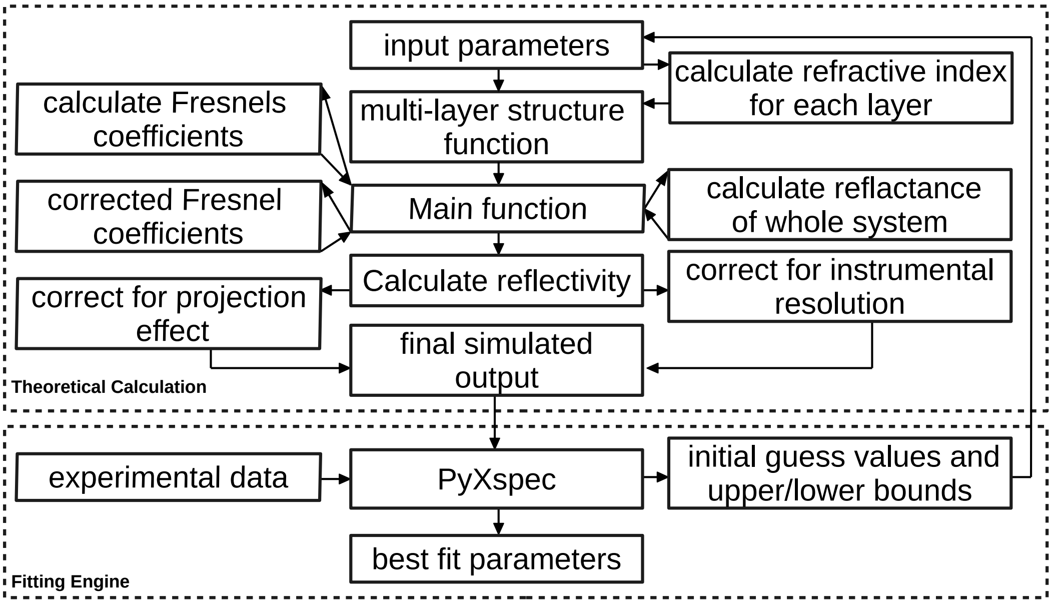

Figure 6.15: Flow chart representing the algorithm employed in DarpanX and fitting DarpanX model in PyXspec.

a stand-alone package, a higher level class named '*Multilayer*' is implemented. It includes different methods for various applications such as calculating the optical functions, plotting the final output of a calculation, etc. The '*Multilayer*' class also provides the flexibility to design any multilayer structure, like single-layer, constant period bi-layer, depth-graded, cluster-graded, or any random layer structure defined by the layer materials and thicknesses. The details of the DarpanX classes, their methods, and how to use them are described in the user manual; dar (2020).

DarpanX can also be used as a local model in PyXspec (Python interface to XSPEC), where the experimental XRR data can be loaded and fitted with the reflectivity model to determine the parameters of the multilayer structure. Note that, the default XSPEC minimization method is a modified Levenberg-Marquardt algorithm but it is also possible to use other algorithm such as Minuit2 migrad method and Minuit2 simplex method as mentioned in the XSPEC user manualxsp (2020). The results in the present work used the modified Levenberg-Marquardt algorithm. The lower block of Figure 6.15 shows the fitting of experimentally measured reflectivity data with the theoretical model by using PyXspec. A Python routine is included to link the DarpanX and PyXspec, which creates an object of the PyXspec class '*Model*'. This object can be used as a local model of PyXspec for the DarpanX module and can be accessed from the interactive Python shell. Once DarpanX is loaded as a model in PyXspec, various parameters of the multilayer structure can be constrained to be constant or free for fitting. For free parameters, initial guess values and bounds are to be provided. The initial model function is computed with these values as input, and then observed XRR data can be fitted to obtain best-fit parameters.

Computation of refractive indices of various materials from their X-ray form factors (f1 and f2) are carried out by the methods of a class named '*nkcal*'. The f_1-f_2 data sets from NIST are reformatted and included with DarpanX. There is a provision to compute the refractive indices of compounds if their density is provided as an input. The optical constants for all the 92 elements as well as some common compound materials are pre-calculated using the '*nkcal*' class and are distributed with the DarpanX package. It is also possible for users to provide alternate data sets of form factors or optical constants in the prescribed format (as described in the user manual dar (2020)) for use with DarpanX.

DarpanX software package also has provision to parallelize the computation of reflectivity over an array of energies or angles. This significantly reduces the time required to calculate optical functions for a multilayer structure with a large number of layers. For this purpose, it uses the Python multiprocessing library. Users can provide the number of cores to be used as an input to avail of the parallelization option in DarpanX. Apart from this in-built parallelization in DarpanX, PyXspec has its own parallelization capability, where it performs multiple iterations required for fitting on different threads. Thus, for experimental XRR data fitting, one can use either the parallelization option in DarpanX or PyXspec.

DarpanX is distributed under the GNU General Public License (GPL). It can run on any platform that supports Python. However, for the XRR data fitting, the platform should also support PyXspec. DarpanX package is available on GitHub [*].

---

[*] https://github.com/biswajitmb/DarpanX.git

6.5.1 Validation of algorithms

In order to validate the DarpanX algorithms, we compare the computed reflectivity against the results from the widely used software IMD. The reflectivity calculation depends on the optical constants (refractive indices) database. DarpanX uses the database formed by using the X-ray form factors imported from NIST as described in Section 6.5. IMD uses different databases by using the combined X-ray form factors from the Center for X-ray Optics (CXRO) and the Lawrence Livermore National Laboratory (LLNL) Windt (2013). Hence, for comparison of the reflectivity calculation from DarpanX with IMD, the reflectivity is calculated by DarpanX by using both the DarpanX database (database-1) and the IMD database (database-2). We have carried out the validation of DarpanX against IMD for an extensive range of parameters and materials. Reflectivity is computed as a function of incident photon angles and energies with DarpanX for single layers of Pt, Ni, C, W, Si, Cu, B_4C, Au, Ag etc. and multilayers of W/Si, W/B_4C, Pt/C, Pt/SiC, Ni/C, Cu/Si etc. with different values of thickness/period ranging from 1Å-1000Å. A similar calculation is performed with IMD, and the results are compared. We find that the reflectivity computed from both software matches very well in all cases if the same optical constant database is used. A few representative results are discussed below.

Single layer

We consider the reflectivity for a single pure Pt layer of thickness 100Å with an ideal interface. The calculation has been done for the reflectivity measurement as a function of the incident beam angle from the interface. The energy of the incident beam is 10.0 keV and 40.0 keV. In Figure 6.16, the outputs of both IMD (star and plus symbols) and DarpanX (solid and dashed lines) are shown. It can be observed that the calculation by DarpanX (solid lines in Figure 6.16) exactly matches with the IMD result (star and plus symbols in Figure 6.16) for both the energies when the IMD database (database-2) is used by DarpanX. The DarpanX calculation by using database-1 (dashed lines in Figure 6.16) slightly differs from the IMD calculation, however, this is expected as the two databases (database-1 and database-2) are generated by using the X-ray form factors available from different sources. The dependence of critical angle (θ_c) with the energy (E) of the incident X-ray beam on the reflecting surface, $\theta_c \propto \frac{1}{E}$ is clearly visible in Figure 6.16. With the increase of incident X-ray energy from 10 keV to 40 keV the critical angle (θ_c) decreases from 0.46° to 0.16°.

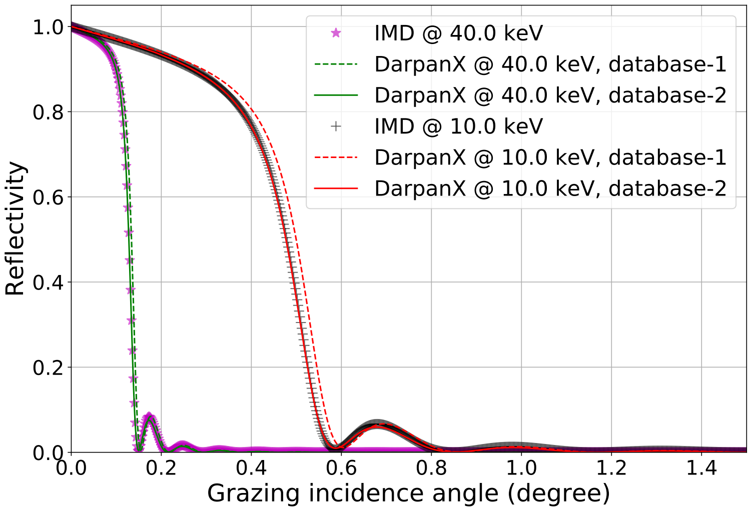

Figure 6.16: Comparison of reflectivity computed with DarpanX and IMD for single Pt layer of thickness 100 Å as a function of incident angle. Here database-1 or database-2 represents, which optical constant database is used in the calculation. The database-1 is the DarpanX database formed by the X-ray form factors available from NIST and database-2 is that given in the IMD package formed by the combined X-ray form factors available from CXRO and LLNL.

Constant period Multilayer

Constant period multilayers contain alternate layers of high Z and low Z materials of the constant period (total thickness of high Z and low Z material of each bilayer). For verification of DarpanX, we calculate the reflectivity for a constant period of 60 bilayer Ni/C system. We take the period of the system as 50.0Å with the gamma(Γ) value (ratio of high-Z thickness to the total thickness of each bilayers) as 0.4. Figure 6.17 shows the reflectivity of this multilayer system as a function of the incident angle at an energy of 16.75 keV. From Figure 6.17, it is clear that the reflectivity computed by DarpanX (red dashed) by using IMD database (database-2) at each Bragg peak, as well as below critical angle matches with the output of IMD (black plus symbols). The blue dashed lines in the top panel of Figure 6.17 shows the DarpanX calculation by using the database-1, where it slightly differs from the IMD calculation (black plus symbols). The bottom panel shows residuals (between DarpanX and IMD calculations), which are negligible when the DarpanX used the database-2 (red solid line). Finite residuals are present when the DarpanX used the database-1 (blue solid line).

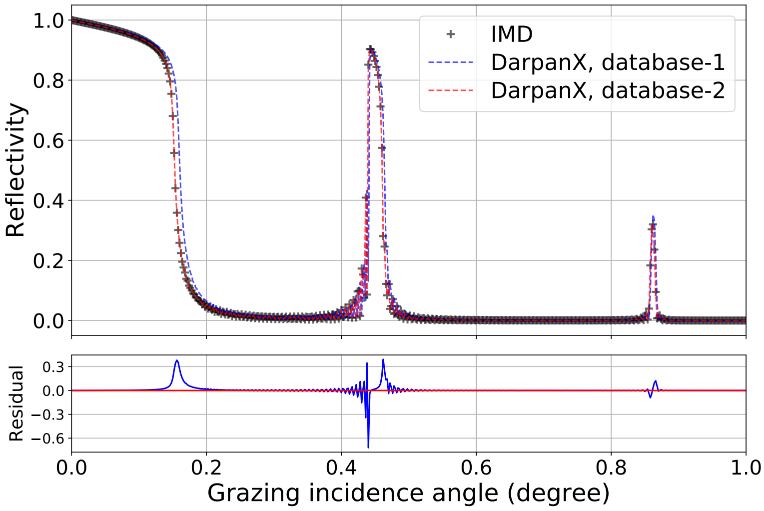

Figure 6.17: Comparison of reflectivity computed with DarpanX and IMD: For a Ni/C multilayer system with 60 bilayers of constant period of 50.0Å and $\Gamma = 0.4$ at incident energy of 16.75 keV ($\lambda = 0.74$Å). All other conventions are same as Figure 6.16

Depth-graded Multilayer

We calculate the reflectivity for a multilayer depth-graded Pt/SiC system (Figure 6.19) of 150 bilayers, which is one of the NuSTAR multilayer recipeBrejnholt (2012)s. Here the period of the Pt/SiC bilayer is changing from the top layer to the bottom layer according to the equation:6.23 Joensen et al. (1993); Brejnholt (2012).

$$d_i = \frac{a}{(b+i)^c} \tag{6.23}$$

where, i=1,2...N is the number of bilayer, $a = d_{min}(b+N)^c$, $b = \frac{1-N.k}{k-1}$ and $k = (\frac{d_{min}}{d_{max}})^{\frac{1}{c}}$. Here d_{min}, d_{max} are the bottom most and top most d-spacing (or period) respectively and c controls the slop between these extreme value over the

$Material$	d_{max} (Å)	d_{min} (Å)	N	Γ_{top}	Γ	c	σ (Å)
Pt/SiC	128.10	31.70	150	0.7	0.45	0.245	4.5

Table 6.1: Multilayer depth-graded recipe details. d_{max} and d_{min} is the maximum and minimum period corresponding to the top and bottom most bilayer. N and Γ are the number of bilayers and gamma factor respectively. Γ_{top} is the gamma factor corresponding to the top most layer. c controls the slope between these extreme values of d_{max} and d_{min} over the N layers.

N-bilayers. Figure 6.18 shows the thickness of each layer. Table-6.1 gives the parameters of the depth-graded multilayer.

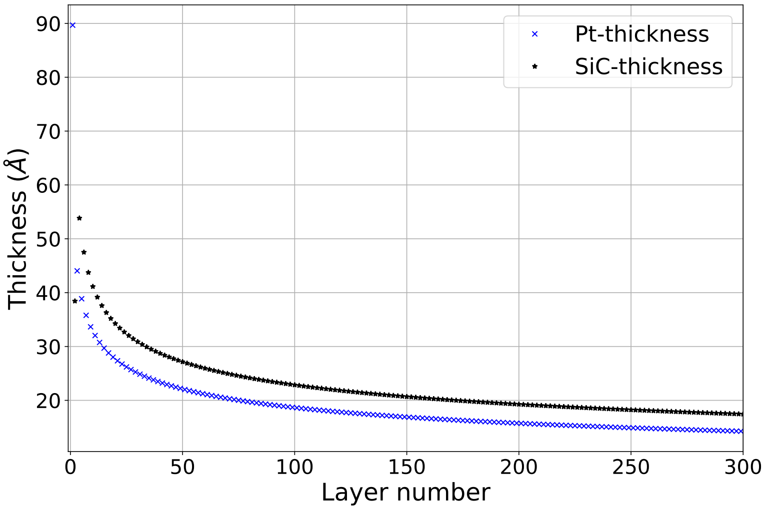

Figure 6.18: Thickness variation of the Pt/SiC depth-graded system.

The reflectivity has been calculated as a function of incident energy varying from 0.01 keV to 79.0 keV with the incident angle of the beam kept at a constant value of 0.077^o. Figure 6.19 shows the reflectivity computed from DarpanX and IMD, which match very well, if the same optical constant database is used. The bottom panel shows residuals (between DarpanX and IMD calculations), which are negligible (blue solid line) when both the DarpanX and IMD uses the same database (database-2). Finite residuals (green solid line) are present when the DarpanX used the database-1.

The accuracy of the DarpanX to calculate the X-ray reflectivity of single-layer or multilayer system is established with these results discussed in Section 6.5.1 and Section 6.5.1.

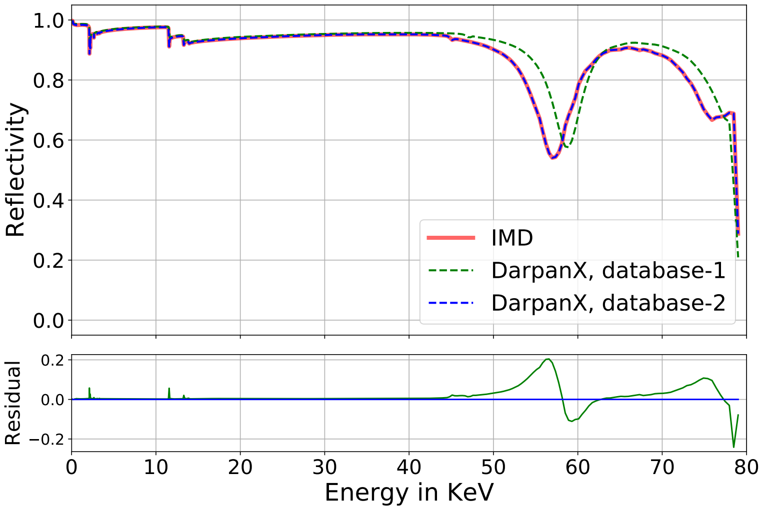

Figure 6.19: Comparison of relefectivity of Pt/SiC depth-graded system computed with DarpanX and IMD. Note that the higher value of Γ_{top} as given in Table 6.1, applies only to the top bilayer (i.e. $d_{N=1}$ which has the period d_{max}). The thicker heavy material on the top improves total external reflectivity efficiency significantly below the critical energy, E_c . Here database-1 or database-2 represents, which optical constant database is used in the calculation.

6.6 Experimental validation

DarpanX model is further validated experimentally by employing it in the analysis of X-ray reflectivity measurements of single and multilayer samples. Here, we have shown the XRR analysis for two Single-layer (W and Si) mirrors, which are prepared in our lab and the XRR measurements are carried out as discussed in Section 6.3.2 and Section 6.4 respectively.

Two constant period W/B_4C multilayer samples with number of bilayers (N) 170 and 50 are also used to demonstrate the XRR analysis using DarpanX. This samples are deposited on a 0.5 mm thick n-type Si substrate of dimension 30 × 30 mm^2. They consists of 170 and 50 number of bilayers fabricated by using the facility at Raja Ramanna Center for Advanced Technology (RRCAT), Indore. XRR measurements for these samples were carried out with the facility at RRCAT. The details of the sample and XRR measurements are given in Panini et al. (2018)Singam et al. (2018).

Single-layer (W and Si) and multilayer (W/B_4C with N=170 and W/B_4C with N=50, where N is the number of bilayers) thin film samples are prepared, and reflectivity measurements are carried out for these samples. The observed data is then fitted with the DarpanX.

6.6.1 XRR Analysis with DarpanX

Single-layer

XRR measurements (cyan plus points) for Si and W single layers are shown in Figure 6.21 left and right panels respectively. As the top layer of the thin film exposed to the atmosphere would get oxidized, a thin oxide layer of SiO_2 (above Si) and WO_3 (above W) are included in the models used to fit the XRR data. We keep both the thicknesses of oxide (SiO_2/WO_3) and material (Si/W) layers as free variables for the DarpanX fitting. Along with thicknesses, we consider, oxide and material densities, surface roughnesses (σ) of the three interfaces (*ambient/oxide* , *oxide/material* and *material/substrate*) as free parameters. The instrumental resolution defined as the standard deviation of the Gaussian convolution function is also considered as a free parameter. Fit results from DarpanX (red) are overplotted with the XRR data in Figure 6.21. The best-fit parameters obtained are given in Table 6.2. Note that the W density for the WO_3/W sample is very low (close to the density of its oxide) compared to the original density. This may be because the thickness of the W layer is very less. As a result, most of it oxidized.

$Material$	d_{layer} (Å)	d_{oxide} (Å)	ρ_{oxide} (g/cm^3)	ρ_{layer} (g/cm^3)	σ_1 (Å)	σ_2 (Å)	σ_3 (Å)	$Resolution$ (deg)
$SiO2/Si$	161.26	71.65	2.17	2.10	9.52	1.10	3.13	0.001
WO_3/W	32.31	14.93	2.72	7.94	4.11	9.84	4.34	0.001

Table 6.2: Fitted parameters of the XRR measurement of the single-layer samples. d_{layer} and d_{oxide} are the thicknesses of oxide and coating materials respectively. Same as thicknesses, ρ_{oxide} and ρ_{layer} are the densities of oxide and coating materials. σ_1 , σ_2 and σ_3 are the surface roughness of the three interfaces (ambient/oxide, oxide/layer, and layer/substrate) as discussed in the text.

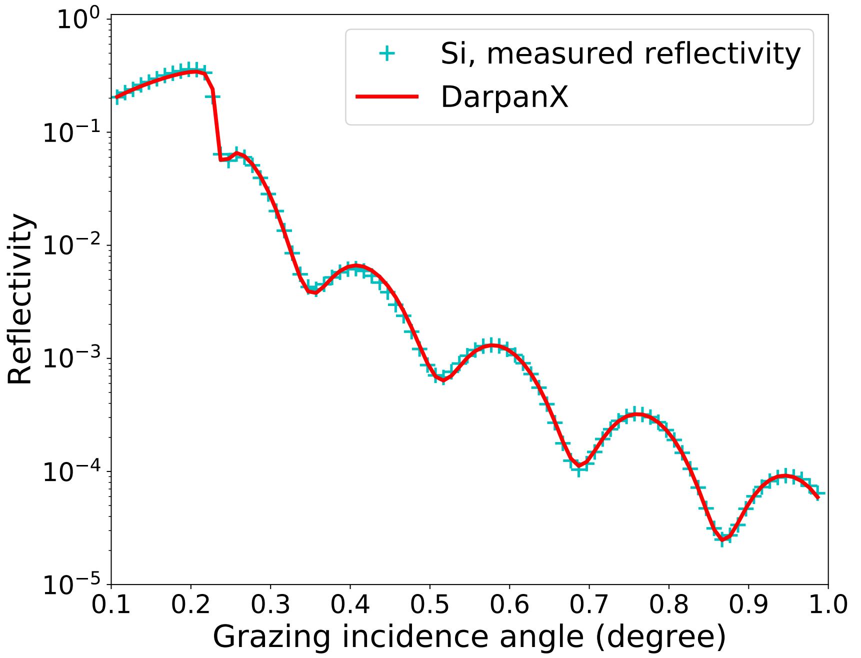

Figure 6.20: XRR reflectivity data(cyan) over plotted with DarpanX model (red) of Single Si-layer layers deposited at PRL coating facility. The fitted parameters are summarized in Table 6.2.

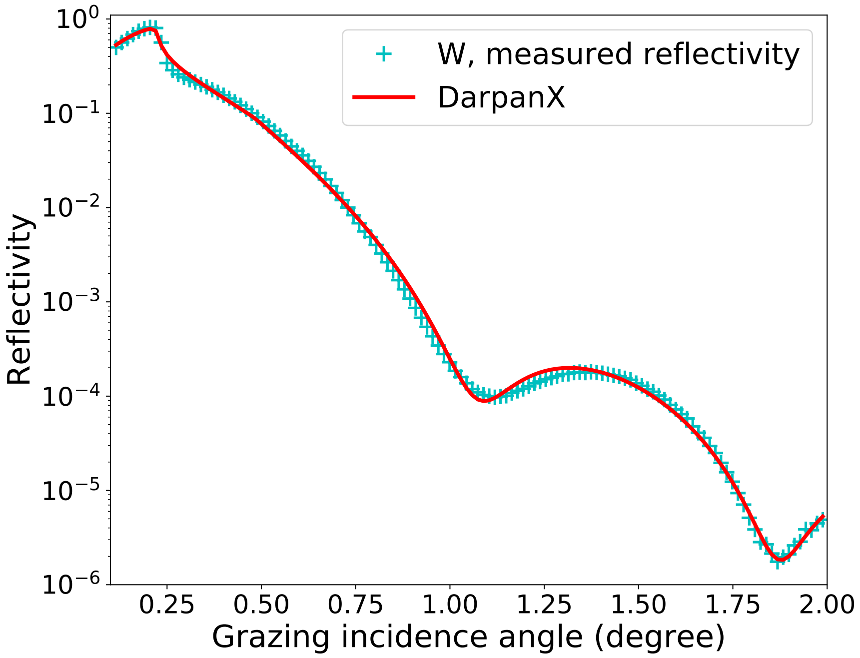

Figure 6.21: XRR reflectivity data(cyan) over plotted with DarpanX model (red) of single-W layer deposited at PRL coating facility. The fitted parameters are summarized in Table 6.2.

Multilayer

Figure 6.23 shows the XRR measurements (cyan plus points) of the multilayer samples of W/B_4C (number of bilayers, N=170 and N=50). In the first step, data are fitted with DarpanX by considering constant period bilayer models (number of bilayers, N=170 and N=50 respectively). For the analysis, the multilayer period (d = total thickness of W and B_4C), gamma factor (Γ = ratio of W thickness to the period), along with the surface roughnesses of the *ambient*/W (σ_1), W/B_4C (σ_2), B_4C/W (σ_3) and substrate (σ_4) interfaces are kept as a free variable. The best fit results are overplotted on the observation in Figure 6.22 and 6.6.1, and the resultant parameters are summarised in the first and second row of Table 6.3.

Sample	*Bilayers* (N)	*Model*	d (Å)	Γ	ρ_W (g/cm^3)	ρ_{B_4C} (g/cm^3)	σ_1 (Å)	σ_2 (Å)	σ_3 (Å)	σ_4 (Å)	*Resolution* (deg)
W/B_4C	170	BL	19.19	0.39	19.61	2.90	3.17	12.24	1.64	19.37	0.015
W/B_4C	50	BL	47.30	0.41	20.65	1.85	7.09	1.10	6.19	13.37	0.015
W/B_4C	170	CG1	-	-	20.48	2.23	8.60	2.15	8.92	13.85	0.015
W/B_4C	50	CG1	-	-	17.16	2.34	2.66	1.66	1.64	13.37	0.015
W/B_4C	170	CG2	-	-	19.69	2.30	8.18	-	-	13.97	0.015
W/B_4C	50	CG2	-	-	16.09	2.25	2.64	-	-	13.20	0.015

Table 6.3: Fitted parameters of the Multilayer samples. d and Γ are period and gamma factor. ρ_W and ρ_{B_4C} are the density of W and B_4C respectively. σ_1, σ_2, σ_3, and σ_4 are the surface roughness of *ambient*/W, W/B_4C, B_4C/W interfaces and substrate respectively. Resolution is the instrumental angular resolution in degree. BL represent the Bi-Layer model. CG1 represents the Cluster-Graded model with different values of period and gamma at each block (Figure 6.27). CG2 represent the model with different roughness values (σ_2 and σ_3), period, and gamma value at each block (Figure 6.31).

The best fit model of the experimental XRR scan result, as shown in Figure 6.22 and 6.6.1, indicates that there is a deviation between the experimental data and fitted model at the higher-order Bragg peaks. An additional peak (at $\theta \approx 4.5$) in Figure 6.22 just below the second Bragg peak suggests that there might be variation in thickness within the multilayer system, i.e., it deviates slightly from the constant period. If we consider the parameters of each layer, such as thickness, density, and surface roughness, to be independent, there would be a large number of free parameters for fitting. To avoid this, we segregated

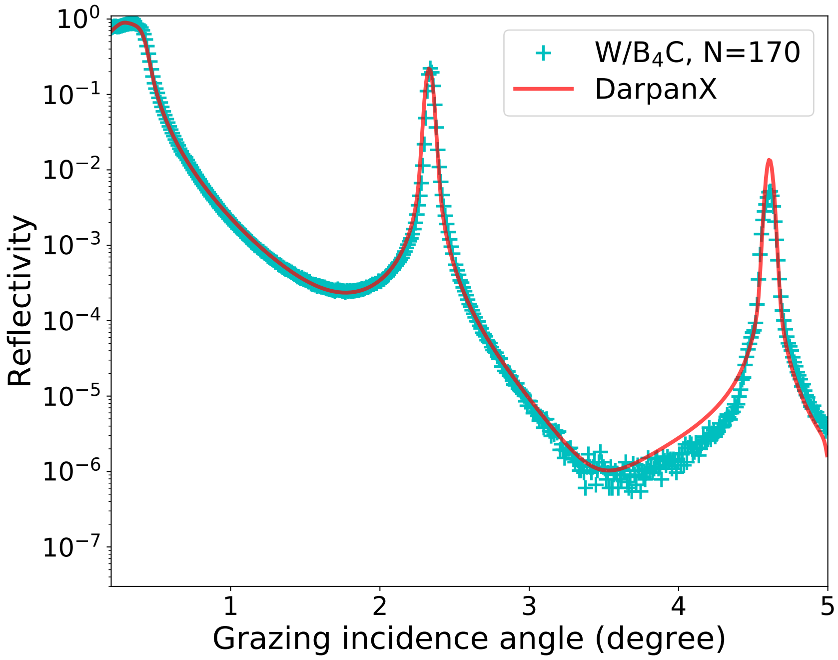

Figure 6.22: XRR reflectivity data(cyan) of W/B_4C multilayer sample (with N number of bi-layers) fitted (red) with constant period bilayer model of N=170. The fitted parameters are summarized in the first and second row of Table 6.3.

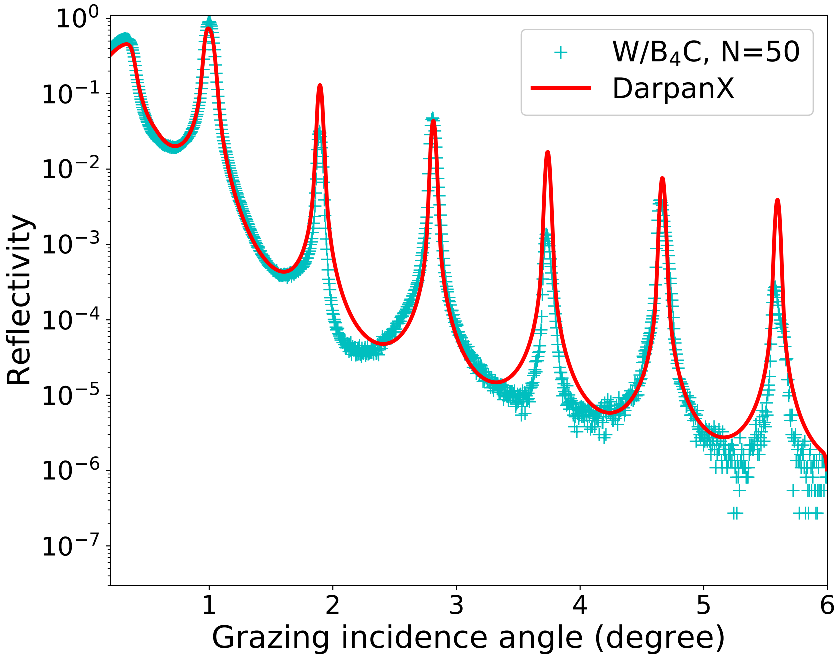

Figure 6.23: XRR reflectivity data(cyan) of W/B_4C multilayer sample (with N number of bi-layers) fitted (red) with constant period bilayer model of N=50. The fitted parameters are summarized in the first and second row of Table 6.3.

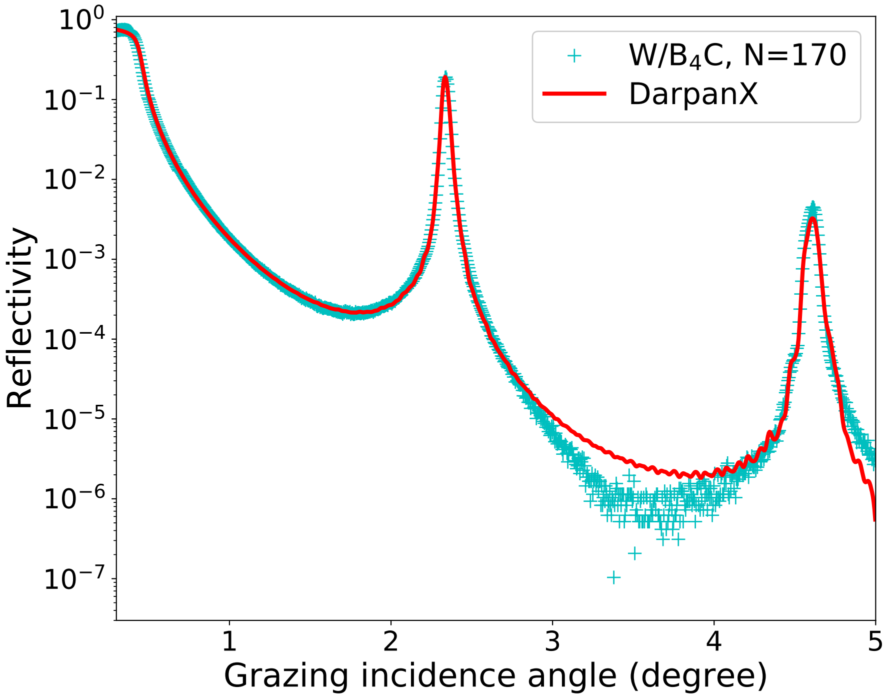

Figure 6.24: XRR reflectivity data(cyan) of W/B_4C multilayer sample of N=170 bi-layers fitted (red) with a cluster-graded model and considering the period and gamma are varying (Figure 6.27) in stacks.

the N=170 and N=50 bilayer systems as a succession of 10 and 5 blocks formed by 17 and 10 bilayers each. This type of multilayer structure is called cluster gradedJoensen et al. (1993). As a result, any period variation of the layers will be approximately modeled. We assume the density of B_4C, W, and the surface roughnesses of B_4C/W, W/B_4C- interfaces remain the same over the multilayer stack and keep them as free variables for fitting. The multilayer XRR data is fitted with an overall set of 27 (for N=170) and 18 (for N=50) free parameters, and the result is shown in Figure 6.24 and 6.6.1. Figure 6.27 shows the variation of the *period* and *gamma* to each block of 17 and 10 bilayers through the whole multilayer stacks. The best-fit parameters that are common to all blocks are shown in the third (for N=170) and fourth (for N=50) row of Table 6.3.

It is seen from the Figure 6.25, that the measured reflectivity curve is well modeled by DarpanX except for a slight difference between the higher Bragg peaks. These deviations may be because of the fact that the surface roughness values of B_4C/W and W/B_4C- interfaces are not the same throughout

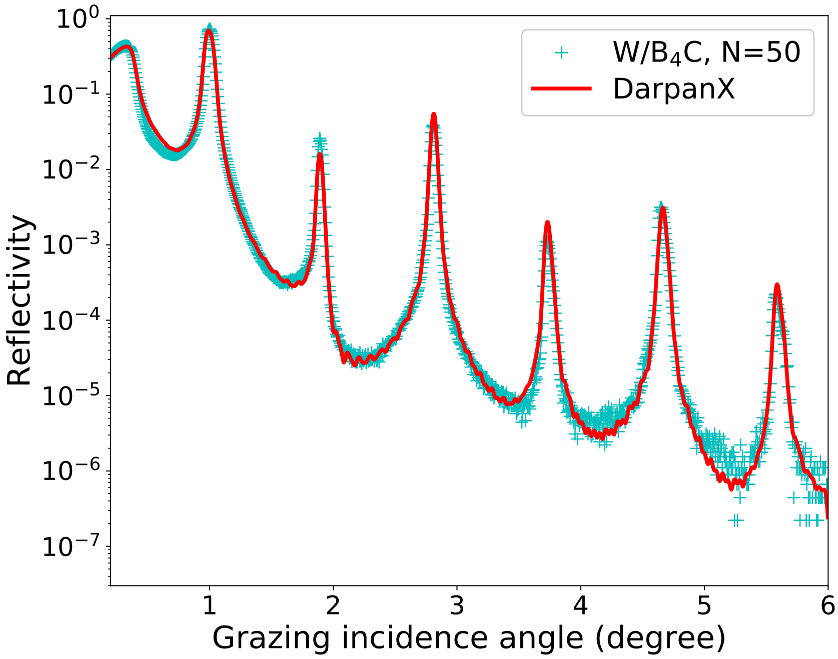

Figure 6.25: XRR reflectivity data(cyan) of W/B_4C multilayer sample of N=50 bi-layers fitted (red) with a cluster-graded model and considering the period and gamma are varying (Figure 6.27) in stacks.

the multilayer stack. In order to verify that, we keep the interlayer roughness values of each block of the cluster-graded model as a free variable. Figure 6.29 shows the fitted data. The variation of roughness, period and gamma with each block is shown in Figure 6.27. The best-fit parameters that are common to all blocks are shown in the fifth (for N=170) and sixth (for N=50) rows of Table 6.3.

The variation of period and gamma values within the different blocks of the cluster-graded model are less and it gives a better fit than the constant period bilayer model. Thus it can be seen that XRR data for the multilayer sample is well modeled with DarpanX providing measurements of multiple parameters.

The capability of the DarpanX model in PyXspec to fit the X-ray reflectivity measurements of single-layer and multilayer samples to obtain the parameters of the system is established with these results. It also offers flexibility to carry out fitting with complex definitions of a multilayer structure.

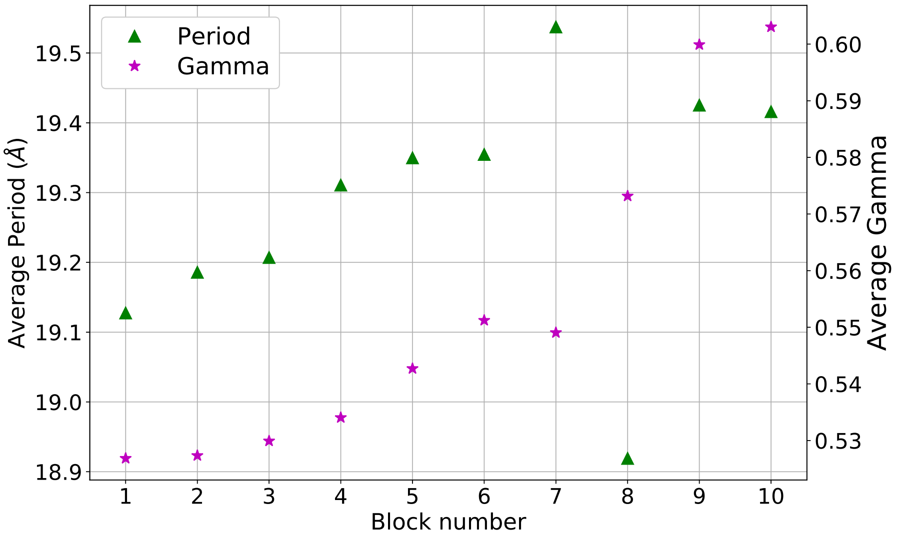

Figure 6.26: Variation of average *period* and Γ of W/B_4C bilayers at each block of cluster-graded model for sample N=170

6.7 Summary

We have initiated the development of the X-ray mirrors towards the potential use in the future Indian X-ray astronomy mission and, in this context, a multilayer coating facility based on RF magnetron sputtering technique has been set up. In order to design multilayer mirrors and to characterize them using X-ray reflectivity (XRR) measurements, we have developed the DarpanX package that computes the reflectivity and other optical functions of multilayer systems. It can be used as a model for the X-ray fitting software XSPEC, which has robust fitting capabilities and thus allows to estimations of various multilayer parameters. XSPEC has several physical models, which are generally used to fit the Astronomical data. So far there are no models present within XSPEC to fit the XRR data. DarpanX adds this missing capability to XSPEC and thus makes XRR fitting/modeling much more widely available. DarpanX has easy access to model the uncertain factor of the multilayer structure, such as cluster-graded or adding an extra top oxide layer/layers, etc. The DarpanX algorithms are extensively tested for various types of multilayer structures. It has been used to fit the experimentally measured X-ray reflectivity data for both single and multilayer samples and has been found to provide good fits.

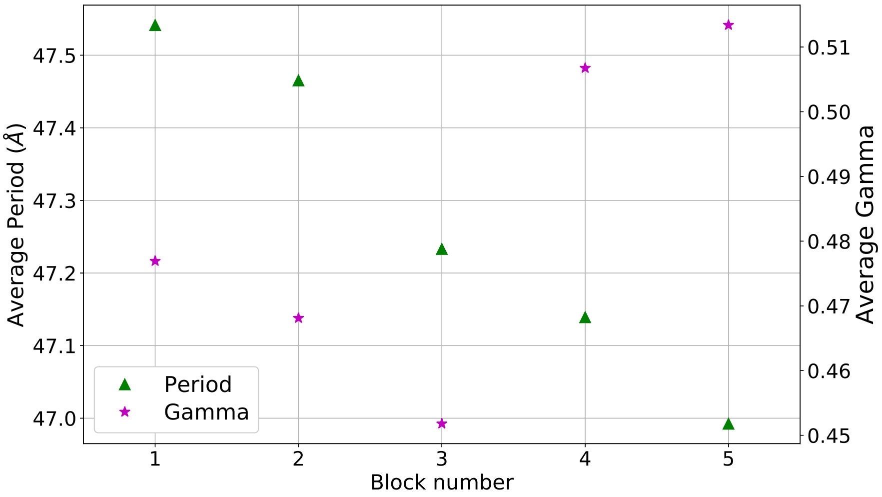

Figure 6.27: Variation of average *period* and Γ of W/B_4C bilayers at each block of cluster-graded model for sample N=50.

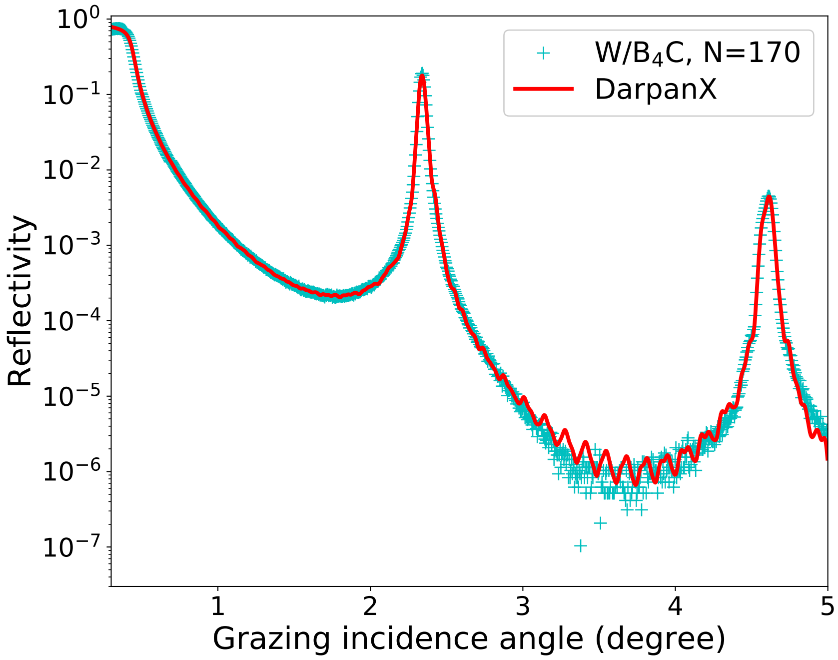

Figure 6.28: XRR reflectivity data(cyan) of W/B_4C multilayer sample of N=170 bi-layers fitted (red) with a cluster-graded model and considering the period, gamma and roughness values of W/B_4C and B_4C/W interfaces are varying (Figure 6.31) in stacks.

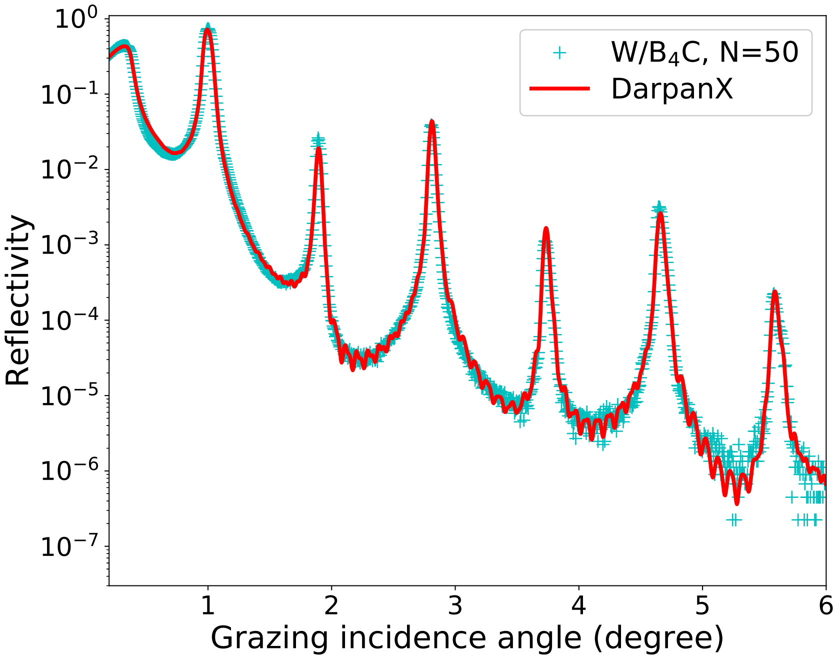

Figure 6.29: XRR reflectivity data(cyan) of W/B_4C multilayer sample of N=50 bi-layers fitted (red) with a cluster-graded model and considering the period, gamma and roughness values of W/B_4C and B_4C/W interfaces are varying (Figure 6.31) in stacks.

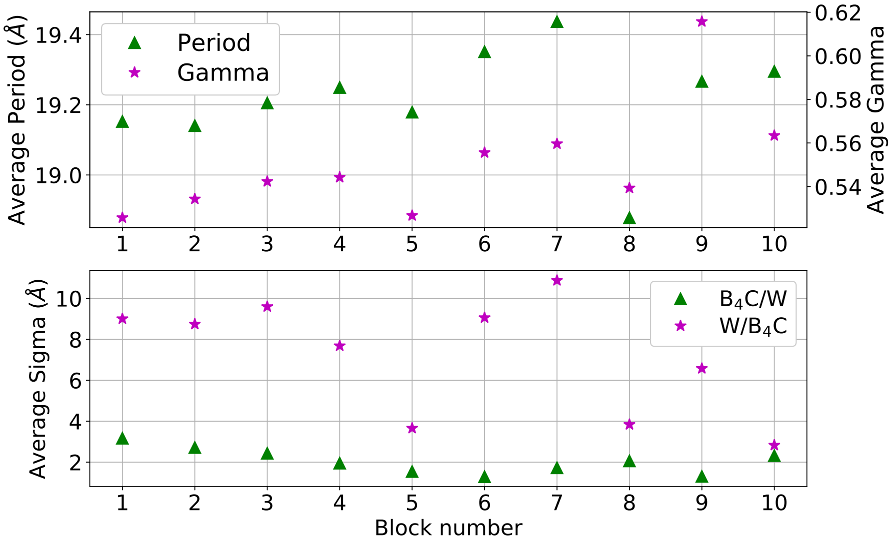

Figure 6.30: Variation of average *period*, Γ of W/B_4C bilayers and roughness values of W/B_4C and B_4C/W interfaces at each block of cluster-graded model for sample N=170.

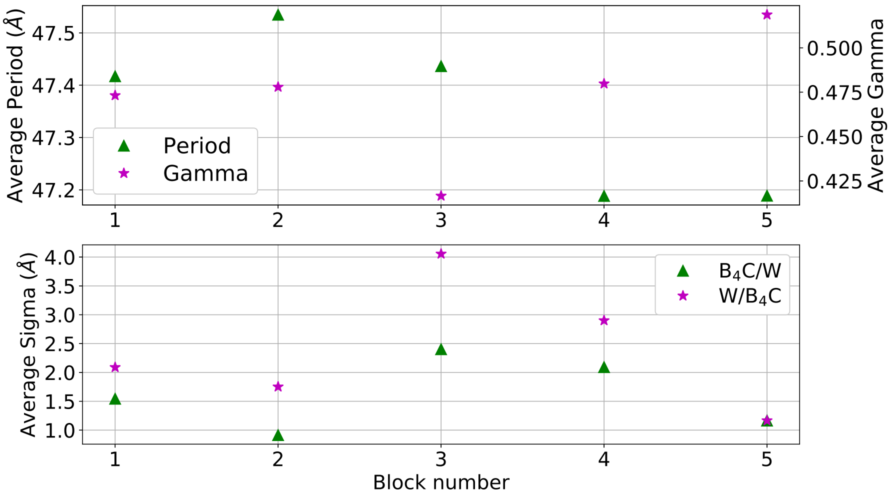

Figure 6.31: Variation of average *period*, Γ of W/B_4C bilayers and roughness values of W/B_4C and B_4C/W interfaces at each block of cluster-graded model for sample N=50.

DarpanX is developed in python3 and is packaged as a module that can be imported into interactive python shells or scripts. The scripting capability makes it easy to optimize the multilayer design to suit specific optical design or any other applicable constraints. Also, the parallel processing capability of DarpanX makes it faster in the case of a large number of iterations required for the calculation. DarpanX can be used as a stand-alone package to design any multilayer structure and estimate its physical properties.

DarpanX codes are publicly distributed and anybody can use/edit them or add different modules for other purposes. In the near future, it is planed to add the other module for the design of X-ray optics and estimate the different properties of it, such as the effective area of different types of optics, where the multilayer calculation will do by using the existing module and the other calculation (like geometrical calculation, etc.) will do by the new module. Also, an addition of a ray-tracing module to simulate the performance of the designed optics will be very helpful. The multilayer design and characterization, using DarpanX, of the X-ray mirrors for the future astronomical telescope will be reported in subsequent works.

Chapter 7

Conceptual design of Solar Imaging X-ray Spectrometer (SIXS)

A simultaneous imaging spectroscopic instrument in X-ray waveband is essential to understand the time and spatial evolution of the coronal plasma properties, as discussed in Chapter 6.1. However, with the lack of such an instrument, in the present thesis we have extensively used the disk-integrated spectroscopic observations of the Sun in the soft X-ray energy range. In this chapter, we describe a conceptual design of a soft X-ray imaging spectroscopic instrument for future missions.

7.1 Introduction

Broad-band spectroscopic observation of the Sun in the soft X-ray energy band with a good energy resolution is important to probe the coronal plasma properties (see Chapter 2.2), e.g., the FIP effect (Chapter ,1.3), coronal heating (Chapter ,1.2) etc. In the present thesis work we have extensively used the disk-integrated soft X-ray (1-15 keV) observations of the Sun by XSM to understand the FIP effect (Chapters 3, and 4) and the coronal heating (Chapter 5) problem. However, the lack of the imaging capability of XSM restricts probing the variation of the FIP effect and heating parameters (e.g., heating frequency) within different regions of the solar corona (e.g., within an AR) as discussed in Chapter 6 (Figure 6.1). To gain our knowledge of the mechanism behind the FIP effect, and coronal heating, along with several other phenomena (e.g., understanding the origin of the slow solar wind) we need a sensitive imaging spectroscopic observation in the soft X-ray energy range with a good energy resolution, and spatial resolution. Primarily, an imaging spectroscopic instrument requires X-ray optics along with a focal plane detector module. X-ray optics works in the grazing incident reflection of the X-rays by the X-ray mirrors, and we have initiated the development of the X-ray mirrors for future X-ray optics as discussed in Chapter 6. Here, we propose a conceptual design of a soft X-ray telescope named "*Solar Imaging X-ray Spectrometer (SIXS)*" for the simultaneous imaging spectroscopy of the Sun in the energy band of 0.5 keV to 15.0 keV.

SIXS consists of X-ray optics and a pixelated detector module, which can provide the spatial and energy information of the photons. A schematic diagram of the instrument is shown in Figure 7.1. Since such an X-ray telescope needs to be in space, it is important to consider the constraints imposed by the satellite platforms. Here we are considering, such a telescope onboard a future Indian satellite platform without requiring a deployment system that limits the focal length up to 200 cm. We choose a smaller size of the optics with a radius of 5 cm. The spatial resolution of the instrument is limited by the focal length and the detector pixel size. As the focal length is fixed to 200 cm, considering the availability of X-ray detector configurations, the spatial resolution of the instrument is restricted to $\sim 4''$, which is sufficient to achieve its scientific goals as discussed in Section 7.2. The specifications of the instrument are summarized in Table 7.1.

The rest of the chapter is organized as follows; Section 7.2 describes the primary scientific objectives. Section 7.3 and Section 7.4 describe the optics and detector descriptions. After discussing the capability of the instrument to achieve its science goals in Section 7.5, we summarize the work in Section 7.6.

Focal length	200.0 cm
Optics Diameter	10.0 cm
FOV	$> \pm 15'$
Energy resolution	better than 150 eV at 5.9 keV
Energy range	0.5-10 keV
Spatial Resolution	moderate ($\sim 4''$)

Table 7.1: Initial parameters of the SIXS.

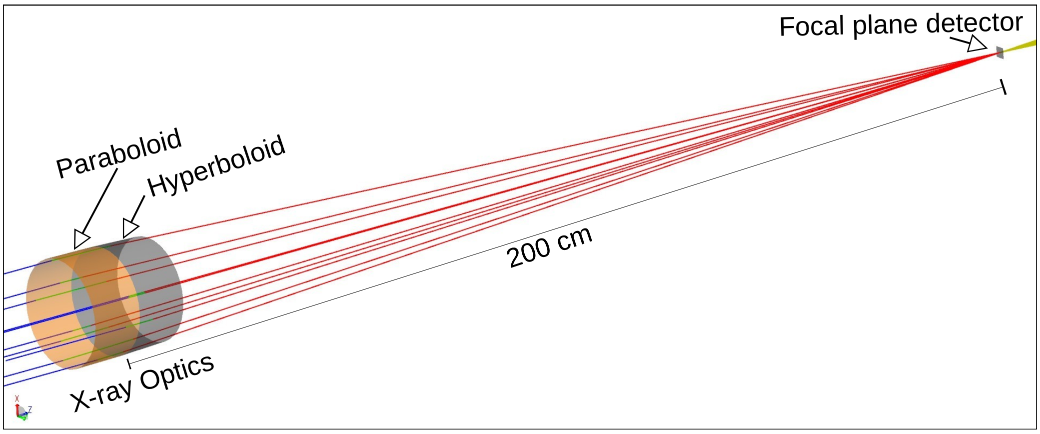

Figure 7.1: Schematic of ray tracing of the proposed SIXS instrument.

7.2 Scientific objectives

The broad-band spatially resolved X-ray spectral observation of the SIXS will enable to explore the various scientific problems in solar physics research. Some of these areas are described in the below Sections.

7.2.1 Determine the heating frequency of quiescent corona

Understanding the mechanism that heats the solar corona to several orders of magnitude higher than the surface temperature remains a long-standing problem in heliophysics. It is well accepted that the magnetic field of the Sun plays a crucial role in heating the corona. The foot-points of the magnetic fields are randomly moved by the convective motions below the photosphere, causing either building up the magnetic stress within the fields or generating waves depending on the time sale of motion (Klimchuk, 2006). Dissipation of magnetic stress (Parker, 1988) is known as DC heating, whereas the dissipation of waves (Alfvén, 1947) is known as AC heating. Most of the models explaining coronal heating suggest that the heating is impulsive in nature (Klimchuk, 2006), so-called nanoflare (Klimchuk, 2015) heating with a release of energies less than 10^{25} ergs. Though the direct observation of these small-scale heating is yet to be observed by the present generation instruments, it is believed that the time-scale of heating or their occurrence frequency is discriminated between different heating scenarios. Depending on their frequency, they are classified into two categories – High-Frequency (HF) and Low-Frequency (LF). In HF heating the cooling time scale is short compared with the time between successive events (T_{wait}). The plasma could not be cool enough between the events; in this case, the plasma would be heated steadily, resulting in almost isothermal plasma distribution (Klimchuk, 2017). On the other hand, for the LF heating, the plasma cooled significantly before the successive events, and the plasma may have a broad distribution of temperature at any particular time. Thus the temperature distribution of the plasma characterized by the Differential Emission Measure (DEM) or Emission Measure Distribution (EMD) (Chapter 2.5) determines the heating frequency (see Figure 2.17 of Chapter 2.6).

Several observational and theoretical studies have suggested that the "cool" portion of the EMD, below a peak temperature, T_m can be described by $\mathrm{EMD}(T < T_m) \sim T^{\alpha}$ (Carole, 1976; Cargill, 1994; Cargill & Klimchuk, 2004) whereas the "hot" portion can be described by $\mathrm{EMD}(T > T_m) \sim T^{-\beta}$. Though both the EMD slopes (α and β) are important diagnostic for determining the heating frequency, the present generation instruments with a little sensitivity at "hot" plasma limit the accurate estimation of the high-temperature slope, β (Winebarger et al., 2012). Definitive measurement of the high temperature (e.g., >5 MK for AR structures) plasma is primarily restricted by two factors – (i) The high-temperature plasma is expected to exist a little in amount compared with the cool (e.g., 2-5 MK for AR core) plasma and (ii) non-equilibrium ionization (NEI) at these high temperatures can forbid some of the emission lines (Bradshaw & Klimchuk, 2011). At present, the DEM estimation relies on the operating instruments in EUV and X-ray wave bands, including Atmospheric Imaging Assembly (AIA: Lemen et al. (2012)) onboard Solar Dynamic Observatory, X-ray telescope (XRT: Golub et al. (2007)) onboard the Hinode satellite, and EUV Imaging Spectrometer (EIS: Culhane et al. (2007)) onboard Hinode. AIA has several EUV channels primarily sensitive to sets of ionized Fe lines, whereas EIS is a spectrometer containing the elemental lines of Mg, Si, Fe, S, and Ca. XRT uses a combination of broad-band filters sensitive to soft X-rays from different ionized Fe emission lines integrated together. Among these instruments, XRT is useful to constrain the higher temperature DEM up to 6 MK for the AR core. Winebarger et al. (2012) showed that the DEM derived from XRT and EIS has a "blind spot" in measuring the high-temperature emission. They are not sensitive to measure the emission above 6 MK with an emission measure less than 10^{27} cm^{-5} for AR core.

In addition to producing line emissions, the heated plasma also generated continuum emissions, e.g., by thermal Bremsstrahlung (see Chapter 2.2), which is particularly noticeable at higher (e.g., > 4 keV) energies (Figure 2.5). The continuum emission is relaxed from the effect of NEI and is possible to detect by a sensitive instrument at higher energies, e.g., in hard X-rays. Detection of hard X-rays indicate the presence of very hot (> 8 MK) plasma. The hard X-ray observation is carried out in several instruments e.g., Reuven Ramaty High Energy Solar Spectroscopic Imager (RHESSI: Lin et al. (2002)), Spectrometer Telescope for Imaging X-rays (STIX: Krucker et al. (2020)) onboard Solar Orbiter etc. But most of these instrument uses an indirect imaging technique to image the hard X-rays and they are designed to observe the solar flares. The sensitivity of these instruments is less to study the quiescent corona. The sensitivity can be improved using X-ray optics, and it has been implemented in Focusing Optics X-ray Solar Imager (FOXSI: Krucker et al. (2014); Glesener et al. (2016)) sounding rocket experiment. The first three successful fight observations of FOXSI were used to constraint the DEM of quiescent AR (Ishikawa et al., 2017) and flaring ARs (Athiray et al., 2020). Ishikawa et al. (2017) found the evidence of very hot (> 10 MK) emission from quiescent AR that might indicate low-frequency heating. In addition, the Nuclear Spectroscopic Telescope Array (NuSTAR: Harrison et al. (2013)), which is a NASA Astrophysics Small Explorer mission, also uses X-ray optics. Though NuSTAR was not designed for the solar observations, it has observed the Sun several times and helps to constrain the high-temperature emission (e.g., Hannah et al. (2016)).

Thus, the detection of the continuum emission, at higher energies is an important task to measure the high-temperature emission and constraint the heating frequency of the quiescent corona. The XSM (see Chapter 2.3.2) spectrometer working in the energy range of 1-15 keV can observe the continuum. Though, XSM does not have any X-ray optics, because of its unique design, it has very good sensitivity and dynamic range. It provides the disk-integrated observation of the Sun. Using the XSM observation combined with AIA during the minimum of solar cycle 24, we have derived the DEM and have estimated the heating frequency of the average quiet Sun XBPs. The derived DEM showed that the low-temperature emission is constrained by AIA, whereas the high-temperature emission is constrained by the XSM (Chapter 5). XSM has a very good sensitivity to measure the high-temperature plasma emission, where the sensitivity of AIA drops off (Figure 2.12). However, the unavailability of imaging capability of XSM makes it impossible to determine the spatial variation of the heating frequency within the coronal structures which is important as the temperature is highly dynamic throughout the coronal structures. Determining the DEM map and hence the heating frequency of the coronal structures is possible using a spatially resolved XSM like spectroscopic observation. The proposed SIXS instrument will provide the spatially resoled spectrum in the energy range of 0.5-15 keV. Thus SIXS observations will be useful to determine the spatially resolved heating frequency of the coronal structures.

7.2.2 Constraining the flare frequency distribution

Earlier observations of the solar flares (above B class) found that their occurrence frequency as a function of energy follows a negative power law. The smaller flares occur more frequently than the larger flares. Thus extrapolating the observed flare frequency power-law at lower energies could infer the frequency of the nanoflares. However, in this case, we assume that the nanoflares follow the same power-law as high energetic flares, which might not be correct always. The

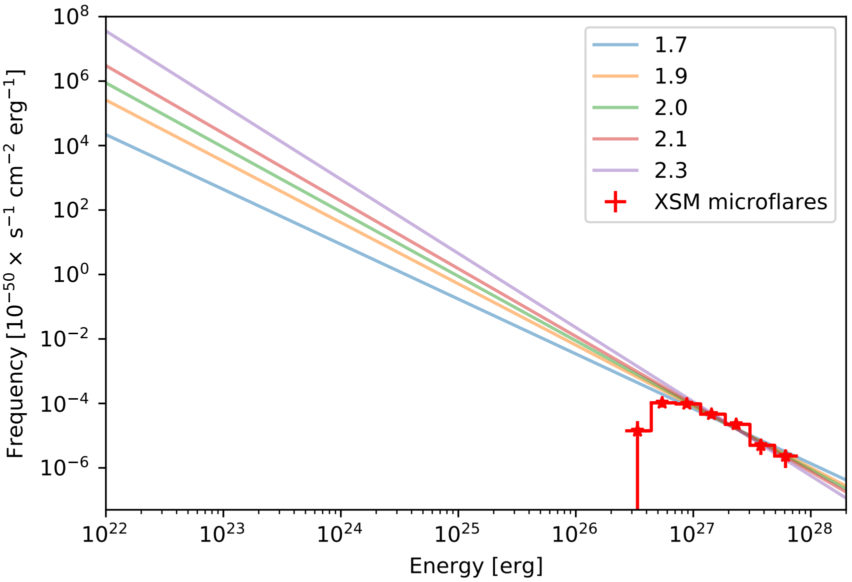

Figure 7.2: Flare frequency distribution. Red points are the XSM observed microflare frequency distribution and the solid lines represent power-law functions of different slopes, following the XSM microflare distribution.

slope of the flare frequency distribution is highly dependent on the detection statistics of both small (e.g., A-class or below) and large (e.g., B-lass and above) flares. Thus one of the prime focus in the field is to detect the smaller flaring events using a sensitive instrument to constrain the flare frequency distribution at both the low and high energies. The sensitivity of the XSM makes it possible to detect a large number of smaller sub-A class flares in the energy range of $\sim 3 \times 10^{26}$ ergs to $\sim 6 \times 10^{27}$ ergs (Vadawale et al., 2021b). These microflares are found to occur in the quiet Sun regions, outside the conventional ARs during the minimum of solar cycle 24. Figure 7.2 (red points) shows the frequency distribution of the XSM observed sub-A class flares. It is found that the observed distribution could be described by the power-law of slopes ranging from -1.7 to -2.3 (color solid lines). To constrain the power-law slope detection of smaller flares is necessary. Since XSM observes disk integrated emission, it can not detect very small flares in presence of X-ray emission from the rest of the corona. In the spatially resolved observations, such small flares need to be detected only against local background and hence much small flares can also be detected. The spatially resolved observations of the SIXS will provide the opportunity to detect such small flares to constraint the flare frequency distribution at lower energies.

7.2.3 Mapping the coronal abundances

In addition to the determination of coronal heating frequency to understand the coronal heating mechanism, another interest in the community is to understand the mechanism of the FIP effect, a phenomenon where the low-FIP elements are found to be 3-4 times higher (FIP bias) in abundant in the core of the ARs, compared to their photospheric values (see Chapter 1.3). Whereas the abundances of high-FIP elements are found to be either depleted or remain the same in the corona. Earlier studies found that the different coronal structures show different FIP biases, e.g., ARs have a FIP bias of ~ 3, whereas the XBPs have a value of ~ 2 (see Chapter 3). Though the true origin of the FIP effect is yet to be understood, in the quiescent corona, it is believed to be dependent on magnetic activity. The FIP bias is also found to vary during the evolution of solar flares which can provide us an important clue about the flaring mechanism and its relation to the FIP effect (see Chapter 4). The abundances are also found to vary with the solar wind speed. The slow-speed solar wind had an abundance close to coronal loop solar corona, whereas high-speed wind from polar coronal holes had a much lower amount of FIP fractionation (Von Steiger et al. (2000); Feldman et al. (1998); Bochsler (2007); Laming (2015)). Thus, the measurement of abundances at the different spatial regions on the solar disk can provide an important clue to the origin of the slow solar wind, which is another debatable topic of research in the entire solar physics community.

Measurements of the abundances in absolute scale, i.e., with respect to Hydrogen are non-trivial. Several high-resolution spectrometers have been used for the measurement of the abundances, but most of them provide the relative abundance of a low FIP element with respect to a high FIP element. Thus sometimes it is difficult to say whether the abundance of the low-FIP element is increased or the high-FIP element is decreased in the measured FIP bias. For example, the operating spectrometer, Hinode/EIS can measure the spatially resolved abundances but not on the absolute scale. Absolute measurements of the abundances require a simultaneous observation of the emission lines along with the continuum, where, the continuum is believed to depend primarily on the abundance of H. It is possible from a broad-band spectroscopic measurement with a good energy resolution in the X-ray energy band, e.g., 0.5 - 15.0 keV. The XSM measures the broad-band X-ray spectrum in the energy range of 1-15 keV with a very good energy resolution of better than 180 eV at 5.9 keV. Thus XSM can observe emission line complexes of different ionization states of several elements (e.g., Mg, Al, Si, S, etc) along with the continuum. XSM has been used to derive the elemental abundances of the quiet Sun XBPs (Chapter 3.3), ARs (Chapter 3.4), and during the evolution of small flares (Chapter 4). The XSM has the capability of measuring the abundances, with respect to the continuum. However, in the flaring temperatures, it has been seen that, continuum emission is slightly dependent on the abundances of the elements having a higher presence in the solar atmosphere (e.g., *O* or *Fe*; see Chapter 4.4, and Figure 4.16). The strong emission lines of O, and *Fe* are appear in the energy range of 0.5-1.0 keV. As the XSM can measure the X-ray spectrum from 1 keV onward, it is not possible to determine the abundances of O and Fe. Also due to the lack of imaging capability, XSM can not provide spatial information. As SIXS will provide the spatially resolved spectra in the energy range of 0.5-15 keV, it will provide the spatially resolved measurement of the abundances including O and Fe. The Spatially resolved measurement of the abundances will be useful to understand how the abundances are evolve within the different coronal structures and magnetic field activity.

7.2.4 Non-thermal emission of the quiescent corona

The presence of the non-thermal emission in the quiescent corona indicates the existence of the small-scale reconnection events producing the nanoflares that could heat the solar corona. At lower energies, the thermal emission of the solar corona is much higher than the non-thermal emission. However, the non-thermal emission usually dominates at higher X-ray energies (e.g., for the big flares it has been found to dominate much above 10 keV (Lin & Hudson, 1976; Benz, 2017)), where the thermal emission is very faint. The broad-band soft X-ray spectra of quiet Sun XBPs (Figure 3.6) and AR (Figure 3.9) observed by the

XSM found that the thermal spectrum is dominant up to an energy of ∼2.3 keV and 3.3 keV respectively and after that, the non-solar background emission dominates. The primary origin of this non-solar emission is Cosmic X-ray Background (CXB) (Mithun et al., 2020b). It is possible that the non-thermal emission from the quiescent corona is below the non-solar background emission observed by XSM. Thus, by reducing the background of the instrument, the existence of the non-thermal component could be possible to verify. Because of the larger field-of-view (FOV) and spatially integrated observation of the XSM, its background is higher but it will be much smaller in the proposed SIXS due to its imaging capability.

The solar corona is highly dynamic, e.g., the X-ray flux (1-8Å) can vary from 10^{-8} $W\ m^{-2}$ (A-class) to 10^{-4} $W\ m^{-2}$ (X-class). Thus designing an instrument to cover such a large dynamic range is challenging. As the primary scientific goal of the present design is to measure the X-ray spectrum during the small flares and from the quiescent corona, it is optimized for the sensitive measurement of the lower X-ray flux of activity (e.g., below the M-class). The larger solar flares are well studied in the last few decades by various instruments (above M class) and thus are not the prime focus of the SIXS. The above Sections (7.2.1-7.2.4) describe the few major scientific objectives of the SIXS. Apart from these, SIXS will also be able to provide important clues to understanding the many other interesting phenomena, e.g., the mechanism of the small class (e.g., B-class and below) of solar flares, which are less studied in the literature due to the lack of sensitive instruments.

7.3 Optics design

The proposed instrument consists of X-ray optics along with a pixelated detector module. We use Wolter-I optics to image the X-rays. Wolter-I geometry can provide an efficient imaging performance in X-ray and EUV wavelength. It has been used in a few earlier missions to image the Sun, e.g., XRT onboard Hinode or AIA onboard SDO. In this section, we estimate the design parameter of the required Wolter-I optics using the initial parameters summarized in Table 7.1.

A Wolter-I optics is consist of truncated parboiled and hyperboloid mirrors. Figure 7.3 shows a schematic of a Wolter-I design, where L_P and L_H are the length of the parabolic and hyperbolic surfaces, r_o is the radius of the optics, *Gap* is the mechanical gap between the parabolic and hyperbolic surfaces. We can write Equation of paraboloid, vertex at Z_P with a radius of P_r as:

$$r_p^2 = 2P_r(Z - Z_P) \tag{7.1}$$

Similarly the Equation of hyperboloid centered at Z_h is,

$$\frac{(Z - Z_h)^2}{a^2} - \frac{r_h^2}{b^2} = 1 \tag{7.2}$$

The eccentricity of the hyperbola is related with the semi-major (a) and semi-minor (b) axis as:

$$\epsilon = \sqrt{\frac{b^2}{a^2} + 1} \tag{7.3}$$

The separation between the two hyperboloid foci is $2a\epsilon$. Superposing the rear hyperboloid focus on the paraboloid focus, the front hyperboloid focus becomes the telescope focus as, $f = Z_f - Z_o$. Considering the origin of our coordinate system is at Z_1 in front of the paraboloid mirror's front edge, the paraboloid and hyperboloid vertex can be estimated from Equations 7.4 and Equations 7.5.

$$Z_P = Z_1 + L_P + \frac{Gap}{2} + f + 2a\epsilon + \frac{P_r}{2} \tag{7.4}$$

$$Z_h = Z_1 + L_P + \frac{Gap}{2} + f + a\epsilon \tag{7.5}$$

Thus, the optical design of a Wolter I telescope can be completely specified by the three independent parameters P_r, a, and b (or P_r, a, and ϵ).

An optimized (maximized effective collecting area) Wolter-I telescope is obtained by considering equal grazing angles of reflection from the paraboloid and the hyperboloid, near their point of intersection. This constraint reduces the number of independent parameters in the optical design to two. In our case,

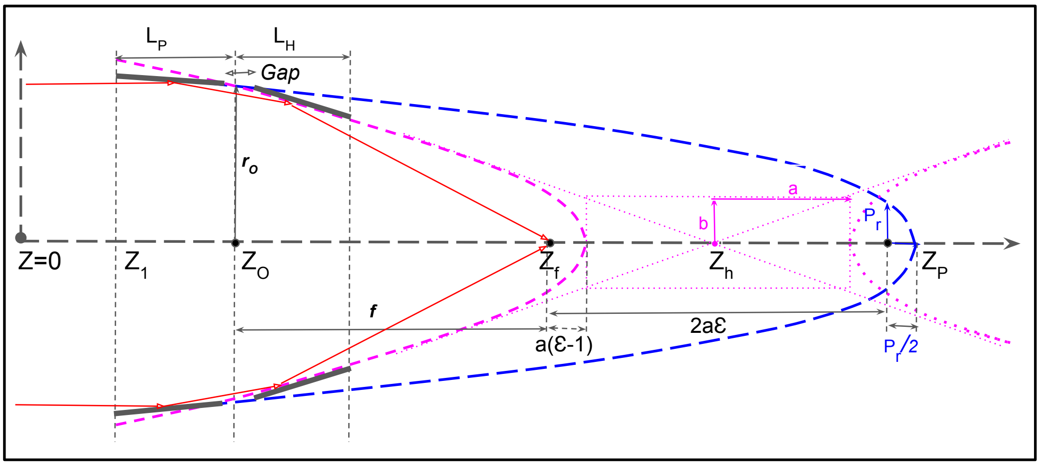

Figure 7.3: The geometry of the Wolter-I optics.

we choose the telescope radius at the intersection point of the paraboloid and hyperboloid mirrors as r_0, and the nominal focal length of f. Considering the r_0 and f as design parameters, the grazing angle (α) at the intersection and the other parameters associated with the paraboloid and hyperboloid mirror surfaces can be calculated as (Saha et al., 2004),

$$\alpha = \frac{1}{4}tan^{-1}(\frac{r_0}{f}) \tag{7.6}$$

$$P_r = -r_0 tan(\alpha) \tag{7.7}$$

$$\epsilon = \frac{1}{(2cos(2\alpha) - 1)} \tag{7.8}$$

$$P_h = \epsilon P_r \tag{7.9}$$

$$a = \frac{P_h}{\epsilon^2 - 1} \tag{7.10}$$

$$b = \sqrt{a \times P_h} \tag{7.11}$$

In addition to the telescope r_0 and f the optical design parameters include the length of the paraboloid mirror (L_P), hyperboloid mirror (L_H), and the mechanical gap between them at their intersection plane(Gap).

The on-axis collecting area of the Wolter-I optics can be easily estimated using Equation 7.12 (Pareschi et al., 2021).

$$A_0 = 8\pi f L \alpha^2 \tag{7.12}$$

From the ray tracing analysis van Speybroeck & Chase (1972) found that the geometric collecting area represented by Equation 7.12 varies with the off-axis angle (θ) as,

$$A_\theta = A_0(1 - \frac{2\theta}{\pi\alpha}) \tag{7.13}$$

Multiplying the geometrical collecting area with the reflectivity of the paraboloid and the hyperboloid mirror provides the effective area of the optics as follows:

$$A_{Eff}(\theta, E) = A_\theta R_P(\theta + \alpha, E) R_H(\theta + \alpha, E) \tag{7.14}$$

Here, $R_P(\theta + \alpha, E)$ and $R_H(\theta + \alpha, E)$ are the reflectivity of the paraboloid and the hyperboloid mirrors for the grazing incident reflection with an angle close to $(\theta + \alpha)$.

In our proposed design we consider a focal length (f) and radius (r_o) of the Wolter-I optics as 200 cm and 5 cm. The length of the parabolic (L_P) and hyperbolic (L_H) mirrors are chosen as 5 cm each. We also consider a mechanical gap (*Gap*) between the parabolic and hyperbolic mirrors as 0.1 cm. Considering a reflecting coating of single layer Iridium (Ir) of thickness 200 Å and surface roughness of 4 Å, we estimate the reflectivity of the mirror surfaces ($R_P(\theta+\alpha, E)$ and $R_H(\theta + \alpha, E)$) using the DarpanX code as discussed in Chapter 6. After estimating the reflectivity, we estimate the the on-axis and off-axis effective area using Equation 7.14 as shown in Figure 7.4a. The optics effective area is very good up to an energy of 10 keV and after that, it is reducing sharply because of the drop in the reflection efficiency of the mirrors. However, the higher energy reflectivity can be improved by using a multilayer coating instead of a single layer (see Chapter 6.2.2).

The Wolter-I optics can provide the perfect image for the on-axis sources. However, it does not follow the Abbe sign condition specifically for the off-axis sources, we need to know the rms blur circle radius (σ_D) of the Point Spread Function (PSF) at the focal plane that determines the performance of the optics. van Speybroeck & Chase (1972) provides an analytic expression of the rms blur circle radius of the Wolter-I optics that has been used by several

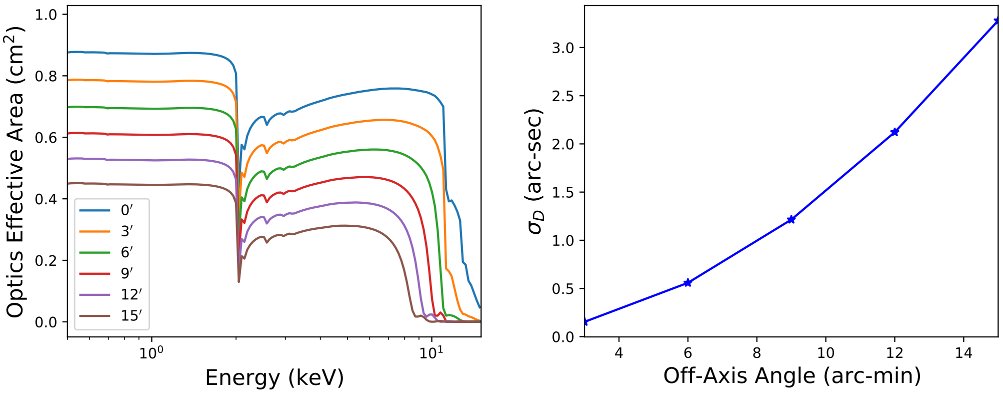

Figure 7.4: Panel **a**: Optics effective area as a function of energy for on-axis (blue solid line) and off-axis locations of the source. Panel **b**: Variation of the rms blur circle radius with off-axis angles of the source.

earlier studies and can be written as (Pareschi et al., 2021),

$$\sigma_D = 0.2\frac{tan^2(\theta)}{tan(\alpha)}\frac{L}{f} + 4tan(\theta)tan^2(\alpha) \tag{7.15}$$

Here, σ_D is in radian. The first term in the RHS represents the aberration effect mainly the spherical aberration and field curvature, while the second term represents the coma. Figure 7.4b shows the variation of the σ_D with the off-axis angles of the incident photons. We find that the designed optics can provide an RMS radius of less than 4 arc-sec within the required field-of-view (FOV) of $\pm 0.15'$ (radius of the Sun).

Using the initial parameters of r_0, f, L_P, L_H, and Gap we estimate the location of all the components of the optics to perform a ray-tracing analysis to see its performance. For this purpose, we use the non-sequential mode of ZEMAX ray-tracing software. Figure 7.1 shows the design of the optics within ZEMAX, where sets of a parallel beam of rays are incident on the optics which is further focused at its focal plane at f=200 cm. The details of the ray-tracing results and their comparison with the analytic results as discussed in the previous sections will be reported in future work.

We have estimated the effective area and σ_D of the optics. However, in reality, both the effective area and σ_D of the telescope also depend on the detector properties e.g., efficiency (or quantum efficiency), number of resolving elements or pixels, etc. In Section 7.4 we describe the possibility of using different types of detectors.

7.4 Detector module

The idea of the present design is to achieve spatially resolved spectroscopic measurements using a pixelated array of calibrated detectors that can estimate the energy of the incident photons (see Chapter 2.3.1). In this case, the energy resolution, spatial resolution, cadence, and sensitivity of the instrument are largely dependent on the detector properties. Choosing a detector for SIXS should satisfy the below list of criteria (CR):

CR-I : The detector efficiency should be capable to detect the X-rays in the energy range of 0.5 keV to 15 keV with a spectral resolution of better than 150 eV at 5.9 keV.

CR-II : Spatial resolution, which depends on the pixel size of the detector. Considering the 200 cm of focal length with a moderate spatial resolution of $4''$, in our case, the pixel size should be smaller than 40 μm.

CR-III : The cadence should be better than a few seconds.

CR-IV : The dynamic range should be capable to detect the photon counts from quiet Sun to moderate solar flares.

In the below sections, We describe the different possible detectors that can fulfill the required specifications mentioned above.

X-ray CCD: One possibility of using the X-ray CCD detector consists of multiple small pixels arranged in a compact volume. CCDs are a very efficient position-sensitive detector and are used in multiple missions (e.g., Chandra X-ray Observatory (Garmire et al., 2003), XMM-Newton (Strüder et al., 2001a), Swift XRT (Godet et al., 2007)) to achieve imaging spectroscopic studies for astronomical sources. X-ray CCD technology is now well established and can easily be possible to achieve the required energy resolution (CR-I) and spatial resolution (CR-II). However, the problem with using CCD is its limited dynamic range of detecting photons (CR-III). If multiple photons fall on a few close-by pixels within the single read-out frame, it is measured as a single photon of energy equal to the added energies of all the photons. This phenomenon is known as the *pile-up* of photons. It causes the CCD to inefficiently energy measurements of very bright sources (e.g., solar flares). As the X-ray activity of the Sun is very dynamic from very low (e.g., quiescent corona) to high (e.g., large solar flares) values, using CCD for solar imaging spectroscopic observation is challenging and requires a proper optimization of the instrument. However, as the SIXS is designed to observe the quiescent solar corona as well as the small flares, the X-ray CCD, similar to the EPIC pn-CCD used in XMM-Newton will fulfill the requirements.

Position sensitive SDD: The Silicon Drift Detector (SDD: Chapter 2.3.2) can be optimized for the required dynamic range (CR-IV), cadence (CR-III), and energy resolution (CR-I). An SDD is used in XSM for the disk-integrated spectroscopic observation of the Sun, and we found its performance is very good for an X-ray spectroscopic observation from quiet solar corona to large solar flares (see Figure 2.10). But at present, the pixelated SDD arrays are not readily available commercially for position-sensitive spectral measurements. Developing the SDD array is an active topic of research and development at various places (e.g., Evangelista et al. (2018)). Evangelista et al. (2018) designed and developed a 4×4 array of SDD with a pixel area of $500\mu m \times 500\mu m$. Considering the present technological developments, an SDD array will be the best detector for future imaging spectroscopic instruments.

X-ray microcalorimeter: The X-ray microcalorimeter array can achieve the required specification (CR-I to CR-IV). X-ray microcalorimeter array is the major advance recently made in the transition-edge sensor (TES) detector technology that enables energy resolution of better than a few eV ($<$ 10 eV Bandler et al. (2019); Doriese et al. (2017)), which is much better than our requirement. But these kinds of detectors are challenging to develop as they work in a very low-temperature environment cooled by cryogenic technology. A very few astronomical missions (e.g, Suzaku XRS: Kelley et al. (2007), Hitomi: Eckart et al. (2016)) employed this type of detector for the imaging spectroscopic observation of astrophysical sources. However, these types of detectors are yet to be considered for solar observation. A recent white paper by Laming et al. (2010) talking about the scientific objective of the X-ray microcalorimeter for solar observations.

In the present day, as the X-ray CCD technology becomes mature enough to be used in space-based instrumentation, we consider a CCD array as a detector for the SIXS. The efficiency of the normal X-ray CCDs is poor at higher energies (e.g., > 2 keV). Thus we propose to use the pn-CCD (Strüder et al., 2001b), similar to the one used in XMM-Newton. We derive the quantum efficiency (QE) of the detector consisting of an oxide layer of 20 nm followed by a $300\mu m$ Si block. For this purpose, we use the X-ray form factor data available from the NIST. The derived QE curve is shown in Figure 7.5. Convolution of the QE, with the optics effective area as shown in Figure 7.4a, provides the net effective area of the instrument as shown in Figure 7.6.

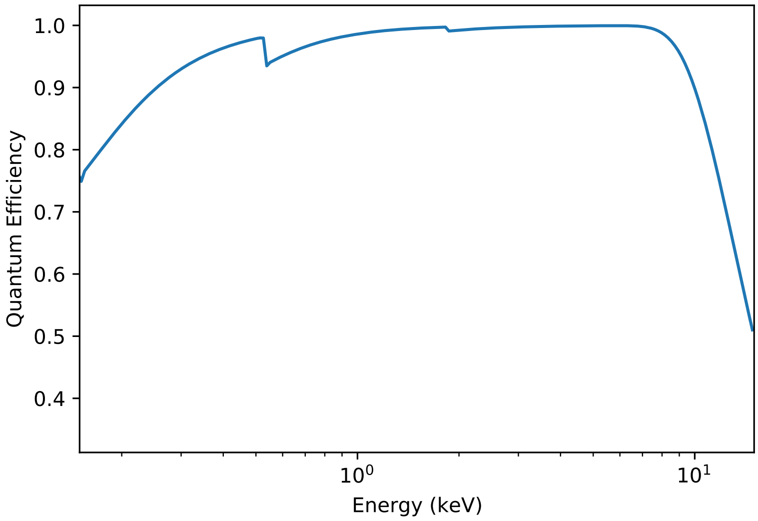

Figure 7.5: Quantum efficiency of pn-CCD.

7.5 Instrument capability

To achieve the science objectives mentioned in Section 7.2, the proposed instrument should have the following capabilities:

SO-I. Detection sub-A class solar flares whose peak flux in the GOES 1-8Å

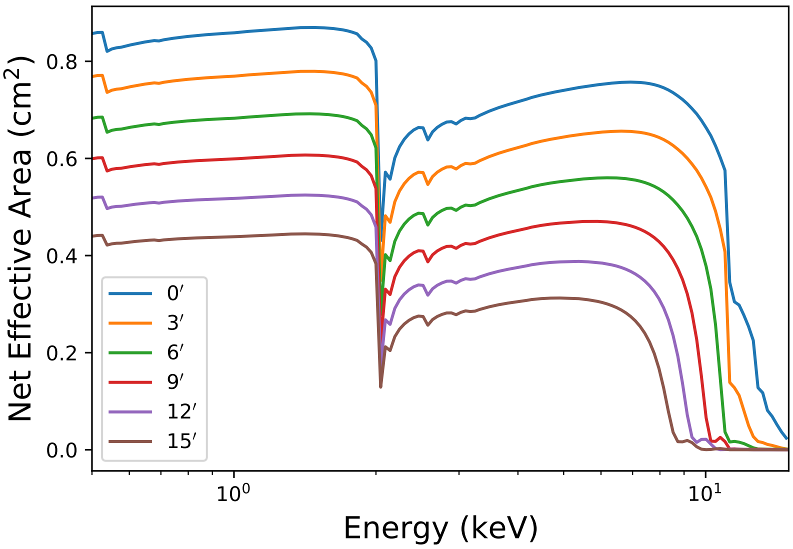

Figure 7.6: Net effective area of the proposed instrument.

channel is below 10^{-8} Wm^{-2} to constraint the flare frequency distribution at lower energies (Section 7.2.2).

SO-II. Sensitivity of detecting the hot plasma of low emission measure to constraint the heating frequency of the quiescent corona (Section 7.2.1).

SO-III. Measuring the absolute elemental abundances of the solar corona and their evolution (Section 7.2.3).

SO-IV. Non-solar background of the instrument should be small enough to verify the presence of the non-thermal emission from the quiescent solar corona (Section 7.2.4).

In the following sections We discuss each of the points mentioned above.

7.5.1 Detection of sub-A class flares

The sensitivity of the instrument to detect the smallest solar flare could be estimated by simulating the observed spectra for different classes of solar flares and comparing them with the spectra of background non-flaring solar corona. If the flare spectrum is higher than the background spectrum then only the instrument will be able to detect that flare. For this purpose, we simulate the flare spectra using the temperature and emission measure values from the earlier observations and theoretical predictions. Figure 7.7 show the EM versus temperature for the lowest X-ray flares observed by the various instrument reported in the earlier studies. The dashed lines in the figure represent the Isoflux curves corresponding to 1–8 Å flux. For example, the blue points are the sub-A class (A0.01-A0.1) flares (Vadawale et al., 2021b) found to occur in the quiet Sun, whereas the cyan points represent the A-class flares in the AR (Lakshitha et al., 2022) as observed by XSM, during the minimum of solar cycle 24. We simulate the expected X-ray spectra for the SIXS for the solar flares of A0.00001-B1 by choosing the typical temperature and EM values from the Isoflux curves as shown by green boxes in Figure 7.7. Figure 7.8 shows the simulated spectra for all the flare classes.

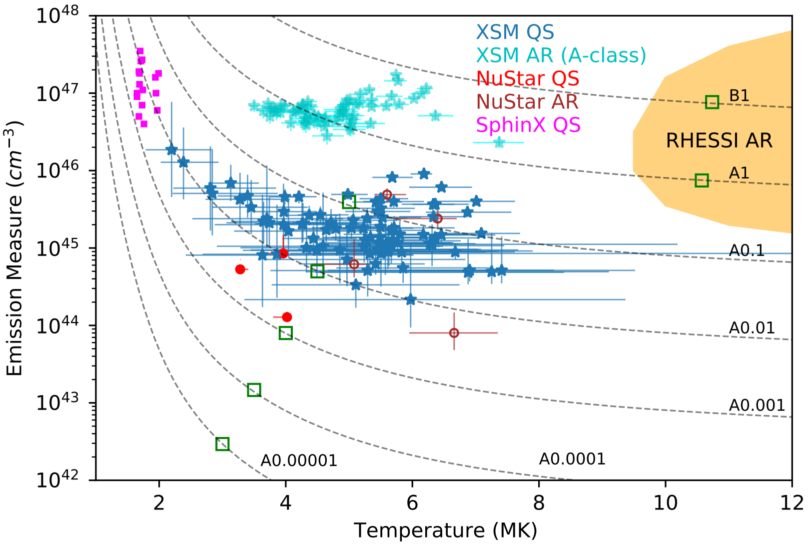

Figure 7.7: The temperature and EM of the observed X-ray solar flares by different instruments are reported in the literature. Note that we have not included the larger solar flares (e.g., C-class and above). Blue and cyan points with error bars represent the sub-A class and A-class flares observed by XSM, within the quiet-Sun (Vadawale et al., 2021b) and ARs (Lakshitha et al., 2022) respectively. Pink, red, and brown points represent the flares observed by SphinX (Sylwester et al., 2019) and NuSTAR (Glesener et al., 2017; Wright et al., 2017; Hannah et al., 2019; Cooper et al., 2020), respectively. The orange shaded region represents the parameter space for the small AR flares observed by RHESSI (Hannah et al., 2008). The dashed lines show the Isoflux curves corresponding to 1–8 Å X-ray flux levels from A0.00001 (10^{-13} W m^{-2}) to B1 (10^{-7} W m^{-2}). The green square points represent the parameter values used for the simulated spectra as mentioned in the text.

Most of the quiet Sun sub-A class flares (blue error bars in Figure 7.7) observed by XSM were found to be associated with the X-ray Bright Point

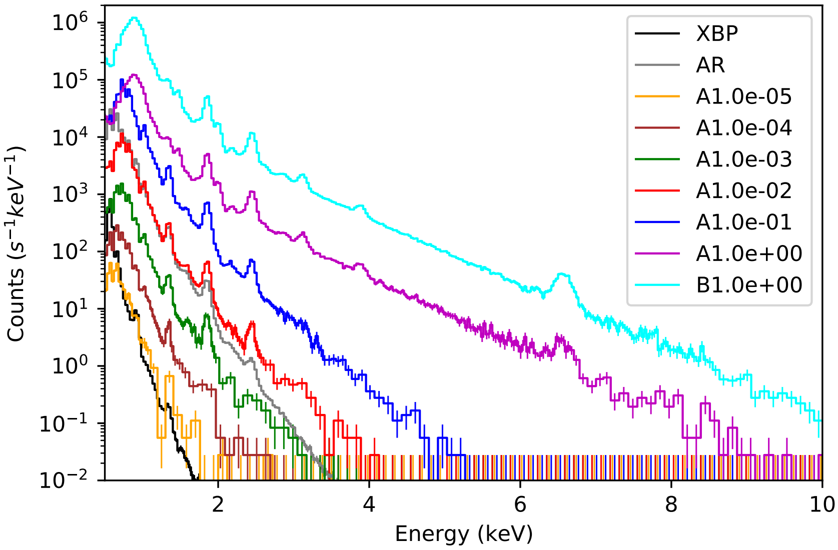

Figure 7.8: Simulated spectra of the XBP (black), AR (grey), and different classes of the solar flare as observed by the proposed instrument.

(XBP). Thus, for the quiet Sun sub-A class flares the background non-flaring emission from the flaring region originates from the XBP emission. Using the DEM of the XBP (Figure 5.6a, blue color), we derive the expected spectrum observed by the SIXS from a resolving element of $4'' \times 4''$ as shown in Figure 7.7 (black color). We find that the spectrum of the Ae-5 class flare is almost comparable with the non-flaring XBP spectrum that concludes the emission from this flare is difficult to distinguish from the non-flaring emission. Whereas the spectrum of the Ae-4 flare is one order of magnitude higher than the XBP spectrum. Thus the SIXS might be able to detect the flare above the Ae-4 class, which is two orders of magnitude lower than the XSM observed sub-A class (A0.01) flares in the quiet Sun regions. This will be useful to fill the gap of the quiet Sun flare frequency distribution at lower energies ($< 10^{26}$ erg in Figure 7.2) to constrain the flare frequency distribution.

Similarly, we simulate the expected AR spectrum corresponding to a resolving element of $4'' \times 4''$ area on the Sun (grey color). For this purpose, we have used the AR DEM reported by Del Zanna (2013). Comparing the quiescent AR spectrum with the flaring spectrum, we conclude that the SIXS will be able to detect the 0.1A-class flares and above within the ARs.

7.5.2 Constraining the heating frequency in quiescent corona

One of the scientific goals of the SIXS is to determine the heating frequency of the quiescent corona by deriving the 'hot' part of the DEM. Deriving the hot part of the DEM requires the sensitivity of the instrument to detect the emission from very hot plasma, which is known to exist in a small amount in the quiescent corona (Section 7.2.1). For this purpose, we derive the temperature response function of SIXS by dividing its energy band (0.5-15 keV) into multiple channels on a logarithmic scale of $\Delta logE = 0.1$. The temperature responses are constructed from individual isothermal emission models over a logarithmic grids ($\Delta logT = 0.1$) from $logT = 5.0$ to $logT = 7.5$ (see Chapter 2.3.4) and using the coronal abundances compiled in the CHIANTI database of "$sun\_coronal\_feldman\_1992\_ext.abund$". Solid curves in Figure 7.9 show the derived temperature response functions. All of these response functions are less sensitive at lower temperatures, whereas at high temperatures their sensitivity is more. This is because of the fact that the high-temperature plasma mostly emits the X-rays whereas the low-temperature plasma emits in the EUV waveband. Thus we combine the X-ray observations of the SIXS with the operating EUV observation (e.g., AIA), to detect the plasma at both low and high temperatures. The dashed curves in Figure 7.9 show the temperature response functions for AIA channels (see Chapter 2.4.3).

To estimate the capability of detecting the heating frequency, we simulate a typical coronal loop heated by (i) low-frequency (LF) events and (ii) high-frequency (HF) events separately and estimate the DEM for each case. For this purpose, we use the EBTEL++ code (see Chapter 2.6). Using the model DEM we estimate the expected counts of the AIA and SIXS energy bands and then using these estimated counts we recover the DEM. We use the Regularized Inversion method for the DEM recovery as described in Chapter 2.5.3. Consider a typical AR loop of half-length 40 Mm that is heated by the LF and HF events of the triangular heating profile of peak heating rate, H_0 and waiting time of T_{wait} between the events (see Chapter 5.4.2 for details of EBTEL++ heating

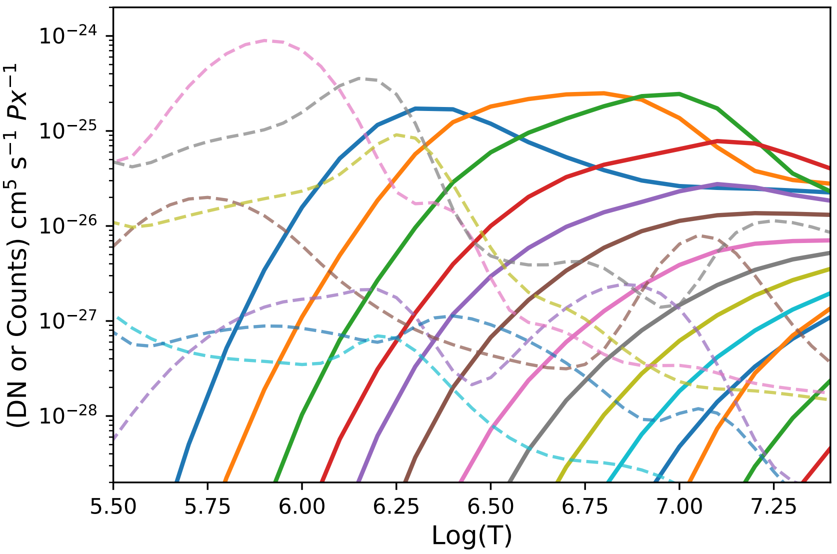

Figure 7.9: Temperature response functions for the AIA channels (dashed curves) and for the SXIS (solid curves). The unit of y-axis is 'DN cm^5 s^{-1} Px^{-1}' for AIA and 'Counts cm^5 s^{-1} Px^{-1}' for SXIS.

profile).

LF heating events: We simulate the AR loop heated by LF events of different waiting times (T_{wait}) and the heating rate as provided in Table 7.2. Figure 7.10a shows the temperature evolution of the simulated loop and the dashed curves in Figure 7.10b show the simulated DEMs for different LF events. From the simulated DEM (dashed curves) we recover the observed DEM as shown by error bars. The emission measure loci curves for the heating events of $T_{wait} = 8000s$ are shown in the same plot (magenta color). We find that the high-temperature DEM is well-matched with the simulated DEM, whereas the low-temperature DEM deviates slightly. This is due to the fact that the low-temperature DEM is constrained by the AIA channels which are broad-band.

HF heating events: We simulate the AR loop heated by HF events of different waiting times and the heating rate as provided in Table 7.2. Figure 7.11a shows the temperature evolution of the simulated loop and the dashed curves in Figure 7.11b show the simulated DEM for different HF events. We recover the observed DEMs from the simulated counts at different energy bands of AIA and SIXS. The observed DEMs are shown by error bars, which are well agreed with the model DEMs (dashed curves).

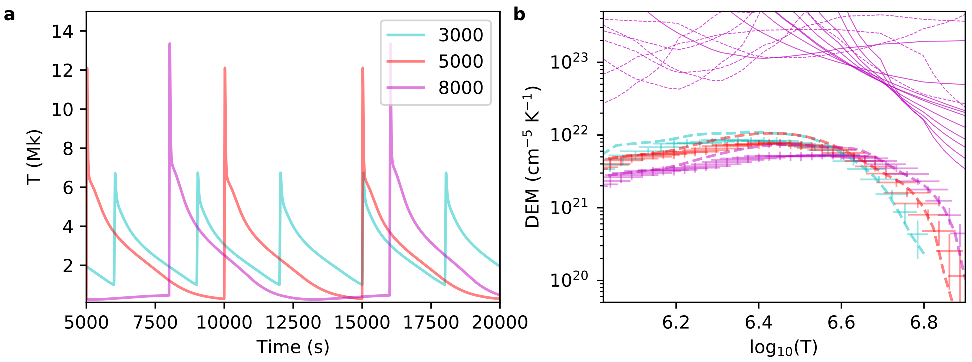

Figure 7.10: Panel **a** represents the temperature evolution with time for an AR loop of half-length 40 Mm, heated by LF frequency heating of different heating timescales (T_{wait}), as mentioned in the legend. Panel **b** shows the simulated DEM (dashed curves) of the different heating events represented in the same color as Panel **a**and error bars represent the observed DEM from the simulated data. The pink dotted and solid curves represent the loci curves observed by the AIA and SIXS channels for the T_{wait} = 8000 case.

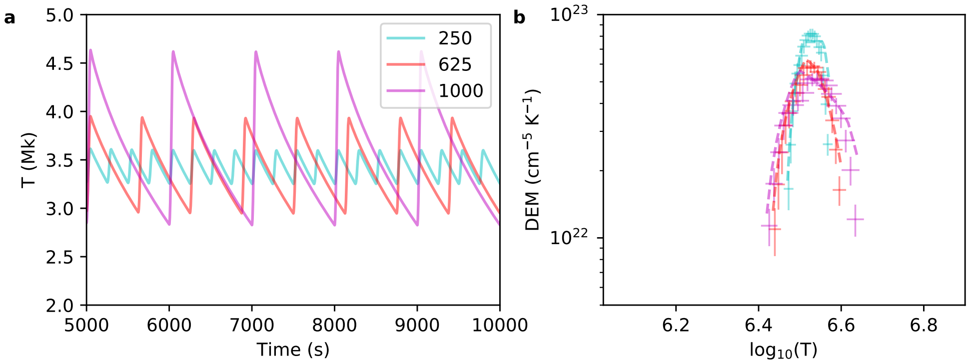

Figure 7.11: Same as Figure 7.10 but the loop is heated with HF events of different T_{wait} as mentioned in the legend of Panel **a**

7.5.3 Measuring the spatially resolved elemental abundance

The SIXS instrument is designed to measure spatially resolved emissions from both the spectral lines and continuum. The energy band (0.5-15.0 keV) and the energy resolution of better than 150 eV at 5.9 keV for the SIXS are sufficient to detect the line complex of the elements O, Fe, Mg, Al, Si, S, Ar, Ca, and Ni depending on the plasma temperatures. For example, Figure 7.12 shows the expected spectrum of a single SIXS pixel for quiet Sun XBP (black curve) and quiescent AR (grey curve). SIXS will provide the spatially resolved elemental abundance map of the coronal structures (e.g., ARs) along with the time evolu-

Events	T_{wait} s	H_0 erg s^{-1} cm^{-3}
LF	3000	0.15
	5000	0.25
	8000	0.35
HF	250	0.02
	625	0.05
	1000	0.1

Table 7.2: Simulation parameters for an AR loop of 40 Mm heated by LF and HF heating events.

tion of the abundances during small solar flares. These capabilities of SIXS will fulfill one of the major scientific objectives discussed in Section 7.2.3.

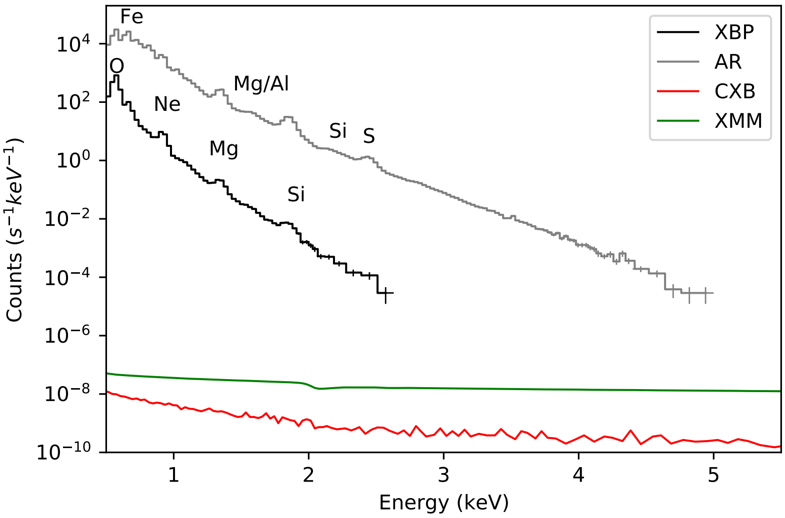

Figure 7.12: Expected spectrum of a single pixel of the SIXS for XBP (black) and AR (grey). The background emission detected by a single resolving element is also shown by red and green curves. The red curve represents the background contribution by CXB and the green curve is derived from the observed background by XMM-Newton.

7.5.4 Detection of non-thermal emission is quiescent corona

Determining the non-thermal component of the quiescent solar corona requires detecting the X-ray photons at higher energies, e.g., above 3 keV for XBP (Section 7.2.4). For these, the instrument's non-solar background should be small.

One of the prime sources of non-solar X-ray emission is CXB photons. However, the focusing capabilities of the SIXS are helpful to reject the CXB photons coming from random directions to reach the detector plane. We estimate the expected CXB emission by SIXS using the CXB model provided by Türler et al. (2010). The CXB model Türler et al. (2010) for the unit solid angle is multiplied by the solid angle of a single resolving element of SIXS and then convolved with the SIXS response matrix. The CXB spectrum of a single resolving element of SIXS is shown by the red curve in Figure 7.12. We find that the CXB spectrum of a single-pixel of SIXS is much smaller and the total count rate of 1.48×10^{-8} c/s. In addition to the CXB, the detector noise and the satellite platform will also contribute to the total background of the instrument. Thus, we estimate the typical background of SIXS from the observed background emission of XMM-Newton, normalized with the SIXS effective area of a single pixel, as shown by the green color in Figure 7.12. We find that the background of the SIXS is much smaller, which will be able to verify the detection of the non-thermal component of the quiescent solar corona at higher energies.

7.6 Summary

We have provided a conceptual design for the Solar Imaging X-ray Spectrometer (SIXS), which operates in the X-ray energy range of 0.5-15.0 keV. The instrument has an energy resolution of greater than 150 eV at 5.9 keV and a spatial resolution of $4''$. Numerous significant, long-standing issues in heliophysics can be solved by the suggested design. It will be able to aid in our knowledge of the FIP effect and coronal heating, two significant issues in astrophysics. The proposed SIXS's primary scientific goals have been described, and in order to attain these goals, we have tested the instrument's performance. The SIXS might be implemented with the current technology within five to eight years because of its simple design.

Chapter 8

Summary and Future Work

8.1 Summary

Since it was discovered that the solar corona has a temperature in the millions of degrees Kelvin, making it much hotter than the sun's surface, the actual physical mechanism underlying this phenomenon has remained a mystery. Based on our current understanding of the issue, it is thought that the corona is heated by the continual deposition of small-scale energy. An essential indicator of the underlying heating mechanisms is the frequency of the energy deposition.

When compared to the lower atmosphere, the solar corona's elements (such as Fe, O, Ni, etc.) are strongly ionized due to the high temperature. Their relative quantities are expected to remain constant throughout the solar atmosphere because the plasma's source is the same. However, the EUV and X-ray spectroscopic observation discovered that the elements with First Ionization Potential (FIP) less than 10 eV (known as low FIP elements) are 3-4 times higher (FIP bias) in abundance within the closed-loop active corona than their photospheric abundances. While the elements with FIP greater than 10 eV (high FIP elements) are found to be almost the same or depleted in the corona. The precise cause of this phenomenon, known as the "FIP Effect", is still a mystery. However, in light of contemporary knowledge, it is thought that the FIP effect is a byproduct of the coronal heating mechanism.

We use X-ray spectroscopic measurements of the sun made by the Solar

X-ray Monitor (XSM) onboard India's Chandrayaan-2 satellite to understand the FIP effect in different coronal features (ARs, XBPs, and small solar flares) as well as to comprehend the heating frequency of the quiescent XBPs. XSM is a new generation broadband spectrometer that operates in the soft X-ray energy range of 1 to 15 keV. XSM offers a good energy resolution of better than 180 eV at 5.9 keV, the highest sensitivity in this energy range, and the fastest cadence (1s). We also used observations from other instruments, such as the Helioseismic and Magnetic Imager (HMI) on the Solar Dynamic Observatory (SDO), and the X-ray telescope (XRT) on the Hinode satellite, and the Atmospheric Imaging Assembly (AIA) on the Solar Dynamic Observatory (SDO). Additionally, we have taken advantage of the hydrodynamic models of the coronal loops to interpret our results in determining the coronal heating frequency.

In order to understand both the FIP effect and the coronal heating issue, we are emphasizing the need for future imaging spectroscopic investigations of the Sun in the X-ray energy range. In preparation for the anticipated need for X-ray optics in the future imaging spectroscopic instrument, we have started the development of X-ray mirrors. For the next expedition, we present a conceptual design for the solar imaging X-ray spectroscopic instrument. The key findings of this thesis work are summarised in the sections below:

Chapter 3: XSM carried out a prolonged observation during the minimum of solar cycle 24, covering the years 2019-2020. Looking into the number of sunspot-less days, this was the quietest solar minimum in the last hundred years. By modeling broadband X-ray spectra from XSM, we estimate the temperature and emission measure of the AR and quiet Sun XBPs. We also obtain the abundances of Mg, Al, and Si relative to H. We find that the derived parameters of AR and quiet Sun XBPs remain nearly constant over time with a temperature around $\sim$3 MK and $\sim$2 MK, respectively. The obtained abundances of Mg, Al, and Si show the FIP bias $\sim$2 for quiet Sun XBPs, which is lower than the values obtained in active regions ($\sim$3). This is the first time we have provided a prolonged study of the abundances of XBPs, and shows a lower FIP bias compared with the ARs. The results are consistent with the ponderomotive force model of the FIP effect, which is widely considered to be responsible for the coronal FIP bias. Having the lower magnetic activity of the XBPs, it is expected to have a low FIP bias compared with the ARs.

Chapter 4: During the minimum of Solar Cycle 24, XSM observed nine B-class flares ranging from B1.3 to B4.5. Using time-resolved spectroscopic analysis during these flares, for the first time, we examined the evolution of FIP bias during the small flares. Our results suggest a variation of FIP bias during the flares, and we propose two scenarios to explain the results. The first scenario is based on the evaporation velocity of the flaring plasma from the lower to the upper atmosphere, and the second one relies on the flare-driven Alfvén waves.

Chapter 5: Utilizing the unique X-ray observations of XSM and combined with EUV observations of AIA/SDO, we have estimated the plasma emissions of the XBPs at different temperatures, characterized by Differential Emission Measure (DEM). We compared the observed DEM with the modeled DEM obtained from the hydrodynamic simulation of XBPs. Our results suggest that the frequent heat deposition by impulsive events can mention the heating of XBPs plasma.

Chapter 6: In the previous chapters, we have studied solar corona during the minimum of solar cycle 24 from the disk-integrated observations of XSM. During this minimum period, as the Sun's activity was very low, it could be possible to study the integrated plasma parameters from XBPs, ARs, and small solar flares. However, studying the spatiotemporal evolution of the individual features (e.g., XBPs, ARs, etc.) on the solar disk demands an imaging spectroscopic observation in the X-ray energy range. An imaging spectroscopic instrument requires an X-ray optics. Realizing X-ray optics is challenging due to the energetic nature of X-ray photons. It is feasible to reflect the X-rays using X-ray mirrors of defined geometry and specifications. We have initiated the development of the X-ray mirrors toward the potential requirement for X-ray optics, and, in this context, a multilayer coating facility based on the RF magnetron sputtering technique has been set up. In order to design the X-ray mirrors and characterize them using X-ray reflectivity (XRR) measurements, we have developed the DarpanX package that computes the reflectivity and other optical functions of X-ray mirrors. DarpanX is developed in python3 and is packaged as a module that can be imported into interactive python shells or scripts. DarpanX can be used as a stand-alone package to design any X-ray mirror structure and estimate its physical properties. DarpanX codes are publicly distributed; anybody can use/edit them or add different modules for other purposes.

Chapter 7: We emphasized the requirement of a future X-ray imaging spectroscopic instrument for the Sun and provide a conceptual design for the Solar Imaging X-ray Spectrometer (SIXS). SIXS operates in the X-ray energy range of 0.5-15.0 keV. The instrument has an energy resolution of greater than 150 eV at 5.9 keV and a spatial resolution of $4''$. Numerous significant, long-standing issues in heliophysics can be solved by the suggested design. It will be able to advance our understanding of the FIP effect and coronal heating, two crucial astrophysical problems. We have outlined the main scientific objectives of the proposed SIXS and evaluated the instrument's capability to meet these objectives.

8.2 Future Works

Using the broad-band X-ray spectroscopic observations, we have extensively studied the elemental abundance evolution of the quiet Sun XBPs, ARs, and small flares (Chapter 3 and 4). Though the abundances of XBPs and ARs are found to remain constant in time, during the flares, the abundances vary from coronal to near photospheric values (Chapter 4). During the impulsive phase of the flare, the abundances reduce from the coronal to near photospheric values, and during the decay phase, the abundances quickly recover to the coronal values. To explain these observations, we proposed two possible physical scenarios. To validate these proposed scenarios, a details simulation effort is required that can be attempted in a future study. This will also help us to improve our understanding of the relation between the flaring mechanisms and the FIP effect.

In Chapter 5, we studied the heating of X-ray bright points (XBP). We estimated the DEM of XBPs and compared it with the modeled DEM obtained from the coronal loop simulation. In the present work, the DEM is modeled by considering the release of magnetic energy from the breaded magnetic field lines. Here, the exact mechanism which is responsible for releasing the magnetic energy has not been studied. This can be studied in the future along with other possible heating scenarios (e.g., by the dissipation of Alfvén wave, the energy released by magnetic reconnection, etc.).

In the present work, we established the methodology of determining the DEM using the combined data of the XSM and AIA. XSM is sensitive to much higher temperatures, whereas the other instruments (e.g., AIA) are sensitive to lower temperatures. The combined data of the XSM and other instruments will provide a unique opportunity to estimate the DEM of ARs and flares. Thus one of the immediate future work would be to constrain the DEM of ARs and flares at both low and high temperatures using the combined data of XSM and AIA.

XSM is observing the Sun from the minimum of solar cycle 24 and is expected to continue the solar observation at least in the rising phase of the solar cycle 25. XSM spectrum can provide accurate measurements of the plasma parameters, i.e., temperature, EM, and abundances. Thus in the near future, the XSM observations will be useful in studying the variation of the plasma properties with the activity of the Sun.

In this work, we have initiated the development of the X-ray mirrors and X-ray optics at Physical Research Laboratory, India, as a potential requirement for future X-ray instrumentation. This development will be continued further.

Bibliography

2020, DarpanX User's Manual, Available at https://github.com/biswajitmb/DarpanX/blob/master/DarpanX_UserManual.pdf [Cited on pages 151 and 152.]

2020, X-Ray Form Factor, Attenuation, and Scattering Tables, Available at https://physics.nist.gov/PhysRefData/FFast/html/form.html (2020/01/01) [Cited on page 149.]

2020, An X-Ray Spectral Fitting Package; User's Guide for version 12.11, Available at https://heasarc.gsfc.nasa.gov/xanadu/xspec/XspecManual.pdf [Cited on pages 39 and 151.]

Acton, L. W., Culhane, J. L., Gabriel, A. H., et al. 1980, *Solar Physics*, 65, 53 [Cited on page 33.]

Agostinelli, S., Allison, J., Amako, K., et al. 2003, Nuclear Instruments and Methods in Physics Research A, 506, 250 [Cited on page 31.]

Alfvén, H. 1947, *Monthly Notices of Royal Astronomical Society*, 107, 211 [Cited on page 172.]

Allison, J., Amako, K., Apostolakis, J., et al. 2006, IEEE Transactions on Nuclear Science, 53, 270 [Cited on page 31.]

—. 2016, Nuclear Instruments and Methods in Physics Research A, 835, 186 [Cited on page 31.]

Antonucci, E., Dennis, B. R., Gabriel, A. H., & Simnett, G. M. 1985, *Solar Physics*, 96, 129 [Cited on page 87.]

Arnaud, K., Dorman, B., & Gordon, C. 1999, XSPEC: An X-ray spectral fitting package, ascl:9910.005 [Cited on pages 39, 42, 80, and 133.]

Arnaud, K. A. 1996, in Astronomical Society of the Pacific Conference Series, Vol. 101, Astronomical Data Analysis Software and Systems V, ed. G. H. Jacoby & J. Barnes, 17 [Cited on page 60.]

Aschwanden, M. J. 2004, Physics of the Solar Corona. An Introduction [Cited on pages 5, 11, 12, 16, 26, 27, 28, 29, and 116.]

Athiray, P. S., Vievering, J., Glesener, L., et al. 2020, *The Astrophysical Journal*, 891, 78 [Cited on pages 76, 103, 105, 112, and 173.]

Babcock, H. W. 1961, *The Astrophysical Journal*, 133, 572 [Cited on page 12.]

Bandler, S. R., Chervenak, J. A., Datesman, A. M., et al. 2019, Journal of Astronomical Telescopes, Instruments, and Systems, 5, 021017 [Cited on pages 34 and 184.]

Barnes, W. T., Cargill, P. J., & Bradshaw, S. J. 2016, *The Astrophysical Journal*, 829, 31 [Cited on pages 52 and 116.]

Barnes, W. T., Cargill, P. J., & Bradshaw, S. J. 2016, The Astrophysical Journal, 833, 217 [Cited on page 52.]

Benz, A. O. 2017, Living Reviews in Solar Physics, 14, 2 [Cited on pages 89 and 177.]

Björck, M., & Andersson, G. 2007, Journal of Applied Crystallography, 40, 1174 [Cited on page 132.]

Bochsler, P. 2007, *The Astronomy and Astrophysics Review*, 14, 1 [Cited on pages 20 and 176.]

Boerner, P., Edwards, C., Lemen, J., et al. 2012, *Solar Physics*, 275, 41 [Cited on page 106.]

Boerner, P. F., Testa, P., Warren, H., Weber, M. A., & Schrijver, C. J. 2014, *Solar Physics*, 289, 2377 [Cited on page 103.]

Born, M., Wolf, E., Bhatia, A. B., et al. 1999, Principles of Optics: Electromagnetic Theory of Propagation, Interference and Diffraction of Light, 7th edn. (Cambridge University Press), doi:10.1017/CBO9781139644181 [Cited on page 136.]

Bradley, L., Sipőcz, B., Robitaille, T., et al. 2021, astropy/photutils: 1.2.0, doi:10.5281/zenodo.5525286 [Cited on page 107.]

Bradshaw, S. J., & Cargill, P. J. 2006, *Astronomy & Astrophysics*, 458, 987 [Cited on page 100.]

Bradshaw, S. J., & Klimchuk, J. A. 2011, *The Astrophysical Journal Supplement Series*, 194, 26 [Cited on page 172.]

Bradshaw, S. J., & Viall, N. M. 2016, *The Astrophysical Journal*, 821, 63 [Cited on page 100.]

Brejnholt, N. 2012, PhD thesis, DTU Space — National Space Institute — Technical University of Denmark [Cited on page 155.]

Brooks, D. H., Baker, D., van Driel-Gesztelyi, L., & Warren, H. P. 2017, Nature Communications, 8, 183 [Cited on page 56.]

Brooks, D. H., Warren, H. P., Williams, D. R., & Watanabe, T. 2009, *The Astrophysical Journal*, 705, 1522 [Cited on pages 50, 68, 101, and 124.]

Brosius, J. W., Daw, A. N., & Rabin, D. M. 2014, *The Astrophysical Journal*, 790, 112 [Cited on pages 18 and 101.]

Cargill, P. J. 1994, *The Astrophysical Journal*, 422, 381 [Cited on pages 18 and 172.]

Cargill, P. J., Bradshaw, S. J., & Klimchuk, J. A. 2012, *The Astrophysical Journal*, 752, 161 [Cited on page 51.]

Cargill, P. J., Bradshaw, S. J., & Klimchuk, J. A. 2012, The Astrophysical Journal, 758, 5 [Cited on pages 51 and 116.]

Cargill, P. J., & Klimchuk, J. A. 2004, *The Astrophysical Journal*, 605, 911 [Cited on pages 18 and 172.]

Carmichael, H. 1964, A Process for Flares, Vol. 50, 451 [Cited on page 86.]

Carole, J. 1976, Philosophical Transactions of the Royal Society of London Series A, 404, doi:10.1098/rsta.1976.0037 [Cited on page 172.]

Carroll, B. W., & Ostlie, D. A. 1996, An Introduction to Modern Astrophysics [Cited on pages 7, 8, and 9.]

Caspi, A., Woods, T. N., & Warren, H. P. 2015, The Astrophysical Journal, 802, L2 [Cited on pages 18, 57, and 101.]

Cheung, M. C. M., Boerner, P., Schrijver, C. J., et al. 2015, *The Astrophysical Journal*, 807, 143 [Cited on page 47.]

Christe, S., Hannah, I. G., Krucker, S., McTiernan, J., & Lin, R. P. 2008, The Astrophysical Journal, 677, 1385 [Cited on page 78.]

Christensen-Dalsgaard, J., Dappen, W., Ajukov, S. V., et al. 1996, Science, 272, 1286 [Cited on page 8.]

Cooper, K., Hannah, I. G., Grefenstette, B. W., et al. 2020, *The Astrophysical Journal Letters*, 893, L40 [Cited on pages 76 and 187.]

Culhane, J. L., Hiei, E., Doschek, G. A., et al. 1991, *Solar Physics*, 136, 89 [Cited on page 33.]

Culhane, J. L., Harra, L. K., James, A. M., et al. 2007, *Solar Physics*, 243, 19 [Cited on page 173.]

Czaykowska, A., Pontieu, B. D., Alexander, D., & Rank, G. 1999, The Astrophysical Journal, 521, L75 [Cited on page 88.]

Dahlburg, R. B., Laming, J. M., Taylor, B. D., & Obenschain, K. 2016, *The Astrophysical Journal*, 831, 160 [Cited on pages 6, 69, and 89.]

De Pontieu, B., Hansteen, V. H., McIntosh, S. W., & Patsourakos, S. 2009, *The Astrophysical Journal*, 702, 1016 [Cited on page 127.]

Del Zanna, G. 2013, *Astronomy & Astrophysics*, 558, A73 [Cited on pages 70, 71, 92, and 188.]

—. 2019, *Astronomy & Astrophysics*, 624, A36 [Cited on pages 56, 101, and 124.]

Del Zanna, G., Dere, K. P., Young, P. R., & Landi, E. 2021, *The Astrophysical Journal*, 909, 38 [Cited on pages 26, 30, and 79.]

Del Zanna, G., & Mason, H. E. 2014, *Astronomy & Astrophysics*, 565, A14 [Cited on page 56.]

—. 2018, Living Reviews in Solar Physics, 15, 5 [Cited on pages 21, 28, 30, 47, 56, 79, 101, and 103.]

Del Zanna, G., Tripathi, D., Mason, H., Subramanian, S., & O'Dwyer, B. 2015, *Astronomy & Astrophysics*, 573, A104 [Cited on pages 18 and 101.]

Del Zanna, G., & Woods, T. N. 2013, *Astronomy & Astrophysics*, 555, A59 [Cited on page 76.]

Del Zanna, G., Mondal, B., Rao, Y. K., et al. 2022, arXiv e-prints, arXiv:2207.06879 [Cited on pages 75, 84, and 86.]

Dennis, B. R., Phillips, K. J. H., Schwartz, R. A., et al. 2015, *The Astrophysical Journal*, 803, 67 [Cited on pages 57 and 76.]

Doriese, W. B., Abbamonte, P., Alpert, B. K., et al. 2017, Review of Scientific Instruments, 88, 053108 [Cited on pages 34 and 184.]

Doschek, G. A., & Warren, H. P. 2019, *The Astrophysical Journal*, 884, 158 [Cited on page 56.]

Drake, G. W. F. 1986, *Physical Review A*, 34, 2871 [Cited on page 30.]

Duncan, J., Glesener, L., Grefenstette, B. W., et al. 2021, *The Astrophysical Journal*, 908, 29 [Cited on page 76.]

Eckart, M. E., Adams, J. S., Boyce, K. R., et al. 2016, in Society of Photo-Optical Instrumentation Engineers (SPIE) Conference Series, Vol. 9905, Space Telescopes and Instrumentation 2016: Ultraviolet to Gamma Ray, ed. J.-W. A. den Herder, T. Takahashi, & M. Bautz, 99053W [Cited on page 184.]

Evangelista, Y., Ambrosino, F., Feroci, M., et al. 2018, Journal of Instrumentation, 13, P09011 [Cited on page 184.]

Feldman, U. 1992, *Physica Scripta*, 46, 202 [Cited on pages 19, 20, 31, 56, 66, 67, 72, and 76.]

Feldman, U., & Laming, J. M. 2000, *Physica Scripta*, 61, 222 [Cited on pages 19, 20, and 56.]

Feldman, U., Mandelbaum, P., Seely, J. F., Doschek, G. A., & Gursky, H. 1992, *The Astrophysical Journal Supplement Series*, 81, 387 [Cited on pages 70 and 71.]

Feldman, U., Schuhle, U., Widing, K. G., & Laming, J. M. 1998, The Astrophysical Journal, 505, 999 [Cited on pages 20 and 176.]

Feldman, U., & Widing, K. G. 1990, *The Astrophysical Journal*, 363, 292 [Cited on page 76.]

—. 1993, *The Astrophysical Journal*, 414, 381 [Cited on page 56.]

—. 2003, *Space Science Reviews*, 107, 665 [Cited on pages 19, 20, and 56.]

Fletcher, L., & Hudson, H. S. 2008, The Astrophysical Journal, 675, 1645 [Cited on page 89.]

Fletcher, L., Dennis, B. R., Hudson, H. S., et al. 2011, *Space Science Reviews*, 159, 19 [Cited on page 88.]

Fludra, A., & Schmelz, J. T. 1999, *Astronomy & Astrophysics*, 348, 286 [Cited on pages 56, 66, 67, 71, and 72.]

Fontenla, J. M., Avrett, E. H., & Loeser, R. 1990, *The Astrophysical Journal*, 355, 700 [Cited on page 11.]

Freeland, S. L., & Handy, B. N. 1998, *Solar Physics*, 182, 497 [Cited on pages 103 and 105.]

Gabriel, A. H. 1976, Philosophical Transactions of the Royal Society of London Series A, 281, 339 [Cited on page 11.]

Garmire, G. P., Bautz, M. W., Ford, P. G., Nousek, J. A., & Ricker, George R., J. 2003, in Society of Photo-Optical Instrumentation Engineers (SPIE) Conference Series, Vol. 4851, X-Ray and Gamma-Ray Telescopes and Instruments for Astronomy., ed. J. E. Truemper & H. D. Tananbaum, 28–44 [Cited on page 183.]

Glesener, L., Krucker, S., Hannah, I. G., et al. 2017, *The Astrophysical Journal*, 845, 122 [Cited on page 187.]

Glesener, L., Krucker, S., Christe, S., et al. 2016, in Society of Photo-Optical Instrumentation Engineers (SPIE) Conference Series, Vol. 9905, Space Telescopes and Instrumentation 2016: Ultraviolet to Gamma Ray, ed. J.-W. A. den Herder, T. Takahashi, & M. Bautz, 99050E [Cited on page 173.]

Glesener, L., Krucker, S., Duncan, J., et al. 2020, *The Astrophysical Journal Letters*, 891, L34 [Cited on page 76.]

Godet, O., Beardmore, A. P., Abbey, A. F., et al. 2007, in Society of Photo-Optical Instrumentation Engineers (SPIE) Conference Series, Vol. 6686, UV, X-Ray, and Gamma-Ray Space Instrumentation for Astronomy XV, ed. O. H. Siegmund, 66860A [Cited on page 183.]

Golub, L., Deluca, E. E., Sette, A., & Weber, M. 2004a, in Astronomical Society of the Pacific Conference Series, Vol. 325, The Solar-B Mission and the Forefront of Solar Physics, ed. T. Sakurai & T. Sekii, 217 [Cited on pages 47 and 48.]

Golub, L., Deluca, E. E., Sette, A., & Weber, M. 2004b, in Astronomical Society of the Pacific Conference Series, Vol. 325, The Solar-B Mission and the Forefront of Solar Physics, ed. T. Sakurai & T. Sekii, 217 [Cited on page 105.]

Golub, L., Krieger, A. S., Silk, J. K., Timothy, A. F., & Vaiana, G. S. 1974a, *The Astrophysical Journal Letters*, 189, L93 [Cited on page 13.]

—. 1974b, *The Astrophysical Journal Letters*, 189, L93 [Cited on page 68.]

Golub, L., Deluca, E., Austin, G., et al. 2007, *Solar Physics*, 243, 63 [Cited on pages 11, 12, 45, 67, 105, and 173.]

Hannah, I. G., Christe, S., Krucker, S., et al. 2008, The Astrophysical Journal, 677, 704 [Cited on pages 78, 121, and 187.]

Hannah, I. G., Kleint, L., Krucker, S., et al. 2019, *The Astrophysical Journal*, 881, 109 [Cited on page 187.]

Hannah, I. G., & Kontar, E. P. 2012, *Astronomy & Astrophysics*, 539, A146 [Cited on pages 47, 49, 50, and 111.]

Hannah, I. G., Grefenstette, B. W., Smith, D. M., et al. 2016, *The Astrophysical Journal Letters*, 820, L14 [Cited on page 174.]

Hara, H., & Nakakubo-Morimoto, K. 2003, *The Astrophysical Journal*, 589, 1062 [Cited on page 13.]

Harrison, F. A., Craig, W. W., Christensen, F. E., et al. 2013, The Astrophysical Journal, 770, 103 [Cited on page 173.]

Hénoux, J.-C. 1998, *Space Science Reviews*, 85, 215 [Cited on page 19.]

Hirayama, T. 1974, *Solar Physics*, 34, 323 [Cited on page 86.]

Houck, J. C., Davis, J. E., Huenemoerder, D., et al. 2013, ISIS: Interactive Spectral Interpretation System for High Resolution X-Ray Spectroscopy, ascl:1302.002 [Cited on page 133.]

Hudson, H. S. 1991, *Solar Physics*, 133, 357 [Cited on page 76.]

Ishikawa, S.-n., Glesener, L., Krucker, S., et al. 2017, Nature Astronomy, 1, 771 [Cited on pages 18, 101, 105, and 173.]

Jackson, J. D. 1999, Classical electrodynamics, 3rd edn. (New York, NY: Wiley) [Cited on page 136.]

Janardhan, P., Bisoi, S. K., Ananthakrishnan, S., Tokumaru, M., & Fujiki, K. 2011, *Geophysical Research Letters*, 38, L20108 [Cited on page 57.]

Janardhan, P., Bisoi, S. K., Ananthakrishnan, S., et al. 2015, Journal of Geophysical Research (Space Physics), 120, 5306 [Cited on page 57.]

Joensen, K. D., Voutov, P., Szentgyorgyi, A., et al. 1995, Appl. Opt., 34, 7935 [Cited on page 131.]

Joensen, K. D., Christensen, F. E., Schnopper, H. W., et al. 1993, in Society of Photo-Optical Instrumentation Engineers (SPIE) Conference Series, Vol. 1736, SPIE Proceedings, ed. R. B. Hoover, 239–248 [Cited on pages 131, 155, and 162.]

Kariyappa, R., Deluca, E. E., Saar, S. H., et al. 2011, *Astronomy & Astrophysics*, 526, A78 [Cited on page 69.]

Kashyap, V., & Drake, J. J. 1998, *The Astrophysical Journal*, 503, 450 [Cited on page 47.]

Katsukawa, Y., & Tsuneta, S. 2001, *The Astrophysical Journal*, 557, 343 [Cited on page 100.]

Kelley, R. L., Mitsuda, K., Allen, C. A., et al. 2007, *Publications of the Astronomical Society of Japan*, 59, 77 [Cited on page 184.]

Kirkpatrick, P., & Baez, A. V. 1948, Journal of the Optical Society of America (1917-1983), 38, 766 [Cited on page 130.]

Klimchuk, J. A. 2006, *Solar Physics*, 234, 41 [Cited on pages 15, 16, 17, 18, 100, 126, 171, and 172.]

—. 2015, Philosophical Transactions of the Royal Society of London Series A, 373, 20140256 [Cited on pages 18, 52, 100, 116, 119, and 172.]

—. 2017, arXiv e-prints, arXiv:1709.07320 [Cited on pages 88 and 172.]

Klimchuk, J. A., Patsourakos, S., & Cargill, P. J. 2008, *The Astrophysical Journal*, 682, 1351 [Cited on pages 51, 116, 118, and 125.]

Knoll, G. F. 1979, Radiation detection and measurement [Cited on page 32.]

Kopp, R. A., & Pneuman, G. W. 1976, *Solar Physics*, 50, 85 [Cited on page 86.]

Kosugi, T., Matsuzaki, K., Sakao, T., et al. 2007, *Solar Physics*, 243, 3 [Cited on pages 12 and 45.]

Krieger, A. S., Vaiana, G. S., & van Speybroeck, L. P. 1971, in Solar Magnetic Fields, ed. R. Howard, Vol. 43, 397 [Cited on page 13.]

Krucker, S., Christe, S., Glesener, L., et al. 2014, *The Astrophysical Journal Letters*, 793, L32 [Cited on page 173.]

Krucker, S., Hurford, G. J., Grimm, O., et al. 2020, *Astronomy & Astrophysics*, 642, A15 [Cited on page 173.]

Kuhar, M., Krucker, S., Glesener, L., et al. 2018, *The Astrophysical Journal Letters*, 856, L32 [Cited on pages 14 and 76.]

Lakshitha, N., **Mondal**, B., Narendranath, S., & Paul, K. 2022, Under preparation [Cited on page 187.]

Laming, J. M. 2004, *The Astrophysical Journal*, 614, 1063 [Cited on pages 19, 20, 56, 88, and 89.]

—. 2009, *The Astrophysical Journal*, 695, 954 [Cited on pages 20, 56, and 69.]

—. 2012, *The Astrophysical Journal*, 744, 115 [Cited on page 20.]

Laming, J. M. 2015, Living Reviews in Solar Physics, 12, 1 [Cited on pages 20, 56, and 176.]

—. 2017, The Astrophysical Journal, 844, 153 [Cited on page 89.]

Laming, J. M. 2021, *The Astrophysical Journal*, 909, 17 [Cited on page 20.]

Laming, J. M., Adams, J., Alexander, D., et al. 2010, arXiv e-prints, arXiv:1011.4052 [Cited on page 185.]

Lanzafame, A. C., Brooks, D. H., & Lang, J. 2005, *Astronomy & Astrophysics*, 432, 1063 [Cited on pages 101 and 124.]

Leibacher, J., Sakurai, T., Schrijver, C. J., & van Driel-Gesztelyi, L. 2010, Solar Physics, 263, 1 [Cited on page 78.]

Lemen, J. R., Title, A. M., Akin, D. J., et al. 2012, *Solar Physics*, 275, 17 [Cited on pages 10, 45, 78, and 172.]

Lin, R. P., & Hudson, H. S. 1976, *Solar Physics*, 50, 153 [Cited on page 177.]

Lin, R. P., Dennis, B. R., Hurford, G. J., et al. 2002, *Solar Physics*, 210, 3 [Cited on page 173.]

Madjarska, M. S. 2019, Living Reviews in Solar Physics, 16, 2 [Cited on pages 101, 113, and 125.]

Mandrini, C. H., Démoulin, P., & Klimchuk, J. A. 2000, *The Astrophysical Journal*, 530, 999 [Cited on pages 126 and 128.]

Mason, H. E. 1975, *Monthly Notices of Royal Astronomical Society*, 171, 119 [Cited on page 57.]

Meyer, J. P. 1985, *The Astrophysical Journal Supplement Series*, 57, 173 [Cited on page 56.]

Mithun, N. P. S., Vadawale, S. V., Shanmugam, M., et al. 2020a, Experimental Astronomy, arXiv:2007.07326 [Cited on pages 36 and 58.]

Mithun, N. P. S., Vadawale, S. V., Sarkar, A., et al. 2020b, *Solar Physics*, 295, 139 [Cited on pages 36, 58, 60, 63, and 178.]

Mithun, N. P. S., Vadawale, S. V., Patel, A. R., et al. 2021, Astronomy and Computing, 34, 100449 [Cited on pages 36 and 58.]

Mitra-Kraev, U., & Del Zanna, G. 2019, *Astronomy & Astrophysics*, 628, A134 [Cited on page 76.]

Mondal, B., Vadawale, S. V., Mithun, N. P. S., et al. 2021a, Astronomy and Computing, 34, 100446 [Cited on page 129.]

Mondal, B., Sarkar, A., Vadawale, S. V., et al. 2021b, arXiv e-prints, arXiv:2107.07825 [Cited on pages 42 and 75.]

Moore, C. S., Caspi, A., Woods, T. N., et al. 2018, *Solar Physics*, 293, 21 [Cited on page 57.]

Nakagawa, Y., & Raadu, M. A. 1972, *Solar Physics*, 25, 127 [Cited on page 114.]

Narendranath, S., Sreekumar, P., Alha, L., et al. 2014, *Solar Physics*, 289, 1585 [Cited on page 57.]

Narendranath, S., Sreekumar, P., Pillai, N. S., et al. 2020a, *Solar Physics*, 295, 175 [Cited on page 57.]

—. 2020b, *Solar Physics*, 295, 175 [Cited on page 76.]

Nelson, A. 2006, Journal of Applied Crystallography, 39, 273 [Cited on page 132.]

Nevot, L., Pardo, B., & Corno, J. 1988, Revue de Physique Appliquee, 23, 1675 [Cited on page 139.]

Nita, G. M., Viall, N. M., Klimchuk, J. A., et al. 2018, *The Astrophysical Journal*, 853, 66 [Cited on pages 51 and 113.]

Oda, M. 1965, Appl. Opt., 4, 143 [Cited on page 44.]

Panini, S., Nayak, M., Shyama Narendranath, K., et al. 2018, Journal of Optics (India), 47, 91 [Cited on page 157.]

Pareschi, G., Spiga, D., & Pelliciari, C. 2021, X-ray Telescopes Based on Wolter-I Optics [Cited on pages 180 and 182.]

Parker, E. N. 1988, *The Astrophysical Journal*, 330, 474 [Cited on pages 17, 18, 116, 127, and 171.]

Pesnell, W. D., Thompson, B. J., & Chamberlin, P. C. 2012, *Solar Physics*, 275, 3 [Cited on pages 9 and 45.]

Phillips, K. J. H., Feldman, U., & Landi, E. 2008, Ultraviolet and X-ray Spectroscopy of the Solar Atmosphere [Cited on page 10.]

Pipin, V. V., & Tomozov, V. M. 2018, Astronomy Reports, 62, 281 [Cited on page 56.]

Pottasch, S. R. 1963, *The Astrophysical Journal*, 137, 945 [Cited on pages 6, 19, and 56.]

Reale, F., & Orlando, S. 2008, *The Astrophysical Journal*, 684, 715 [Cited on page 100.]

Ryan, D. F., Milligan, R. O., Gallagher, P. T., et al. 2012, The Astrophysical Journal Supplement Series, 202, 11 [Cited on page 88.]

Saba, J. L. R. 1995, Advances in Space Research, 15, 13 [Cited on pages 19, 20, and 56.]

Saha, T. T., Content, D. A., & Zhang, W. W. 2004, in Society of Photo-Optical Instrumentation Engineers (SPIE) Conference Series, Vol. 5168, Optics for EUV, X-Ray, and Gamma-Ray Astronomy, ed. O. Citterio & S. L. O'Dell, 346–351 [Cited on page 180.]

Sakamoto, Y., Tsuneta, S., & Vekstein, G. 2008, *The Astrophysical Journal*, 689, 1421 [Cited on page 100.]

Scherrer, P. H., Schou, J., Bush, R. I., et al. 2012, *Solar Physics*, 275, 207 [Cited on pages 9 and 113.]

Schmelz, J. T., Reames, D. V., von Steiger, R., & Basu, S. 2012, *The Astrophysical Journal*, 755, 33 [Cited on pages 56, 66, and 67.]

Schmelz, J. T., Reames, D. V., von Steiger, R., & Basu, S. 2012, The Astrophysical Journal, 755, 33 [Cited on page 72.]

Schwab, B. D., Sewell, R. H. A., Woods, T. N., et al. 2020, *The Astrophysical Journal*, 904, 20 [Cited on page 57.]

Seehafer, N. 1978, *Solar Physics*, 58, 215 [Cited on page 114.]

Seely, J. F., Kowalski, M. P., Hunter, W. R., & Gutman, G. 1996, Appl. Opt., 35, 4408 [Cited on page 131.]

Shanmugam, M., Vadawale, S. V., Patel, A. R., et al. 2020, Current Science, 118, 45 [Cited on page 35.]

Singam, P. 2019, PhD thesis, doi:10.13140/RG.2.2.30197.63205 [Cited on page 142.]

Singam, P. S., Nayak, M., Gupta, R., et al. 2018, Journal of Astronomical Telescopes, Instruments, and Systems, 4, 1 [Cited on page 157.]

Spiga, D. 2005, PhD thesis, Physics and Astronomy — University of Milan-Bicocca, doi:10.13140/RG.2.2.34002.81602 [Cited on pages 139 and 142.]

Spiga, D., Mirone, A., Ferrero, C., et al. 2004, in Society of Photo-Optical Instrumentation Engineers (SPIE) Conference Series, Vol. 5536, Advances in Computational Methods for X-Ray and Neutron Optics, ed. M. Sanchez del Rio, 71–80 [Cited on page 132.]

Spiga, D., Mirone, A., Pareschi, G., et al. 2006, in Society of Photo-Optical Instrumentation Engineers (SPIE) Conference Series, Vol. 6266, Space Telescopes and Instrumentation II: Ultraviolet to Gamma Ray, 626616 [Cited on page 132.]

Stearns, D. G. 1989, Journal of Applied Physics, 65, 491 [Cited on page 140.]

Stoev, K. N., & Sakurai, K. 1999, Spectrochimica Acta Part B: Atomic Spectroscopy, 54, 41 [Cited on page 139.]

Strong, K. 1979, PhD thesis, University College London, UK [Cited on page 48.]

Strüder, L., Briel, U., Dennerl, K., et al. 2001a, *Astronomy & Astrophysics*, 365, L18 [Cited on page 183.]

—. 2001b, *Astronomy & Astrophysics*, 365, L18 [Cited on page 185.]

Sturrock, P. A. 1966, *Nature*, 211, 695 [Cited on page 86.]

Sylwester, B., Phillips, K. J. H., Sylwester, J., & Kepa, A. 2015, *The Astrophysical Journal*, 805, 49 [Cited on page 76.]

Sylwester, B., Sylwester, J., Phillips, K. J. H., Kepa, A., & Mrozek, T. 2014, The Astrophysical Journal, 787, 122 [Cited on pages 20 and 76.]

Sylwester, B., Sylwester, J., Siarkowski, M., et al. 2019, *Solar Physics*, 294, 176 [Cited on pages 14, 65, 124, and 187.]

Sylwester, J., Gaicki, I., Kordylewski, Z., et al. 2005, *Solar Physics*, 226, 45 [Cited on pages 33 and 34.]

Tawara, Y., Yamashita, K., Kunieda, H., et al. 1998, in Society of Photo-Optical Instrumentation Engineers (SPIE) Conference Series, Vol. 3444, X-Ray Optics, Instruments, and Missions, ed. R. B. Hoover & A. B. Walker, 569–575 [Cited on page 131.]

Thompson, M. J., Toomre, J., Anderson, E. R., et al. 1996, Science, 272, 1300 [Cited on page 12.]

Tripathi, D., Klimchuk, J. A., & Mason, H. E. 2011, The Astrophysical Journal, 740, 111 [Cited on pages 18 and 101.]

Türler, M., Chernyakova, M., Courvoisier, T. J. L., et al. 2010, *Astronomy & Astrophysics*, 512, A49 [Cited on page 193.]

Vadawale, S. V., Mondal, B., Mithun, N. P. S., et al. 2021a, The Astrophysical Journal Letters, 912, L12 [Cited on pages 55, 101, 105, 107, and 125.]

Vadawale, S. V., Mithun, N. P. S., Mondal, B., et al. 2021b, The Astrophysical Journal Letters, 912, L13 [Cited on pages 14, 60, 76, 78, 102, 123, 127, 175, and 187.]

Vaiana, G. S., Davis, J. M., Giacconi, R., et al. 1973a, *The Astrophysical Journal Letters*, 185, L47 [Cited on page 13.]

Vaiana, G. S., Krieger, A. S., & Timothy, A. F. 1973b, *Solar Physics*, 32, 81 [Cited on page 13.]

Van Doorsselaere, T., Srivastava, A. K., Antolin, P., et al. 2020, *Space Science Reviews*, 216, 140 [Cited on page 16.]

van Speybroeck, L. P., & Chase, R. C. 1972, *Applied Optics*, 11, 440 [Cited on page 181.]

Vanitha, M., Veeramuthuvel, P., Kalpana, K., & Nagesh, G. 2020a, in 51st Annual Lunar and Planetary Science Conference, Lunar and Planetary Science Conference, 1994 [Cited on page 35.]

Vanitha, M., Veeramuthuvel, P., Kalpana, K., & Nagesh, G. 2020b, in Lunar and Planetary Science Conference, Lunar and Planetary Science Conference, 1994 [Cited on page 58.]

Veck, N. J., & Parkinson, J. H. 1981a, *Monthly Notices of Royal Astronomical Society*, 197, 41 [Cited on page 48.]

—. 1981b, *Monthly Notices of Royal Astronomical Society*, 197, 41 [Cited on page 90.]

Veck, N. J., Strong, K. T., Jordan, C., et al. 1984, *Monthly Notices of Royal Astronomical Society*, 210, 443 [Cited on page 48.]

Viall, N. M., & Klimchuk, J. A. 2012, *The Astrophysical Journal*, 753, 35 [Cited on page 100.]

—. 2013, *The Astrophysical Journal*, 771, 115 [Cited on page 100.]

—. 2015, *The Astrophysical Journal*, 799, 58 [Cited on page 100.]

Vignaud, G., & Gibaud, A. 2019, Journal of Applied Crystallography, 52, 201 [Cited on page 132.]

Von Steiger, R., Schwadron, N. A., Fisk, L. A., et al. 2000, *Journal of Geophysical Research*, 105, 27217 [Cited on page 176.]

Walker, A. B. C., J. 1972, *Space Science Reviews*, 13, 672 [Cited on page 57.]

Walker, A. B. C., J., Rugge, H. R., & Weiss, K. 1974a, *The Astrophysical Journal*, 188, 423 [Cited on page 57.]

—. 1974b, *The Astrophysical Journal*, 192, 169 [Cited on page 57.]

Warren, H. P. 2014a, *The Astrophysical Journal Letters*, 786, L2 [Cited on pages 20 and 76.]

—. 2014b, *The Astrophysical Journal Letters*, 786, L2 [Cited on page 57.]

Warren, H. P., Byers, J. M., & Crump, N. A. 2017, *The Astrophysical Journal*, 836, 215 [Cited on page 47.]

Weissman, P. R., McFadden, L.-A., & Johnson, T. V. 1999, Encyclopedia of the solar system [Cited on page 7.]

Wenzel, K. P., Marsden, R. G., Page, D. E., & Smith, E. J. 1992, *Astronomy and Astrophysics Supplement Series*, 92, 207 [Cited on page 20.]

Widing, K. G., & Feldman, U. 2001, The Astrophysical Journal, 555, 426 [Cited on page 88.]

Windt, D. L. 1998, Computers in Physics, 12, 360 [Cited on page 132.]

—. 2013, IMD Version 5.0 Installation Guide and User's Manual, Available at `http://www.rxollc.com/idl/` (2020/01/01) [Cited on pages 139 and 153.]

Windt, D. L. 2015, in Society of Photo-Optical Instrumentation Engineers (SPIE) Conference Series, Vol. 9603, Optics for EUV, X-Ray, and Gamma-Ray Astronomy VII, 96031C [Cited on page 131.]

Windt, D. L., Donguy, S., Hailey, C. J., et al. 2003, in Society of Photo-Optical Instrumentation Engineers (SPIE) Conference Series, Vol. 4851, X-Ray and Gamma-Ray Telescopes and Instruments for Astronomy, ed. J. E. Truemper & H. D. Tananbaum, 639–646 [Cited on page 131.]

Winebarger, A. R., Schmelz, J. T., Warren, H. P., Saar, S. H., & Kashyap, V. L. 2011, The Astrophysical Journal, 740, 2 [Cited on pages 18, 101, and 105.]

Winebarger, A. R., Warren, H. P., Schmelz, J. T., et al. 2012, *The Astrophysical Journal Letters*, 746, L17 [Cited on page 70.]

Winebarger, A. R., Warren, H. P., Schmelz, J. T., et al. 2012, The Astrophysical Journal, 746, L17 [Cited on pages 172 and 173.]

Withbroe, G. L., & Noyes, R. W. 1977, *Annual Review of Astronomy and Astrophysics*, 15, 363 [Cited on pages 15 and 125.]

Wolter, H. 1975, Mirror systems with grazing incidence as image-forming optics for X-rays Transl. into ENGLISH from Ann. Phys. (Leipzig), ser. 6, v. 10, 1952 p 94-114, 10, 94 [Cited on pages 44 and 131.]

Wright, P. J., Hannah, I., Grefenstette, B., et al. 2017, in AAS/Solar Physics Division Meeting, Vol. 48, AAS/Solar Physics Division Abstracts #48, 108.02 [Cited on pages 105 and 187.]

Zarro, D. M., & Lemen, J. R. 1988, *The Astrophysical Journal*, 329, 456 [Cited on page 88.]

Zhang, W. W. 2009, in Society of Photo-Optical Instrumentation Engineers (SPIE) Conference Series, Vol. 7437, Optics for EUV, X-Ray, and Gamma-Ray Astronomy IV, ed. S. L. O'Dell & G. Pareschi, 74370N [Cited on page 146.]